Title

Spectroscopic Measurements of Oxide Nanoparticles in Aqueous Environments as a Probe of Nano-Bio Interactions and Nanoconfinement

Author

Sit, Izaac Cuiting

Publication Date

2022

Peer reviewed|Thesis/dissertation

UNIVERSITY OF CALIFORNIA SAN DIEGO

Spectroscopic Measurements of Oxide Nanoparticles in Aqueous Environments as a Probe of Nano-Bio Interactions and Nanoconfinement

A Dissertation submitted in partial satisfaction of the requirements
for the degree Doctor of Philosophy

in

Chemical Engineering

by

Izaac Cuiting Sit

Committee in charge:

Professor Vicki Grassian, Chair
Professor Shaochen Chen, Co-Chair
Professor Jesse Jokerst
Professor Andrew Kummel

2022

The Dissertation of Izaac Cuiting Sit is approved, and it is acceptable in quality and form for publication on microfilm and electronically.

University of California San Diego

2022

DEDICATION

To my mom and brother

and

in memory of, Mary Fraser Sit, Nenita Carvajal, Johnson Cuiting, and Man Ping Chen

Thank you for all your unconditional love and support

TABLE OF CONTENTS

LIST OF FIGURES

LIST OF TABLES

LIST OF ABBREVIATIONS

2DCOS	Two-Dimension Correlation Spectroscopy
AMTIR	Amorphous material transmitting infrared radiation
ATR-FTIR	Attenuated Total Reflectance-Fourier Transform Infrared
BSA	Bovine serum albumin
DNA	Deoxyribonucleic acid
dAMP	Deoxyadenosine monophosphate
dCMP	Deoxycytidine monophosphate
dGMP	Deoxyguanosine monophosphate
dTMP	Deoxythymidine monophosphate
eDNA	Environmental deoxyribonucleic acid
Nano-Bio	Nanoparticle-Biological
NP	Nanoparticle
SI	Supplemental Information

ACKNOWLEDGEMENTS

To Rosita Sit, I can only imagine how difficult it was to raise two boys but you did mom. I will never know the full extent of all the sacrifices and hard work you had to do for us to achieve our goals, but I will be forever grateful, thank you. To my brother, Zachary Sit, who constantly looked out for me, I couldn't have asked for a better bigger brother and role model. I aspire to be a fragment of what my mom and brother are. Thank you both for your unconditional love and support.

Thank you to the rest of my family for your support. To the other doctor in the family, Dr. Siu Po Sit, thank you for pushing me to continue my education and believing in me get a doctorate. You wouldn't have let me forget that I could have gotten a doctorate anyway, so I really had no choice. Onion rings and sweet potato fries are on me next time. Ian and Holly Sit, thanks for gaming with me while writing my thesis and giving me a break from reality. Marc and Mao Carvajal, thank you for living in Canada and providing a safe place to see family, relax, and eat poutine. To my aunt Miranda Chu, thank you for believing in my education and supporting me. I'll never make as good lo mai gai as you do. To the family I've lost along the way who would have loved to see me complete this milestone, I wish you were here and I dedicate my dissertation to you. I love you and I'll see you on the other side. To my friends from UC Berkeley, thank you for believing in and supporting me. I would not know what true friendship was if it was not for Benson Jung, Alisa Bowen, and Yirang Park.

I met Megan Liang at the end of my first year at UCSD. Stressed, crazy-eyed, and carrying 10 textbooks into the study room, I don't know how you were attracted to me but I trapped you. You think it's the other way around but it really isn't. You were there through the highs and lows of graduate school. You *tried* to stay up with me during my 4AM writing sessions, refilled my

water, and brought me snacks to make sure I wasn't hungry. You convinced me to adopt the best dog in the world. You are my rock and were a person of comfort and stability through the tough times. You are the sunshine in my life and I am forever grateful for your support. I love you and I will be your always be your cheeseman. I can't wait to experience life and travel with you.

I would like to thank Professor Vicki Grassian for her support as I would not have achieved as much as I did without her. I still remember the day I met her in early 2017. I received notice that I was accepted into UCSD into the graduate program but it was a two-week deadline before I had to register. I didn't not know which lab I wanted to join and I was scrambling to find a suitable lab. I scheduled meeting with professors and flew down to San Diego, disheveled and stressed but armed with a box full of buttery, sugary cookies with one week until registration deadline. The first two professors were not a good fit and the sun was setting. I walked into Dr. Grassian's office, showed her my resume, offered her some cookies, and she welcomed me to the lab within 10 minutes of talking to her. I don't remember what exactly happened because I blacked out from my nervousness but those had to be some fantastic cookies. Five and a half years later, after numerous projects, collaborations, connections, and lifetime friends, I'm still disheveled but I've managed to have a fantastic mentor that has facilitated my professional growth with opportunities I could have only dreamed of. Thank you for giving me the opportunity to work and learn from you.

I would like to thank my collaborators during my time at UCSD, Dr. Jesse Jokerst and Dr. Shaochen Chen. I would not have had an amazing opportunity to move to and do research at Sandia National Laboratory in New Mexico, without Dr. Anastasia G. Ilgen. A huge thank you to admins Dana Jimenez, Monica Castrejon, and Carmen Alfaro. You are the backbone of the graduate student population and are the unsung heroes of the departments.

UCSD wouldn’t be as enjoyable as it was if it wasn’t for my lab mates and friends. To the 6PM club, Dr. Man Luo, Dr. Victor Or, and Renee Tam, it was fun watching numerous sunsets together. To my mentees, Sayuri Sagisaka and Eleanor Quirk, one of my greatest achievements in graduate school was to help you both get into graduate school. Beyond papers, collaborations, this is something I hold tightest to my heart. I’m thankful to the boiz, Dr. Michael Alves and Dr. Victor Or, for all the laughs and the publication we all co-authors on. You both were people I could rely on to regularly drink afternoon tea with and get me through the day. To Deborah Kim and Stephanie Mora Garcia, the laughter in the office between you two lightened up the space. You both were always someone I could talk and vent to. Dr. Mona Shrestha and Dr. Natalia Gonzalez-Pech, you were awesome role models of what postdocs should be like. Dr. Yash Mantri, it was a crazy five years and I’m glad the housing algorithm matched us in graduate housing. It was a blast living and somehow collaborating with you on a project. I’d like to thank my dog Pancha for all her love and keeping me company, sunbathing next to me while I’m working from home. You’ll always be the best girl.

A portion of Chapter 1 is reproduced from Annual Review of Analytical Chemistry: Sit, I.; Wu, H.; Grassian, V. H. Environmental Aspects of Oxide Nanoparticles: Probing Oxide Nanoparticle Surface Processes Under Different Environmental Conditions. 2021, 14 (1), 489-514. The dissertation author is the first author of this paper.

A portion of Chapter 2 is reproduced with permission from the Annual Review of Analytical Chemistry: Sit, I.; Wu, H.; Grassian, V. H. Environmental Aspects of Oxide Nanoparticles: Probing Oxide Nanoparticle Surface Processes Under Different Environmental Conditions. 2021, 14 (1), 489-514. The dissertation author is the first author of this paper.

Chapter 3, in full, is a reprint of the material as it appears in Langmuir. Sit, I.; Sagisaka, S.; Grassian, V. H. Nucleotide Adsorption on Iron(III) Oxide Nanoparticle Surfaces: Insights into Nano–Geo–Bio Interactions Through Vibrational Spectroscopy. 2020, 36 (51), 15501–15513. The dissertation author is the first author of this paper.

Chapter 4, in full, has been accepted for publication of the material as it may appear in Langmuir. Sit, I.; Quirk, E.; Hettiarachchi, E.; Grassian, V. H. Differential Surface Interactions and Surface Templating of Nucleotides (dGMP, dCMP, dAMP, and dTMP) on Oxide Particle Surfaces. The dissertation author is the first author of this paper.

Chapter 5, in full, has been submitted for publication of the material as it may appear in Journal of Physical Chemistry A. Sit, I.; Young, M. A.; Kubicki, J. D.; Grassian, V. H. Distinguishing Different Surface Interactions for Nucleotides Adsorbed onto Hematite and Goethite Particle Surfaces Through ATR-FTIR Spectroscopy and Ab-Initio Calculations. The dissertation author is the first author of this paper.

Chapter 6, in full, has been submitted for publication of the material as it may appear in Environmental Science: Nano. Sit, I.; Grassian, V. H.; Ilgen, A. G. Formic and Acetic Acid pK_a Values Increase Under Nanoconfinement. The dissertation author is the first author of this paper.

Chapter 7, in full, is a reprint of the material as it appears in Polyhedron. Sit, I.; Xu, Z.; Grassian, V. H. Plasma Protein Adsorption on TiO_2 Nanoparticles: Impact of Surface Adsorption on Temperature-Dependent Structural Changes. 2019, 171, 147–154. The dissertation author is the co-first author of this paper.

A portion of Chapter 8 is reproduced with permission from Journal of Physical Chemistry C. Mantri, Y.; Sit, I.; Zhou, J.; Grassian, V. H.; Jokerst, J. V. Photoacoustic Enhancement of Ferricyanide-Treated Silver Chalcogenide-Coated Gold Nanorods. 2022, 126 (17), 7605–7614.

The dissertation author is a co-author of this paper. A portion of Chapter 8 has been submitted for publication of the material as it may appear in Environmental Science and Technology. Miller, K. L.; Sit, I.; Xiang, Y.; Wu, J.; Pustelnik, J.; Tang, M.; Kiratitanaporn, W.; Grassian, V. H.; Chen, S. Evaluation of CuO Nanoparticle Toxicity on 3D Bioprinted Human iPSC-derived Cardiac Tissues. The dissertation author is a co-author of this paper.

VITA

2015 B.S. in Chemical Engineering and Materials Science and Engineering, University of California, Berkeley

2019 M.S. in Chemical Engineering, University of California San Diego

2022 Ph.D. in Chemical Engineering, University of California San Diego

PUBLICATIONS

Sit, I.; Quirk, E.; Hettiarachchi, E.; Grassian, V. H. Differential Surface Interactions and Surface Templating of Nucleotides (dGMP, dCMP, dAMP, and dTMP) on Oxide Particle Surfaces. *Langmuir*. 2022. Accepted

Alves, M. R.; Deeleepojananan, C.; Or, V. W.; **Sit, I.**; Grassian V. H. Insights into Interactions of Chlorine-Based Cleaning Products with Indoor Relevant Surfaces. *Environmental Chemistry*. 2022. Accepted

Sit, I.; Young, M. A.; Kubicki, J. D.; Grassian, V. H. Distinguishing Different Surface Interactions for Nucleotides Adsorbed onto Hematite and Goethite Particle Surfaces Through ATR-FTIR Spectroscopy and DFT Calculations. *J. Phys. Chem. A.* 2022, Submitted

Sit, I.; Grassian, V. H.; Ilgen, A. G. Formic and Acetic Acid pKa Values Increase Under Nanoconfinement. *Environ. Sci.: Nano.* 2022. Submitted

Miller, K. L.; **Sit, I.**; Xiang, Y.; Wu, J.; Pustelnik, J.; Tang, M.; Kiratitanaporn, W.; Grassian, V. H.; Chen, S. Evaluation of CuO Nanoparticle Toxicity on 3D Bioprinted Human iPSC-derived Cardiac Tissues. *Environ. Sci. Technol.* 2022. Submitted

Mantri, Y.; **Sit, I.**; Zhou, J.; Grassian, V. H.; Jokerst, J. V. Photoacoustic Enhancement of Ferricyanide-Treated Silver Chalcogenide-Coated Gold Nanorods. *J. Phys. Chem. C* 2022, 126 (17), 7605–7614.

Karimova, N. V; Luo, M.; **Sit, I.**; Grassian, V. H.; Gerber, R. B. Absorption Spectra and the Electronic Structure of Gallic Acid in Water at Different pH: Experimental Data and Theoretical Cluster Models. *J. Phys. Chem. A* **2022**, *126* (2), 190–197.

Sit, I.; Wu, H.; Grassian, V. H. Environmental Aspects of Oxide Nanoparticles: Probing Oxide Nanoparticle Surface Processes Under Different Environmental Conditions. *Annu. Rev. Anal. Chem.* 2021, 14 (1), 489–514.

Sit, I.; Sagisaka, S.; Grassian, V. H. Nucleotide Adsorption on Iron(III) Oxide Nanoparticle Surfaces: Insights into Nano–Geo–Bio Interactions Through Vibrational Spectroscopy. *Langmuir* 2020, 36 (51), 15501–15513.

Li, Y.; Shrestha, M.; Luo, M.; **Sit, I.**; Song, M.; Grassian, V. H.; Xiong, W. Salting Up of Proteins at the Air/Water Interface. *Langmuir* 2019, 35 (43), 13815–13820.

Sit, I.; Xu, Z.; Grassian, V. H. Plasma Protein Adsorption on TiO2 Nanoparticles: Impact of Surface Adsorption on Temperature-Dependent Structural Changes. *Polyhedron* 2019, 171, 147–154.

Panganiban, B.; Qiao, B.; Jiang, T.; DelRe, C.; Obadia, M. M.; Nguyen, T. D.; Smith, A. A. A.; Hall, A.; **Sit, I.**; Crosby, M. G.; Dennis, P. B.; Drockenmuller, E.; Olvera de la Cruz, M.; Xu, T. Random Heteropolymers Preserve Protein Function in Foreign Environments. *Science.* 2018, *359* (6381), 1239–1243

FIELD OF STUDY

Major Field of Study: Chemical Engineering

Studies in Chemical Engineering and Analytical Chemistry

Professor Vicki H. Grassian

ABSTRACT OF THE DISSERTATION

Spectroscopic Measurements of Oxide Nanoparticles in Aqueous Environments as a Probe of Nano-Bio Interactions and Nanoconfinement

by

Izaac Cuiting Sit

Doctor of Philosophy in Chemical Engineering

University of California San Diego, 2022

Professor Vicki Grassian, Chair
Professor Shaochen Chen, Co-Chair

Nanoparticles are commonly found in everyday life ranging from additives in consumer products to naturally occurring minerals. Despite being either engineered or naturally occurring, these nanoparticles often interact with environmental aqueous systems that are rich in biomolecules or can be internalized into the human body to encounter biological fluids. Adsorption of biomolecules onto nanoparticle surfaces often changes physicochemical properties, reflecting properties of adsorbed components rather than the nanoparticle. These property changes can influence intermolecular interactions and reduce the number of free molecules in solution, restricting bioavailability. Moreover, the adsorption process can change protein and DNA conformation where misfolded structures can lead to diseases such as, Alzheimer's and Creutzfeldt-Jakob disease. As these nanoparticle-biological complexes move through different biomes, variations in pH and temperature or exposure to nanoscale confinement can occur. The changes to surrounding conditions can further alter the adsorbed composition, biomolecule structure, and nanoparticle physicochemical properties. To predict the fate of these dynamic processes in a multicomponent system, it is necessary to understand the detailed surface chemistry occurring at the nano-bio interface. This dissertation aims to probe the effects of environmental conditions on the stability and persistence of biomolecules and small organic acids on metal oxide nanoparticles and within metal oxide nanoscale pores. These interactions are probed using vibrational spectroscopy as well as other complementary spectroscopic and microscopic techniques. The results from this dissertation provide insights into metal oxide nanoparticle surface chemistry and nanoscale confinement to better understand nano-bio interactions over a range of environmental conditions.

Chapter 1. Introduction

Nanotechnology is a rapidly developing field that has become prevalent in everyday use.[1] Nanomaterial applications impact human life in various ways, which include drug delivery and therapeutics, medical imaging, water filtration, cosmetics, and sunscreen.[2–5] With increasing use of engineered nanomaterials in consumer and commercial applications comes inevitable exposure to biological and environmental systems. Since physiochemical properties of nanomaterials are highly dependent on surface chemistry, it is important to monitor these dynamic processes. In aqueous systems, for example, molecular adsorption and interactions with nanoparticle (NP) surfaces occur, and the formation of an adsorbed layer can alter the physicochemical properties of the NP.[6,7] Size and surface charge can determine the biodistribution and toxicity of internalized NPs[5,8–11] and, when in the environment, particle aggregation impacts sedimentation and translocation through different groundwater biomes. Furthermore, once introduced into a biomolecular-rich milieu containing proteins, lipids, and nucleic material, a biocorona forms. This corona is a dynamic molecular multilayer that can undergo exchange with bulk solution components, altering the nanoparticle-biological (nano-bio) physicochemical properties. As this nano-bio entity passes through different environmental conditions, such as pH and temperature, additional changes can occur to corona composition and surface chemistry. For this reason, it is imperative to understand the biocorona and physicochemical properties because they often determine the fate and transport of NPs within physiological and environmental systems.[5] Ligand adsorption is one important aspect of surface chemistry that results in a new surface identity and surface composition that are greatly affected by solution pH, temperature, and the presence of other ligands.[6,12,21–25,13–20] The pH often determines the surface charge distribution, which is

especially crucial for adsorption processes involving electrostatic interactions. Chemical interactions of surface functional groups and the surface are largely modified by pH. Changes to solution temperature can irreversibly affect biomolecular structure, and specific functions can be lost.[26,27] In addition to the effects of pH and temperature, recent studies have started to focus on the influence of surfaces precoated with molecules, either purposefully or from the surrounding environmental and biologically relevant milieux.[12–17,25,28,29] Metal oxides are prevalent in the environment, whether as engineered anthropogenic or naturally occurring geochemical entities, and they provide active sites for intermolecular interactions that can be detected using vibrational spectroscopy. Of the many types of nanomaterials, nano-TiO_2 is both found in the environment and one of the most produced engineered nanomaterials, with 10,000 tons produced annually, followed by 1,600 tons of ZnO.[30,31] Many of these engineered NPs have already been found in environmental aqueous systems due to sewage treatment plants, waste incineration plants, and landfills.[30,32] Furthermore, use of TiO_2 in consumer products includes sunscreens, paints, food additives, and cosmetics[30,32–34], which has warranted multitudes of studies assessing the effects of NP exposure in the environment and biological systems.[5,7,35–40] NP surfaces evolve in complex aqueous media due to adsorption, desorption, and displacement reactions that significantly alter NP properties and affect their lifetimes in the environment. Adsorption of naturally occurring molecular species, such as oxyanions, amino acids, humic substances, and proteins, on NPs has attracted much attention because they provide a practical understanding of physiochemical property changes when NPs are in different environmental and biological compartments.[41–45] Herein, we focus on reviewing studies of surface chemistry using vibrational spectroscopy on common metal oxide NPs, such as TiO_2, SiO_2, and Fe_2O_3.

In this chapter, we focus on infrared spectroscopy as a tool that can provide insight into NP surface chemistry in aqueous media. Attenuated total reflectance–Fourier transform infrared (ATR-FTIR) spectroscopy studies are highlighted as a specific application of infrared

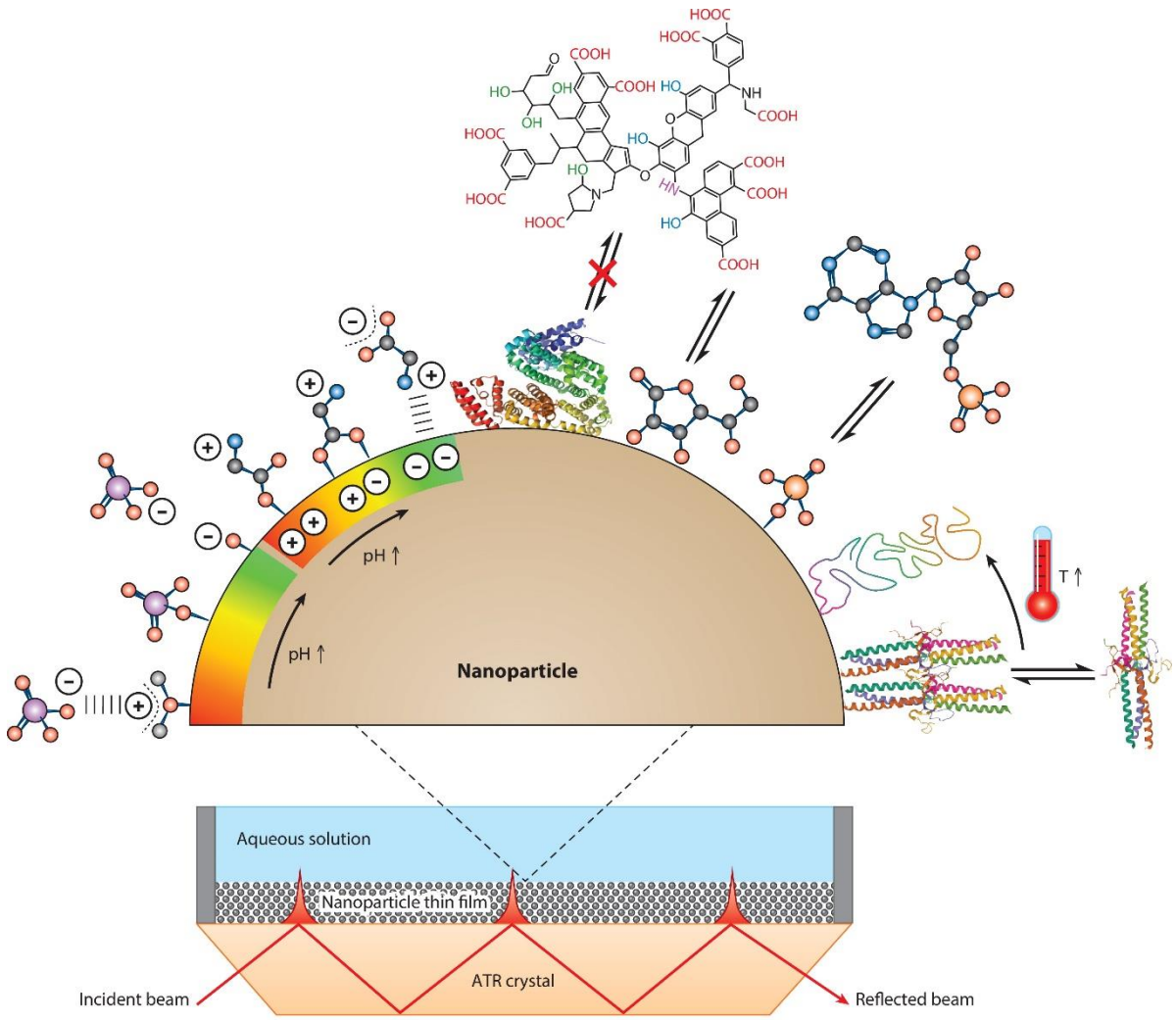

Figure 1.1 ATR-FTIR spectroscopy experiment schematic

Pictorial representation of a typical attenuated total reflectance–Fourier transform infrared (ATR-FTIR) spectroscopy experiment and different surface processes. Several dynamic physicochemical processes, such as surface adsorption, pH-induced transformations, displacement reactions, and temperature effects that can occur on nanoparticle (NP) surfaces under different conditions of pH and temperature in different environments can be probed.

spectroscopy. One of the primary features of ATR-FTIR spectroscopy is in-situ, aqueous measurements to probe molecularly dynamic interactions, such as protein conformational changes[28,46,47], displacement reactions[48], and chemical transformations[49–51] on NP surfaces. Most

importantly, ATR-FTIR spectroscopy with a horizontal flow cell is able to study the kinetics of adsorption in the presence of a strong absorption solvent, such as water, in-situ.[6,10,53–57,12,18,28,41,43,46,47,52] Studies that involve horizontal flow cells are able to flow solutions over thin films to investigate NP-induced changes as a function of time, thus changing experimental conditions and adsorbate surface concentration. A pictorial representation of several types of transformations on NP surfaces that can be probed using ATR-FTIR spectroscopy is shown in **Figure 1.1**. These dynamic processes and interactions include surface adsorption and desorption, displacement, electrostatic interactions, and structural transformations as a function of pH and temperature. As shown, the adsorption of oxyanion molecules and amino acids comprises a mixture of physisorption and chemisorption interactions that are pH dependent. Additionally, competitive adsorption of molecules can occur where adsorbates occupy the same surface-binding sites. This is due to the various surface affinity energetics and is behind the concept of the dynamic exchange process occurring for biocoronas. Moreover, by adsorbing biomolecules such as proteins and DNA onto particle surfaces, conformational changes due to denaturants can be mitigated and molecules can be stabilized. This stabilization effect can increase the persistence and bioavailability of biomolecules in the environment. In this review, we first discuss NP surfaces and the propensity of certain ligands that preferentially bind to them, then provide a brief overview of ATR-FTIR spectroscopy. We then present several case studies, focusing on the surface chemistry influenced by environmental factors: (a) the effects of environmental pH on the adsorption and structures of the adsorbed molecules; (b) synergistic effects of competing molecules on adsorption, including displacement and coadsorption; and (c) the temperature effects on conformation of adsorbed proteins. This is followed by a discussion of two-dimensional correlation spectroscopy (2DCOS) as an analysis method for understanding surface adsorption and

surface chemistry in multicomponent, multivariable systems. Finally, we present an outlook of challenges and future opportunities.

1.1 Environmental Aspects of the Surface Chemistry of Oxide Nanoparticles

Surface chemistry focuses on the phenomena and reactions occurring at the surface or interface, including surface adsorption, surface displacement, ligand reactions, and redox reactions. Molecular adsorption to surfaces can be reversible and/or irreversible, often referred to as physisorption and chemisorption. Physisorption interactions are derived from intermolecular forces (e.g., Van der Waals), whereas chemisorption involves the formation of chemical bonds by transferring, exchanging, and sharing electrons between adsorbate and adsorbent. Typically, chemisorption has a stronger binding energy than physisorption through formation of chemical bonds and thus a smaller interaction distance.[58] The adsorption of molecules depends on the NP

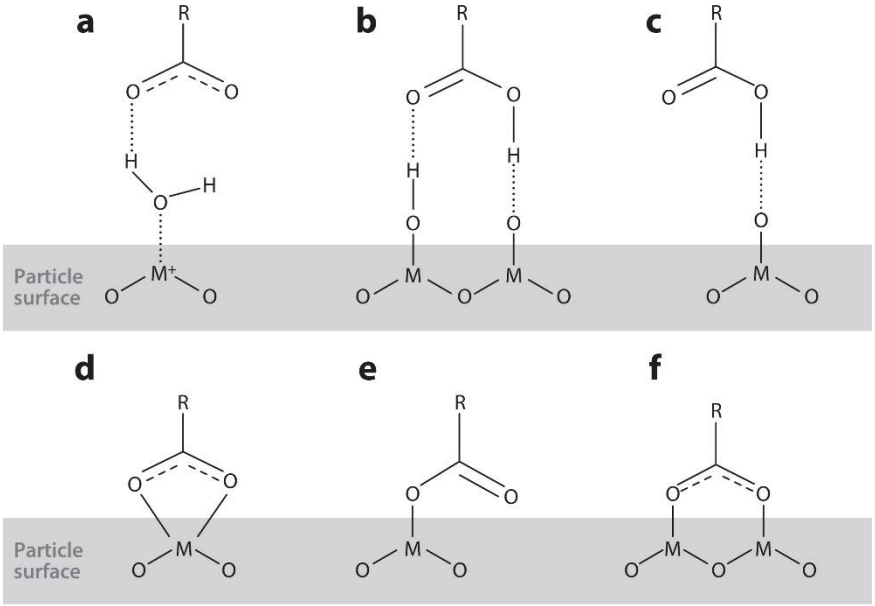

Figure 1.2 Surface binding coordination modes

Possible binding modes of −COOH onto a metal oxide nanoparticle surface. (a) Electrostatic attraction, (b,c) H-bonding, (d) bidentate chelating, (e) monodentate binding, and (f) bidentate bridging.

composition owing to different surface affinities between chemical groups.[59] As a result of water dissociation, hydroxylation can occur on metal oxide surfaces to form surface hydroxyl groups.[60]

Molecules with carboxylic, hydroxyl, silane, and phosphate groups are easily chemisorbed to oxide surfaces (Fe_3O_4 and TiO_2) through surface hydroxyl groups, which are called ligand exchange reactions. Carboxylic and oxyanion moieties[6,61–68] (e.g., carbonate, phosphate, sulfate, and arsenate) are known to complex with surface hydroxyl groups through either physisorption or chemisorption. **Figure 1.2a–c** displays various physisorption modalities for carboxylic acids through hydrogen bonding, whereas **Figure 1.2d–f** shows three main chemisorption modes: bidentate bridging, monodentate binding, and bidentate chelating. Generally, chemisorption requires more energy and is more stable than physisorbed molecules due to bond formation. Moreover, adsorption energies are dependent on crystal facets, as determined using ATR-FTIR and ab initio calculations.[62] For phosphate adsorption onto iron oxide, the NP-oxyanion complex is pH and crystal facet dependent and usually a mixture of multiple modes.[65] This mixture of complexations highlights the different adsorption energies associated with each complex.[61,62] As a result of specific environmental conditions, these different adsorption energies, and subsequently desorption energies, can determine which binding mode is the most prevalent. This can yield insight into changing surface charges as the dominant mode changes from deprotonated monodentate binding to bidentate chelating or bridging. Moreover, the adsorbed adsorbates can compete with other moieties by occupying binding sites[69] , preventing conformational change[28], or by changing NP surface charge.[55] Thus, the liquid-solid interface is important to probe for many biological or environmental systems where water is present. For these reasons, we concentrate this discussion on the water-solid interface in this review. For an oxide NP, the surface is covered by hydroxyl groups and can range from 1 to 10 $-OH/nm^2$, depending on particle composition.[70–72] When oxide NPs are in an aqueous medium, the surface can be charged due to protonation and deprotonation processes of the surface hydroxyl groups.[73] Protonation and deprotonation are

highly influenced by the surrounding pH, and for metal oxides (M), the protonation states are described as below[6,74]:

$$\equiv MOH \leftrightarrow MO^- + H^+ \qquad \textbf{Equation 1.1}$$

$$\equiv MOH + H^+ \leftrightarrow MOH_2{}^+ \qquad \textbf{Equation 1.2}$$

The pH-dependent protonation and deprotonation states change the surface charge of the particle and form the basis of many electrostatic interactions and particle isoelectric point. The pH effects on the adsorption of various types of molecules on NPs are discussed later.[28,46–48,54,57]

1.1.1 pH Effects

Changes to pH can drastically influence NP interactions with the surrounding milieu. Protic molecules have pKa values that correspond to the pH where (de)protonation occurs and the charge of a molecule can be changed. As stated by Equation 1.1 and Equation 1.2, NPs can be charged. The pH where the negative ($[MO^-]$) and positive ($[MOH_2{}^+]$) surface concentrations are equal, a surface charge of 0, is called the point of zero charge (PZC). At a pH lower than then PZC, the particle is positively charged. If the pH is higher than the PZC, the particle is negatively charged. PZC and isoelectric points (IEP) are often used interchangeably but have a subtle distinction between the two terms. The PZC refers to a pristine particle surface, whereas the IEP is where the zeta potential of a particle is zero. The IEP encompasses the PZC and includes any ligands, adsorbed species, or ions surrounding the particle. If it is a pristine particle surface, the PZC is equal to the IEP. The PZC of some common metal oxide surfaces are 1 to 4 for SiO_2, 5.5 to 6.7 for TiO_2, 7 to 8.9 for α-Fe_2O_3, 7.9 to 9 for Al_2O_3, and 6.9 to 9.6 for α-FeOOH to name a few.[75] There is a wide range of PZC for these particles because the value can depend on the synthesis method, morphology, measurement method, and phase of the particle due to the presence of different faces with different hydroxyl group densities and PZC values.

As NPs are transported through different environmental conditions, variations in solution pH can occur. Previous studies reported environmentally relevant pH values ranging from 5 to 8 that can cause alterations to surface charge, molecular speciation, and surface chemistry.[76–78] With an abundance of different naturally occurring oxide NPs and physicochemical properties, it is necessary to understand how nano-bio complexes respond to pH.

Metal oxide chemisorption is highly dependent on surface charges and ligand exchange reactions with surface hydroxyl groups. For example, selenium predominantly enters the environment via anthropogenic sources and is detrimental to aquatic life. Remediation of selenium using various natural minerals as an adsorbent is one common method for its removal. Lounsbury et al. studied the *in-situ* adsorption of Se(VI) ions on nano-hematite and showed that NP adsorption capacity is dependent on pH and surface area.[78] Moreover, above pH 6, Se(VI) forms primarily outer-sphere complexes, and the amount of Se(VI) adsorbed is influenced by readily accessible reactive sites. Furthermore, another study revealed that the amount of Se(VI) remediated decreases with increasing pH on alumina.[79] The spectroscopic results show that the Se(VI) outer-spherical bidentate surface complex is the dominant interfacial species.

Oxyanions, such as phosphate, carbonate, and arsenate, are prevalent in both biological and environmental milieux and can readily adsorb onto NP surfaces. Rubasinghege et al. investigated the proton-promoted dissolution of α-FeOOH caused by carbonate and phosphate adsorption on micro- and nanorods.[64] Upon oxyanion adsorption, there is a loss of molecular symmetry that can affect the number of peaks and spectra. For example, carbonate symmetry is lowered from D3h to C2v with a loss of degeneracy and subsequently fewer active IR peaks. Similarly, phosphate symmetry decreases from C3v to C2v or lower. Moreover, by comparing solution phase to adsorbed phase spectra, new peaks appear that correspond to oxyanion-binding

complexation with the surface. The symmetric and asymmetric wavenumber splitting of the ν_3 mode can elucidate the specific binding mode complex. For carbonate, the smaller splitting for microrods suggests a monodentate complexation, whereas for nanorods, bidentate chelating is dominant. For phosphate, there are multiple peaks present, suggesting a mixture of surface complexes. These spectroscopic differences can be used to determine the adsorption binding mode on the NP surface, which can affect macroscopic aggregation and lower dissolution rates. In the case of microrod adsorption of phosphate, the inner-sphere complexation with Fe(III) made the particle more dissolution susceptible than carbonate. Conversely, for nanorods, carbonate adsorption made the particle more readily dissolvable. In general, particle reactivity increases with smaller particles. However, this study emphasized that particle dissolution can occur over the range of sizes investigated. The study also emphasized that particle size can impact surface adsorption of these oxyanions due to differences in surface site density and the propensity of different surface planes.[80–82]

Many adsorbed complexes depend on solution pH, and for proteins in solution, it has been shown that secondary structural changes can occur at different pH values. However, adsorbed protein conformational changes in response to solution pH are yet to be fully understood. When metal oxide NPs interact with milieux containing biological components, the formation of a biocorona occurs. In the case of a solution containing proteins, a protein corona occurs. This corona is the result of dynamic, competitive adsorption of proteins with different affinities to particle surfaces and changes in physiochemical properties. Some of the more pliable, soft proteins can undergo conformational changes and alter protein structure to conform to the surface.[83] To better understand the effects of protein adsorption onto metal oxide surfaces, a thorough investigation of amino acid surface interactions is necessary. Mudunkotuwa & Grassian have examined l-histidine

adsorption onto TiO_2 NPs with ATR-FTIR spectroscopy to investigate surface complexation and adsorption kinetics and mechanisms.[41] In particular, the 1,800–1,200 cm^{-1} bands were curve fitted to elucidate specific functional group interactions with the TiO_2 surface. By monitoring the intensity changes in solution phase and the adsorbed phase spectra, they concluded that the imidazole side chain, amine group, and π-orbital interacted with the hydroxylated surface.

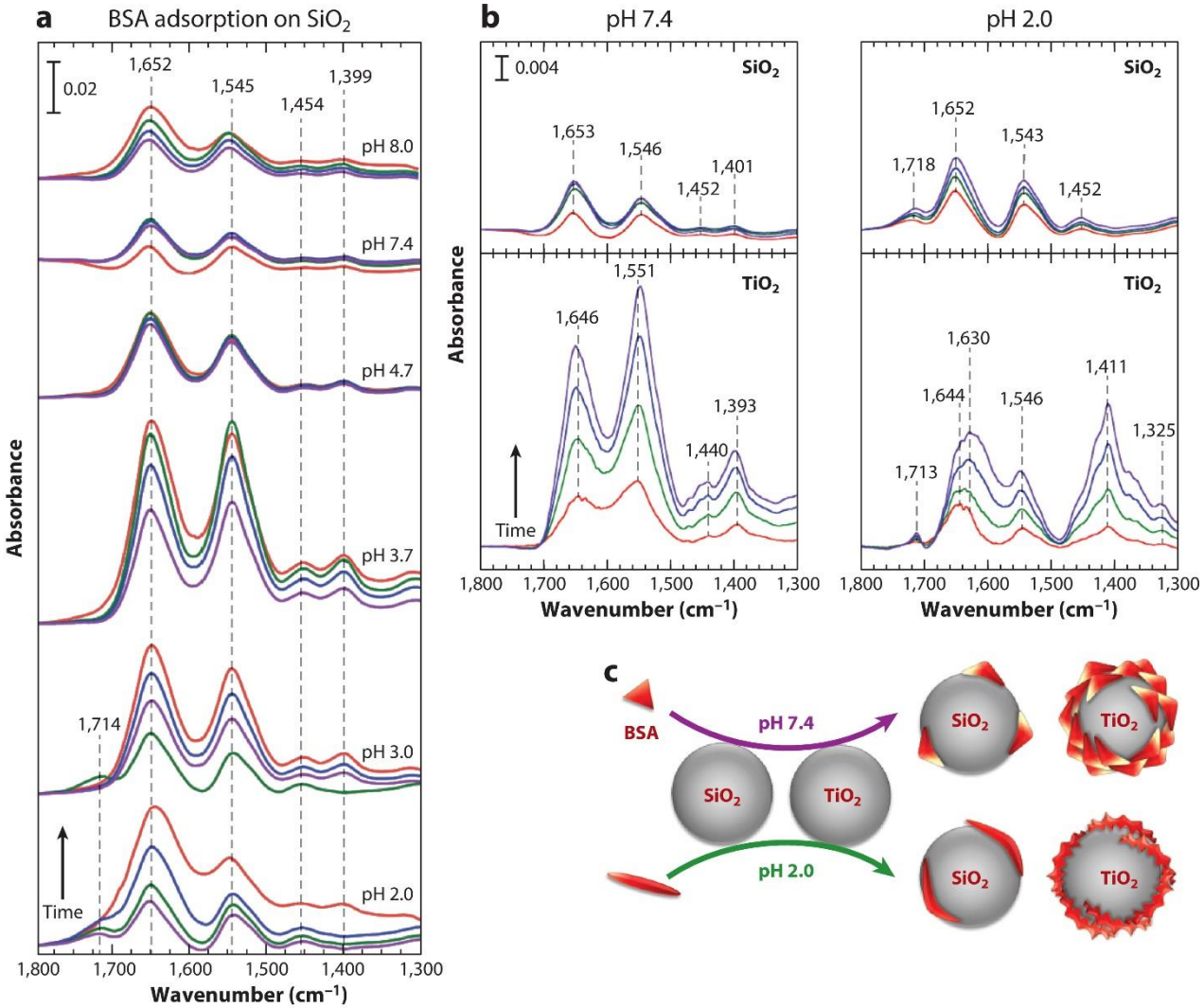

Figure 1.3 ATR-FTIR spectra of BSA adsorbed onto metal oxide nanoparticle

(a) Attenuated total reflectance–Fourier transform infrared (ATR-FTIR) spectra of 1 mg/mL bovine serum albumin (BSA) adsorbed onto the SiO_2 nanoparticle surface at different pHs with increasing time. Representative adsorption spectra shown after 30 min (purple), 60 min (blue), 90 min (green), and after 60 min desorption (red). Adapted with permission from Reference 46; copyright 2017 American Vacuum Society. (b) ATR-FTIR spectra of BSA adsorbed onto different oxide nanoparticle surfaces. Representative spectra increase in time points, 10, 30, 60, and 90 min from bottom to top. (c) The effects of BSA adsorption onto metal oxide nanoparticle surfaces.

Adsorption isotherms and surface charge measurements also indicated that electrostatics play a role in the surface chemistry but are not the only interaction. Clearly, this is not a simple interaction but is one comprised of multiple, complex adsorption modes. To expand the suite of amino acid interactions with TiO_2, Ustunol et al. investigated the effects of pH on additional amino acids, i.e., l-lysine, l-glycine, l-glutamic acid, and l-serine.[6] By using multiple experimental pH ranges that also coincided with different amino acid speciation, the authors could monitor peak shift and intensity to the $\nu_s(COO^-)$ and $\nu_{as}(COO^-)$. These carboxylate vibrational modes are important to determine binding modes by taking the difference between the two stretches. Deacon & Phillips found a general relationship between frequency splitting between the antisymmetric and symmetric COO^- stretching vibrations ($\Delta\nu_{as\text{-}s}$) and the coordination on metals.[84] This general relationship indicates that $\Delta\nu_{as\text{-}s}$(monodentate) > $\Delta\nu_{as\text{-}s}$(ionic) > $\Delta\nu_{as\text{-}s}$ (bidentate bridging) > $\Delta\nu_{as\text{-}s}$ (bidentate chelating). This correlation is empirical but is a good starting place to decipher possible coordination surface complexes. The bond formed from a monodentate to a bidentate coordination releases energy and lowers the energy of the molecule.

Protein conformation has been reported to change with surrounding pH environment.[85–87] For example, as pH decreases, BSA elongates and has various conformational forms that change from normal form to fast form and extended form.[47,85] Proteins, including BSA, have characteristic IR absorption bands in the ranges of 1,700–1,600 cm^{-1}, 1,600–1,500 cm^{-1}, and ~1,500–1,200 cm^{-1} corresponding to amide I, II, and III, respectively. These bands originate from amino acid intermolecular interactions yielding protein secondary structure. Amide I and II are typically used for secondary structure analysis, as the two bands are the most sensitive to conformational change with the highest intensities. Givens et al. studied the BSA adsorption on SiO_2 NPs as a function of pH and concluded that the spectral intensity of adsorbed protein is the highest at the NP isoelectric

point (**Figure 1.3a**).[46] Moreover, adsorbed BSA shows distinct IR band profiles between different pH values ranging from 2 to 8, particularly the appearance of a 1,700 cm^{-1} band assigned to protonated carboxylic groups within the amino acid residues at lower pHs. Deconvolution of amide I indicated that the adsorbed proteins onto NP surfaces undergo conformational changes involving secondary structural changes regardless of pH. The pH effects on adsorption on NPs are mainly due to electrostatic interaction or ligand exchange reactions.[88–91] The surface charge on the silica surface is regulated by the protonation and deprotonation reactions of dissociable functional groups. As previously mentioned, the surface charge density that is important to the interaction between BSA and silica surface is highly dependent on the solution pH.[47,74] Because adsorption on metal oxide surfaces can be through surface hydroxyl groups, BSA shows a weaker binding affinity onto SiO_2 than TiO_2 owing to a lower surface hydroxyl group density.[72] This can be seen in **Figure 1.3b**, where the amide I and II intensities are much higher for TiO_2 as compared to SiO_2.[47] Moreover, the relative ratio of the amide I/II band shows an adsorbed conformational difference between substrates. Between pHs on TiO_2 substrate, the pH 2 amide I band appears to be highly distorted, suggesting major conformational changes under acidic conditions. **Figure 1.3c** summarizes the effect of pH and NP composition on the adsorption of BSA onto NP surfaces by emphasizing the solution phase conformational dependence, conformational change, and protein loading.

Apart from proteins, humic substances are another type of macromolecule that are present in environmental systems and consist of large, often aromatic, conjugated structures with various functional groups, including carboxylic acids, thiols, and amides. Humic substances are produced from degradation of biological organisms and are highly prevalent in soils. Thus, the adsorption of humic substances on metal oxide surfaces has attracted much attention. The adsorption of humic

substances onto a TiO_2 NP surface has been shown to increase the dispersion and stability in aqueous systems owing to increased surface charge density.[92] Jayalath et al. found that Suwannee River humic acid (SRHA) showed pH-dependent adsorption mechanisms and intermolecular interactions with TiO_2 NPs.[54] Using ATR-FTIR spectroscopy, the researchers suggested that environmentally complex acid molecules are predominantly bound to surface hydroxyl groups via carboxylic groups and are irreversibly adsorbed. Moreover, the binding mode of SRHA is highly dependent on pH and is observed to be primarily monodentate and bidentate, bridging inner-sphere complexation at lower pH values.[93] Upon adsorption, SRHA induces a negative surface charge, increases electrostatic repulsion, and increases the stability of NPs by reducing aggregation. Smaller agglomerates are more persistent in aqueous systems because of the reduced sedimentation rates, which is why SRHA was shown to potentially increase both the transport and bioavailability of nanoscale TiO_2.

1.1.2 Synergistic Effects due to Coadsorption

The adsorption of molecules is also influenced by moieties on NP surfaces in various pH environments.[57] The kinetics are changed by the presence of these surface coatings because they compete for adsorption sites and displacement processes.[12,28,48] Environmental and biological systems are often composed of molecularly diverse components, and the displacement process of adsorbed components with higher affinity molecules is necessary to predict the fate and transport of NPs. Situm et al. investigated the adsorption behavior of dimethylarsinic acid (DMA) and arsenate on hematite NPs preexposed to citrate, oxalate, and pyrocatechol.[12] The results showed a strong dependence on the desorption of preadsorbed components due to surface complexation. Strongly bound inner-sphere citrate and pyrocatechol were not as easily displaced with arsenate compared to outer-sphere oxalate. When DMA was used as the desorbing agent, it did not remove

as many organics compared to arsenate due to a weaker outer-sphere complexation to hematite after displacement. The degree of adsorbate displacement is highly dependent on the product surface complexation. Kim & Doudrick indicated that precoated TiO_2 NPs with oxalate hinder the adsorption of BSA.[29] The authors suggested a multistep kinetic pathway starting with the ramping adsorption rate of BSA as oxalate was displaced. Interestingly, oxalate peak intensities were seen to increase over time after initial desorption decreased, suggesting a temporary displacement or rearrangement of adsorbates while BSA desorption slowed until saturation was reached. However, the amount of BSA adsorbed was reduced when oxalate was present. The degree of BSA adsorption-induced denaturation was dependent on the type of oxalate binding mode to the surface. In the presence of a more complex macromolecule such as natural organic matter, BSA adsorption was hindered on TiO_2 NPs but a small amount was still coadsorbed.[25] Coadsorption with buffer molecules such as phosphate is a consequential factor on the degree of conformation change for BSA adsorbed to NP surfaces.[28] At acidic pH values, phosphate was shown to prevent conformational changes by occupying surface hydroxyl groups. The phosphate surface complexation and the electrostatic interactions between the phosphate coated TiO_2 NPs and BSA

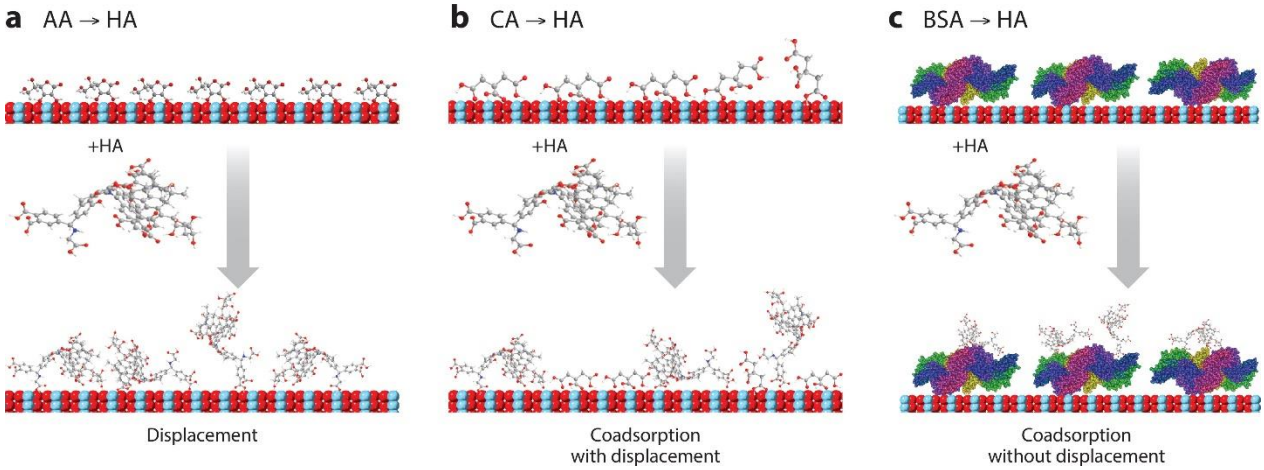

Figure 1.4 Humic acid displacement reactions on TiO_2

Displacement reactions of humic acid (HA) on TiO_2 nanoparticles precoated with (a) ascorbic acid (AA), (b) citric acid (CA), and (c) bovine serum albumin (BSA).

are pH dependent, favoring attraction at lower pH values. This study shows that coadsorbed phosphate affects protein stability and affinity toward NP surfaces.

Recent research conducted by the Grassian group extended understanding of the adsorption of humic acid on various environmentally relevant surface coatings, ascorbic acid, citric acid, and BSA.[48] As expected, results showed that the extent of displacement correlated with binding complexation and surface affinity (**Figure 1.4**). By comparing solution phase spectra to adsorbed spectra, the authors suggested that small molecules such as ascorbic acid are bound to TiO_2 through the enediol functional groups, while citric acid was shown to bind to TiO_2 via monodentate and bidentate bridging complexation modes. As previously mentioned, BSA undergoes conformational change to conform to the surface and is irreversibly adsorbed through the various functional group multivalent interactions. In order to investigate displacement reactions on the TiO_2 surface, single component spectra were compared to multicomponent, coadsorbed spectra. When humic acid was introduced as a coadsorbate onto an ascorbic acid and citric acid precoated surface, they were shown to either fully displace or partially displace, respectively (**Figure 1.4a,b**). For BSA, humic acid was seen to form layers on top of adsorbed BSA, highlighting that BSA has a higher affinity to the surface (**Figure 1.4c**). Humic acid adsorption behavior is dependent on the presence of coadsorbates, and structural stability can change by interacting with other multifunctional macromolecules. This study shows the effects of binding modes on the reversibility and displacement tendencies of some environmentally relevant adsorbates.

1.1.3 2DCOS to Investigate Environmental DNA Adsorption and Other Surface Processes

2DCOS is a spectral processing tool that analyzes spectral data to produce maps that determine the sequential order of change in spectral peaks. As a system is perturbed by an external variable, which could time, concentration, pH, or temperature, changes in spectral intensities

and/or peak positions changes can occur. 2DCOS compares spectra and determines how similar or dissimilar spectra are with respect to each other. This results in heat maps that indicate the peaks that are most responsive to the external perturbation. These maps can be analyzed to yield sequential peak changes. Thus, 2DCOS can be quite powerful in analyzing spectroscopic data for

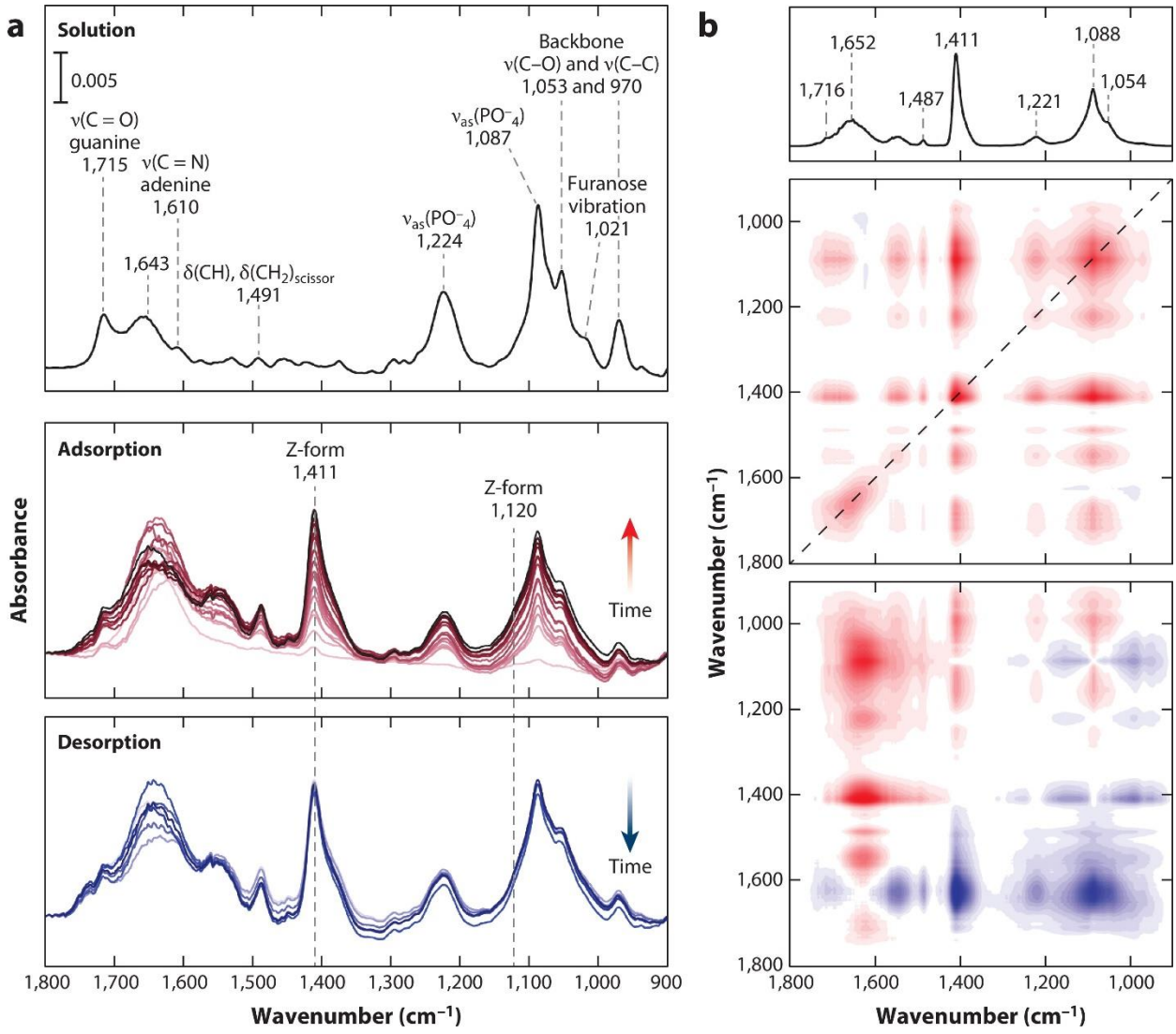

Figure 1.5 ATR-FTIR spectra and 2DCOS maps of eDNA adsorbed on hematite

(a) Original attenuated total reflectance–Fourier transform infrared (ATR-FTIR) spectra for environmental DNA (eDNA) in 30 mM NaCl at pH 5, 1.5 ug/mL in solution phase (top), adsorbed on hematite nanoparticles at 0.1 ug/mL shown every 10 min for 150 min (middle) and desorbed with NaCl shown every 10 min for 60 min (bottom). (b) Two-dimensional correlation spectroscopy (2DCOS) maps for eDNA adsorption onto a hematite nanoparticle surface at pH 5 using ATR-FTIR spectra. Autocorrelation spectrum (top), synchronous 2DCOS map (middle), and asynchronous 2DCOS map (bottom). The dotted line in the synchronous 2DCOS corresponds to the intensity line trace autocorrelation spectrum, highlighting the peaks most responsive to the external perturbation, time. Red and blue for the synchronous and asynchronous 2DCOS map correspond to positive and negative values, respectively.

systems that are sensitive to external perturbations. A more thorough discussion of how these spectra are processed can be found in Chapter 2.

These systems can be proteins or biological in nature because protein structure is highly sensitive to the surrounding environment. For example, 2DCOS has been used to determine the sequential protein secondary structural changes. A recent study by Schmidt & Martínez probed BSA conformational change as a function of particle loading on montmorillonite.[52] Structural changes were proposed as a function of surface concentration by determining the sequential structure changes using 2DCOS. Barreto et al., analyzed BSA adsorption onto hematite as a function of surface concentration.[94] At the initial stages of adsorption, which is low surface coverage, the protein adsorption is due to protein-mineral interactions and the protein undergoes significant unfolding. As the surface coverage increases, adsorbed BSA refolds and leads to a more compact loading on the hematite surface.

Figure 1.5a shows an example of the use of 2DCOS using ATR-FTIR spectra for a different biological sample, namely environmental DNA (eDNA) at pH 5 in solution phase, adsorbed onto α-Fe_2O_3 NP surfaces and desorbed from the surface with NaCl solution. By comparing the solution phase to adsorbed spectra, one can identify specific functional group surface interactions by observing frequency shifts and band shape differences. Some peaks remain unchanged, specifically 1715 cm^{-1} and 1,491 cm^{-1} assigned to ν(C = O) guanine and δ(CH), $\delta(CH)_{scissor}$, respectively. The 1643 cm^{-1} and 1,610 cm^{-1} peaks cannot be resolved and are merged, centered around ~1650 cm^{-1}, suggesting there is some interference from the broad water bending mode due to the low concentration of adsorbed eDNA molecules. Phosphodiester peaks centered at 1225 cm^{-1} and 1087 cm^{-1} are seen to slightly broaden, whereas the presence of the eDNA Z-form conformation is seen to appear once adsorbed onto hematite. The purine and pyrimidine bases

are on the interior of the double helix, while the phosphodiester and deoxyribose remain on the exterior, suggesting interaction with the surface is most likely via the phosphate or sugar. This specific interaction with the surface has been reported and simulated for other surfaces.[95,96] DNA has three conformations, A-, B-, and Z-forms; the A- and B-forms are most common, but Z-form exists in small quantities in cells. Increasing in vertical distance between base pairs are the A-, B-, and Z-forms. Interestingly, peaks indicative of the Z-form conformation is only seen to appear when adsorbed on hematite, where it is not observed in solution. Moreover, in a previous study by Schmidt & Martínez, the Z-form peaks are not observed when DNA is adsorbed onto goethite, which suggests that DNA retains the B-form solution phase secondary structure.[95] As a desorbing

Table 1.1 2DCOS analysis of eDNA adsorbed on hematite

Two-dimensional correlation spectroscopy (2DCOS) analysis for environmental DNA adsorption on a hematite surface at pH 5 showing relevant synchronous and asynchronous cross peak signs and sequential order.

Cross Peak	Synchronous	Asynchronous	Order
(1,716, 1,652)	+	−	1,716 < 1,652
(1,716, 1,487)	+	NA	NA
(1,716, 1,411)	+	+	1,716 > 1,411
(1,716, 1,221)	+	NA	NA
(1,716, 1,088)	+	+	1,716 > 1,088
(1,716, 1,054)	+	+	1,716 > 1,054
(1,652, 1,487)	+	+	1,652 > 1,487
(1,652, 1,411)	+	+	1,652 > 1,411
(1,652, 1,221)	+	+	1,652 > 1,221
(1,652, 1,088)	+	+	1,652 > 1,088
(1,652, 1,054)	+	+	1,652 > 1,054
(1,487, 1,411)	+	+	1,487 > 1,411
(1,487, 1,221)	+	+	1,487 > 1,221
(1,487, 1,088)	+	+	1,487 > 1,088
(1,487, 1,054)	+	+	1,487 > 1,054
(1,411, 1,221)	+	NA	NA
(1,411, 1,088)	+	NA	NA
(1,411, 1,054)	+	+	1,411 > 1,054
(1,221, 1,088)	+	NA	NA
(1,221, 1,054)	+	NA	NA
(1,088, 1,054)	+	+	1,088 > 1,054

solution is flowed over the eDNA-coated surface, minimal peak changes are observed, indicating that the eDNA is irreversibly adsorbed on the surface. This difference in secondary structure highlights the surface chemical dependence on adsorbent composition.

2DCOS analysis can be done for ATR-FTIR spectra to yield autocorrelation and synchronous and asynchronous maps, as shown in **Figure 1.5b**. The autocorrelation intensity spectrum yields peaks that are the most responsive to the external perturbation and time, whereas synchronous and asynchronous maps can indicate the sequential order of peak changes. The autocorrelation spectrum shows several peaks that can be used to determine the sequential order change as eDNA adsorbs onto the hematite surface. The 2DCOS maps can be interpreted by using Noda's rule, which is dependent on the positive or negative signs for synchronous and asynchronous maps. The corresponding cross peak signs are seen in **Table 1.1**. All the synchronous cross-peak values are positive, which is expected because all the peaks increase in intensity as eDNA adsorbs to the surface. However, some asynchronous cross-peak values are zero, which has been previously reported and is caused by frequency or bandwidth changes.[18,52] Cross peaks with an asynchronous value of zero will be ignored when the sequential order is determined, which will result in overlapping peak changes. Sequential peak changes can be determined as the following: 1652 cm^{-1} → 1716 cm^{-1}, 1487 cm^{-1} → 1411 cm^{-1}, and 1221 cm^{-1} → 1054 cm^{-1}. The 1652 cm^{-1} broad band is seen to first change, possibly due to the water reorientation needed for eDNA to adsorb to the surface. The 1411 cm^{-1} Z-form peak is seen to change before the final phosphodiester surface interactions, suggesting that the eDNA secondary structure develops, then the phosphodiester interacts with the surface to yield an equilibrated NP-biomolecule complex. 2DCOS can elucidate the dynamic adsorption steps for many biological molecules, oxyanions, and other environmentally relevant species.

Humic acid, being a complex, multifunctional, large macromolecule, is a standard source of investigation to determine the fate of the moiety in the environment. Many studies model the presence of humic acid in aqueous environments and adsorb the molecule onto surfaces relevant in the environment. Chen et al. modeled humic acid adsorption on TiO_2 at various pH values with ATR-FTIR spectroscopy.[97] The study concluded that the structure of humic acid is dependent on the surface charge and pH of the environment where at low pH, humic acid is aggregated and functional groups are located inside the molecule. At higher pH levels, the molecules begin to dissociate and break apart, exposing more functional groups that can bind to the surface. With the use of 2DCOS, Chen et al. were able to determine the sequential attachment of humic acid functional groups as a function of pH. A sequential order of functional group interaction with the surface shows there is a preferential binding of functional groups to the surface as a function of pH.

1.2 Description of Thesis Chapters

Chapter 2 will focus on the detailing the experimental methods used in this dissertation. This chapter will explain the theory, experimental setup, and processing for ATR-FTIR spectroscopy. The details of the theory behind 2DCOS and how this analysis is done, will also be discussed.

Chapter 3 probes the impact of pH and coadsorption of a nucleotide and oxyanion phosphate onto hematite. This chapter investigates the adsorption behavior of deoxyadenosine monophosphate at slightly acidic and basic environments which results in electrostatic dominant interactions. The competitive adsorption of oxyanion phosphate with the nucleotide is also analyzed. An adsorption pathway is also proposed from the results of 2DCOS. This chapter

provides a further understanding of the geo-bio and nano-bio interactions and interfaces at environmentally relevant conditions.

Chapter 4 expands on Chapter 3 by investigating the adsorption of four nucleotides on titanium dioxide as a function of pH and the coadsorption of complementary or noncomplementary base pairs. This chapter has similar conclusions with respect to pH as Chapter 3 but builds a more complex system by introducing a second nucleotide. The addition of a second nucleotide changes the adsorption behavior depending on whether the two nucleotides are complementary or noncomplementary. This chapter highlights the synergistic interaction between two nucleotides and provides insight into the formation of prebiotic life with the templating of nucleotides on mineral surfaces.

Chapter 5 investigates the surface chemistry of adsorbed nucleotides for the four nucleotides on hematite and goethite using ab-initio calculations. This chapter probes the surface chemistry of nucleotides adsorption on two different mineral surfaces by comparing spectra collected from experimental and ab-initio calculations. This chapter emphasizes the surface chemistry dependence on nanoparticle composition.

Chapter 6 discusses the effects of nanoconfinement on acid-base properties for two simple organic acids. This chapter investigates the effects nanoconfinement within porous silica to elucidate the surprising shift on pK_a values for formic and acetic acids. This chapter uses the two model organic acids to pave the way for a unifying theory predicting the impact of nanoconfinement on acid-base chemistry.

Chapter 7 assesses the difference in structural stability of two blood plasma proteins in solution and adsorbed using temperature. This chapter uses a subset of 2DCOS to analyze the

denaturation temperature of the two model proteins and the effects of adsorption on protein stability.

Chapter 8 highlights the applications for and implications to human health of nanoparticles using spectroscopy. This chapter is comprised of two collaboration projects where ATR-FTIR spectroscopy was used to provide insight into the structure-property relationship of ligands with gold nanorods and to characterize irreversible protein coatings on copper oxide particles which were then tested for cardiotoxicity.

1.3 Acknowledgements

A portion of Chapter 1 is reproduced from Annual Review of Analytical Chemistry: Sit, I.; Wu, H.; Grassian, V. H. Environmental Aspects of Oxide Nanoparticles: Probing Oxide Nanoparticle Surface Processes Under Different Environmental Conditions. 2021, 14 (1), 489-514. The dissertation author is the first author of this paper.

Chapter 2. Experimental Methods

In this chapter, general experimental used throughout this dissertation will be discussed and described. Primarily, attenuated total reflectance-Fourier transform infrared (ATR-FTIR) spectroscopy will be explained. A spectral processing method called two-dimensional correlation spectroscopy (2DCOS) methodology will be described in detail. Both techniques have been used extensively in this dissertation.

2.1 Attenuated Total Reflectance-Fourier Transform Infrared Spectroscopy

Reflection IR spectroscopy can be employed for samples that are difficult to measure with conventional transmission FTIR spectroscopy.[98] Reflection IR spectroscopy can be classified as internal or external reflection. Internal reflection is based on interaction of the infrared radiation between the sample and the higher refractive index medium, whereas external reflection stems from reflected radiation from the sample surface. Herein, the focus is on ATR spectroscopic techniques, namely, ATR-FTIR spectroscopy. A typical ATR-FTIR spectroscopy experiment probing the surface chemistry of NP surfaces is shown in **Figure 2.1a**. First, a thin film is formed by drop-casting NPs dispersed in a solvent and allowing them to dry. Second, a background solution is flowed over the thin film to collect a background and to remove any loosely bound particles. The flow stream can then be switched to the sample solution and spectra can be collected as a function of flow time. **Figure 2.1b** shows a cross-sectional scanning electron microscope (SEM) image of a typical TiO_2 thin film. As observed in the micrograph, the thin film represents aggregated NPs, not dispersed, isolated particles.

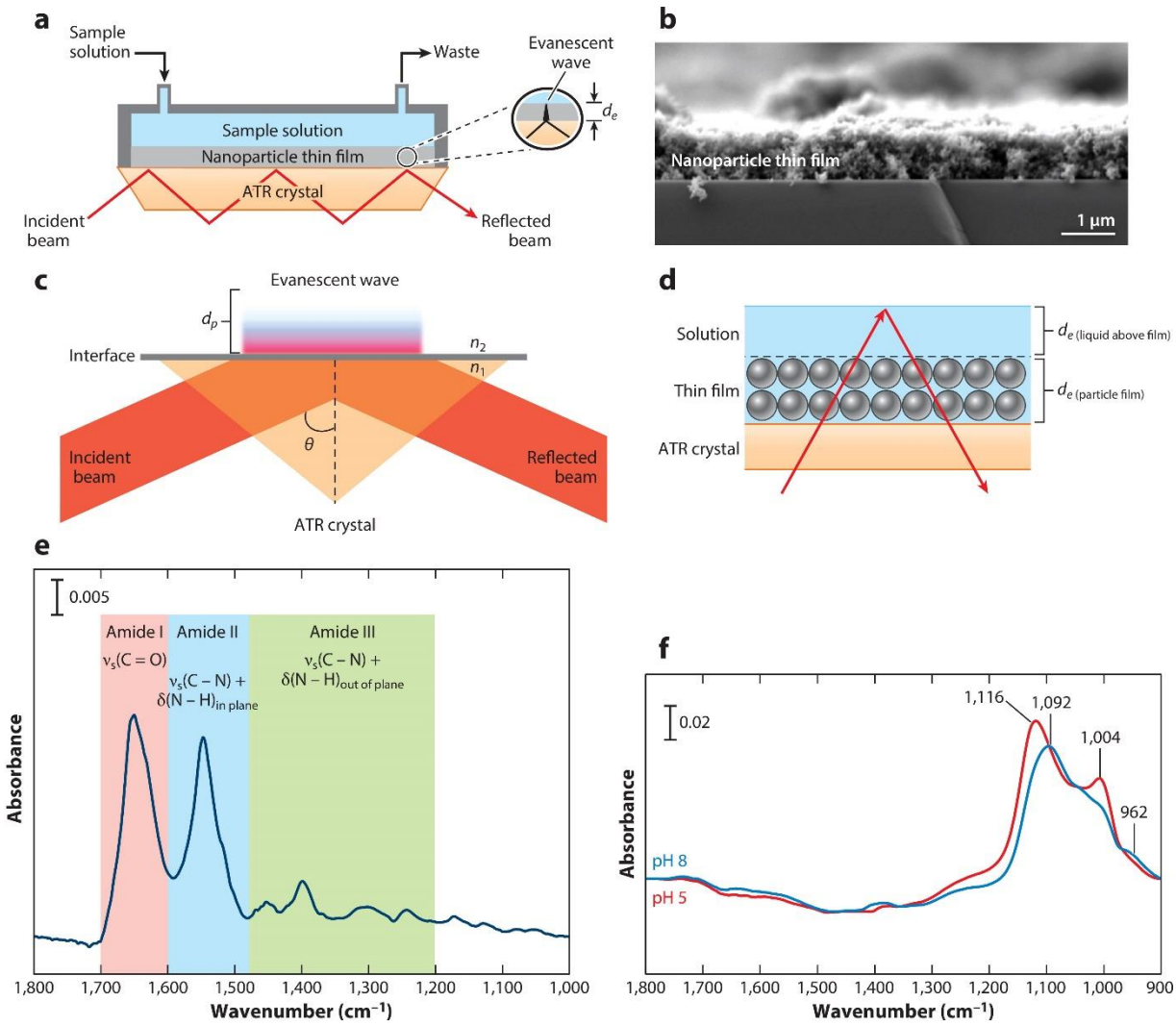

Figure 2.1. ATR-FTIR experimental setup and theory, SEM of thin film, and protein spectrum

(a) Schematic representation of the experimental setup up for attenuated total reflectance–Fourier transform infrared (ATR-FTIR) spectroscopy used to study the liquid–solid interface. (b) Cross-sectional scanning electron microscope micrograph of a TiO_2 P25 film on the substrate. (c) Electromagnetic wave reflection depicting the evanescent wave near the interface in an internal reflection element. (d) Illustration of the effective penetration depth for a nanoparticle thin film. (e) Solution phase spectrum of bovine serum albumin (BSA) highlighting the various amide bands (I, II and III) associated with protein secondary structure. (f) Adsorbed phosphate spectra on α-Fe_2O_3 at two different pH, 5 and 8. These differences demonstrate pH dependent surface complexation modes.

ATR-FTIR spectroscopy is developed based on the total internal reflection phenomenon that occurs at the interface when a light beam propagates from a medium of high refractive index n_1 (optically denser medium; internal reflective element) to a medium of low refractive index n_2 (optically rarer medium; sample). The reflection generates an evanescent electric field, the

direction of which is perpendicular to the interface, as illustrated in **Figure 2.1c**.[99] The electric field amplitude exponentially decays with distance from the interface, as shown by **Equation 2.1**:

$$E = E_0 e^{-z/d_p} \qquad \textbf{Equation 2.1}$$

where E represents the electric field amplitude of the evanescent wave, E_0 is the electric field amplitude at the crystal interface, z is distance from the interface, and d_p is penetration depth. It is useful to note that d_p is not constant but dependent on the incident wavelength and refractive index of the interfacial sample, as described by **Equation 2.2**[100]:

$$d_p = \frac{\lambda}{2\pi\left(n_1^2 \sin^2\theta - n_2^2\right)^{1/2}} = \frac{\lambda_1}{2\pi\left(\sin^2\theta - n_{21}^2\right)^{1/2}}, \qquad \textbf{Equation 2.2}$$

where λ is incident light wavelength, n_1 is the refractive index of the internal reflective element (ATR crystal), n_2 is the refractive index of the sample, n_{21} is the relative index of refraction n_2/n_1, θ is the incident angle, and λ_1 is λ/n_1. Note that d_p expressed by **Equation 2.2** is for a homogeneous solution. For total reflectance to occur, the refractive index of the crystal must be much larger than the sample. For aqueous samples where n_2 is 1.33, all the commonly used crystals such as diamond, Ge, ZnSe, and amorphous material transmitting infrared radiation (AMTIR), with an n_1 of 2.4, 4, 2.4, and 2.5, respectively, are acceptable to use.[101] However, each type of crystal is only usable within their working pH range. The working pH range is 1-14, 1-14, 5-9, and 1-9 for diamond, Ge, ZnSe, and AMTIR, respectively. Despite the wide working pH range for many of these crystals, careful selection of crystal housing is also important. The standard flow cell is nickel coated aluminum, however when dealing with acidic or basic samples, it is wise to use a Teflon coated cell to minimize corrosion. The standard flow cell is susceptible to corrosion at the extreme

working pH range and to large ionic strengths. So careful consideration of the ATR crystal and housing is important for experimental design.

Spectra are obtained by measuring the absorption of the evanescent wave from IR active moieties at the interfacial region. This feature makes ATR-FTIR spectroscopy more relevant for studying the interfacial region than more conventional transmittance FTIR in the presence of a strong absorbing solvent such as water. Therefore, *in-situ* ATR-FTIR spectroscopy can be applied to examine adsorption kinetics and molecular structural change associated with adsorption.

In addition to qualitative analysis, ATR-FTIR spectroscopy also offers semiquantitative information. The number of reflections in the internal reflecting element can be a single bounce or a multibounce ATR. The relationship between absorbance and interfacial concentrations follows Beer's law. The derived format of Beer's law for quantitative ATR-FTIR spectroscopy is shown in **Equation 2.3**:

$$A = -\log R = \varepsilon n d_e c \qquad \textbf{Equation 2.3}$$

where R is reflectivity of ATR, ε is the molar absorption coefficient, n is the number of active internal reflections in the reflection element, de is the effective evanescent wave penetration depth, and c is the concentration of absorbing species. Here, because of the presence of an NP thin film, the assumption of a homogeneous solution is invalid. Thus, an effective evanescent wave must be used, as shown by **Equation 2.4**[100,102]:

$$d_e = \frac{n_{21} d_p}{2\cos\theta}\left(e^{-2z_1/d_p} - e^{-2z_2/d_p} \right)\left(E_{02}^{r}\right)^2 \qquad \textbf{Equation 2.4}$$

where z_1 and z_2 are the distances extending from the ATR plate representing film thickness, and E^r_{02} is the relative electric field amplitude at z = 0 in the sample. **Figure 2.1d** shows an illustration

of the effective penetration depth extending through the particle film and into the bulk aqueous solution. The effective penetration depth is therefore:

$$d_e = d_{e(\text{liquid above film})} + d_{e(\text{particle film})}. \qquad \textbf{Equation 2.5}$$

To probe the surface chemistry of a nanoparticle surface, a solution spectrum needs to be collected. This spectrum is taken of only the ligand in solution without the nanoparticle present. This serves as a reference spectrum to compare to when nanoparticles are present. Any spectral differences, such as peak shifting, broadening, and intensity changes, can be attributed to the ligand interacting with the particle surface. Once the ligand solution spectrum is taken, the nanoparticles can then be exposed to the ligand solution. A colloidal suspension of nanoparticles can be prepared by sonication. The suspension can be pipetted onto the ATR crystal and dried to leave a thin film of particles. A background solution can be flowed over the film and a spectrum can be collected. Then, the ligand solution is flowed over the film and temporal, *in-situ* spectra can be taken in regular intervals. However, careful consideration needs to be given in the number of scans and resolution of the spectra. The higher the resolution and number of scans, the longer it takes for a spectrum to be collected. This affects how regular the temporal spectra are taken. There is a balance between high resolution spectra and how often spectra can be taken.

Several examples of ATR-FTIR spectra can be seen in **Figure 2.1e-f**. Distinct amide I, II, and III bands are visible in the aqueous bovine serum albumin (BSA) solution phase spectra of 10 mg/mL, shown in **Figure 2.1e**. These bands are sensitive to conformational changes and can be used to estimate secondary structures for proteins. Secondary structure changes caused by external variables such as pH, ionic strength, or adsorption can be monitored by curve fitting the amide I band. In **Figure 2.1f**, adsorbed oxyanion phosphate at pH 5 and 8 has differing band shape profiles within the 1,200–900 cm^{-1} band, indicating varying surface complexation modes. This pH

dependence affects adsorbate protonation states and sorption energetics, altering subsequent interactions with other bulk components. ATR-FTIR spectroscopy is a multifaceted tool that can be used to probe nanomaterial interfaces both quantitatively and qualitatively. Moreover, this technique can be used *in-situ* to monitor multicomponent molecular kinetics, chemical reactions and transformation, and thermodynamics to better understand interfacial surface chemistry.[55,76,103–106] The thin films and solution are highly modular, increasing the usability and versatility of ATR-FTIR, where the limitations are often within experimental conditions such as internal reflective element pH compatibility.

2.2 Two-Dimensional Correlation Spectroscopy

2DCOS has been used as an analytical method to study changes induced by external perturbations such as temperature, surface reactions, pH, and adsorbate concentration.[18,48,97,107] In typical one-dimensional spectroscopic experiments, an electromagnetic probe is used to investigate interactions of the probe and system. However, once an external perturbation is used to stimulate the system, spectral intensity changes can occur. 2DCOS is a way of aggregating spectra to establish whether intensity fluctuations are correlated and to determine the sequential sequence of peak changes. Spectra analyzed by 2DCOS should be taken in regular intervals from the external perturbation. For example, Sit et al., used 2DCOS to analyze the secondary structural changes of two blood plasma proteins in solution and adsorbed as a function of temperature.[18] The spectra was taken as a function of increasing temperature by increments of 0.5℃, where the temperature was the external perturbation variable. Experiments that have regular intervals of the external perturbation, like increasing time, pH, or concentration are ideal for 2DCOS. In another study by Sit et al., a monophosphate nucleotide was adsorbed onto hematite particles and an adsorption mechanism was proposed with the help of results from the sequential peak change

determined by 2DCOS.[76] Both papers will be highlighted in this dissertation. Schmidt and Martinez used 2DCOS to suggest several pathways for bovine serum albumin conformations adsorbed on montmorillonite.[52] 2DCOS is useful to analyze spectral data to propose mechanisms and pathways due to some external perturbation to a system. In the case of ATR-FTIR spectra, it is incredibly useful as experiments are often taken as a function of time which can be correlated to surface coverage or concentration, pH, or temperature

These transient spectral fluctuations are deemed dynamic spectra $\tilde{y}$(v,t) and are defined by

$$\tilde{y}(v,t) = \begin{cases} y(v,t) - \bar{y}(v), & T_{min} \leq t \leq T_{max} \\ 0, & otherwise \end{cases} \quad \textbf{Equation 2.6}$$

$$\bar{y}(v) = \frac{1}{T_{max} - T_{min}} \int_{\boldsymbol{T_{min}}}^{\boldsymbol{T_{max}}} y(v,t)dt \quad \textbf{Equation 2.7}$$

where ν is the spectral variable (wavenumber for FTIR spectra), t is the perturbation variable, and $\bar{y}$(ν) is considered the reference spectrum that could be the initial state before perturbation but is customarily equal to the averaged spectrum.

2DCOS can be considered a quantitative intensity comparison of two spectra between some perturbation interval. This is a way to visualize similarity or dissimilarity of the correlations between intensity fluctuations. The similarity between two spectra as the perturbation variable is changed is measured using the synchronous spectrum, $\Phi(\nu_1, \nu_2)$. Likewise, the out-of-phase or dissimilarity between two spectra is measured using the asynchronous spectrum, $\Psi(\nu_1, \nu_2)$. For a set of m equally spaced spectra between the interval of T_{min} and T_{max}, along the perturbation variable t, the synchronous and asynchronous 2D correlations are given by

$$\Phi(v_1, v_2) = \frac{1}{m-1} \tilde{\boldsymbol{y}}(v_1)^{\intercal} \tilde{\boldsymbol{y}}(v_2) \quad \textbf{Equation 2.8}$$

$$\Psi(v_1, v_2) = \frac{1}{m-1} \tilde{\boldsymbol{y}}(v_1)^{\intercal} \boldsymbol{N_{ij}} \tilde{\boldsymbol{y}}(v_2) \quad \textbf{Equation 2.9}$$

The N_{ij} term refers to the i^{th} row and j^{th} column element in the Hilbert-Noda transformation matrix (N_{ij}), which is defined as

$$\tilde{\boldsymbol{y}}(\upsilon) = \begin{bmatrix} y(\upsilon, t_1) \\ y(\upsilon, t_2) \\ \vdots \\ y(\upsilon, t_m) \end{bmatrix} \qquad \textbf{Equation 2.10}$$

The synchronous and asynchronous correlation maps can be analyzed by following Noda's rules. The $\Phi(\nu_1, \nu_1)$ diagonal peaks are always positive and correspond to the peaks that are more responsive to the external perturbation and are called the autocorrelation peaks. These autocorrelation peaks can be correlated to each other and a sequential order of how the peaks are changing can be determined. This can be done by using whether the signs of $\Phi(\nu_1, \nu_2)$ and $\Psi(\nu_1, \nu_2)$ are positive or negative. If $\Phi(\nu_1, \nu_2)$ is positive, then ν_1 and ν_2 intensity values are changing in the same direction, whether increasing or decreasing, whereas, if $\Phi(\nu_1, \nu_2)$ is negative, then ν_1 and ν_2 intensity values are changing in opposite directions; i.e., one is increasing and the other is decreasing. The sequential order spectral variations can be determined using the signs of both asynchronous and synchronous correlation maps. If $\Phi(\nu_1, \nu_2)$ and $\Psi(\nu_1, \nu_2)$ are the same signs, the change to ν_1 occurs before changes to ν_2. If the signs are negative, then the change to ν_1 occurs after changes to ν_2. If there is a zero value for the correlation map, then the bands have no correlation.

Generalize 2DCOS can be used to determine the sequential changes with respect to an external perturbation but additional analysis can be used to pinpoint an interval that has the most spectral changes. This is a subset of 2DCOS called moving window 2DCOS (MW2D). Instead of the synchronous and asynchronous maps that plot the spectral variable versus spectral variable, MW2D yields a map of external perturbation versus spectral variable. As the system is probed by the external perturbation, the spectra will change in response to the external perturbation. However, there could be a certain value of the external perturbation at which the spectra undergo drastic changes when compared to previous spectra. This type of analysis has been previously used

to determine the temperature denaturation onset for proteins[18], phase transition temperatures[108], and pH induced protein conformation changes[109]. MW2D theory can mostly be found elsewhere but as an approximation, MW2D correlation maps are proportional to the square of the derivative along the perturbation axis.[110–112]

Importantly, recent 2DCOS experiments have been used along with IR spectroscopy to investigate different NP surface interactions such as oxyanion adsorption[113,114], protein conformational change[18,52,115–117], and displacement reactions[48]. An article by Pazderka et al., provides insight into how to generate 2DCOS synchronous and asynchronous maps on MATLAB with generic code testing to ensure the algorithm runs correctly.[118] Additional resources discussing 2DCOS can be found elsewhere by Dr. Isao Noda, the founder of 2DCOS.[110–112,119,120] Generated synchronous and asynchronous maps can be checked with literature and a program developed by Dr. Noda called 2dShige (Shigeaki Mortita, Kwansei-Gaukuin University, 2004–2005).[118] The MATLAB code that was used for this dissertation can be found in Appendix A and Appendix B.

2.3 Acknowledgements

A portion of Chapter 2 is reproduced with permission from the Annual Review of Analytical Chemistry: Sit, I.; Wu, H.; Grassian, V. H. Environmental Aspects of Oxide Nanoparticles: Probing Oxide Nanoparticle Surface Processes Under Different Environmental Conditions. 2021, 14 (1), 489-514. The dissertation author is the first author of this paper.

Chapter 3. Nucleotide Adsorption on Iron (III) Oxide Nanoparticle Surfaces: Insights into Nano-Geo-Bio Interactions Through Vibrational Spectroscopy of dAMP on Hematite

3.1 Abstract

Molecular processes at geochemical interfaces impact many environmental processes that are critical to the fate and transport of contaminants in water systems. Often these interfaces are coated with natural organic matter, oxyanions, or biological components, yet little is understood about these coatings. Herein, we are interested in better understanding the interaction of biological components with nanoscale iron oxide minerals. In particular, we use attenuated total reflectance Fourier transform infrared (ATR-FTIR) spectroscopy to investigate the adsorption behavior of deoxyadenosine monophosphate (dAMP) on hematite nanoparticle surfaces as a function of pH and in the presence and absence of adsorbed phosphate. These results show that fewer nucleotides adsorb at higher pH. Additionally, when phosphate anions are pre-adsorbed, nucleotide adsorption is significantly limited due to site-blocking by adsorbed inorganic phosphate. The pH dependence provides insights into the adsorption process and the importance of electrostatic interactions. Pre-adsorbed phosphate affects the binding mode of dAMP, suggesting synergistic interactions between the co-adsorbates. Two-dimensional correlation spectroscopy was used to further analyze the infrared spectra. Based on this analysis, a dAMP adsorption pathway onto a pre-adsorbed phosphate hematite surface was proposed, suggesting the displacement of adsorbed phosphate by dAMP. Overall, this study provides some insights into geochemical-biological interactions on nanoscale iron oxide surfaces using vibrational spectroscopy.

3.2 Introduction

The most abundant transition metal present in Earth's crust is iron in the form of iron-containing particles including iron oxides, with particle sizes often on the nanoscale,[121,122] can provide a surface for biomolecular adsorption.[123] Aqueous environments such as ground water in contact with iron oxide surfaces are often composed of a complex multitude of constituents such as oxyanions, biomacromolecules, and heavy metals which all have different binding affinities.[62,65,66,124–126] With the abundance of extracellular nucleotides found in water from active or passive cellular extrusion or by cellular lysis, understanding this nano-bio interaction is of particular interest.[127] Additionally, the adsorption of biomonomer nucleotides onto geochemical surfaces has been proposed to be related to the origin of prebiotic life, increasing the local concentration under rather dilute solution phase concentrations.[128,129] Adsorbed nucleotides can polymerize to form DNA and RNA which have been seen to be stabilized on surfaces, increasing the persistence in water as well as providing a source of genetic information for gene transfer.[127] Another source of nucleotides entering the environment is through sewage, where nucleotide concentrations in urine can range from nanomolar to a few hundred micromolar.[130]

Nucleotide and nucleoside adsorption onto other metal oxide and clay surfaces has been investigated but adsorption onto iron oxide surfaces has yet to be fully explored. For example, adsorbed purine and pyrimidine nucleotides on TiO_2 were quantified as a function of pH and concluded that at higher pH, there were fewer nucleotides on the surface.[131,132] It was suggested this behavior could be due to electrostatic interactions where TiO_2 has an isoelectric point around 6.5. At environmentally relevant pH values between 5-8, the phosphate functional group on the nucleotide is deprotonated, inducing a negative charge which does not favorably adsorb onto a negatively charged TiO_2 surface at higher pH values. On clay surfaces, the chemistry of nucleotide

adsorption has been investigated with similar results via ligand exchange with the phosphate and surface hydroxyl groups.[129,133,134] Additionally, it has also been observed that nucleobases and nucleosides can interact with clay surfaces between the purine or pyrimidine rings and surface hydroxyl groups.[135,136] Clearly, the surface chemistry depends on the various nucleobase derivatives with these different surfaces.

Other than one at a time surface adsorption studies, it is necessary to build up complexity using multicomponent systems to start to predict and model geochemical interfaces in more realistic environments. Another common component in environmental aqueous systems is phosphate, where the amount of free phosphate in groundwater can be influenced by adsorption and which can impact biogeochemical cycles.[137] Excessive amounts of phosphate due to long-term anthropogenic sources from industrial and agricultural effluents can lead to eutrophication, the rapid growth of aqueous plants leading to the death of animals due to an oxygen deficiency.[138] Leaky sewage lines and septic tanks that can leach into groundwater have orthophosphate concentrations as high as 400 μM while measured aqueous groundwater well concentrations around 60 μM.[139] Adsorbed phosphate surface chemistry is highly pH dependent and involves several multivalent species and coordination modes.[140] For example, Elzinga et al. concluded that the phosphate complexation to hematite was dependent on both pH and surface coverage.[65] *Ab initio* quantum chemical calculations and experimental studies for phosphate adsorption on iron oxides, such as hematite, goethite and ferrihydrite, have provided additional insights into the interaction of phosphate with these different iron oxides.[62,64,66,141,142] Particularly relevant to the current study is that phosphate has been shown to competitively adsorb to the same binding sites as biomolecules[6,28] and other oxyanions[143–147]. An investigation of the surface chemistry between

nucleotides and geochemical surfaces in complex milieu is needed to better understand environmental interfaces.

To probe the dynamic surface chemistry occurring between nucleotides and iron oxide nanoparticle surfaces, a surface sensitive, *in-situ* method is needed. For this reason, attenuated total reflectance Fourier transform infrared (ATR-FTIR) spectroscopy proves to be an ideal technique for these studies. By comparing the spectrum of solution phase nucleotide to that of an adsorbed nucleotide, it is possible to observe peak shifts in band position, intensity, and shape to elucidate the details of the surface chemistry. Different phosphate binding mode coordinations can be distinguished on the surface of an iron oxide surface by observing phosphate band shape changes. As components adsorb onto the nanoparticle surfaces, co-adsorbate interactions can arise. Then to process and elucidate changing spectral features as a function of the external perturbation, two-dimensional correlation spectroscopy (2DCOS) can be used. In general, 2DCOS can be used to analyze the spectral peaks in a system that is perturbed by an external variable such as temperature, pH, and for this study, time.[110] Interpretation of 2DCOS allows for the correlation of spectral peak changes with respect to other peaks, as well as sequential peak changes with respect to time. 2DCOS has previously been used to assess the effects of surface adsorption on protein stability[18,52] and ligand exchange[48]. Herein, we use 2DCOS to correlate oxyanion phosphate absorptions with nucleotide absorptions to determine sequential peak changes.

In this study the adsorption of deoxyadenosine monophosphate (dAMP), a nucleotide, onto high surface area hematite nanoparticles, α-Fe_2O_3, in the presence or absence of phosphate is explored at pH 5 and 8. Single component dAMP solution phase spectrum was compared to adsorbed spectrum to understand the nano-bio interaction. To build complexity, effects of phosphate were used to model the impact of oxyanions on the adsorption behavior of dAMP. These

time-dependent spectra were processed using 2DCOS to elucidate adsorption and desorption mechanisms. Finally, a nucleotide adsorption pathway was proposed using results from ATR-FTIR spectroscopy and 2DCOS. Overall, this study provides a further understanding of these geo-bio and nano-bio interactions and interfaces at environmentally relevant concentrations.

3.3 Experimental Methods

3.3.1 Materials

2'-Deoxyadenosine-5'-monophosphate (dAMP), Disodium phosphate, sodium chloride, 1N hydrochloric acid, and 1N sodium hydroxide was purchased from Sigma-Aldrich. The chemical structure of dAMP is shown in Figure 3.1. Hematite (α-Fe_2O_3) was purchased from Alfa Aesar (stock #44666). dAMP has a molecular weight of 331 g/mol and four pKa values, 0.9, 3.7, 6.1, and 13.1.[148] All chemicals were used without additional purification.

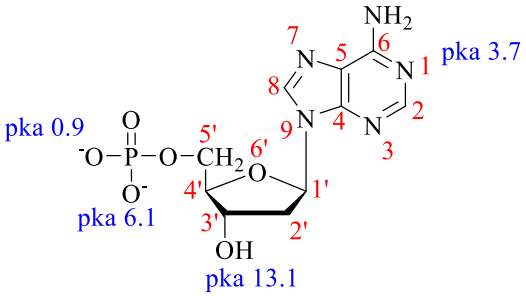

Figure 3.1 Chemical structure of 2'-Deoxyadenosine-5'-monophosphate (dAMP) and pK_a values

3.3.2 Iron Oxide Nanoparticle Characterization

The crystalline phase of α-Fe_2O_3 nanoparticles was confirmed with X-Ray Diffraction (XRD) using an APEX II Ultra diffractometer with Mo Kα radiation at λ= 0.71073 Å. To measure nanoparticle size, 10 uL of a sonicated 0.03 g/L α-Fe_2O_3 suspension was placed on a formvar/carbon coated 100 mesh copper grid and dried. The copper grid was then analyzed using

a JEM-1400 Plus Transmission electron microscope (TEM) at 80 kV. Size distributions were analyzed with ImageJ software using more than 100 particles. Average particle sizes were fit to a Gaussian function. For specific surface area, a Quantachrome Nova 4200e analyzer was used to measure a Brunauer-Emmett-Teller (BET) N_2 adsorption isotherm. ~100-120 mg of α-Fe_2O_3 particles were loaded into the glass cell and degassed for 18 hours at 150 °C. BET data were analyzed using a 15 multipoint curve.

3.3.3 Attenuated Total Reflectance – Fourier Transform Infrared Spectroscopy

A description of the setup for ATR-FTIR measurements has been given previously.[101] Briefly, ATR-FTIR spectroscopy is based on the total internal reflection of an infrared beam at an interface between an optically dense medium and an optically rare medium. This total internal reflection creates an evanescent wave within the high refractive index medium that exponentially decays into lower refractive index medium. The ATR accessory was a horizontal flow cell with an amorphous material transmitting IR radiation (AMTIR) crystal. Infrared spectra were collected using a Nicolet iS10 FTIR spectrometer (Thermo-Fisher) equipped with a mercury cadmium telluride detector (MCT/A). Spectra were collected at a resolution of 4 cm^{-1} and averaged over 100 scans in the spectral range extending from 750 to 4000 cm^{-1}. All ATR-FTIR spectra were collected and background subtracted using a linear baseline between 900-1800 cm^{-1} with the OMNIC 9 software.

Solution phase spectra of dAMP were taken to observe any spectral changes compared to adsorbed dAMP onto α-Fe_2O_3. Solutions of 6 mM dAMP in 10 mM NaCl aqueous solution were prepared and titrated to pH 5 and pH 8 using HCl or NaOH. First, a background spectra of 10 mM NaCl at the corresponding pH was taken after purging atmospheric gases out of the sample

chamber for approximately 30 minutes. Then, 800 uL of the dAMP solution was pipetted onto the crystal and a spectrum was collected after purging for an additional 30 minutes.

For single-component dAMP adsorption measurements, a α-Fe_2O_3 thin film was prepared by sonicating 5 mg of α-Fe_2O_3 in 800 uL of Milli-Q water and then drop casted onto an AMTIR crystal. The hydrosol was left to dry overnight, leaving a α-Fe_2O_3 thin film. To remove loosely packed α-Fe_2O_3 particles and to collect a background spectrum, 10 mM NaCl at pH 5 solution was flowed over the thin film with a peristaltic pump at ~1 mL/min for 30 minutes. A solution of 30 μM dAMP in 10mM NaCl was sonicated and titrated to pH 5 with HCl and NaOH and then flowed over the film at ~1 mL/min for 90 minutes, while spectra were collected every 5 minutes. Then, a desorption solution of 10mM NaCl was flowed over the film for 90 minutes. The same method was done to collect single-component adsorption spectra at pH 8.

For multi-component adsorption spectral measurements an α-Fe_2O_3 thin film was prepared and a solution of 300 μM phosphate (Na_2HPO_4) solution in 10 mM NaCl was titrated to pH 5 with HCl and NaOH. To saturate the film with phosphate, the 300 μM Na_2HPO_4 solution was flowed over the thin film for 90 minutes and spectra were collected every 5 minutes. For the co-adsorption experiments, 30 μM dAMP solution in 10mM NaCl was flowed over the phosphate saturated film at ~1 mL/min for 150 minutes where spectra were collected every 5 minutes. The same method was done for pH 8.

3.3.4 Two-Dimensional Correlation Spectroscopy (2DCOS)

2DCOS is an analytical tool to investigate spectral changes caused by external perturbations such as time, pH, concentration, and temperature. 2DCOS analysis was previously described[18] and the details of the mathematical construct can be found elsewhere.[110,112,119] Sequential molecular functional group interactions with the surface can be determined using

generalized 2DCOS synchronous (Φ) and asynchronous (Ψ) correlation maps and can be interpreted using Noda's rules.[119] Briefly, the $\Phi(\nu_1, \nu_1)$ diagonal peaks are always positive and correspond to the peaks that indicate the most responsive peaks to the external perturbation and can be deemed the autocorrelation peaks. The off-diagonal $\Phi(\nu_1, \nu_2)$ peaks, cross peaks, are coupled spectral intensity changes and indicate intensity directional changes. A positive $\Phi(\nu_1, \nu_2)$ value suggests that both ν_1 and ν_2 are changing in the same direction, either both increasing or decreasing. A negative $\Phi(\nu_1, \nu_2)$ value suggests the opposite, where ν_1 is increasing and ν_2 is decreasing or vice versa. The Ψ correlation map can be used to determine sequential changes to spectra. If the sign of $\Phi(\nu_1, \nu_2)$ is the same as $\Psi(\nu_1, \nu_2)$, then ν_1 occurs before ν_2 whereas if the sign of $\Phi(\nu_1, \nu_2)$ and $\Psi(\nu_1, \nu_2)$ are opposite, then ν_1 occurs after ν_2. All computational algorithms were checked by generating simulated spectra and compared to literature and 2dShige version 1.3 (Shigeaki Mortita, Kwansei-Gaukuin University, 2004–2005) developed by Noda as already discussed in Chapter 2.[118,120]

3.4 Results and Discussion

3.4.1 Iron Oxide Nanoparticle Characterization

Iron oxide nanoparticles were characterized using different methods and the data are presented in **Figure 3.2**. The average size of iron oxide nanoparticles was determined to be 84 ± 53 nm by analyzing the TEM micrograph (**Figure 3.2a**). The micrograph also indicates a small deviation from spherical particles with an aspect ratio, which is the ratio of particle width to length, being slightly larger than one (1.3 ± 0.2). The particles are also seen to be aggregated. **Figure 3.2b** shows the iron oxide XRD pattern consisting of single-phase hematite. The experimental set-up for ATR-FTIR is shown in **Figure 3.2c** where the thin film is first made, then a sample solution is

flowed over the thin film where *in-situ* measurements can be collected. The BET surface area of hematite used is 24 m^2/g.

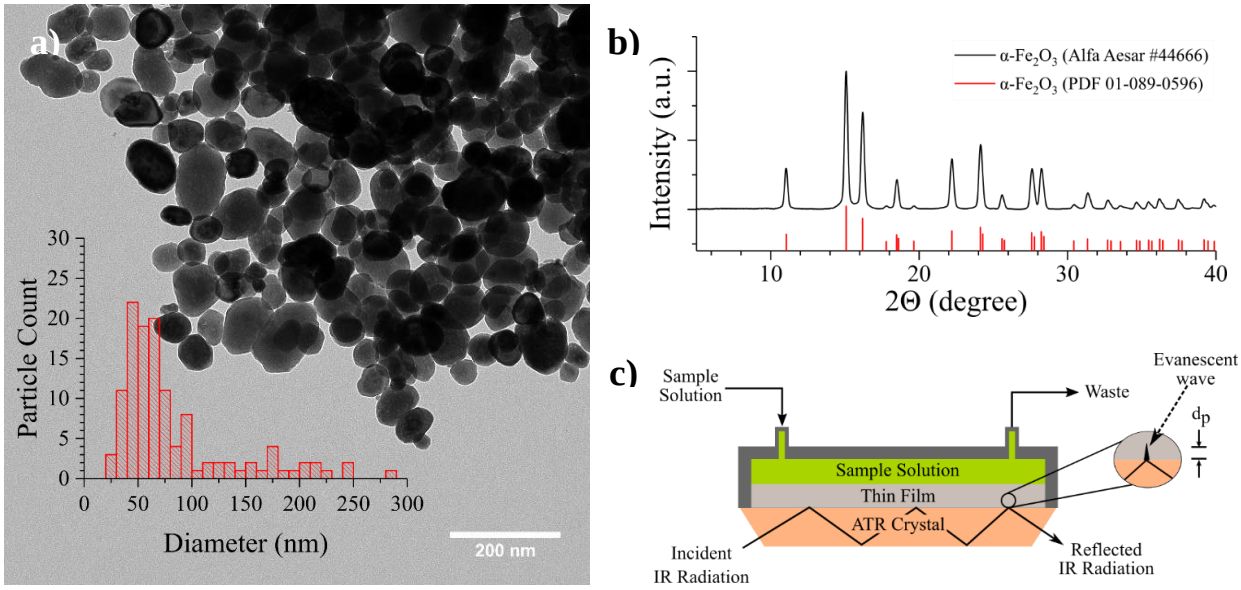

Figure 3.2 α-Fe_2O_3 nanoparticle characterization and experimental schematic

a) TEM micrograph with size distribution analysis (insert). b) XRD data of α-Fe_2O_3. c) Representative diagram of the ATR-FTIR experimental set-up with an evanescent wave penetration depth, d_p.

3.4.2 Analysis of Solution Phase and Adsorbed Nucleotide

dAMP consists of a phosphate group, sugar ribose, and adenine nucleobase. The aqueous solution phase spectra of dAMP at pH 5 and pH 8 are shown in **Figure 3.3** (top). Using the Hendersen-Hasselbalch equation (Supporting Information (SI) **Figure 3.13**), at pH 5, 4.4%, 88.5% and 7.0% are divalent anionic, monovalent anionic, and zwitterionic forms of dAMP, respectively. For pH 8, 98.8% and 1.2% are divalent anionic and monovalent anionic protonation forms of dAMP, respectively. The vibration indicating the basic protonation of $\delta(N1H^+)$ on the adenine nucleobase from the zwitterionic form can be seen at 1707 cm^{-1} for pH 5 but not for pH8. The solution phase phosphate functional group peaks can be seen between 900 to 1200 cm^{-1} and are noticeably different between pH 5 and pH 8. All three speciation forms can be observed in the

solution phase spectrum for pH 5, divalent anionic $\nu_s(PO_3^{-2})$, monovalent anionic $\nu(PO_3H^-)$, and

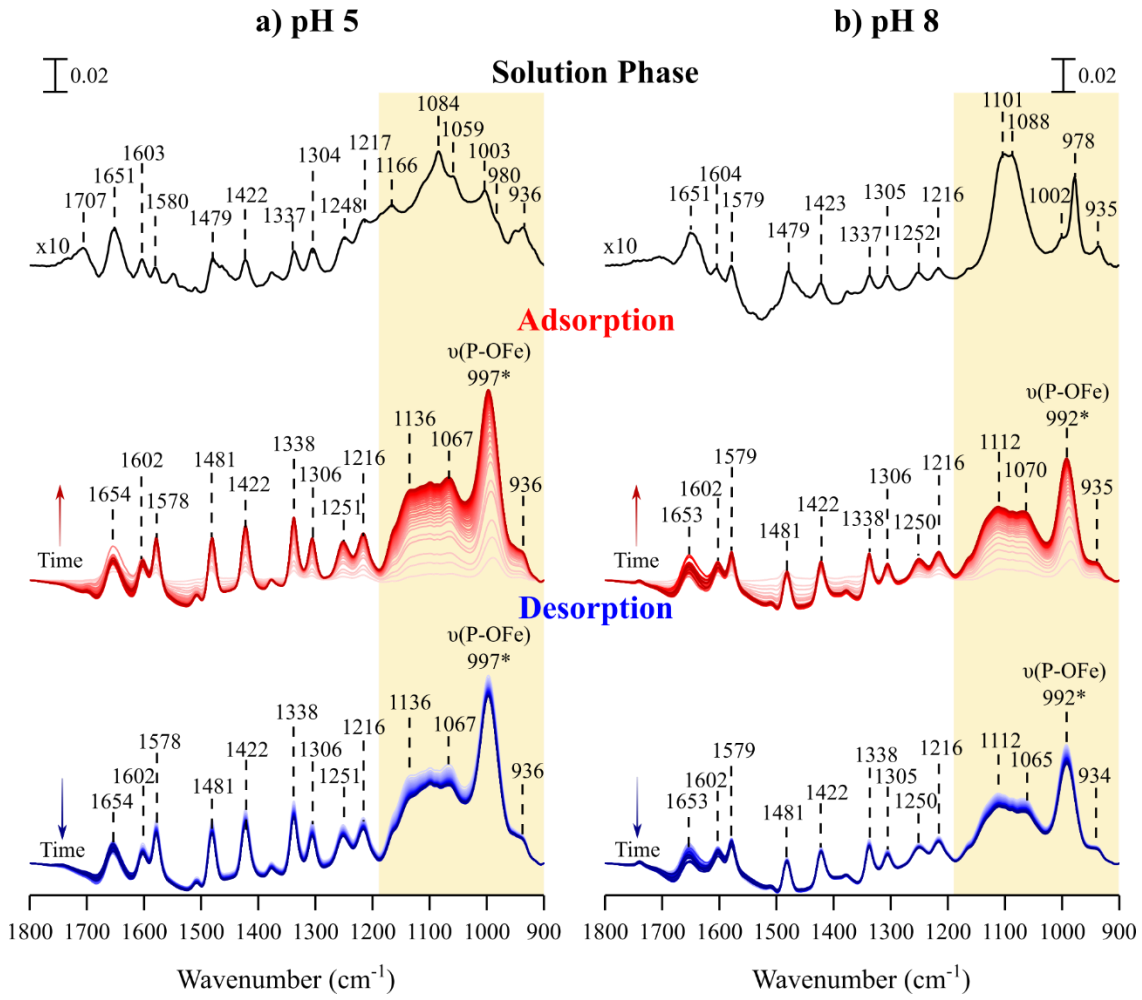

Figure 3.3 ATR-FTIR spectra of deoxyadenosine monophosphate

ATR-FTIR spectra of deoxyadenosine monophosphate at a) pH 5 and b) pH 8 for different stages of the experiment. Solution phase dAMP (top), time dependent adsorption spectra of dAMP onto α-Fe_2O_3 thin film (middle), and time dependent desorption of dAMP with NaCl (bottom). * in the adsorption and desorption spectra represent the ν(P-OFe) vibrational mode used for kinetic analysis. All spectra are on the same absorbance scale. Lighter color spectra represent earlier time points where darker spectral lines represent later time points. Solution phase spectrum are multiplied by 10 to indicate there is minimal absorbance contribution from the bulk in adsorption spectra. The shaded box represents the phosphate band region where spectral differences can be seen between solution and adsorbed phosphate, suggesting surface interactions via the phosphate group.

zwitterionic $\delta(N1H^+)$ at 980, 1059, and 1707 cm^{-1}, respectively. For pH 8, the divalent anionic form is the major form and is observed to have a very sharp peak at 978 cm^{-1}. The monovalent anionic form is not visible as it is within a broad phosphate peak centered around 1101 cm^{-1}. The

phosphate region contains a mixture of multiple speciations with overlapping peaks, which causes significant peak broadening.[62,65]

In **Figure 3.3** (middle), the time resolved spectra for dAMP adsorbed on α-Fe_2O_3 is shown and compared to solution phase spectra to identify specific functional group surface interactions causing frequency shifts and band shape differences. It should be noted the solution phase spectra are scaled ten-fold and the concentration of solution phase dAMP is 200 times more than adsorbed solution flowing over the thin film. This difference in solution phase intensities ensures that dAMP bulk contributions are minimal and peaks in the adsorbed spectra are only that of adsorbed dAMP. The solution and adsorbed phase at pH 5 was compared in **Figure 3.3a**. The adenine and ribose peaks above 1200 cm^{-1} shift minimally, less than 4 cm^{-1}, while retaining similar peak shapes, suggesting little interaction with the hematite surface. This is shown in **Table 3.1** where peak shifts are given and seen to be small for many of the vibrational bands.[126,149–153] However, absorptions <1200 cm^{-1} broaden significantly, suggesting that the hematite surface is largely interacting with the nucleotide phosphate group. It has been previously reported that oxyanion phosphate can coordinate to hematite surfaces to form multiple complexes such as monodentate and bidentate bridging, each with different protonation species.[62,65,141,142,154] Significant P-O band broadening has been previously observed while other functional groups, not directly associated with surface binding, show minimal peak shift and broadening.[153] Furthermore, it has been reported that deprotonation and a mixture of monodentate and bidentate coordination modes can occur on iron oxide surfaces, increasing the surface chemistry complexity.[64,66,155] Drawing on these analogous past studies and since dAMP is observed to adsorb via the phosphate group with band broadening, it is reasonable to suggest that multiple binding coordinations may also exist. The deprotonation of dAMP following a condensation reaction with hematite surface hydroxyl groups is suggested

by Reaction 3.1. The δ($N1H^+$) 1707 cm^{-1} peak is no longer present upon adsorption, indicating another deprotonation step.

$$\equiv Fe - OH + dAMP \rightarrow \equiv Fe - dAMP + H_2O \qquad \textbf{Equation 3.1}$$

The 997 cm^{-1} peak appears for adsorbed dAMP, which is assigned to the ν(P-OFe). The 936 cm^{-1} peak, which is assigned to the δ(POH) vibrational mode in solution, is also present when dAMP is adsorbed onto hematite. Yan et al. studied the glyphosate adsorption onto goethite and observed P-O band broadening with minimal changes to carboxylate and amine related peaks. Within the P-O band envelope, the 936 cm^{-1} was assigned to the binuclear bidentate symmetric stretch and was confirmed with DFT calculations.[153] Similarly, the study confirmed the presence of multiple complexation modes between pH 5-9. Fry et al. used solid-state NMR and *ab-initio* calculations to observe both primarily monodentate and bidentate dAMP surface complexation with alumina at pH 5.5.[156] Therefore the 936 cm^{-1} peak has been assigned to the bidentate binding mode. **Figure 3.3a** (bottom) shows the desorption spectra depicting little change to the spectra other than lower intensity values corresponding to a loss of loosely bound surface adsorbate species and negligible changes to surface chemistry. **Figure 3.14** compares the spectral differences at the last adsorption and desorption time points for both pH values and shows little changes to bands above 1200 cm^{-1} in the spectra and band broadening for absorptions below 1200 cm^{-1}. For the spectra of adsorbed dAMP at pH 8 (**Figure 3.3b**), adenine and ribose sugar show minimal peak shifts and maintain similar peak shape when compared to solution phase. Like pH 5, the phosphate group band broadened, indicating specific interactions with the surface. Additionally, the distinct ν(P-OFe) peak at 992 cm^{-1} is present but not as intense compared to pH 5. The 935 cm^{-1} peak is present, indicating a bidentate surface complex as discussed previously for adsorption of dAMP at pH 5.

Table 3.1 Deoxyadenosine monophosphate vibrational mode assignments in solution at pH 5 and 8 compared to adsorbed deoxyadenosine monophosphate.

Vibrational modes*	Vibrational Frequency (cm^{-1})						Literature Assignment (cm^{-1})
	Solution		Adsorbed		Adsorbed on PO_4 Saturated Surface		
	pH 5	pH 8	pH 5 (Δ)‡	pH 8 (Δ)‡	pH 5 (Δ)‡	pH 8 (Δ)‡	
δ($N1H^+$)	1707						1696[45]
δ(NH_2)	1651	1651	1654 (+3)	1653 (+2)	1651 (+0)	1655 (+4)	1656[9,44-47]
purine ring	1603	1604	1602 (-1)	1602 (-2)	1604 (-1)	1604 (+0)	1607[47]
purine ring	1580	1579	1578 (-2)	1579 (+0)	1578 (-2)	1579 (+0)	1570[47]
ν(N7-C8), δ(C8-H)	1479	1479	1481 (+2)	1481 (+2)	1480 (-1)	1482 (+3)	1477[46], 1480[47]
δ(CH_2)	1422	1423	1422 (+0)	1422 (-1)	1422 (+0)	1423 (+0)	1425[47]
purine ring	1337	1337	1338 (+1)	1338 (+1)	1338 (+1)	1338 (+1)	1331[47]
purine ring	1304	1305	1306 (+2)	1306 (+1)	1306 (+2)	1306 (+1)	1307[47]
δ(C6-NH_2)	1248	1252	1251 (+3)	1250 (-2)	1252 (+4)	1251 (+1)	1254[44], 1249[47]
ν(N9-C1')	1217	1216	1216 (-1)	1216 (+0)	1217 (+0)	1217 (+1)	1212[47]
$\nu_s(PO_2^-)$	1166		1136 (-30)		1167 (+1)		1137[9]
ν(C-O-P, P-O-P)				1112			1114-1118[9]
ν(C-O) sugar		1101					1100[47]
$\nu_{as}(PO_3^{2-})$	1084	1088					1088[47], 1106-1108[9]
ν(PO_3H^-)	1059		1067 (+8)	1070 (+11)			1060[47]
ν(P-O)	1003	1002					996-1002[9]
ν(P-OFe)			997	992	991	983	993[9]
$\nu_s(PO_3^{2-})$	980	978					974[47], 979[9]
ν_s(P-$(OFe)_2$) of bidentate complexes			936	935	939	938	935[48]
δ(POH)	936	935					935[45]

* $\nu_{s/as}$: symmetric/asymmetric stretch vibration; δ: bending vibration

‡ Δ: difference between adsorbed and solution phase wavenumber at last time point collected on ATR-FTIR

However, the adsorbed phosphate region band shapes are different between pH 5 and 8, which suggest a different mixture of surface complexes. This pH dependent binding coordination is not surprising as this phenomenon has been observed in other studies.[65,66,153,157] Upon desorption, there is little change to peak positions or band shapes but lower spectral intensity is observed.

Adsorption and desorption kinetics can be determined by monitoring peak intensities as a function of time and is shown in **Figure 3.4** using ν(P-OFe) peak height. In the adsorption stages, the intensity values seem to exponentially increase and plateaus out suggesting a maximum coated surface. Following this, a desorbing aqueous solution not containing dAMP, was introduced into the flow cell. There is only a small decrease in peak intensity on the time scale of ca. two hours which suggests that most nucleotides are irreversibly bound to the surface regardless of pH. Hematite dissolution at pH 5 would show a continual loss of peak intensities as the number of binding sites is reduced but that is not seen. Lanzl et.al. showed hematite dissolution rates decreased logarithmically as pH increased between 1-2.5.[158] At pH values between 2-6, dissolution rates are even further decreased, suggesting hematite dissolution is not expected at pH 5. One noticeable difference between the two saturated hematite surfaces are the intensity values. At 90 minutes, the intensity for pH 5 is ca. 150% higher than at pH 8, suggesting that nucleotide surface coverage is greater at pH 5. The isoelectric point of hematite is 7.9 and at a lower pH value than this, the particle is positively charged whereas at a higher pH value, the particle is negatively charged. At pH 5, hematite is positively charged and at pH 8, the particle is approximately neutral. At pH 5, dAMP is mostly a monovalent anionic species, thus carrying a negative charge. At pH 8, dAMP is divalent anionic, carrying a more negative charge. Therefore, at pH 5, there is an electrostatic attraction between hematite and dAMP whereas there is reduced interaction at pH 8, explaining the differences in adsorption intensities.

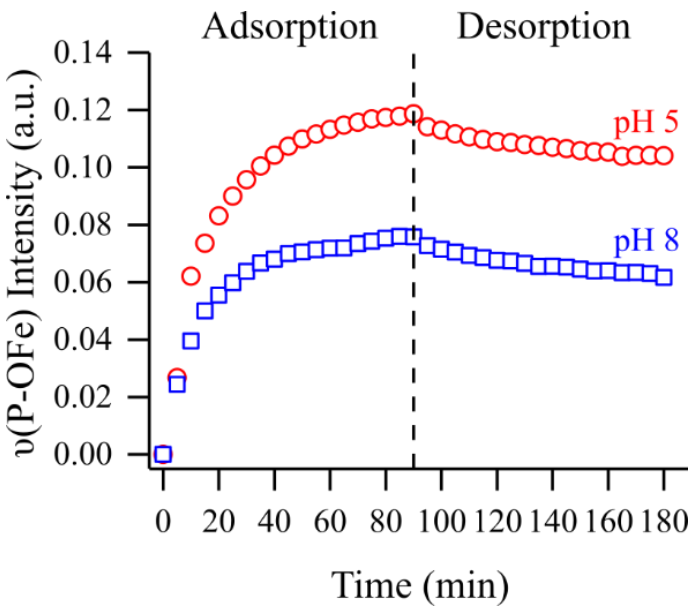

Figure 3.4 dAMP adsorption kinetics onto α-Fe_2O_3 using the ν(P-OFe) vibrational mode intensity occurring at 997 and 992 cm^{-1} for pH 5 and pH 8, respectively

3.4.2 Effects of Adsorbed Oxyanion on dAMP Adsorption on Hematite

Oxyanions are present in groundwater and phosphate is one of the common components.[138,159] As noted above, phosphate adsorption can occur on different types of environmental surfaces. Upon adsorption on iron oxide surfaces, deprotonated phosphate has been observed to lead to negative particle zeta potential values of -15 to -30 mV.[160] This change in zeta potential of the particle can further influence subsequent multicomponent adsorption mechanism.[161] **Figure 3.5a** shows the adsorbed spectra of disodium phosphate on hematite at pH 5 and 8. Most notably are the prominent peaks between 900 to 1200 cm^{-1}, representing the main region where P-O bonds absorb infrared light. The band shapes for this region are different between pH 5 and 8. For pH 5, there are two prominent peaks at 1004 and 1116 cm^{-1} whereas for pH 8, the region is broader, suggesting multiple absorptions contributions. Integrated peak area was done between 900-1200 cm^{-1} instead of peak intensity as the ν(P-OFe) peak was not clear at

all time points for both pHs (**Figure 3.5b**). Adsorbed phosphate peak area is seen to exponentially increase and begin to plateau, suggesting a saturated surface at 90 minutes. Phosphate appears to

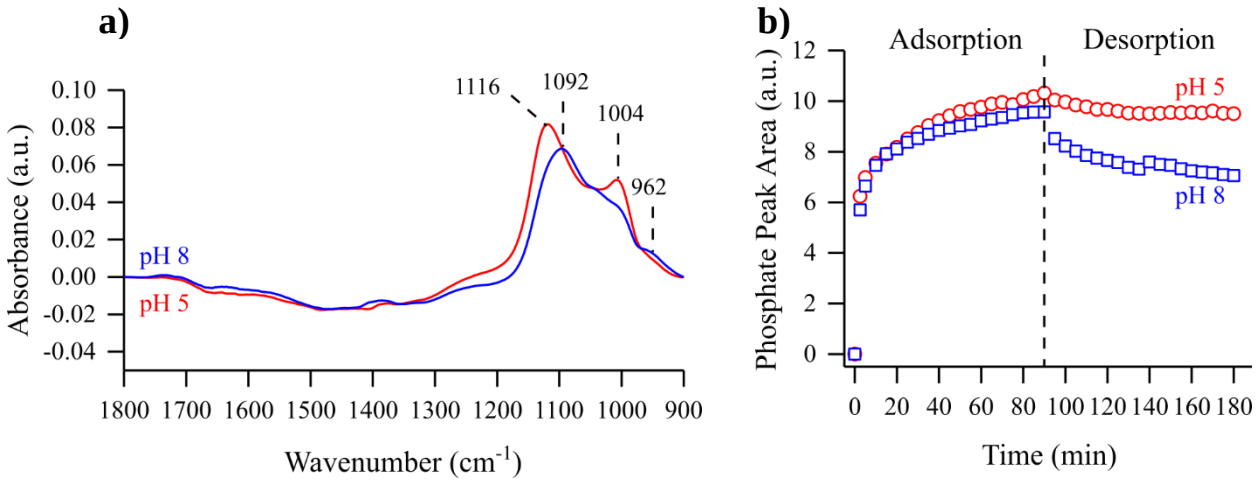

Figure 3.5 Spectra of phosphate adsorbed on hematite and kinetics

Phosphate adsorption onto α-Fe_2O_3 at pH 5 (red) and pH 8 (blue). a) ATR-FTIR spectra of phosphate adsorption at 90 minutes onto α-Fe_2O_3. b) Integrated peak area between 900-1200 cm^{-1} representing the phosphate region for adsorption and desorption.

be irreversibly bound to the surface as the peak area does not fall back to zero when desorbed with water. The time resolved phosphate adsorption and desorption spectra on hematite is shown in **Figure 3.15** and **Figure 3.16** for pH 5 and pH 8, respectively. As mentioned previously, phosphate has been shown to coordinate to the hematite surface hydroxyl groups as a mixture of monodentate and bidentate species and observed here with broad bands.

Figure 3.6 shows the effects of pre-adsorbed phosphate on the adsorption behavior of dAMP. **Figure 3.6a** shows the ATR-FTIR spectra of dAMP adsorption onto a phosphate saturated hematite surface at pH 5 and pH 8. Adenine and ribose groups are observed to have minimal peak shifts compared to solution phase and adsorbed onto a bare surface for both pH values. The ν(P-OFe) shifts from 997 to 991 cm^{-1} and from 992 to 983 cm^{-1} when adsorbed onto a pre-adsorbed phosphate surface at pH 5 and pH 8, respectively. **Figure 3.6b** are the peak intensities for the ν(P-OFe) peak at both pH values. For pH 5 at 90 minutes, the intensity for dAMP adsorbed on a phosphate-hematite surface is 25% of that in the absence of phosphate and 13% for pH 8. This

significant reduction in dAMP adsorbed on the surface suggests that phosphate occupies some of the same binding sites as dAMP. Moreover, the intensity for pH 5 is about twice than that of pH 8

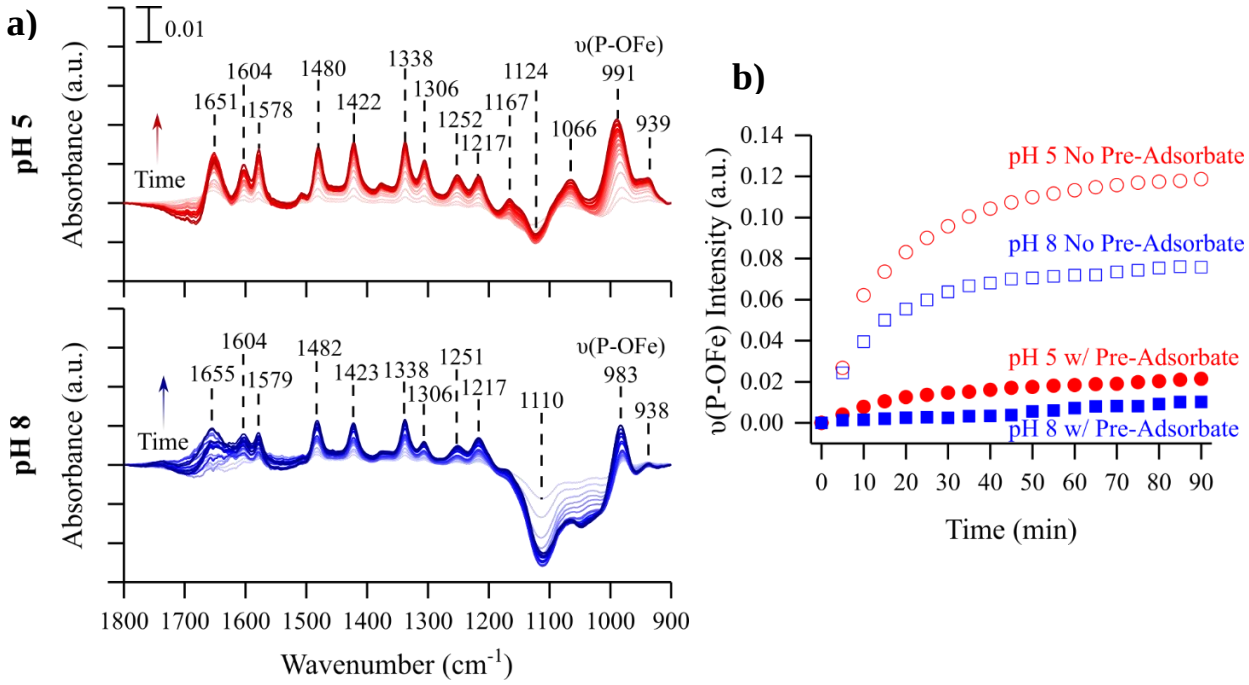

Figure 3.6 ATR-FTIR spectra of dAMP adsorbed on phosphate coated hematite and kinetics

a) ATR-FTIR difference spectra for the displacement of adsorbed phosphate with dAMP at pH 5 (top) and pH 8 (bottom). Spectra were ratioed against saturated phosphate α-Fe_2O_3 film. b) peak height kinetics for the ν(P-OFe) vibrational mode for the adsorption of deoxyadenosine monophosphate on a bare α-Fe_2O_3 surface at pH 5 (red empty circles) and pH 8 (blue empty squares), as well as a pre-adsorbed phosphate α-Fe_2O_3 surface at pH 5 (red filled circles) and pH 8 (blue filled squares).

on a phosphate saturated surface. This phenomenon cannot be solely explained by electrostatics as was hypothesized for surfaces without pre-adsorbed phosphate as both the surface and nucleotide are negatively charged. The surface is negatively charged due to the adsorbed deprotonated phosphate at both pHs. A previous study simulated DNA adsorption onto a MoS_2 surface and concluded that the adsorption energy was mostly due Van der Waal interactions while electrostatics contributed minimally.[96] Furthermore, the study observed that the equilibrated orientation of the DNA strand was perpendicular to the surface via the phosphate terminal backbone. This suggests that the dAMP could be interacting with the surface via Van der Waal

interactions. However, the surface hydroxyl groups are occupied by phosphate oxyanions but the increase in ν(P-OFe) peak intensity suggests dAMP is binding to the surface, not to the pre-adsorbed phosphate. Interestingly, **Figure 3.6a** shows a broad negative peak at earlier adsorption time points around 1124 and 1110 cm^{-1} for pH 5 and 8, respectively. This suggests that pre-adsorbed phosphate is either first desorbed, freeing a coordination site for dAMP or displaced by dAMP. As seen in **Figure 3.5b**, phosphate can be partially desorbed with only aqueous NaCl and in another experiment of washing the pre-adsorbed phosphate with water then adsorbing dAMP (data not shown), the ν(P-OFe) intensity was ca. 2x and 2.5x higher when the film was washed for pH 5 and pH 8, respectively. This intensity difference could suggest that when dAMP is a co-adsorbate with phosphate, there is a synergistic stabilization effect, minimizing the desorption or displacement of phosphate.

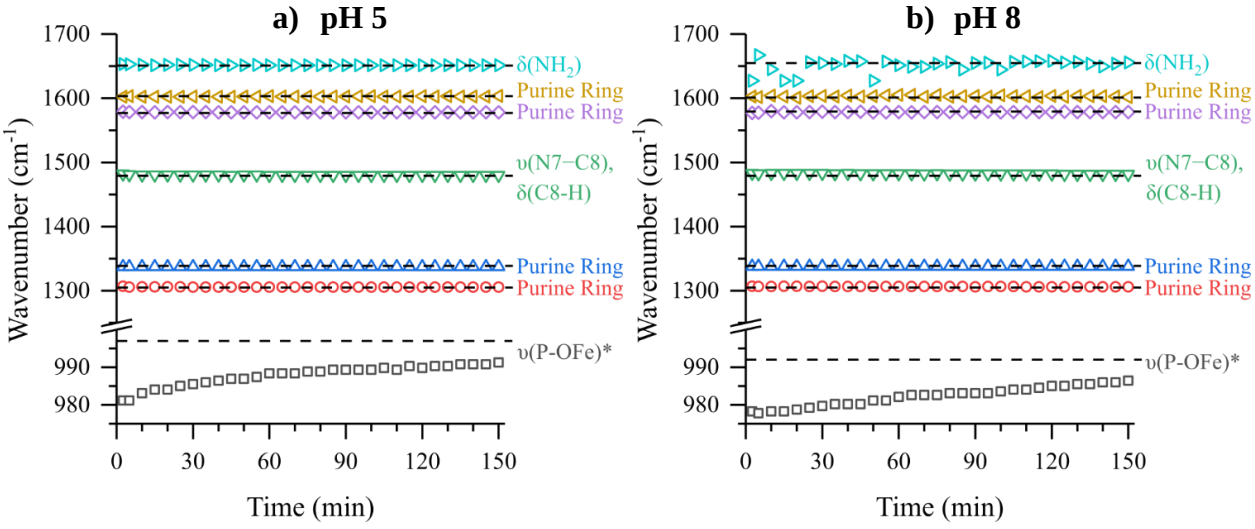

Figure 3.7 dAMP adsorbed on hematite functional group peak positions

dAMP functional group peak positions as a function of time during the adsorption onto a phosphate coated surface α-Fe_2O_3 at a) pH 5 and b) pH 8. Dashed lines represent the solution phase peak positions. ν(P-OFe)* dashed line represents the single component dAMP adsorption onto hematite surface peak position.

When oxyanion phosphate adsorbs to the surface the spectrum has strong, broad peaks centered around 1116 and 1092 cm^{-1} for pH 5 and pH 8, respectively. As dAMP adsorbs onto the phosphate covered surface, it interacts with already adsorbed species, causing changes to spectral

features. The peak loss stemming from the desorption of phosphate could be shifted due to interactions from adsorbing dAMP molecules. This synergistic interaction between co-adsorbates influencing the mechanism of adsorption of another species has been seen in previous studies.[28,153,161]

Peak position shifts can indicate functional group interactions with the hematite surface and could elucidate any time dependent interactions. **Figure 3.7** shows various dAMP functional group peak positions as a function of adsorption time onto a phosphate coated surface. The ν(P-OFe) peak is seen to shift 10 cm^{-1} for pH 5 and 8 cm^{-1} for pH 8 as dAMP adsorbs to the phosphate coated surface. Interestingly, the ν(P-OFe) peak appears to approach the frequency observed for single component dAMP adsorption as noted by the dotted line in **Figure 3.7** for both pH 5 and 8. As pre-adsorbed phosphate is displaced by dAMP, there are fewer co-adsorbate interactions, leading to a peak position that is more closely related to single component adsorbed dAMP. As noted previously, adenine and ribose show no frequency shifts when comparing the frequencies observed in solution compared to when adsorbed. If adenine or ribose peak positions deviated from solution phase at earlier time points, it could be possible that the nucleotide initially interacted with the surface with those functional groups and a molecular reorientation occurred where at equilibrium, the phosphate group complexed with the surface. However, the only peak shifts observed at earlier time points are the phosphate group, indicating a functional group specific interaction with the surface. The small fluctuations for $\delta(NH_2)$ at pH 8 could be due to interference with the broad water bending vibration mode centered around ~1640 cm^{-1}. This is only seen for pH 8 due to the fewer amount of adsorbed dAMP molecules compared to pH 5, thus a potentially larger interference with the water bending mode.

For dAMP to coordinate to the surface, adsorbed phosphate must be desorbed which was observed as negative peak intensities at 1124 and 1110 for pH 5 and pH 8, respectively. Peak loss intensities were shown as a function of adsorption time in **Figure 3.8**. Interestingly, local minima are observed at 35 and 45 min for pH 5 and pH 8, respectively. For the sake of clarity, these time points will be referred to as the critical adsorption time (T_c). At time points earlier than T_c, phosphate is desorbed while dAMP is adsorbing. At T_c, the intensity changes due to phosphate

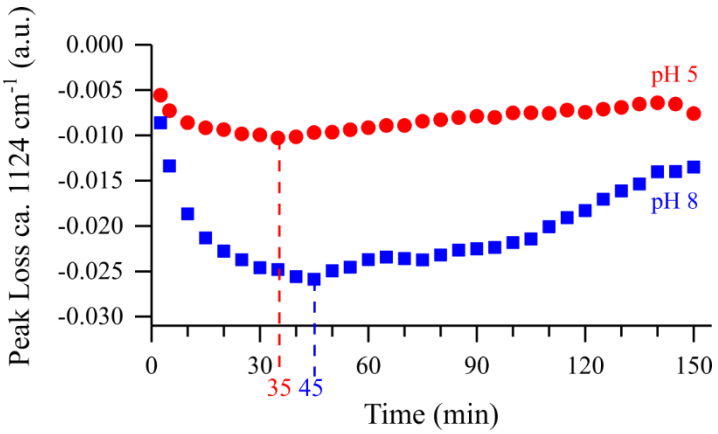

Figure 3.8 Peak loss absorbance kinetics for 1124 and 1110 cm^{-1} in Figure 3.5 for pH 5 and pH 8, respectively

desorption and dAMP adsorption are equal, showing a local minimum. After T_c, the intensity starts to increase as dAMP begins to adsorb to available surface binding sites. As previously mentioned, phosphate has various surface complexes when adsorbed onto the hematite surface. Kubicki et al. simulated phosphate adsorption onto multiple goethite facets which resulted in varying adsorption energies, suggesting that stable complexes are dependent on crystal faces.[62] Phosphate desorption energies are equal to the negative of adsorption energies which suggests there can be specific desorption of complexes depending on desorption energies. Moreover, the standard deviations for the simulated adsorption energies are high, suggesting large uncertainty. This highlights the partial displacement complexity of adsorbed phosphate with dAMP which is dependent on multiple factors including, pH, crystal face, and surface complex.

3.4.4 Two-Dimensional Correlation Spectroscopy

The difference in adsorption mechanism marked by a critical time which differentiates between the desorption of phosphate and the adsorption of dAMP can be analyzed using 2DCOS. 2DCOS can be used to correlate intensity changes as a function of adsorption time and be used to compare the differences in adsorption mechanisms for pH 5 before T_c and after T_c (**Figure 3.9**) and pH 8 before T_c and after T_c (**Figure 3.10**). Autocorrelation spectra represents peaks that are highly correlated to the external perturbation, adsorption time. The autocorrelation spectra can be generated by a diagonal intensity line trace for the synchronous 2DCOS map. The autocorrelation values are always positive and do not indicate whether peaks are increasing or decreasing. Figure 9 shows the 2DCOS autocorrelation spectra and maps for dAMP adsorption onto a phosphate coated surface at pH 5 before T_c (**Figure 3.9a**) and after T_c (**Figure 3.9b**). The autocorrelation spectra highlight phosphate peak shifts between the two regions. Interestingly before T_c, many of the dAMP related autopeaks (1651, 1602, 1578, 1480, 1422, 1337, 1306, 1252, 1120, 988 cm^{-1}) have a larger relative intensity than the 1120 cm^{-1} phosphate peak that desorbs. This could suggest that as phosphate is either displaced or desorbed, dAMP quickly adsorbs and could be supported by the smaller T_c value for pH 5 compared to pH 8. Comparing between T_c regions, the ν(P-OFe) is seen to shift from 988 to 1001 cm^{-1}, a possible change in surface complexation modes for both dAMP and adsorbed phosphate. The sequential order of peak change can be determined applying Noda's rules to the synchronous and asynchronous signs found in **Table 3.2** and **Table 3.3** for before T_c and after T_c at pH 5, respectively. Sequential order of change before T_c was determined to be: 1120 (P-O band) cm^{-1} → 1602 (purine), 940 (P-O band) cm^{-1} → 1578 (purine), 1480 (ν(N7-C8), δ(C8-H)) cm^{-1} → 1422 (δ(CH_2)), 1337 (purine) cm^{-1} → 1651 (δ(NH_2)) cm^{-1} → 1306 (purine), 1064 (P-O band) cm^{-1} → 988 (P-O band) cm^{-1} → 1252 (δ(C6-NH_2) cm^{-1} → 1216 (ν(N9-C1')) cm^{-}

[1]. Unsurprisingly, 1120 cm^{-1} is the first peak to change as phosphate desorbs prior to dAMP adsorption. There are several cross peak values that show a non-zero synchronous value and a zero asynchronous value. This has been previously reported in literature which is caused by frequency or band-width changes that can blur peak position and intensity in 2DCOS.[18,52] For this reason, cross peaks that have a zero asynchronous value will be ignored in determining sequential peak order. After the initial 1120 cm^{-1} change, dAMP associated peaks change indicating the adsorption of the nucleotide onto the surface. Phosphate group related peaks, such as 940, 1064, and 988 cm^{-1}, are seen to change throughout the sequential order, suggesting the constant complexation changes while dAMP adsorbs to the surface. After T_c (**Figure 9b**), the sequential order is: 1604 (purine) cm^{-1} → 1578 (purine) cm^{-1} → 1480 (ν(N7-C8), δ(C8-H)), 1421 (δ(CH_2)), 1337 (purine), 1305 (purine), 1251 (δ(C6-NH_2), 1215 (ν(N9-C1')), 1065 (P-O band) cm^{-1} → 1001 (P-O band) cm^{-1} → 1151 (P-O band), 1100 (sugar) cm^{-1} → 1651 (δ(NH_2)) cm^{-1}. Notably, the 1120 cm^{-1} P-O band is absent in this time region because most of the pre-adsorbed phosphate has been displaced and the peak intensities are increasing due to the adsorption of dAMP. This is marked by adenosine related peaks occurring earlier in the sequence. Moreover, the peaks due to the phosphate group within dAMP peaks are seen at the end of the functional group sequence changes, possibly suggesting the final complexation state where the phosphate group is bound to the surface.

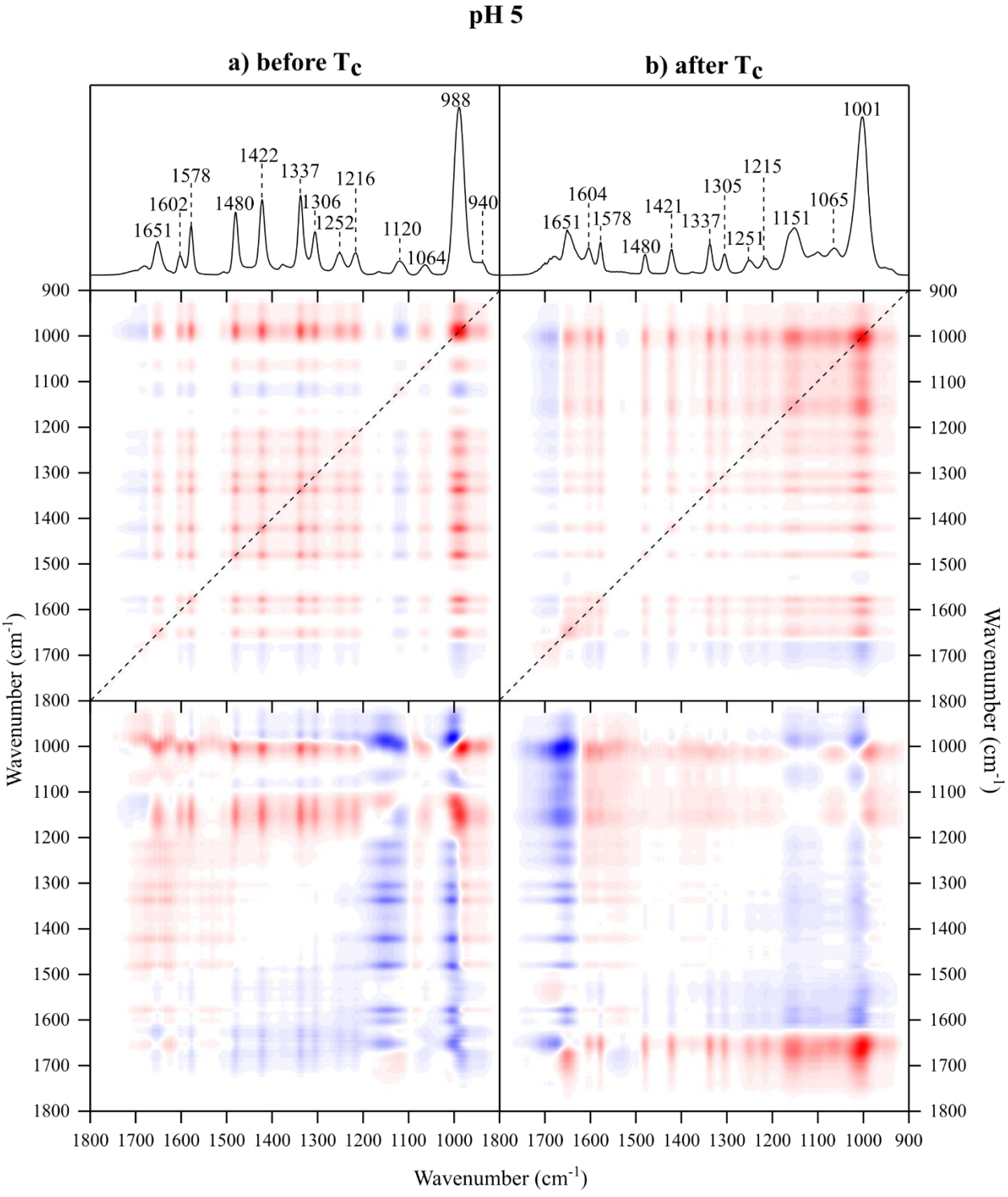

Figure 3.9 2DCOS maps for dAMP adsorbed on phosphate saturated hematite surface at pH 5

2DCOS maps for dAMP adsorption onto phosphate saturated hematite surface at pH 5 (a) before T_c and (b) after T_c. Autocorrelation spectra (top), synchronous 2DCOS map (middle), and asynchronous 2DCOS map (bottom). Dotted line in synchronous 2DOCS correspond to the intensity line trace which is the same as autocorrelation spectra. Red and blue corresponds to positive and negative correlations, respectively.

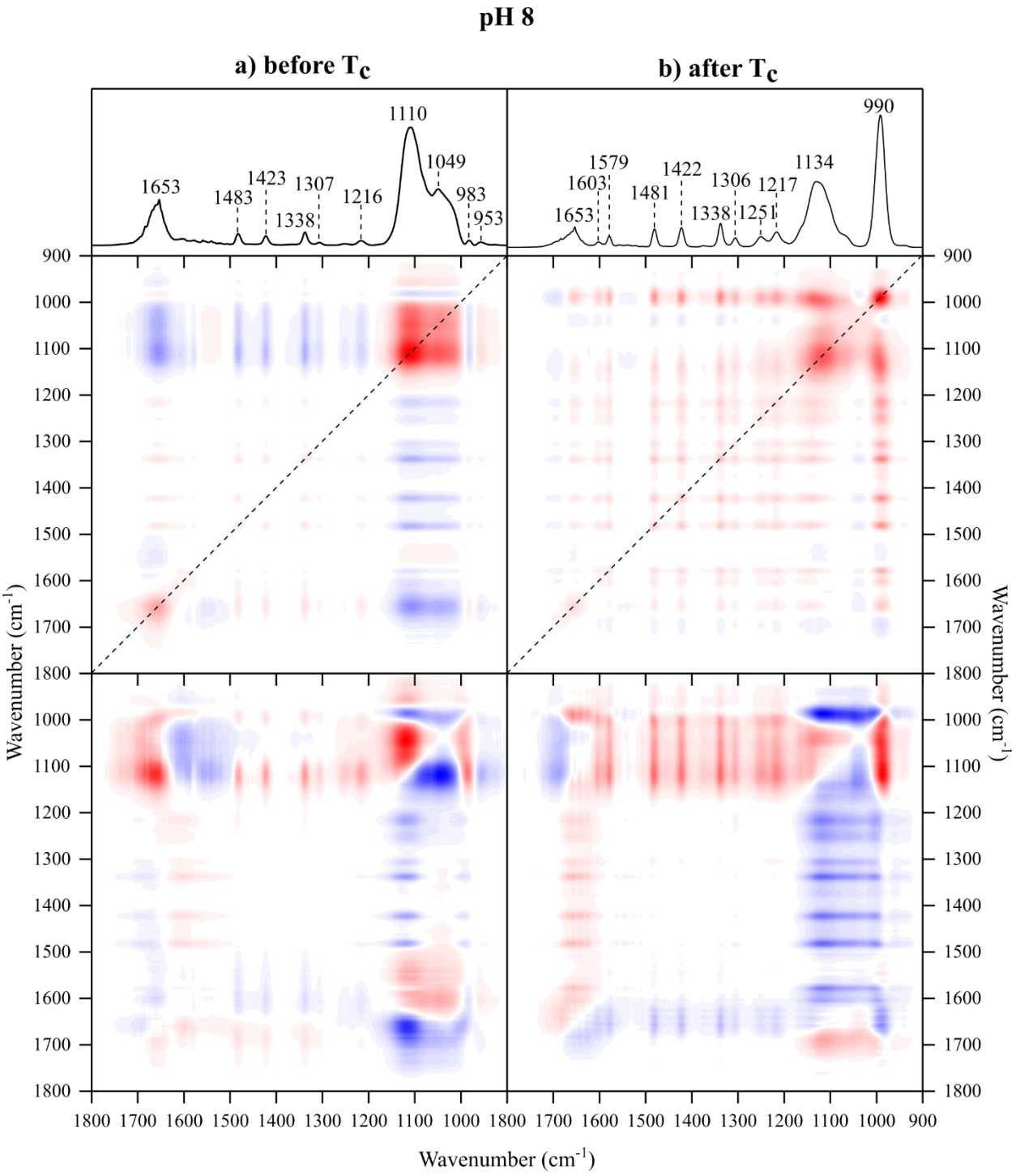

Figure 3.10 2DCOS maps for dAMP adsorption onto phosphate saturated hematite surface at pH 8

2DCOS maps for dAMP adsorption onto phosphate saturated hematite surface at pH 8 (a) before T_c and (b) after T_c. Autocorrelation spectra (top), synchronous 2DCOS map (middle), and asynchronous 2DCOS map (bottom). Dotted line in synchronous 2DOCS correspond to the intensity line trace which is the same as autocorrelation spectra. Red and blue corresponds to positive and negative correlations, respectively.

2DCOS autocorrelation spectra and maps for pH 8 are shown in **Figure 3.10**. Before T_c (**Figure 3.10a**), large, broad phosphate autopeaks are observed which are related to phosphate desorption. dAMP autopeak intensities are low, suggesting a slow adsorption of dAMP molecules as phosphate desorbs. After T_c (**Figure 3.10b**), the 990 cm^{-1} autopeak appears corresponding to dAMP adsorption and surface complexation. The 2DCOS synchronous and asynchronous signs are shown in **Table 3.4** and **Table 3.5** for before T_c and after T_c for pH 8, respectively. In summary, the order of change before T_c is 1110 (P-O band) cm^{-1} → 1483 (ν(N7-C8), δ(C8-H)), 1423 (δ(CH_2)), 1338 (purine), 1307 (purine) cm^{-1} → 1423 (δ(CH_2)), 1338 (purine), 1307 (purine), 1049 (P-O band) cm^{-1} → 1653 (δ(NH_2)), 1423 (δ(CH_2)), 1338 (purine), 1307 (purine) cm^{-1} → 1307 (purine), 1216 (ν(N9-C1')), 957 (P-O band) cm^{-1} → 1307 (purine), 1216 (ν(N9-C1')), 983 (P-O band) cm^{-1}. There is an abundance of peak overlap as well as repeated peaks because of the zero asynchronous values. There are multiple sequential possibilities in which the peaks change, however, the 1110 cm^{-1} peak is seen to be the first to change. Again, this is related to the desorption of phosphate from the surface, allowing dAMP to adsorb. The phosphate peaks are also scattered within the sequential order and identical to pH 5, reflect the constant changes to binding modes of both adsorbed phosphate and dAMP. The peak change after T_c is 1653 (δ(NH_2)) cm^{-1} → 1603 (purine) cm^{-1} → 1579 (purine), 1481 (ν(N7-C8), δ(C8-H)), 1422 (δ(CH_2)), 1338 (purine), 1251 (δ(C6-NH_2), 1217 (ν(N9-C1')) cm^{-1} → 1422 (δ(CH_2)), 1338 (purine), 1306 (purine), 1251 (δ(C6-NH_2) cm^{-1} → 990 (P-O band) cm^{-1} → 1117 (P-O band) cm^{-1}. Like at pH 5, the 1120 cm^{-1} P-O band is not present in the sequence as it is related to the desorption of pre-adsorbed phosphate. Instead, adenosine related peaks are seen earlier in the sequence with phosphate related bands are towards the end of the sequence. The pH 8 sequence for both before T_c and after T_c are analogous to pH 5,

suggesting similar adsorption mechanism but with varying surface complexation species as seen from these ATR-FTIR spectra.

3.4.5 Semi-Quantitative Spectral Linear Convolution

It has been observed that the hematite surface is a mixture of adsorbed oxyanion phosphate and dAMP nucleotide, however, it is unknown the relative percentages of each component. To estimate the mixture of adsorbed phosphate and nucleotide on the hematite surface, independent adsorbed spectra of phosphate and dAMP on hematite were added together at different ratios at pH 5 (**Figure 3.11a**). This analysis was done for only the 900-1200 cm^{-1} phosphate region as higher wavenumber regions for adsorbed phosphate do not show relevant peaks. These independent spectra were added together to and compared to the spectra of a mixed phosphate and nucleotide hematite surface (**Figure 3.11b**). **Figure 3.11c** shows the residuals between the linear convoluted and experimental spectra. The residuals are seen to be oscillating and yield large values, indicating poor linear convolutions. This suggests that the spectra cannot be successfully convoluted using a linear scale and is more complicated than this relatively simplistic analysis. Furthermore, this shows that the assumption of independent adsorbates cannot be made. This simple linear convolution yielding high residuals suggest that the interaction between adsorbates is important. Moreover, it is suggested that the binding coordination of the nucleotide is impacted by pre-adsorbed phosphate when compared to independent adsorption studies. Additionally, the presence of pre-adsorbed phosphate could affect electronic interactions, change binding sites, and could affect adsorbate speciation, affecting nucleotide adsorption spectra.[28,62,161] For all of these

reasons, the fitting residuals are high and a more complex method is needed to quantify the relative amounts of phosphate and dAMP adsorbed onto hematite.

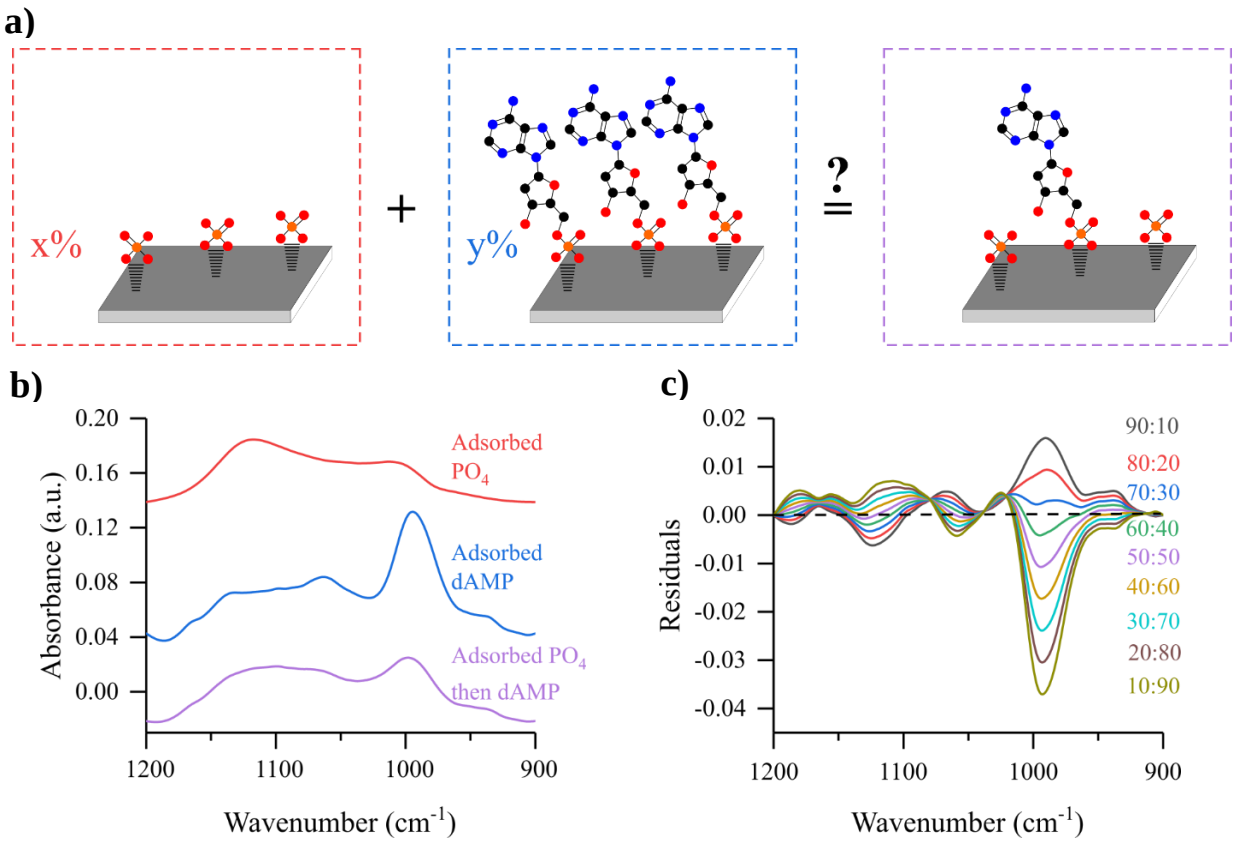

Figure 3.11 Linear convolution of adsorbed species on α-Fe_2O_3

a) Representative cartoon emphasizing the possible percent absorbance intensity of a saturated adsorbed phosphate surface spectrum (red dashed box) added to a percent of saturated adsorbed dAMP surface spectrum (blue dashed box) to yield the spectral absorbance intensity of a multicomponent surface composed of dAMP and phosphate (purple dashed boxed). b) the spectra used for the linear convolution at pH 5. c) the residuals of the experimental spectrum compared to the linear convolution at various percent combinations where the absorbance ratios correspond to % PO_4 : % dAMP. The dotted line represents a perfect overlay of the linear convolution to experimental spectra.

3.4.6 dAMP Adsorption Mechanism on Phosphate Saturated Surface

There are multiple pathways that can lead to the final state where dAMP is coordinated to the hematite surface via phosphate group. There is an initial state where the surface is saturated with adsorbed phosphate and a final state where there is a mixture of dAMP and phosphate, both complexed with the hematite surface; the intermediate adsorption pathway steps of how this final

state is reach is unknown. However, several pathways are possible and can be deduced using ATR-FTIR spectral analysis. **Figure 3.12** is a summary of three proposed pathways. Path 1 shows the promoted displacement of adsorbed phosphate via adenine nucleobase and a molecular reorientation to yield a final complex dAMP state. Path 2 shows the desorption of adsorbed phosphate, creating an available binding site for dAMP coordination via phosphate group. Path 3

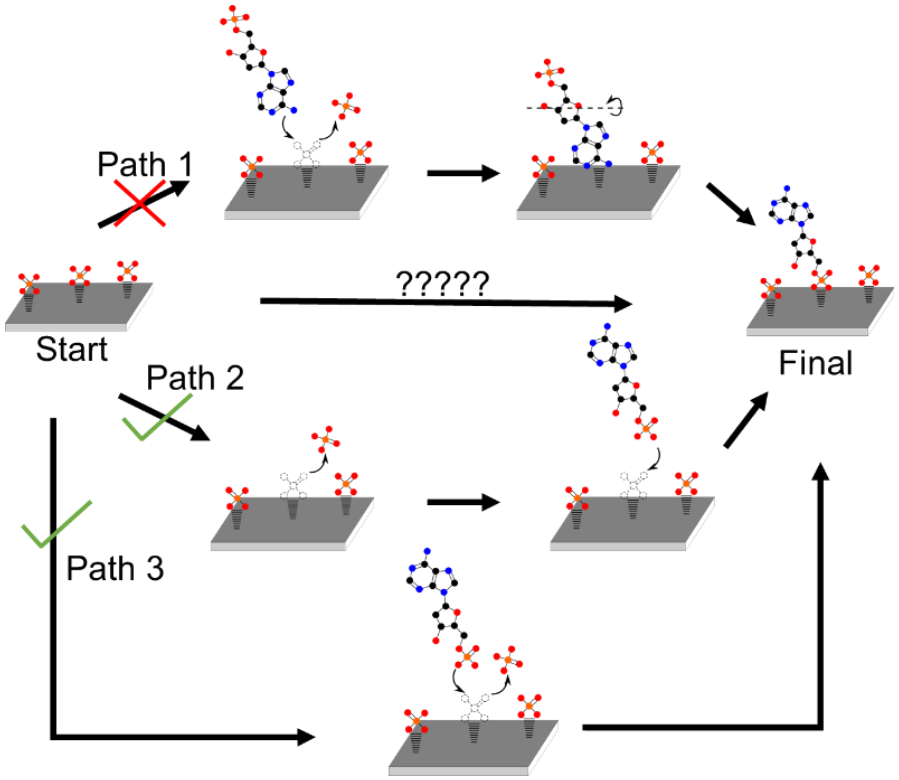

Figure 3.12 Proposed adsorption mechanism for deoxyadenosine monophosphate onto α-Fe_2O_3

a) Schematic representing the possible adsorption pathways where path 1 is the displacement of pre-adsorbed phosphate via the amine functional group and with a molecular reorientation. Path 2 is the desorption of phosphate which frees up an available binding site where dAMP can bind to the surface. Path 3 is the displacement of adsorbed phosphate via the phosphate functional group.

shows the promoted displacement of adsorbed phosphate with dAMP. Path 1 is not likely as adenine peak shifts at earlier time points were not observed (**Figure 3.7**). Path 2 is possible because phosphate was seen to partially desorb with water (**Figure 3.5**) and dAMP is seen to readily adsorb to available binding sites regardless of pH (**Figure 3.4**). Path 3 is also possible because the displacement of adsorbed phosphate with another adsorbate has been observed in other

experiments.[162,163] In summary, the proposed dAMP adsorption mechanism on a phosphate saturated surface is a mixture of multiple pathways that first begins the desorption of adsorbed phosphate to open an available binding site for dAMP to coordinate with.

3.5 Conclusion

Molecular adsorption onto a geochemical surface in environmental milieu can be complex which is why it is not fully understood. However, is an important role in determining the fate and transport of biomolecular components. The results from this study suggest that there are electrostatic interactions between dAMP and hematite nanoparticle surfaces, where there is an increase of adsorbed dAMP at lower pH values. When oxyanion phosphate is present on the hematite surface, a reduction in the amount of dAMP molecules adsorbed to the surface was seen due to the presence and site-blocking of the phosphate as it occupies the same binding sites as dAMP. We show the exchange of pre-adsorbed phosphate molecules with dAMP, indicating a multistep adsorption mechanism. 2DCOS analysis elucidated the order of change to relevant peaks for the phosphate desorption and dAMP adsorption pathway. With the results and analysis, two dAMP adsorption pathways were proposed when adsorbed onto a pre-adsorbed hematite surface. One of which involves the immediate desorption of phosphate followed by the adsorption of dAMP and the secondly involves a slower displacement of potentially more strongly bound phosphate with dAMP. Both pathways result in the surface complexation of the dAMP phosphate group with the hematite surface. This study builds complexity upon single component systems to highlight the importance of geochemical surfaces, environmental factors, and multi-component milieu on molecular stability.

3.6 Acknowledgements

Chapter 3, in full, is a reprint of the material as it appears in Langmuir. Sit, I.; Sagisaka, S.; Grassian, V. H. Nucleotide Adsorption on Iron(III) Oxide Nanoparticle Surfaces: Insights into Nano–Geo–Bio Interactions Through Vibrational Spectroscopy. 2020, 36 (51), 15501–15513. The dissertation author is the first author of this paper.

3.7 Supplemental Information

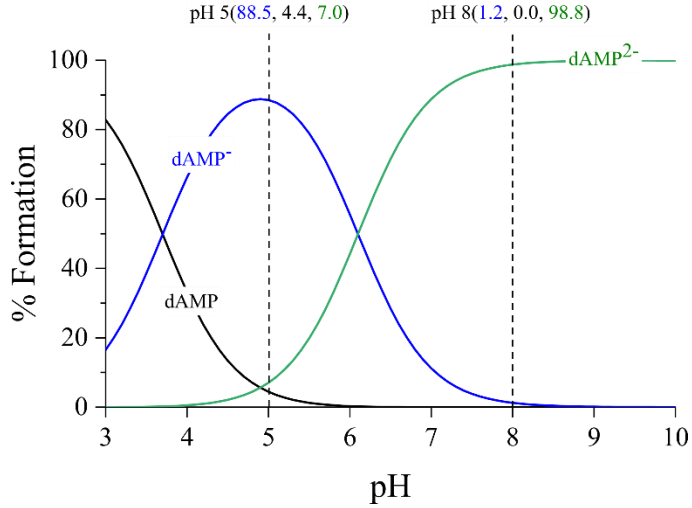

Figure 3.13 Henderson-Hasselbalch speciation curve for dAMP at the experimental pHs investigated

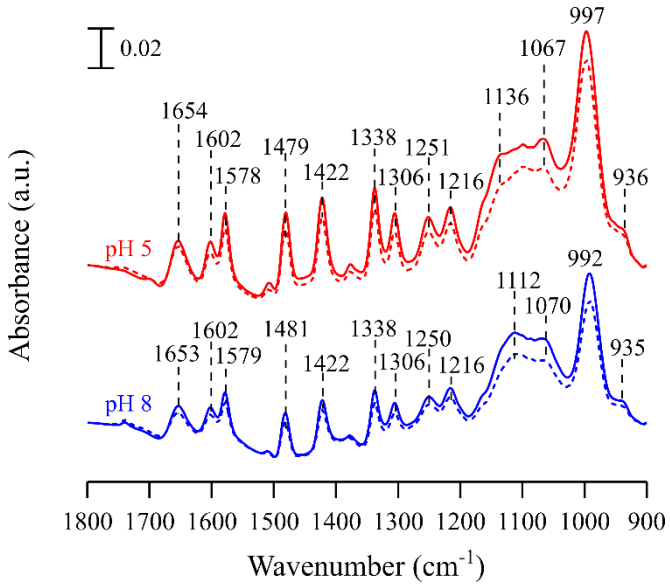

Figure 3.14 Last time point spectra for single component dAMP adsorbed on hematite

Last time point spectra for single component dAMP adsorption and desorption on hematite at pH 5 (red) and pH 8 (blue). Solid line is the 90-minute adsorption spectrum and the dotted line is the 90 minute desorption spectrum.

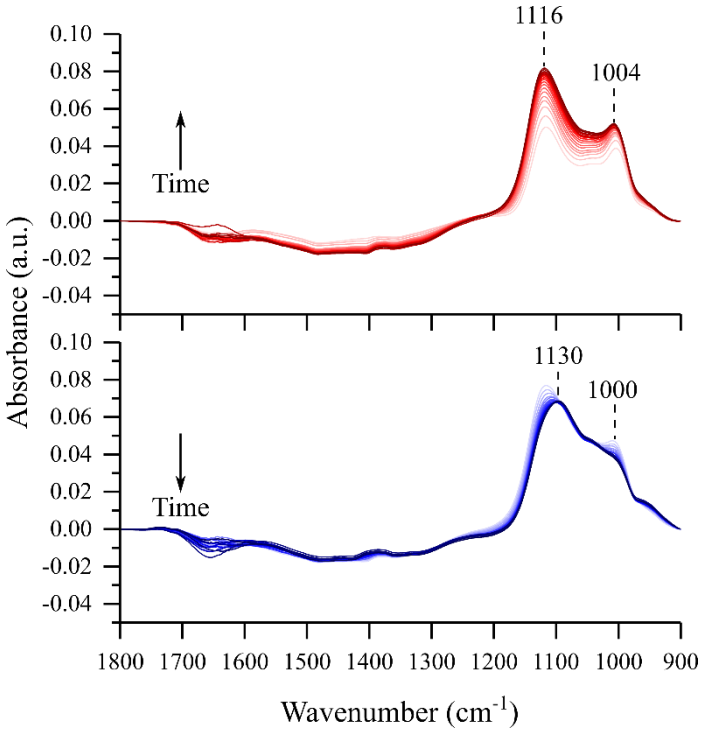

Figure 3.15 ATR-FTIR spectra of phosphate adsorption and desorption on hematite at pH 5

Adsorption (top) onto hematite surface and desorption (bottom) at pH 5 as a function of time.

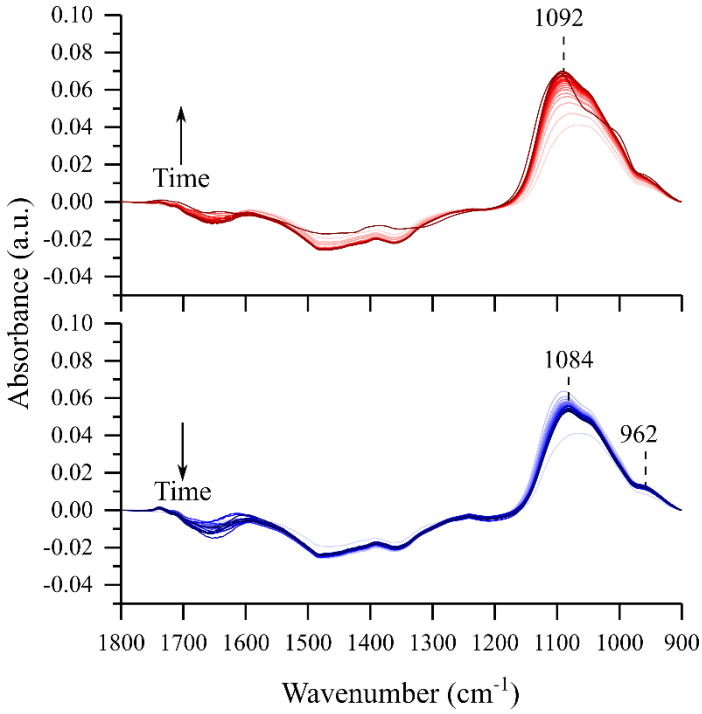

Figure 3.16. ATR-FTIR spectra of phosphate adsorption and desorption on hematite at pH 8

ATR-FTIR spectra of phosphate adsorption (top) onto hematite surface and desorption (bottom) at pH 8 as a function of time.

Table 3.2 2DCOS analysis for dAMP adsorption on a phosphate saturated hematite surface at pH 5 for time points 0-35 minutes showing relevant synchronous and asynchronous cross peaks signs and sequential order

Cross Peak	Synchronous	Asynchronous	Sequence	Cross Peak	Synchronous	Asynchronous	Sequence	Cross Peak	Synchronous	Asynchronous	Sequence
(1651, 1602)	+	-	1651 < 1602	(1578, 1306)	+	+	1578 > 1306	(1337, 1216)	+	+	1337 > 1216
(1651, 1578)	+	-	1651 < 1578	(1578, 1252)	+	+	1578 > 1252	(1337, 1120)	-	+	1337 < 1120
(1651, 1480)	+	-	1651 < 1480	(1578, 1216)	+	+	1578 > 1216	(1337, 1064)	+	-	1337 < 1064
(1651, 1422)	+	-	1651 < 1422	(1578, 1120)	-	+	1578 < 1120	(1337, 988)	+	+	1337 > 988
(1651, 1337)	+	-	1651 < 1337	(1578, 1064)	+	0		(1337, 940)	+	0	
(1651, 1306)	+	+	1651 > 1306	(1578, 988)	+	+	1578 > 988	(1306, 1252)	+	+	1306 > 1252
(1651, 1252)	+	+	1651 > 1252	(1578, 940)	+	-	1578 < 940	(1306, 1216)	+	+	1306 > 1216
(1651, 1216)	+	+	1651 > 1216	(1480, 1422)	+	+	1480 > 1422	(1306, 1120)	-	+	1306 < 1120
(1651, 1120)	-	+	1651 < 1120	(1480, 1337)	+	+	1480 > 1337	(1306, 1064)	+	0	
(1651, 1064)	+	+	1651 > 1064	(1480, 1306)	+	+	1480 > 1306	(1306, 988)	+	+	1306 > 988
(1651, 988)	+	0		(1480, 1252)	+	+	1480 > 1252	(1306, 940)	+	0	
(1651, 940)	+	+	1651 > 940	(1480, 1216)	+	+	1480 > 1216	(1252, 1216)	+	+	1252 > 1216
(1602, 1578)	+	+	1602 > 1578	(1480, 1120)	-	+	1480 < 1120	(1252, 1120)	-	+	1252 < 1120
(1602, 1480)	+	+	1602 > 1480	(1480, 1064)	+	0		(1252, 1064)	+	-	1252 < 1064
(1602, 1422)	+	+	1602 > 1422	(1480, 988)	+	+	1480 > 988	(1252, 988)	+	-	1252 < 988
(1602, 1337)	+	+	1602 > 1337	(1480, 940)	+	-	1480 < 940	(1252, 940)	+	-	1252 < 940
(1602, 1306)	+	+	1602 > 1306	(1422, 1337)	+	0		(1216, 1120)	-	+	1216 < 1120
(1602, 1252)	+	+	1602 > 1252	(1422, 1306)	+	+	1422 > 1306	(1216, 1064)	+	-	1216 < 1064
(1602, 1216)	+	+	1602 > 1216	(1422, 1252)	+	+	1422 > 1252	(1216, 988)	+	-	1216 < 988
(1602, 1120)	-	+	1602 < 1120	(1422, 1216)	+	+	1422 > 1216	(1216, 940)	+	-	1216 < 940
(1602, 1064)	+	+	1602 > 1064	(1422, 1120)	-	+	1422 < 1120	(1120, 1064)	-	-	1120 > 1064
(1602, 988)	+	+	1602 > 988	(1422, 1064)	+	0		(1120, 988)	-	-	1120 > 988
(1602, 940)	+	0		(1422, 988)	+	+	1422 > 988	(1120, 940)	-	-	1120 > 940
(1578, 1480)	+	0		(1422, 940)	+	-	1422 < 940	(1064, 988)	+	+	1064 > 988
(1578, 1422)	+	+	1578 > 1422	(1337, 1306)	+	+	1337 > 1306	(1064, 940)	+	-	1064 < 940
(1578, 1337)	+	+	1578 > 1337	(1337, 1252)	+	+	1337 > 1252	(988, 940)	+	-	988 < 940

Table 3.3 2DCOS analysis for dAMP adsorption on a phosphate saturated hematite surface at pH 5 for time points 35-150 minutes showing relevant synchronous and asynchronous cross peaks signs and sequential order

Cross Peak	Synchronous	Asynchronous	Sequence	Cross Peak	Synchronous	Asynchronous	Sequence	Cross Peak	Synchronous	Asynchronous	Sequence
(1651, 1604)	+	-	1651 < 1604	(1578, 1151)	+	+	1578 > 1151	(1305, 1215)	+	0	
(1651, 1578)	+	-	1651 < 1578	(1578, 1100)	+	+	1578 > 1100	(1305, 1151)	+	+	1305 > 1151
(1651, 1480)	+	-	1651 < 1480	(1578, 1065)	+	+	1578 > 1065	(1305, 1100)	+	+	1305 > 1100
(1651, 1421)	+	-	1651 < 1421	(1578, 1001)	+	+	1578 > 1001	(1305, 1065)	+	0	
(1651, 1337)	+	-	1651 < 1337	(1480, 1421)	+	0		(1305, 1001)	+	+	1305 > 1001
(1651, 1305)	+	-	1651 < 1305	(1480, 1337)	+	0		(1251, 1215)	+	0	
(1651, 1251)	+	-	1651 < 1251	(1480, 1305)	+	0		(1251, 1151)	+	+	1251 > 1151
(1651, 1215)	+	-	1651 < 1215	(1480, 1251)	+	0		(1251, 1100)	+	+	1251 > 1100
(1651, 1151)	+	-	1651 < 1151	(1480, 1215)	+	0		(1251, 1065)	+	0	
(1651, 1100)	+	-	1651 < 1100	(1480, 1151)	+	+	1480 > 1151	(1251, 1001)	+	+	1251 > 1001
(1651, 1065)	+	-	1651 < 1065	(1480, 1100)	+	+	1480 > 1100	(1215, 1151)	+	+	1215 > 1151
(1651, 1001)	+	-	1651 < 1001	(1480, 1065)	+	0		(1215, 1100)	+	+	1215 > 1100
(1604, 1578)	+	+	1604 > 1578	(1480, 1001)	+	+	1480 > 1001	(1215, 1065)	+	0	
(1604, 1480)	+	+	1604 > 1480	(1421, 1337)	+	0		(1215, 1001)	+	+	1215 > 1001
(1604, 1421)	+	+	1604 > 1421	(1421, 1305)	+	0		(1151, 1100)	+	0	
(1604, 1337)	+	+	1604 > 1337	(1421, 1251)	+	0		(1151, 1065)	+	-	1151 < 1065
(1604, 1305)	+	+	1604 > 1305	(1421, 1215)	+	0		(1151, 1001)	+	-	1151 < 1001
(1604, 1251)	+	+	1604 > 1251	(1421, 1151)	+	+	1421 > 1151	(1100, 1065)	+	-	1100 < 1065
(1604, 1215)	+	+	1604 > 1215	(1421, 1100)	+	+	1421 > 1100	(1100, 1001)	+	-	1100 < 1001
(1604, 1151)	+	+	1604 > 1151	(1421, 1065)	+	0		(1065, 1001)	+	+	1065 > 1001
(1604, 1100)	+	+	1604 > 1100	(1421, 1001)	+	+	1421 > 1001	(1216, 940)	+	-	1216 < 940
(1604, 1065)	+	+	1604 > 1065	(1337, 1305)	+	0		(1120, 1064)	-	-	1120 > 1064
(1604, 1001)	+	+	1604 > 1001	(1337, 1251)	+	0		(1120, 988)	-	-	1120 > 988
(1578, 1480)	+	+	1578 > 1480	(1337, 1215)	+	0		(1120, 940)	-	-	1120 > 940
(1578, 1421)	+	+	1578 > 1421	(1337, 1151)	+	+	1337 > 1151	(1064, 988)	+	+	1064 > 988
(1578, 1337)	+	+	1578 > 1337	(1337, 1100)	+	+	1337 > 1100	(1064, 940)	+	-	1064 < 940
(1578, 1305)	+	+	1578 > 1305	(1337, 1065)	+	0		(988, 940)	+	-	988 < 940
(1578, 1251)	+	+	1578 > 1251	(1337, 1001)	+	+	1337 > 1001				
(1578, 1215)	+	+	1578 > 1215	(1305, 1251)	+	0					

Table 3.4 2DCOS analysis for dAMP adsorption on a phosphate saturated hematite surface at pH 8 for time points 45-150 minutes showing relevant synchronous and asynchronous cross peaks signs and sequential order.

Cross Peak	Synchronous	Asynchronous	Sequence	Cross Peak	Synchronous	Asynchronous	Sequence	Cross Peak	Synchronous	Asynchronous	Sequence
(1653, 1603)	+	+	1653 > 1603	(1579, 1481)	+	0		(1422, 1117)	+	+	1422 > 1117
(1653, 1579)	+	+	1653 > 1579	(1579, 1422)	+	0		(1422, 990)	+	+	1422 > 990
(1653, 1481)	+	+	1653 > 1481	(1579, 1338)	+	0		(1338, 1306)	+	0	
(1653, 1422)	+	+	1653 > 1422	(1579, 1306)	+	0		(1338, 1251)	+	0	
(1653, 1338)	+	+	1653 > 1338	(1579, 1251)	+	0		(1338, 1217)	+	0	
(1653, 1306)	+	+	1653 > 1306	(1579, 1217)	+	0		(1338, 1117)	+	+	1338 > 1117
(1653, 1251)	+	+	1653 > 1251	(1579, 1117)	+	+	1579 > 1117	(1338, 990)	+	+	1338 > 990
(1653, 1217)	+	+	1653 > 1217	(1579, 990)	+	+	1579 > 990	(1306, 1251)	+	0	
(1653, 1117)	+	0		(1481, 1422)	+	0		(1306, 1217)	+	-	1306 < 1217
(1653, 990)	+	+	1653 > 990	(1481, 1338)	+	0		(1306, 1117)	+	+	1306 > 1117
(1603, 1579)	+	+	1603 > 1579	(1481, 1306)	+	+	1481 > 1306	(1306, 990)	+	+	1306 > 990
(1603, 1481)	+	+	1603 > 1481	(1481, 1251)	+	0		(1251, 1217)	+	0	
(1603, 1422)	+	+	1603 > 1422	(1481, 1217)	+	0		(1251, 1117)	+	+	1251 > 1117
(1603, 1338)	+	+	1603 > 1338	(1481, 1117)	+	+	1481 > 1117	(1251, 990)	+	+	1251 > 990
(1603, 1306)	+	+	1603 > 1306	(1481, 990)	+	+	1481 > 990	(1217, 1117)	+	+	1217 > 1117
(1603, 1251)	+	+	1603 > 1251	(1422, 1338)	+	0		(1217, 990)	+	+	1217 > 990
(1603, 1217)	+	+	1603 > 1217	(1422, 1306)	+	0		(1117, 990)	+	-	1117 < 990
(1603, 1117)	+	+	1603 > 1117	(1422, 1251)	+	0					
(1603, 990)	+	+	1603 > 990	(1422, 1217)	+	0					

Table 3.5 2DCOS analysis for dAMP adsorption on a phosphate saturated hematite surface at pH 8 for time points 0-45 minutes showing relevant synchronous and asynchronous cross peaks signs and sequential order.

Cross Peak	Synchronous	Asynchronous	Sequence	Cross Peak	Synchronous	Asynchronous	Sequence	Cross Peak	Synchronous	Asynchronous	Sequence
(1653, 1483)	+	-	1653 < 1483	(1483, 983)	+	+	1483 > 983	(1307, 1216)	+	0	
(1653, 1423)	+	0		(1483, 957)	-	0		(1307, 1110)	-	+	1307 < 1110
(1653, 1338)	+	0		(1423, 1338)	+	0		(1307, 1049)	-	0	
(1653, 1307)	+	0		(1423, 1307)	+	0		(1307, 983)	+	0	
(1653, 1216)	+	+	1653 > 1216	(1423, 1216)	+	0		(1307, 957)	-	0	
(1653, 1110)	-	+	1653 < 1110	(1423, 1110)	-	+	1423 < 1110	(1216, 1110)	-	+	1216 < 1110
(1653, 1049)	-	+	1653 < 1049	(1423, 1049)	-	0		(1216, 1049)	-	+	1216 < 1049
(1653, 983)	+	+	1653 > 983	(1423, 983)	+	+	1423 > 983	(1216, 983)	+	0	
(1653, 957)	-	0		(1423, 957)	-	0		(1216, 957)	-	0	
(1483, 1423)	+	0		(1338, 1307)	+	0		(1110, 1049)	+	+	1110 > 1049
(1483, 1338)	+	0		(1338, 1216)	+	0		(1110, 983)	-	-	1110 > 983
(1483, 1307)	+	0		(1338, 1110)	-	+	1338 < 1110	(1110, 957)	+	+	1110 > 957
(1483, 1216)	+	+	1483 > 1216	(1338, 1049)	-	0		(1049, 983)	-	-	1049 > 983
(1483, 1110)	-	+	1483 < 1110	(1338, 983)	+	+	1338 > 983	(1049, 957)	+	+	1049 > 957
(1483, 1049)	-	-	1483 > 1049	(1338, 957)	-	0		(983, 957)	-	+	983 < 957

Chapter 4. Differential Surface Interactions and Surface Templating of Nucleotides (dGMP, dCMP, dAMP, and dTMP) on Oxide Particle Surfaces

4.1 Abstract

The fate of biomolecules in the environment depends in part on understanding the surface chemistry occurring at the biological-geochemical (bio-geo) interface. Little is known about how environmental DNA (eDNA) or smaller components, like nucleotides and oligonucleotides, persist in aquatic environments and the role of surface interactions. This study aims to probe surface interactions and adsorption behavior of nucleotides on oxide surfaces. We have investigated the interactions of individual nucleotides (dGMP, dCMP, dAMP, and dTMP) on TiO_2 particle surfaces as a function of pH and in the presence of complementary and noncomplementary base pairs. Using attenuated total reflectance-Fourier transform infrared spectroscopy, there is an increased number of adsorbed nucleotides at lower pH with a preferential interaction of the phosphate group with the oxide surface. Additionally, differential adsorption behavior is seen where purine nucleotides are preferentially adsorbed, with higher surface saturation coverage, over their pyrimidine derivatives. These differences may be a result of intermolecular interactions between co-adsorbed nucleotides. When the TiO_2 surface was exposed to two component solutions of nucleotides, there was preferential adsorption of dGMP compared to dCMP and dTMP, and dAMP compared to dTMP and dCMP. Complementary nucleotide base pairs showed hydrogen-bond interactions between a strongly adsorbed purine nucleotide layer and weaker interacting hydrogen-bonded pyrimidine second layer. Noncomplementary base pairs did not form a second layer. These results highlight several important findings: (i) there is differential adsorption of nucleotides; (ii) complementary co-adsorbed nucleotides show base pairing with a second layer and the stability

depends on the strength of the hydrogen bonding interactions and; (iii) the first layer coverage strongly depends on pH. Overall, the importance of surface interactions in the adsorption of nucleotides and the templating of specific interactions between nucleotides are discussed.

4.2 Introduction

Aqueous environments in ground water are a complex milieu comprised of oxyanions, biomolecules, and heavy metals, just to name a few components. These interact with each other and geochemical surfaces present in the environment.[18,47,62,65,76,106,164] For biomolecules, interactions with mineral particle surfaces, especially on high surface area nanoscale particles that act as excellent adsorbents,[3,63,65,76,164,165] can change biomolecular structure, physicochemical properties, and electronic states.[18,28,47,104,106] DNA, oligonucleotides, and nucleotide components are often found in the environment through cellular lysis, leaky sewages pipes, and active cellular secretion.[127,130] The role of surfaces and the interactions that occur with surfaces in altering DNA decay rates or stabilization, is not fully understood.[166] The fate of environmental DNA and persistence in aquatic environments is an important question that remains to be answered.

Titanium dioxide particles are found in the environment as a natural mineral or anthropogenic engineered nanomaterials and can provide a surface for biomolecules to adsorb onto.[18,28] These nucleotides compete with other species that are present in environment aqueous systems that make up the ecological-corona surrounding the particle. This ecological-corona is dependent on the components present in the environment surrounding the particle as higher affinity molecules displace lower affinity species. However, to study the evolution of an ecological-corona in multi-component milieu, fundamental interactions need to be understood of single or two component studies to build up in complexity and predict the behavior to model realistic environments. Additionally, adsorbed DNA can translocate far distances, where transfer of non-

native genetic information can occur.[127,167] Despite being transported through different biomes and exposed to milieu with components with varying surface affinities, adsorbed DNA can resist degradation.[166,168,169] Furthermore, prebiotic life was hypothesized to originate from the adsorption of biomonomers onto surfaces, increasing the local concentration and undergoing polymerization to form biomacromolecular structures, like DNA and proteins.[128,129] To investigate how DNA is stabilized on surfaces, it is first necessary to understand the surface chemistry with the individual building blocks, nucleotides.

For the reasons noted above, it is important to use molecular-based probes to interrogate the surface chemistry to gain insight into the reversibility or irreversibility of adsorbed nucleotides and specific surface interactions. There have been several studies of nucleotide and nucleoside adsorption onto clay and iron oxide particles, but few on titanium dioxide.[76,126,150,152,156,165,170,171] The studies thus far on TiO_2, have focused on quantifying nucleotide surface coverage but did not investigate the details of the surface interactions.[131] Cleaves et al. investigated adsorbed nucleobases, nucleosides and monophosphate nucleotides and concluded that monophosphate nucleotides are more strongly bound to rutile surfaces compared to the nucleobases.[171] Zhang et al. adsorbed oligonucleotides onto TiO_2 and suggested the adsorption occurred through backbone phosphate groups but didn't discuss in detail the coordination of phosphate with the surface.[172] In another study, Schmidt et al. investigated the adsorption of environmental DNA (eDNA) onto goethite and observed the preferential adsorption of the phosphate backbone to the surface.[95] Further understanding of the interaction of DNA and the components that make up DNA would require probing the interactions of the phosphate group. The phosphate group binding energies differ between monodentate and bidentate modes which influence how stable nucleotides and DNA are on surfaces.[62]

In this study, *in-situ* attenuated total reflectance-Fourier transform infrared (ATR-FTIR) spectroscopy was used to probe surface interactions of monophosphate nucleotides with TiO_2 (anatase) surfaces. Solution phase spectra were compared to adsorbed spectra as a function of pH to better understand bio-geo interactions and the effects of relevant environmental conditions. To build complexity, two-component nucleotide adsorption showed interesting and different interactions between complementary and noncomplementary base pairs. From these studies, it is shown for the first time that there is differential adsorption of nucleotides and different surface interactions as observed in competitive and complementary base adsorption. Overall, this study provides insight into the bio-geo interactions as well as nucleotide templating that could provide insights into prebiotic DNA interactions.

4.3 Materials and Methods

4.3.1 Materials

2'-deoxycytidine-5'-monophosphate (dCMP), 2'-deoxyguanosine-5'-monophosphate (dGMP), 2'-deoxyadenosine-5'-monophopshate (dAMP), 2'-deoxythmidine-5'-monophosphate (dTMP), sodium chloride, 1N hydrochloric acid, and 1N sodium hydroxide were purchase from Sigma-Aldrich. Anatase TiO_2 particles were purchased from US Research Nanomaterials stock number #US3498. All chemicals were used without additional modification or purification. For clarity, nucleotides have three main functional groups, the nitrogenous ring, ribose sugar ring and the phosphate group. The nitrogenous ring and ribose are defined as the nucleoside. The nucleoside with the phosphate group is the nucleotide.

4.3.2 Particle Characterization

The crystalline phase of TiO_2 was confirmed and determined with X-ray diffraction using an APEX II ultra-diffractometer with Cu Kα radiation at $\lambda = 1.54056$ Å. To determine the primary

TiO_2 particle size, an aqueous suspension of a 0.05 g/L was sonicated with a probe sonicator for 60 seconds with 15 seconds rest over 30 minutes in a room temperature water bath. Afterwards, a 15 uL aliquot was drop casted onto a formvar/carbon-coated 100 mesh copper grid and dried. The copper grid was imaged using an 80kV JEOL-1400 Plus transmission electron microscope. Particle sizes were analyzed using ImageJ software for more than 100 particles. For scanning electron microscope images for particle film morphology, 2.5 mg of particles were sonicated in 700 uL water for 30 seconds. 14 5 mm x 5 mm silicon wafers were laid on ATR crystal and the colloidal suspension was pipetted into the trough. The solution was dried and a wafer was imaged using FEI Quanta FEG 250 at 10 kV. Specific surface area was determined using a Quantachrome Nova 4200e N_2 adsorption isotherm under liquid nitrogen. Samples were first degassed at 120 ˚C for 18 hrs and a 15-multipoint isotherm was collected between P/P_0 of 0.05-0.95.

4.3.3 Zeta Potential using Dynamic Light Scattering (DLS)

An aqueous solution of 2.5 g/L of TiO_2 particles were sonicated for 30 minutes. A solution of 200uM dGMP, 200uM dCMP, 200uM dAMP, and 200uM dTMP were separately prepared. All solutions were titrated to pH 5 and pH 9 using HCl and NaOH. Minimal titrant was used to ensure negligible changes to concentration. Triplicate zeta potential measurements were taken with Malvern Instruments Zetasizer Nano.

4.3.4 Attenuated Total Reflectance-Fourier Transform Infrared (ATR-FTIR) Spectroscopy

The ATR-FTIR spectroscopy set-up has been previously described.[106] Briefly, ATR-FTIR spectroscopy is based on the total internal reflection of an infrared beam at an interface between an optically dense medium (ATR crystal) and an optically rare medium (sample). The reflection of the incident beam at the interface creates an evanescent wave that propagates into the sample where absorption of infrared light can occur, decaying exponentially. The ATR accessory was a

horizontal flow cell with an amorphous material transmitting IR radiation (AMTIR) crystal. Infrared spectra were collected using a Nicolet iS10 FTIR spectrometer (Thermo-Fisher) equipped with a mercury cadmium telluride detector (MCT/A). Spectra were collected at a resolution of 4 cm^{-1} and averaged over 100 scans in the spectral range extending from 750 to 4000 cm^{-1}. All ATR-FTIR spectra were collected and background subtracted using a linear baseline between 900 and 1800 cm^{-1} with the OMNIC 9 software. All spectra taken was after purging atmospheric gases for approximately 30 minutes with zero air. Adsorption spectra were taken every 5 minutes.

Solution phase spectra of dGMP, dCMP, dAMP, and dTMP were taken to compare spectral differences when these nucleotides are adsorbed onto TiO_2. A solution of 2mM dGMP in 10mM NaCl was prepared and titrated to pH 5 or pH 9 using HCl and NaOH. The solution was pipetted onto the AMTIR crystal, and a spectrum was taken using a 10mM NaCl background titrated to the appropriate pH. The same was done for the other nucleotides to collect solution phase spectra for pH 5 and pH 9. The addition of the small volume of titrant has negligible effects on the total ionic strength of the solution.

For single component adsorption, a TiO_2 particle thin film was prepared by sonicating 2.5mg TiO_2 in 500uL of Milli-Q water and pipetting the resulting solution onto the AMTIR crystal. The solution was left to dry overnight, leaving a TiO_2 thin film. A solution of 10 mM NaCl at pH 5 or 9, was flowed over the thin film using a peristaltic pump at ~1 mL/min to remove loose particles and collect a background spectrum. A solution of 20 μM dGMP in 10 mM NaCl titrated to pH 5 or 9 was prepared and flowed over the thin film for 180 minutes. Then, a desorption solution of 10mM NaCl at the corresponding pH was flowed over the film for 120 minutes. The same method was done to collect the other three nucleotide single component adsorption.

For two-component adsorption, a TiO_2 thin film was prepared, 10mM NaCl solution was flowed over to remove loose particles and to collect a background at pH 5 or 9. To keep the number of adsorption sites the same as a single component system, a solution of 10 μM dGMP and 10 μM dCMP was prepared and titrated to pH 5. The solution was flowed over the thin film for 180 minutes. Then a 10 mM NaCl desorption solution was flowed over the film for 120 minutes. The same method was done for 10 μM dAMP and 10 μM dTMP, 10 μM dGMP and 10 μM dTMP, and 10 μM dAMP and 10 μM dCMP.

4.3.5 UV-Vis Surface Coverage Quantification

Separate stock solutions of 1 mM each dGMP, dAMP, dCMP, and dTMP were prepared in 10 mM NaCl and titrated to pH 5. A solution of 10 g/L TiO_2 was prepared in 10 mM NaCl and sonicated for 1 minute to create a colloidal suspension. The suspension was titrated to pH 5. Aliquots of the stock solutions were mixed for a final reaction concentration of 5 g/L TiO_2 and 20 μM nucleotide. These concentrations were analogous to concentration used in the ATR-FTIR experiments. The reactors were put on a rotator for 2 hrs and after, the reactors were centrifuged, and the supernatants were collected. Fresh 20 μM nucleotide stock solution was added and was reacted for another two hours. The reactors were centrifuged for a second time and the supernatants were collected. Both supernatants were analyzed with UV-Vis and a surface coverage was calculated using 20 μM stock measurements and specific surface area measurements. UV-Vis was taken with an Agilent Cary 5000 spectrophotometer in the wavelength range of 200-400 nm at a scan speed of 600 nm/min.

4.4 Results and Discussion

4.4.1 Titanium Dioxide Particle Characterization

Titanium dioxide average particle size was determined to be 29.4 ± 8.5 nm with TEM (**Figure 4.1a**). A micrograph of the particle thin film used for the ATR-FTIR adsorption experiments can be seen in **Figure 4.1b**. The film can be seen to be composed of individual particles and highly aggregated. The particles were confirmed single-phase anatase with XRD (**Figure 4.1c**). Specific surface area of the anatase particles was measured to be 41.4 ± 4.0 m^2/g.

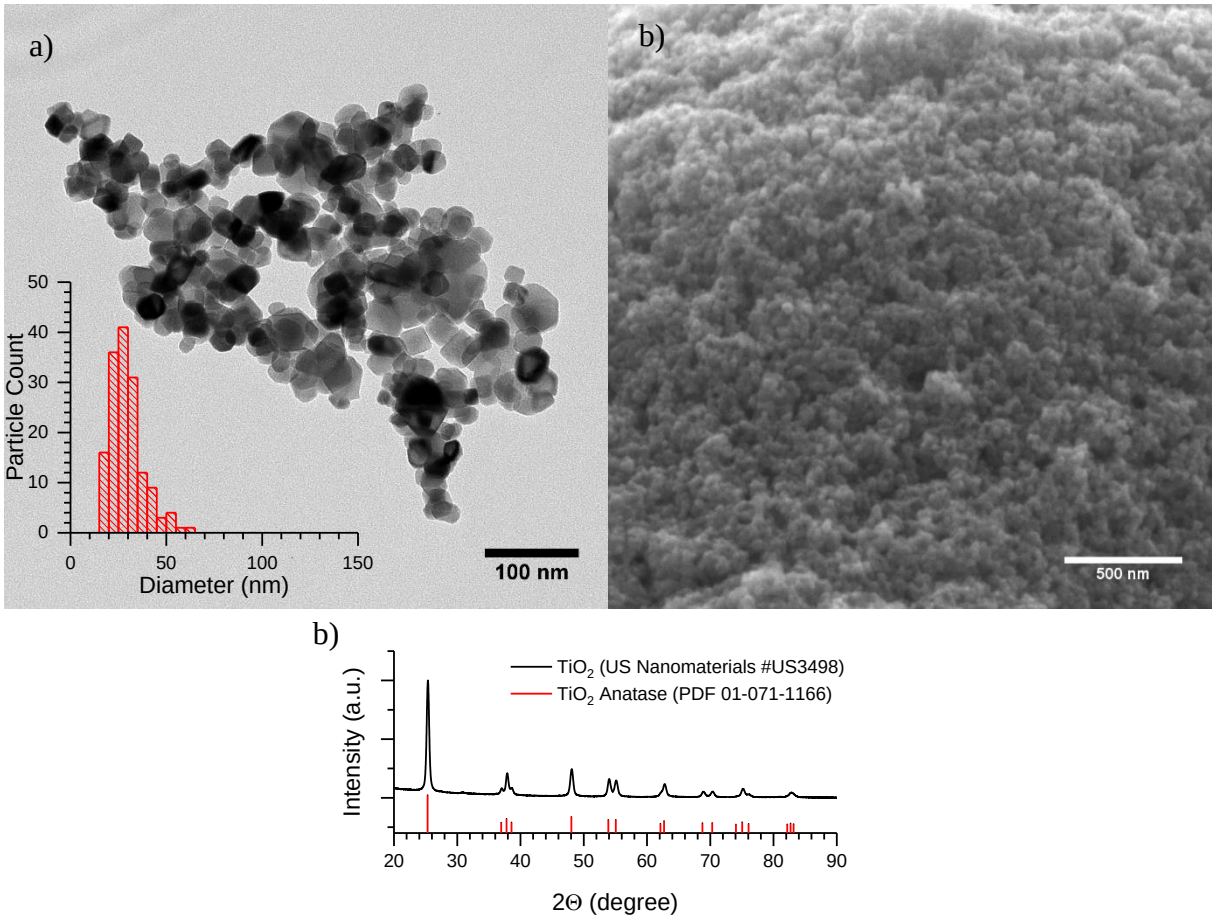

Figure 4.1 Particle characterization for TiO_2 particles

(a) TEM micrograph with size distribution analysis (inset); (b) SEM micrograph of ATR-FTIR particle thin film; (c) XRD data of anatase TiO_2

4.4.2 Analysis of Solution Phase and Single Component Adsorption

Figure 4.2 shows molecular structures of fully protonated forms of dGMP, dCMP, dAMP, and dTMP with pK_a values of the phosphate groups and nitrogenous rings. The speciation of the four nucleotides at different pHs is shown in **Figure 4.2** and a table for the species present at pH 5 and 9 is shown in **Table 4.3**. At pH 5 for dGMP, the amounts of the zwitterionic, monovalent anionic, and divalent anionic forms are 1.8%, 91.0% and 7.2%, respectively. For dCMP at pH 5, these percentages change to 15.6%, 78.2% and 6.2% for the zwitterionic, monovalent anionic, and divalent anionic forms, respectively. For dAMP at pH 5, these are 4.4%, 88.6%, 7.0% are zwitterionic, monovalent anionic, and divalent anionic, respectively, and dTMP are 96.9% and 3.1% monovalent anionic and divalent anionic, respectively. At higher pH, i.e. pH 9, the phosphate group and nitrogenous rings are fully deprotonated leading to all nucleotides residing in their divalent or trivalent anionic forms. These speciation forms have been tabulated in **Table 4.3** for all four nucleotides at pH 5 and 9 and other studies show similar calculations.[76,173] The dominant species for all four nucleotides at pH 5 is monovalent anion while the dominant species at pH 9 is a divalent anion. Since the nucleotides will be negatively charged at both pH 5 and 9, the surface charge of the TiO_2 surface will determine the electrostatic surface interactions.

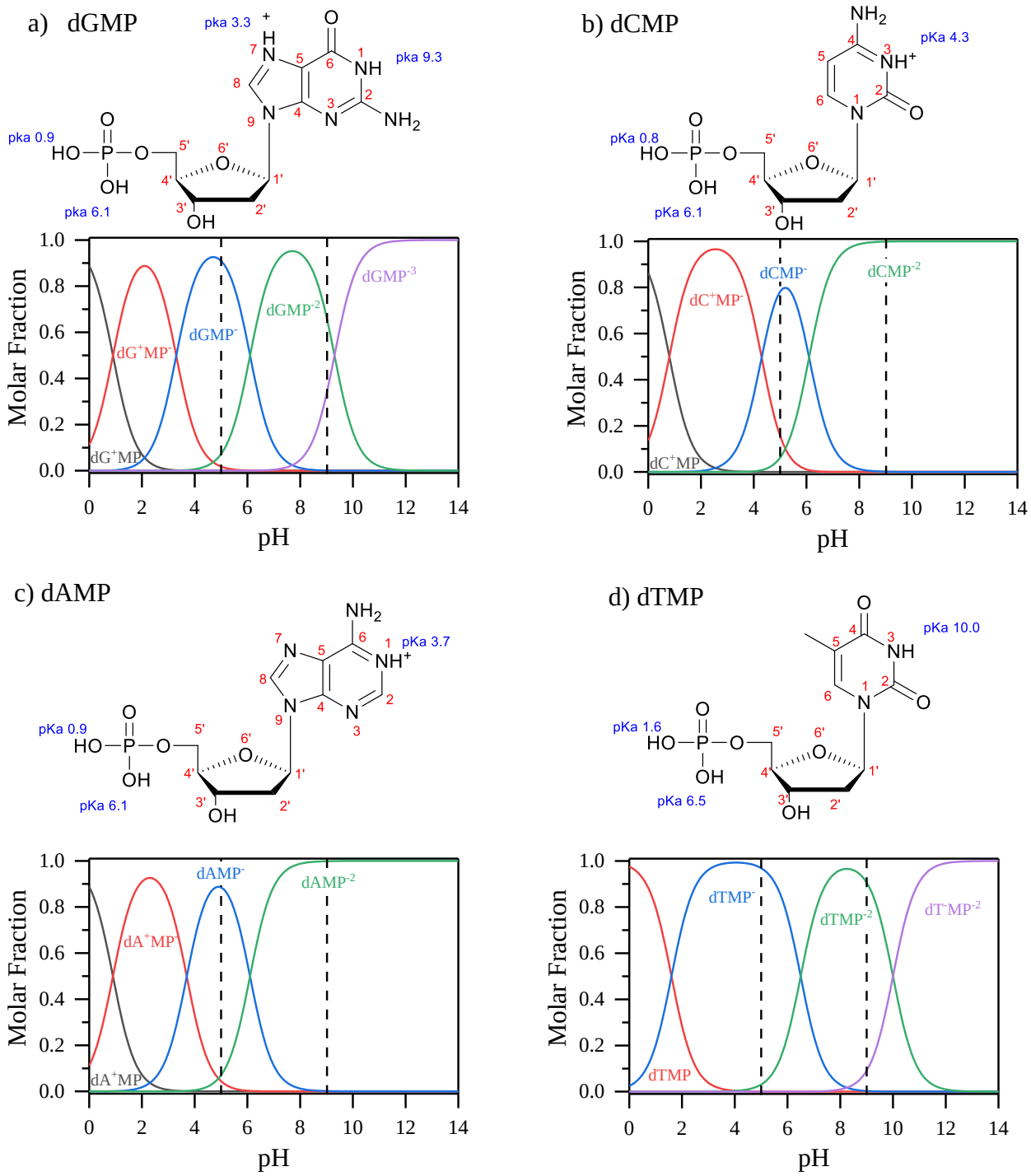

Figure 4.2 Nucleotide structures and speciation diagrams

Fully protonated nucleotide structures and their pK_a values (top) and speciation plots determined from the Henderson-Hasselbalch equation (bottom) are shown for a) deoxyguanosine monophosphate; b) deoxycytidine monophosphate; c) deoxyadenosine monophosphate; d) deoxythymidine monophosphate.

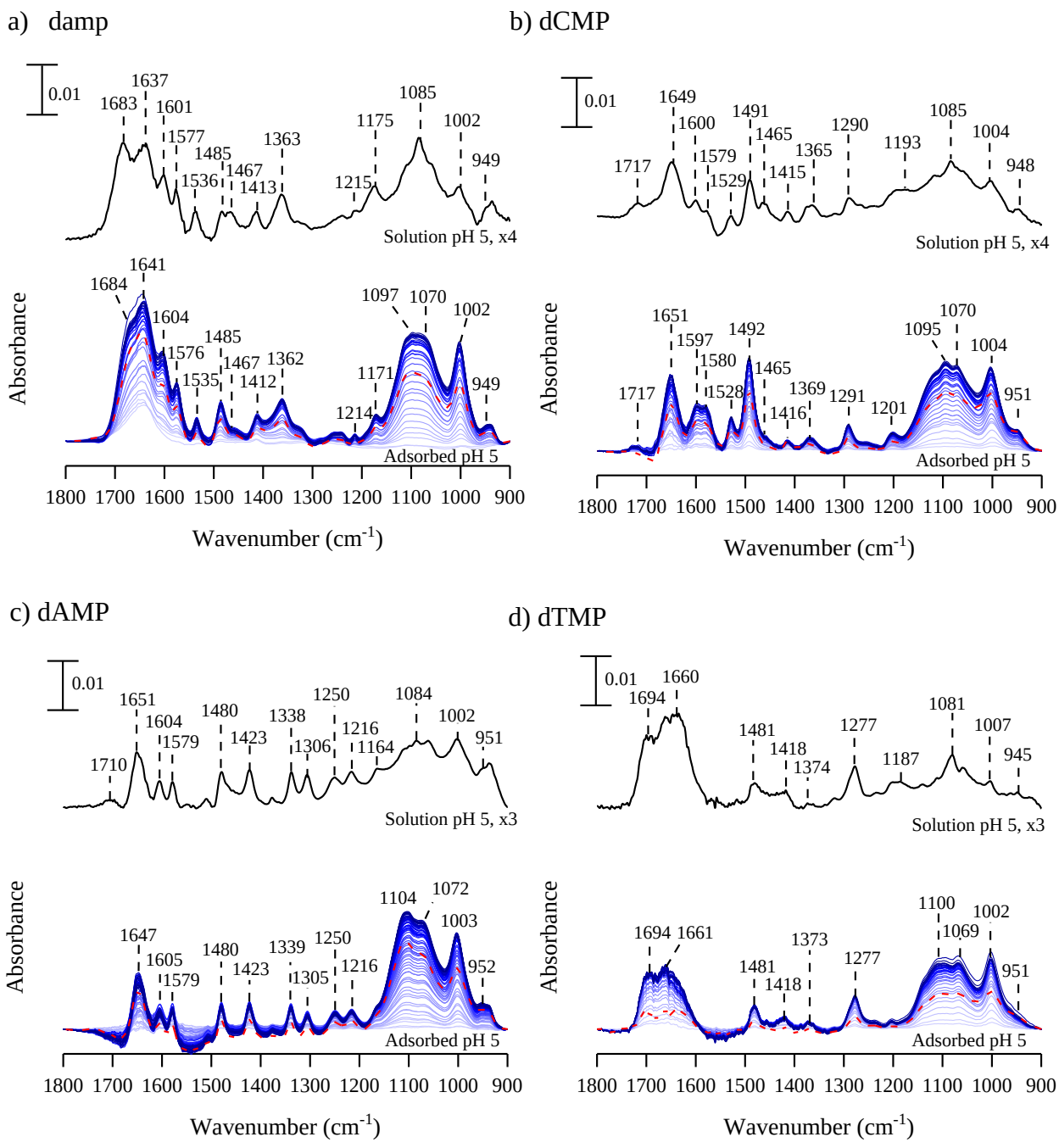

Figure 4.3 ATR-FTIR spectra of solution phase nucleotides and adsorbed on TiO_2

ATR-FTIR spectra at pH 5 of solution phase nucleotides (top) and adsorbed on TiO_2 (bottom) for a) deoxyguanosine monophosphate; b) deoxycytidine monophosphate; c) deoxyadenosine monophosphate; d) deoxythymidine monophosphate. ATR-FTIR spectra are collected as a function of adsorption time. These spectra are shown every 5 minutes from light to dark coloration. The red dotted line represents the desorption spectrum after 120 minutes. Solution phase spectra have been scaled (x3-4) to on the same scale bar.

These speciation forms at pH 5 can be observed in their solution phase spectra which are shown in **Figure 4.3** (top) as well as at pH 9 in **Figure 4.11** (top). In general, the region between 1200 to 1800 cm^{-1} can be assigned to the nucleoside while the 900 to 1200 cm^{-1} region can be assigned to the phosphate group. At pH 5, the phosphate band shape for all the nucleotides is similar given that the phosphate protonation state is identical. For all four nucleotides, the main phosphate absorptions can be grouped in the following: 1164 to 1093, 1081 to 1085, 1002 to 1007, and 945 to 951 cm^{-1}. The 1093 to 1164 and 1081 to 1085 peaks represent the $\nu_{as}(PO_2^-)$ and $\nu_s(PO_2^-)$, respectively. The 1002 to 1007 cm^{-1} peak can be assigned to ν(P-O) while the 945-951 cm^{-1} band is assigned to δ(POH). At pH 9, deprotonation occurs and there is an increase in phosphate symmetry. This leads to a reduction in the number of peaks observed. Mainly, solution phase nucleotide spectra show three main phosphate absorption bands, a broad 1089 cm^{-1} and two more distinct 934 and 978 cm^{-1} peaks. The broadening of the 1089 cm^{-1} $\nu_{as}(PO_3^{2-})$ band and paired with the 978 cm^{-1} $\nu_s(PO_3^{2-})$ when compared to pH 5, is characteristic of a fully deprotonated phosphate group.[65] The 934 cm^{-1} band δ(POH) is very small because the phosphate speciation is heavily dominated by the doubly deprotonated species. The presence of the phosphate bands at both pH 5 and 9 align well with the nucleotide speciation plot. For the solution phase nucleoside spectral features in the 1200 to 1800 cm^{-1} region, there are notable differences between pH 5 and 9. The nucleobase for dAMP and dCMP deprotonates which can be seen by the disappearance of the 1710 and 1717 cm^{-1} $\delta(NH^+)$ bands, respectively. As the dGMP nucleobase undergoes deprotonation from pH 5 to pH 9, the 1693 cm^{-1} $\delta(NH^+)$ band intensity decreases. Vibrational mode assignments for solution and adsorbed nucleotide can be found in **Table 4.4-4.5**.[65,76,126,150,152,153,174,175]

Solution phase nucleotide spectra can be compared to spectra collected of adsorbed phase for nucleotides at pH 5 and 9, where any spectral differences can be attributed to changes due to

surface adsorption. **Figure 4.3** (bottom) shows nucleotide adsorption at pH 5 and **Figure 4.11** (bottom) shows nucleotide adsorption at pH 9. Solution phase spectral intensities are multiplied by a factor of 2-4x and are 100x more concentrated than the bulk solution used for adsorption. This suggests minimal spectral contribution from the solution phase in the adsorption spectra. For adsorbed nucleotides at pH 5, the nucleoside related peaks, between 1200 and 1800 cm^{-1}, have minimal frequency shifting or broadening as a function of surface coverage. Nucleoside band positions also align with those in the solution phase, suggesting minimal direct interactions of these groups occur with the surface and provides a benchmark to study multilayer interactions. Under desorption conditions, bands only decrease in peak intensities and do not have broadening or frequency changes. This indicates the desorption of weakly bound nucleotides.

When the phosphate absorption spectral region from 900 to 1200 cm^{-1} are overlayed for solution phase and adsorbed nucleotide, there is significant broadening due to binding to the TiO_2 surface (**Figure 4.12**). Other studies have reported the preferential adsorption of the phosphate backbone of DNA to surfaces and minimal interaction with the nucleosides.[95,172] There have been previous studies that show adsorbed oxyanion phosphate and nucleotides contains a mixture (de)protonated monodentate and bidentate binding modes on metal oxides.[62,63,65,66,76,156]

Interestingly, the adsorbed spectra for all four nucleotides have similar phosphate band shape between 900 to 1200 cm^{-1}. Specifically, there are four major observable bands in the phosphate region, at ca. 951, 1002, 1069 and 1095 cm^{-1}. All four bands represent major contributions from phosphate coordination to the TiO_2 surface for both monodentate and bidentate modes. This suggests that the four singly adsorbed nucleotides have the same binding surface chemistry to the particle surface. Thus, the nucleotides are coordinated to the TiO_2 surface via the phosphate group.

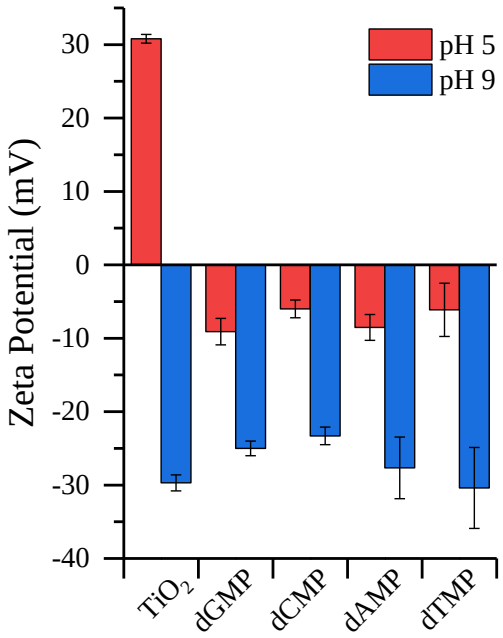

Figure 4.4 Zeta potentials for TiO_2 and solution phase nucleotides at pH 5 (red) and pH 9 (blue)

When the pH is increased to 9 (**Figure 4.11**), the spectral intensities are drastically attenuated when compared to pH 5, corresponding to a decrease in the number of adsorbed nucleotides. **Figure 4.4** shows the zeta potentials for TiO_2 and nucleotides at pH 5 and 9. Under acidic conditions, the surface is positively charged while nucleotides are negatively charged, exhibiting electrostatic attraction. The isoelectric point of TiO_2 is around 6-6.5.[47,172,176] Under basic conditions, both the surface and nucleotides are negatively charged, and electrostatic repulsion can occur, reducing the number of adsorbed nucleotides at higher pH values.

Figure 4.5 shows the adsorption kinetics for the ~1000 cm^{-1} ν(Ti-O-P) and the ~1490 cm^{-1} ν(C-N), δ(C-H) bands at pH 5 as a function of time, representing the phosphate and nucleoside functional groups, respectively. The peak intensities for both the phosphate and nucleoside functional groups show an exponential increase and a plateau, suggesting the surface has reached the maximum number of adsorbed nucleotides with minimal lateral interactions. This behavior has been previously observed in other studies using peak height kinetics and is not surprising to see

minimal lateral and absence of multilayer interactions for single component systems under these conditions.[48,76] Under desorption conditions, intensities exponentially decrease, eventually

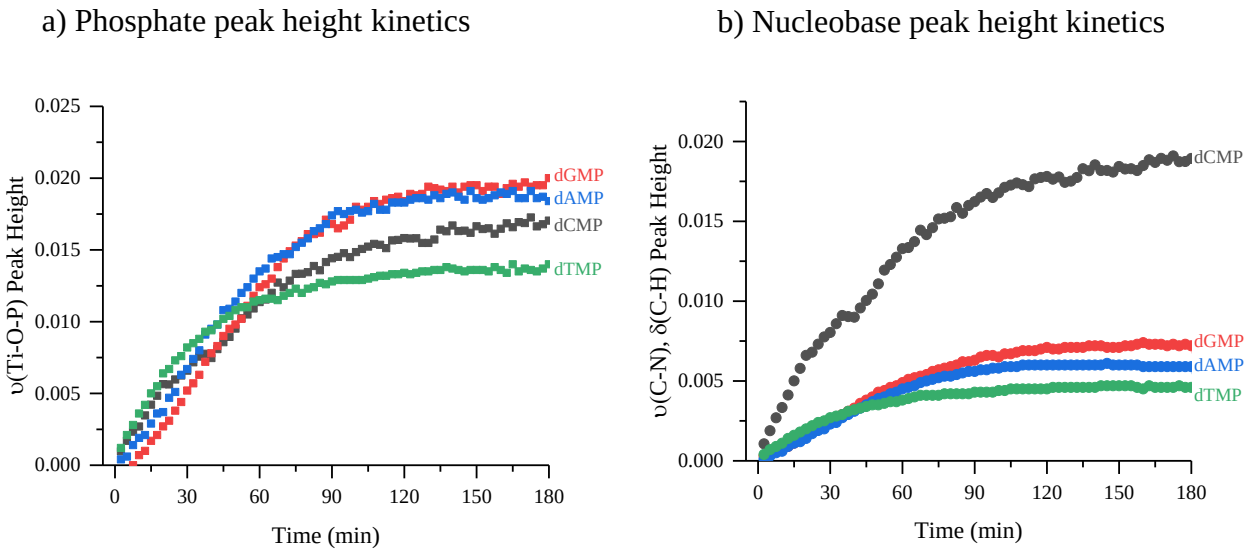

Figure 4.5 Nucleotide adsorption peak height kinetics onto TiO_2 at pH 5 using the (a) ~1000 cm^{-1} ν(Ti-O-P) peak height and (b) ~1490 cm^{-1} ν(C-N), δ(C-H) vibrational bands

slowing the removal of nucleotides. During the desorption stage, the nucleotide intensities do not fall back to zero suggesting that the nucleotides are irreversibly bound to the surface (**Figure 4.13** This suggests that more weakly bonded nucleotides are removed from the surface, leaving directly coordinated nucleotides to the TiO_2 surface. Previous studies have shown that the primary binding mode is monodentate but is often dependent on complexing lattice planes, nanoparticle composition, environmental conditions and is usually a mixture of mono- and bidentate modes.[62,177,178] These dependencies on various factors lead to differences in adsorption energies that can reversibly desorb loosely H-bound adsorbed species while leaving irreversibly adsorbed monodentate or bidentate complexes.[62] The irreversibility of adsorbed mono- and polymeric biomolecules are often observed, however the surface chemistry is often taken for granted and are lightly discussed.[6,46,76,106,115,179] Thus, it is important to understand the fundamental interactions of single or two component systems with surfaces.

Single component adsorption constants for pH 5 can be calculated using the exponential portion of the kinetics assuming a first-order adsorption kinetics up to 95% surface coverage. These calculated values are shown in **Table 4.1**. The adsorption constants, $k_{ads,}$ in order of increasing values follows: dCMP < dTMP < dGMP < dAMP. This suggests that there is a preference of purine nucleotides over pyrimidine nucleotides and this preferential adsorption to

Table 4.1 Relative first order adsorption constants to dAMP up to 95% surface saturation for four nucleotides

	$k_{ads}/k_{ads,dAMP}$
dAMP	1.000
dGMP	0.920
dTMP	0.886
dCMP	0.762

surfaces has been observed in other studies.[133,178,180,181] There are several reasons for differential surface affinities observed. First, electrostatic attraction between the more negative purine nucleotides (dGMP and dAMP) over their pyrimidine counter parts (dCMP and dTMP) with the positively charged TiO_2 surface at pH 5 (**Figure 4.4**). The individual zeta potentials for the pair of pyrimidine and purine nucleotides fall within standard deviations; however, it is clear the purine nucleotides have a lower zeta potential compared to pyrimidine nucleotides. This confirms the preference of purine over pyrimidine nucleotides where electrostatic interactions may play an important role in the interaction with the surface. Secondly, the purine nucleotides may have a greater van der Waal interaction with the surface compared to the pyrimidine nucleotides.[181,182] Thirdly, G and A nucleobases are less soluble than C and T, favoring surface adsorption of G and A to particle surfaces.[133,182] Only through a detailed computational study would these different causes to surface affinity address these different interactions.

Figure 4.6 shows nucleotide surface coverage at pH 5 in increasing values: dTMP, dCMP < dGMP < dAMP. dTMP and dCMP are within the standard deviation and have similar surface coverages. However, the purine nucleotides have a higher surface coverage than pyrimidine nucleotides. These results align well with similar quantitative adsorption studies.[171,177]

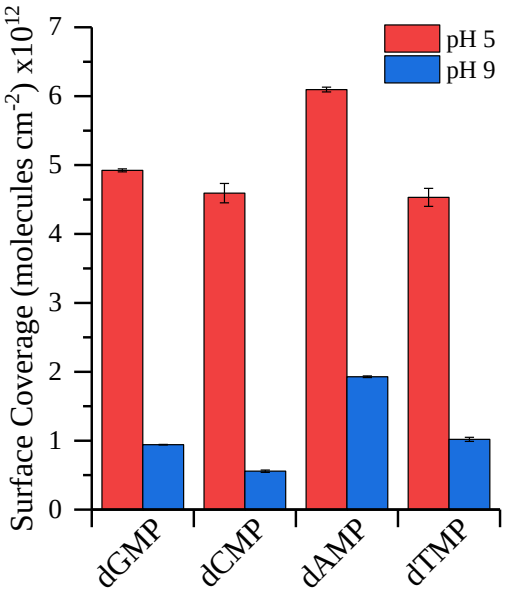

Figure 4.6 Nucleotide surface coverage on TiO_2

Single component nucleotide surface coverage on TiO_2 at pH 5 and 9 in 10mM NaCl. pH 9 surface coverages were scaled from pH 5 using ratioed ATR-FTIR adsorption intensities.

4.4.3 Analysis of Two-Component Noncomplementary and Complementary Base Pair Adsorption

There is typically a mixture of nucleotides in natural aqueous systems, with various surface affinities competing with the surface and interacting as co-adsorbates. To increase complexity to single component experiments and model more realistic systems, two nucleotides were competitively adsorbed onto the surface. **Figure 4.14** shows ATR-FTIR spectra for the adsorption of an equimolar number of nucleotides consisting of either noncomplementary (dGMP-dTMP and dAMP-dCMP) or complementary base pairs (dGMP-dCMP and dAMP-dTMP), on the TiO_2

surface. Despite the bulk solutions comprised of an equimolar mixture of purine and pyrimidine nucleotides, the adsorption spectral features are highly similar to single component purine nucleotide spectra over pyrimidine spectra in all four systems. To emphasize this, **Figure 4.7** shows equilibrated spectra for singly, noncomplementary and complementary adsorbed nucleotides on the oxide surface. In a two-component system, the spectra resemble that of singly adsorbed purine nucleotides, implying the preferential adsorption over the pyrimidine nucleotides. However, there are small spectral contributions from co-adsorbed pyrimidine nucleotides. The singly adsorbed dGMP and noncomplementary dGMP-dTMP spectra show identical spectra with similar 1485 cm^{-1} peak position. However, under complementary base pair conditions of dGMP-dCMP, the 1485 cm^{-1} shifts to 1489 cm^{-1} and has a slightly lower intensity which will be discussed later. It is hypothesized that this is due to a hydrogen bound second layer. In the noncomplementary dAMP-dCMP system, the 1484 cm^{-1} undergoes some broadening and a small 1528 cm^{-1} peak appears when compared to the single dAMP spectrum. This is due to small spectral contributions from co-adsorbed dCMP; however, the surface composition is still dominated by non-interacting adsorbed dAMP. The co-adsorbed dTMP in a second layer for the dAMP-dTMP complementary system is observed, noted by the presence of the 1694 cm^{-1} ν(C=O) peak. After desorption, only 20% of this peak remains on the surface, suggesting reversible adsorption. For all the spectra, the 1200-900 cm^{-1} phosphate region is identical in shape suggesting that the composition of monodentate to bidentate surface complexation modes would be similar in ratios, regardless of nucleotide derivative or in a multicomponent system.

Table 4.2 Relative number of adsorbed nucleotides for non-complementary and complementary base pairs on the TiO_2 surface at pH 5

Base Pair	Relative Adsorbed Nucleotides (%)	
	Purine	Pyrimidine
dGMP-dTMP	100	0
dGMP-dCMP	89.5	21.5
dAMP-dCMP	82.5	17.5
dAMP-dTMP	70.3	29.7

The relative number of adsorbed pyrimidine nucleotides in a co-adsorbed system were estimated by taking a ratio of intensities for single-component to a two-component system. Pyrimidine peaks were chosen that have minimal overlap with purine peaks, specifically the 1694 cm^{-1} for dTMP and the 1292 cm^{-1} peak for dCMP. **Table 4.2** shows the relative adsorbed amount of purine and pyrimidine nucleotides in a co-adsorbed system. Both complementary systems (dGMP-dCMP and dAMP-dTMP) have higher amounts of adsorbed pyrimidine nucleotides than non-complementary systems (dGMP-dTMP and dAMP-dCMP). This suggests that there is a synergistic effect of complementary nucleotides that increase the relative amounts of surface adsorbed pyrimidine nucleotides when compared to non-complementary systems.

The dGMP-dTMP and dAMP-dCMP noncomplementary co-adsorption peak height kinetics are shown for the nucleobase (Figure 8a) and phosphate (Figure S5a) functional groups. The kinetics are identical to single component adsorption in such that it is monotonically

a) Noncomplementary Base Pairs

b) Complementary Base Pair

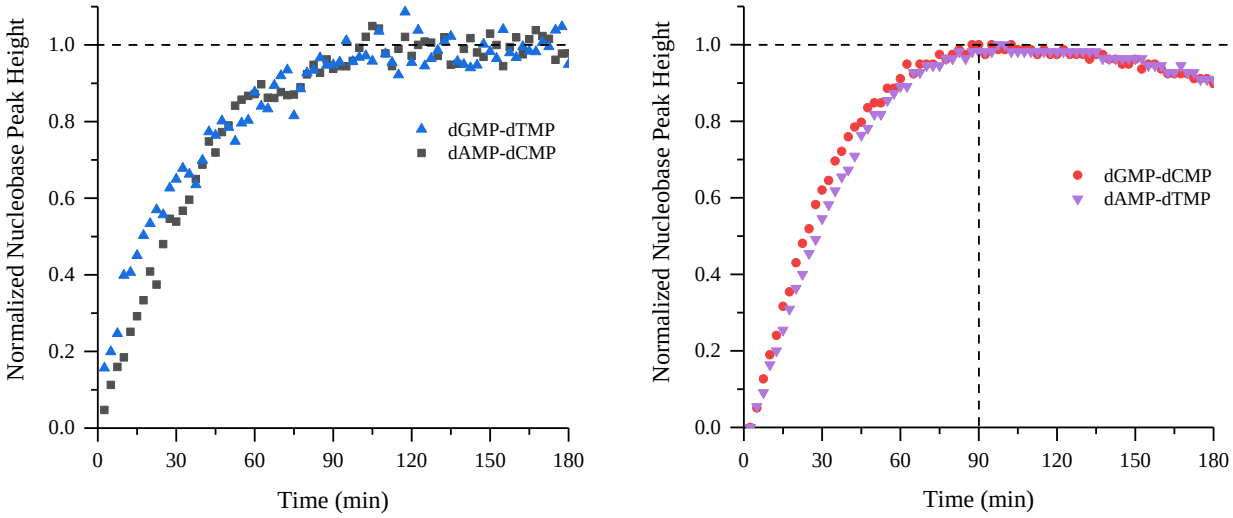

Figure 4.7 Changes to normalized peak height for two component nucleotide base pair adsorption onto TiO_2 at pH 5 using the ca. 1480 cm^{-1} ν(C-N), δ(C-H)

a) noncomplementary nucleotide base pairs dGMP-dTMP (blue triangle) and dAMP-dCMP (gray square). b) complementary nucleotide base pairs dGMP-dCMP (red circle) and dAMP-dTMP (purple down-triangle). The dotted horizontal line emphasizes the decrease in the ν(C-N), δ(C-H) intensity after the 90-minute mark for the complementary base pairs (dGMP-dCMP and dAMP-dTMP) where the noncomplementary base pair kinetics plateau (dGMP-dTMP and dAMP-dCMP)

increasing with an exponential initial growth and plateau. The nucleotides are irreversibly bound to the surface as desorption does not fully remove the nucleotides (**Figure 4.14a-b**). **Figure 4.9** shows a conceptual representation of the preferential direct coordination of purine (dGMP or dAMP) nucleotides to the TiO_2 surface without a second layer and free pyrimidine (dTMP or dCMP) nucleotides in bulk. Additionally, the nucleotides have minimal lateral interactions with co-adsorbates and do not form a multilayer.

For complementary dGMP and dCMP base pair nucleotides, there are other effects that occur when co-adsorbed onto the TiO_2 surface. It is observed that the adsorbed spectra are highly similar to the equilibrated single component dGMP adsorbed spectra in shape, intensity, and band positions (**Figure 4.14c**). This suggests that dGMP has a higher surface affinity than dCMP and the surface is mainly comprised of dGMP. The adsorption kinetics are shown for the nucleobase (**Figure 4.8b**) and phosphate (**Figure 4.15**) functional groups. The 1000 cm^{-1} ν(Ti-O-P) band shows exponential increase followed by slowing and a slight plateau, like single component

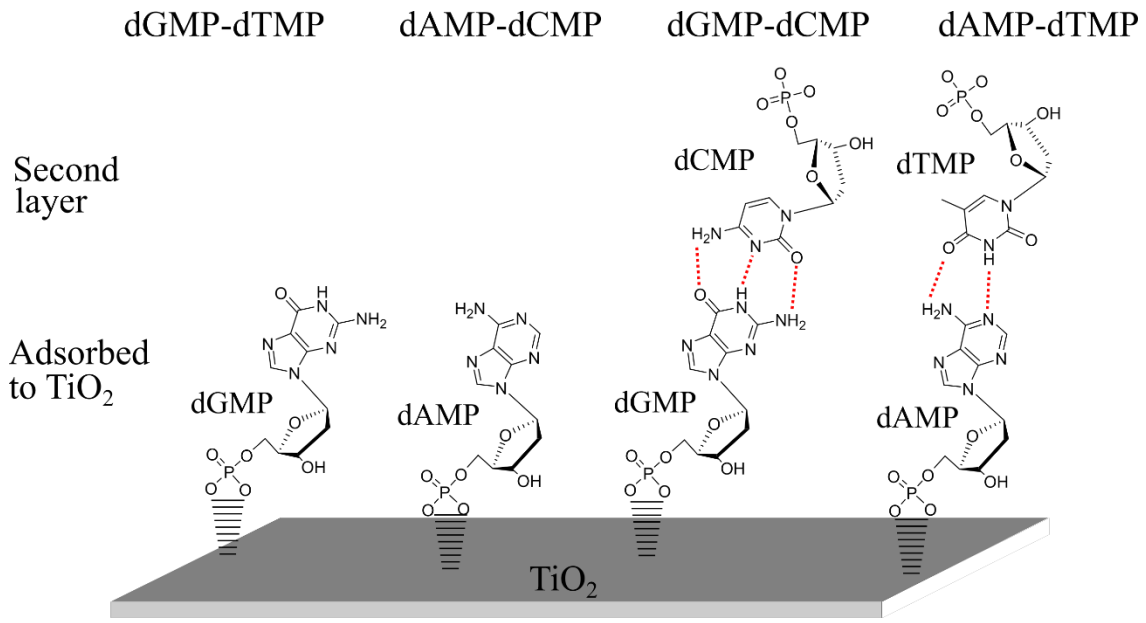

Figure 4.8 Conceptual representation of two component adsorption of nucleotide base pairs on TiO_2

For dGMP-dTMP, there is no interaction between the two nucleotides and dGMP coordinates to the surface while dTMP stays in solution. For dAMP-dCMP, there is no interaction between the two nucleotides and dAMP coordinates to the surface and dCMP remains in solution. For dGMP-dCMP, there is an interaction between nucleotides with dGMP directly coordinating to the surface while interacting through hydrogen-bonds to dCMP in a second layer. For dAMP-dTMP, there is an interaction between nucleotides with dAMP directly coordinating to the surface while interacting through hydrogen-bonds to dTMP in a second layer.

adsorption. However, for the 1489 cm^{-1} ν(C-N), δ(C-H) peak kinetics, a slight inflection point is observed around the 90-minute mark. This is hypothesized to come from a change to the extinction coefficients to the 1489 cm^{-1} vibrational modes as hydrogen bound nucleotides can alter the

dynamic dipole moment.[183–185] After desorption, most of the nucleotides remain on the surface (**Figure 4.16c**).

There are two configurations for hydrogen bound dGMP and dCMP complementary base pairs, specifically, Hoogsteen (HG) and Watson-Crick (WC). Previous studies report that HG is preferred at lower pH due to the protonated dCMP N3-H^+ that hydrogen bonds to dGMP N7 at the nitrogenous rings. WC occurs at higher pH values and dominant at physiological pH.[185] Additionally for dGMP-dCMP, HG forms two H-bonds and WC forms three H-bonds. Stelling et al. investigated the interaction of duplex DNA and identifies IR band assignments to either Hoogsteen or Watson-Crick hydrogen bonding conformations.[185] When WC conformation was switched to HG, a ~30% decrease in the 1498 cm^{-1} N7 peak intensity was noted as a spectral band marker. In our study, observation of other peak shifts as spectral makers is not seen but could be due to the adsorption of nucleotides onto the TiO_2 surface. However, in **Figure 4.8b,** a ~10% decrease in the ν(C-N), δ(C-H) is observed. The intensity decrease is not as significant as previously reported by Stelling et al., but this could be due to the use of single nucleotides over oligonucleotides which could form multiple H-bonding configurations and cause a larger change in intensity. Additionally, at our experimental pH 5, both HG and WC could be possible whereas in the reference, the 30% intensity decrease is from a complete conversion from WC to HG. Therefore, a multilayer of hydrogen bound complementary base pair nucleotides are observed to form on the surface.

At experimental pH 5, both zwitterionic and monovalent anionic forms of dCMP are present in solution, thus the H-bonding configuration could be HG or WC. However, for the adsorbed two component, competitive adsorption spectra, the protonated 1717 cm^{-1} ν(NH^+) dCMP peak is not observed but is seen for adsorbed single component. Since HG requires a protonated

dCMP, the multilayer configuration must be dominated by WC; the multilayer dCMP undergoes a deprotonation to adopt a WC base pairing configuration. Furthermore, WC base pairing can be more energetically stable than HG.[186] To surmise the composition of each layer in the multilayer, previous zeta potential and the preference of pyrimidine over purine nucleotides results suggest that dGMP has the higher surface affinity and would be directly bound to the surface. The second layer could then be comprised of hydrogen bound dCMP pyrimidine ring to the exposed purine ring of dGMP (**Figure 4.9**). This H-bonding conformation is identical to how complementary base pairs interact in DNA. The multilayer formation of complementary base pairs on metal oxide particles is evidence for biomolecular templating, providing insight into the formation of prebiotic life.

For the other complementary base pair, dAMP and dTMP (**Figure 4.14d**), it is more difficult to determine a H-bonding configuration as both HG and WC have two hydrogen bonds and neither case require a protonated nucleotide. However, it is possible to discern which nucleotide is preferentially directly coordinated to the surface. The nucleobase peak intensity as a function of time (**Figure 4.8b**) for the two-component system show an inflection point for the 1480 cm^{-1} ν(C-N), δ(C-H) band at ~90 minutes during adsorption. After desorption, only 20% of the 1694 cm^{-1} ν(C=O) band is seen (data not shown). This is different than the dGMP-dCMP system where the multilayer was stabilized and only minimal decrease in various peak intensities was observed. The 1694 cm^{-1} band can be attributed to dTMP as there is 1694 cm^{-1} present in the single component adsorbate spectrum alone and no such peak is present for dAMP (**Figure 4.3c** and **Figure 4.3d**). The spectral shape resembles adsorbed single component dAMP spectra than single component dTMP. This suggests that a multilayer is formed, and the second layer reversibly adsorbs. In both WC and HG dAMP-dTMP configurations, there are only two H-bonds compared

to the three H-bonds in WC dGMP-dCMP. The reversibility of the multilayer in dAMP-dTMP compared to the relatively irreversibility of dGMP-dCMP could be due to the additional H-bond in WC configuration for dGMP-dCMP, leading to a more stable multilayer. For these reasons, the data show that dAMP is directly coordinated to the TiO_2 surface while dTMP interacts within a

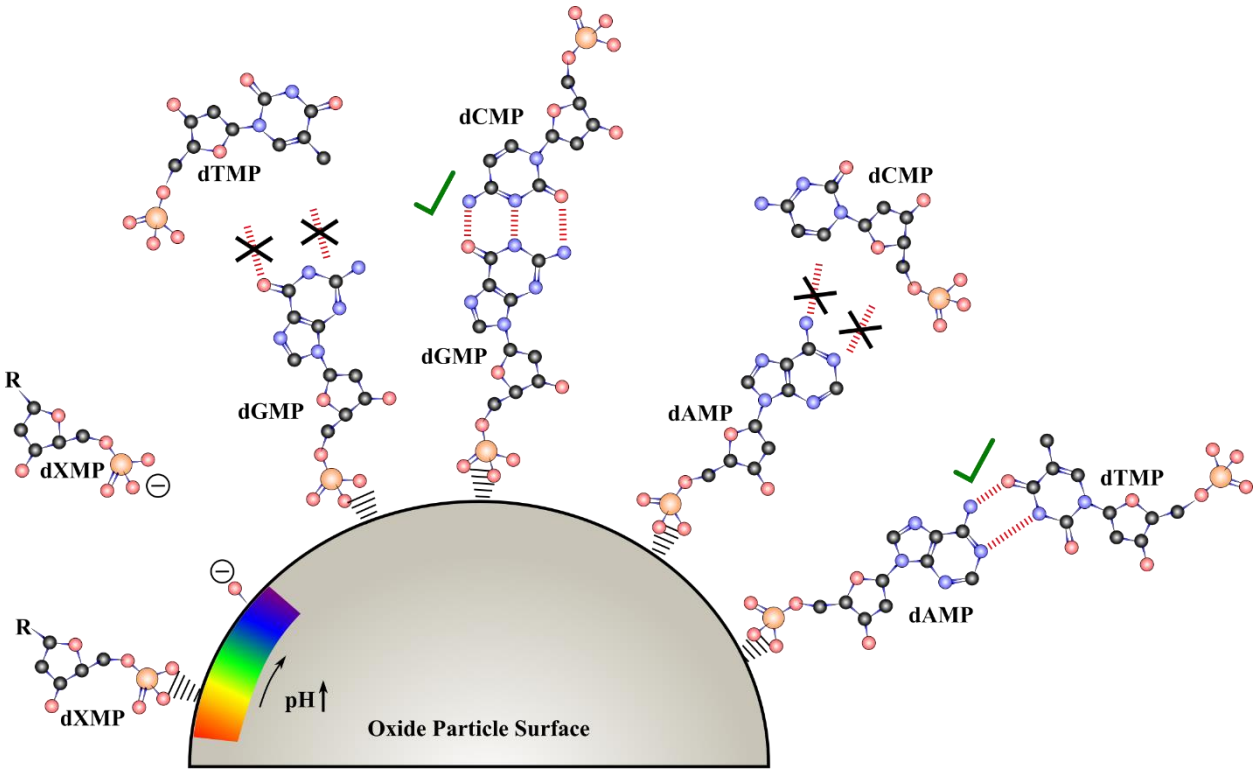

Figure 4.9 Pictorial representation of different surface chemistries occurring on an oxide particle surface for nucleotides

From left to right: electrostatic pH dependence of singly adsorbed nucleotides where nucleotides are attracted at lower pH compared to repelled at higher pH. Two-component adsorption only forms hydrogen bound interactions between strongly bound nucleotide layer and weaker H-bonded second layer with complementary base pairs where noncomplementary nucleotides do not form a second layer. Depicted is also the preferential adsorption of dGMP compared to dCMP and dTMP, and dAMP compared to dTMP and dCMP.

second layer (**Figure 9**). There is a preferential adsorption of purine (dAMP and dGMP) over pyrimidine (dTMP and dCMP) nucleotides to TiO_2 even in more complex systems for the same reasons mentioned previously for single component adsorption. Since the spectra for both complementary base pairs represent more of the adsorbed purine nucleotide, the second layer of

hydrogen bound pyrimidine nucleotides cannot be in a 1:1 ratio to the directly coordinated purine layer; the second layer does not fully cover the first adsorbed layer.

Figure 4.10 depicts the results of this study and shows that there are differential surface interactions and surface templating effects from pH, competitive and complementary base pair nucleotide adsorption. Additionally, this study shows the reduction of nucleotide bioavailability in solution due to adsorption on oxide particle surfaces in aqueous environments at lower pH values. Regardless of nucleotide derivative, the phosphate group is shown to directly coordinate to the oxide surface, leaving the nucleobase free to further interact with components in solution. In systems where there are multicomponent nucleotide solutions, the composition of the adsorbed layer is heavily dominated by the direct surface coordinated purine nucleotides while a second layer only forms in the presence of complementary pyrimidine nucleotides.

4.5 Conclusion

Adsorption of biomolecular components onto geochemical mineral surfaces is important to understand as it can provide insight into the environmental DNA and surface adsorption of these components in the environment as well as the role of surfaces in the origins of prebiotic life. The results from this study show that nucleotides lead to high levels of adsorption at lower pH and little adsorption at higher pH. Spectral broadening in the phosphate band region shows how nucleotides are directly bound to the surface via the phosphate group. The binding mode appears to be similar for all the nucleotides regardless of nucleobase derivative from similar phosphate band absorption shape. This suggests that the surface chemistry in this first adsorbed layer is dependent on surface composition and structure rather than a specific nucleotide composition. However, there is still differential surface interactions leading to different surface coverages and rates of adsorption. Additionally, when nucleotides are co-adsorbed in a two-component system, second layer

formation and specific interactions only occur for complementary base pairs but not for noncomplementary base pairs or single component systems. Overall, the results from this study show that nucleotides can be concentrated from dilute bulk solutions onto geochemical surfaces and can template specific interactions which has consequences for these biological components in the environment for both current considerations and in early Earth.

4.6 Acknowledgements

Chapter 4, in full, has been accepted for publication of the material as it may appear in Langmuir. Sit, I.; Quirk, E.; Hettiarachchi, E.; Grassian, V. H. Differential Surface Interactions and Surface Templating of Nucleotides (dGMP, dCMP, dAMP, and dTMP) on Oxide Particle Surfaces. The dissertation author is the first author of this paper.

4.7 Supplemental Information

Table 4.3 Tabulated speciation forms for the dGMP, dCMP, dAMP and dTMP at pH 5 and 9 as determined using Henderson-Hasselbalch. Speciation forms are shown in percentages

	$dG^{+}MP^{-}$	$dGMP^{-}$	$dGMP^{-2}$	$dGMP^{-3}$
pH 5	1.8	91.0	7.2	0.0
pH 9	0.0	0.1	66.5	33.4

	$dC^{+}MP^{-}$	$dCMP^{-}$	$dCMP^{-2}$	$dCMP^{-3}$
pH 5	15.6	78.2	6.2	0.0
pH 9	0.0	0.1	99.9	0.0

	$dA^{+}MP^{-}$	$dAMP^{-}$	$dAMP^{-2}$	$dAMP^{-3}$
pH 5	4.4	88.6	7.0	0.0
pH 9	0.0	0.1	99.9	0.0

	dTMP	$dTMP^{-}$	$dTMP^{-2}$	$dTMP^{-3}$
pH 5	0.0	96.9	3.1	0.0
pH 9	0.0	0.3	90.6	9.1

Table 4.4 Deoxyguanosine monophosphate and deoxycytidine monophosphate vibrational mode peak assignments in solution at pH 5 and 9 compared to adsorbed on TiO_2 nanoparticles.

Vibrational modes[a]	Vibrational Frequency (cm^{-1})								Literature Assignment (cm^{-1})
	Solution				Adsorbed				
	dGMP		dCMP		dGMP		dCMP		
	pH 5	pH 9	pH 5	pH 9	pH 5 (Δ)[b]	pH 9 (Δ)[b]	pH 5 (Δ)[b]	pH 9 (Δ)[b]	
$\delta(N3H^+)$			1717				1717 (+0)		1707[76], 1696[126]
ν(C6=O6)	1683	1683			1684 (+1)				1698-1678[174]
δ(HOH)	1637	1637	1649	1644	1641 (+4)	1651 (+14)	1651 (+2)	1651 (+7)	
purine/pyrmidine ring	1601		1600		1604 (+3)		1597 (+3)		1603[76], 1607[152]
purine/pyrmidine ring	1577	1577	1579	1577	1576 (-1)	1573 (-4)	1580 (+1)		1580[76], 1570[152], 1575-1590[174]
purine/pyrmidine ring	1536	1540	1529	1541	1535 (+1)		1528 (-1)		1527-1520[174]
ν(C-N), δ(C-H)	1485	1483	1491	1491	1485 (+0)		1492 (-1)	1490 (+1)	1479[76], 1495-1476[174]
purine/pyrmidine ring	1467	1467	1465	1472	1467 (+0)		1465 (+0)		1477-1785[174]
$\delta(CH_2)$	1413	1413	1415		1412 (+1)		1416 (+1)		1422[76] ,1425[152]
purine/pyrmidine ring	1363	1363	1365	1366	1362 (-1)		1369 (+4)		1365-1360[174]
pyrmidine ring			1290	1293			1291 (+1)		1304[76], 1307[152]
ν(N9-C1')	1215				1214 (-1)				1217[76], 1212[152]
$\nu_{as}(PO_2^-)$	1175		1193		1171 (-4)		1201 (+8)		1159[65]
bidentate/monodentate					1097	1090	1095	1090	1115[65], 1105[175]
$\nu_{as}(PO_3^{2-})$		1089		1090					1084[76], 1088[152], 1078[65]
$\nu_s(PO_2^-)$	1085		1085		1070 (-15)		1070 (-15)		1077[65]
ν(P-O)	1002		1004						1002-1003[76], 996-1002[126]
ν(Ti-O-P)					1002	997	1004	994	992-997[76]
$\nu_s(PO_3^{2-})$		978		978					978-980[76], 974[152], 979[126]
δ(POH)	949	934	948	937					935[76], 935[150]
ν_s(P-(OTi)$_2$) of bidentate complexes					949		951		936[76], 935[153]

[a] $\nu_{s/as}$: symmetric/asymmetric stretch vibration; δ: bending vibration

[b] Δ: difference between adsorbed and solution phase wavenumber at last time point collected on ATR-FTIR

Table 4.5. Deoxyadenosine monophosphate and deoxythymidine monophosphate vibrational mode peak assignments in solution at pH 5 and 9 compared to adsorbed on TiO_2 nanoparticles.

Vibrational modes[a]	Vibrational Frequency (cm^{-1})								Literature Assignment (cm^{-1})
	Solution				Adsorbed				
	dAMP		dTMP		dAMP		dTMP		
	pH 5	pH 9	pH 5	pH 9	pH 5 (Δ)[b]	pH 9 (Δ)[b]	pH 5 (Δ)[b]	pH 9 (Δ)[b]	
δ($N1H^+$)	1710								1707[76], 1696[126]
ν(C2=O2)			1694	1694			1694 (+0)	1693 (+1)	1698-1691[174]
δ(HOH)	1651	1647	1660	1634	1647 (-4)		1661 (+1)		
purine ring	1604	1606			1605 (+1)				1603[76], 1607[152]
purine/pyrmidine ring	1579	1577		1575	1579 (+0)	1578 (+1)			1580[76], 1570[152], 1575-1590[174]
purine/pyrmidine ring		1540		1540					1527-1520[174]
ν(C-N), δ(C-H)	1480	1475	1481	1476	1480 (+0)	1477 (+2)	1481 (+0)		1479[76], 1495-1476[174]
δ(CH_2)	1423	1422	1418	1418	1423 (+0)	1422 (+0)	1418 (+0)		1422[76] ,1425[152]
pyrimidine ring			1374				1373 (+0)		1389-1374[174]
purine ring	1338	1338			1339 (+1)	1338 (+0)			1344-1335[174]
purine ring	1306	1306			1305 (-1)				1304[76], 1307[152]
pyrmidine ring			1277	1278			1277 (+0)	1278 (+0)	1281-1275[174]
δ(C6-NH_2)	1250	1253			1250 (+0)	1251 (-2)			1248[76], 1249[152]
ν(N9-C1')	1216	1214			1216 (+0)				1217[76], 1212[152]
$\nu_{as}(PO_2^-)$	1164		1187						1159[65]
bidentate/monodentate					1104	1101	1100	1086	1115[65], 1105[175]
$\nu_{as}(PO_3^{2-})$		1089		1086					1084[76], 1088[152], 1078[65]
$\nu_s(PO_2^-)$	1084		1081		1072 (-12)		1069 (-12)		1077[65]
ν(P-O)	1002		1007						1002-1003[76], 996-1002[126]
ν(Ti-O-P)					1003	1003	1002	999	992-997[76]
$\nu_s(PO_3^{2-})$		978		977					978-980[76], 974[152], 979[126]
δ(POH)	951	934	945	940					935[76], 935[150]
ν_s(P-$(OTi)_2$) of bidentate complexes					952		951		936[76], 935[153]

[a] $\nu_{s/as}$: symmetric/asymmetric stretch vibration; δ: bending vibration

[b] Δ: difference between adsorbed and solution phase wavenumber at last time point collected on ATR-FTIR

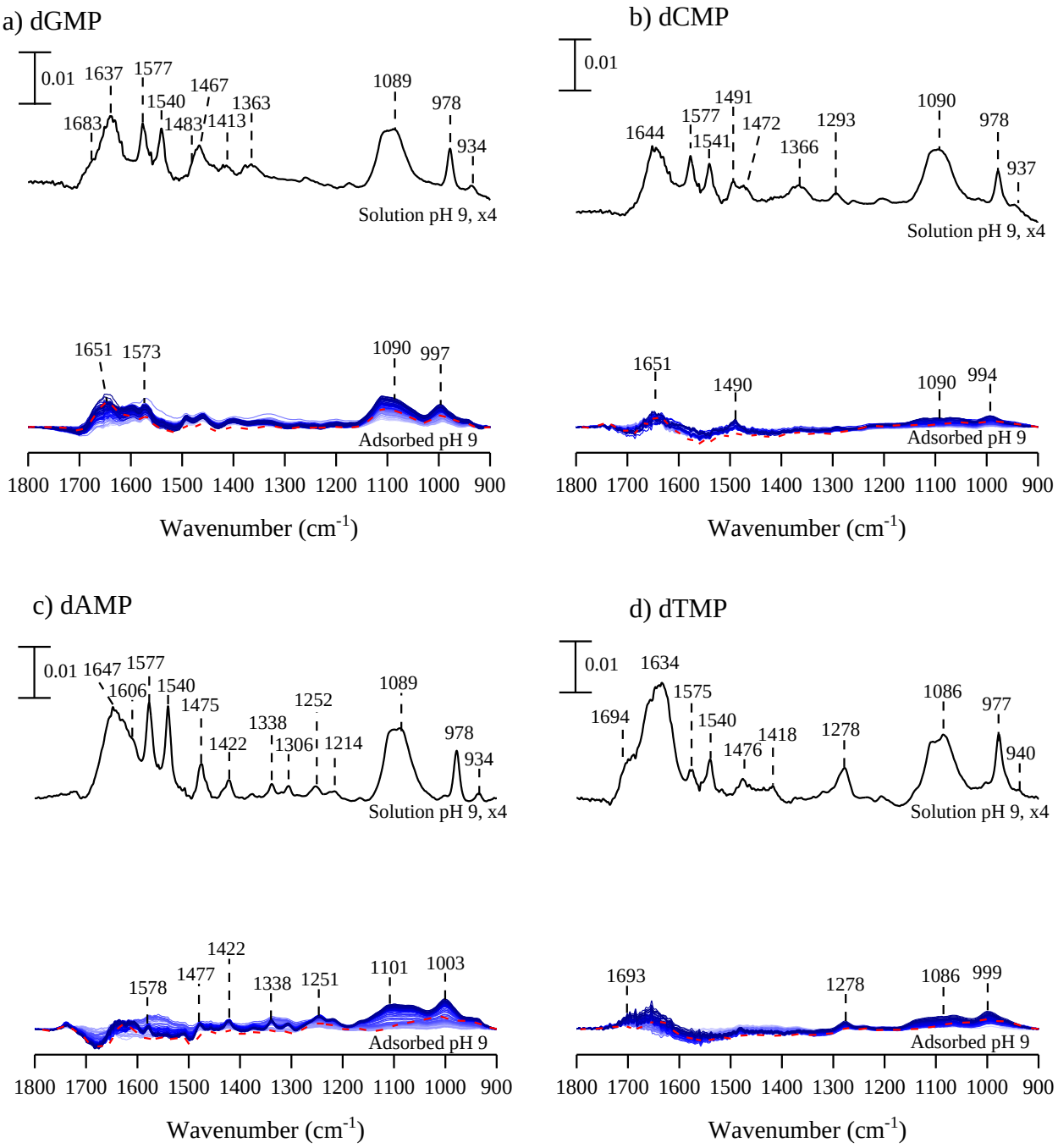

Figure 4.10 ATR-FTIR spectra of nucleotides in solution and adsorbed on TiO_2 at pH 9

ATR-FTIR spectra at pH 9 of solution phase nucleotides (top) and adsorbed on TiO_2 (bottom) for a) deoxyguanosine monophosphate; b) deoxycytidine monophosphate; c) deoxyadenosine monophosphate; d) deoxythymidine monophosphate. ATR-FTIR spectra are collected as a function of adsorption time. These spectra are shown every 5 minutes from light to dark coloration. The red dotted line represents the desorption spectrum after 120 minutes. Solution phase spectra have been scaled (x4) to on the same scale bar.

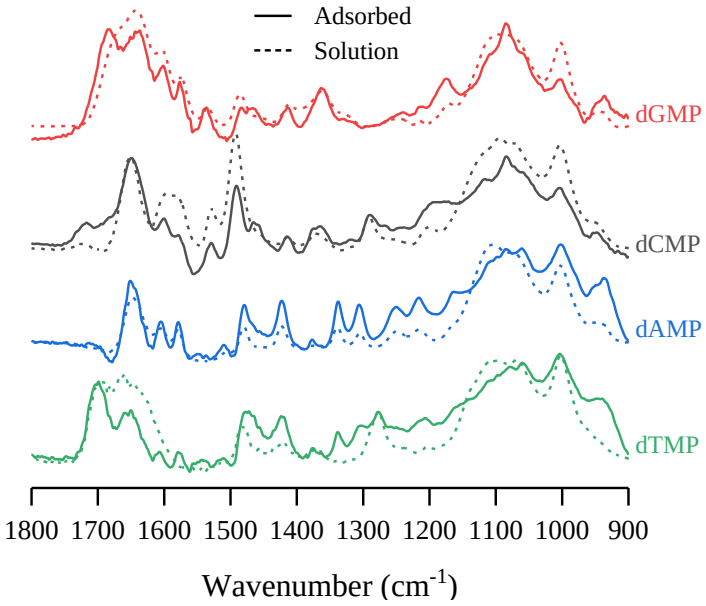

Figure 4.11 Overlayed normalized ATR-FTIR spectra at pH 5 for solution (dotted) and saturated adsorbed (solid) of the phosphate absorption band between 900-1200 cm^{-1} for dGMP, dCMP, dAMP, and dTMP

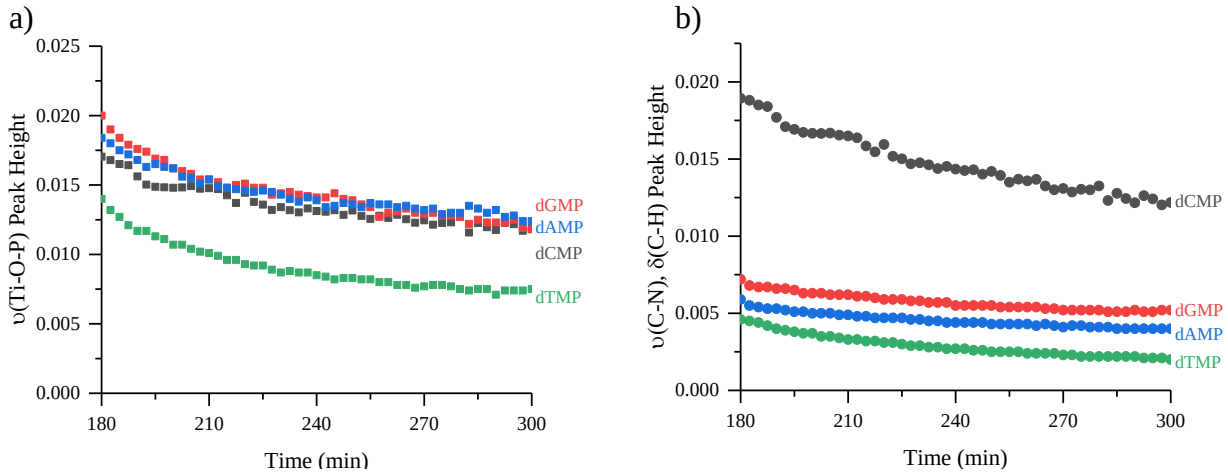

Figure 4.12 One component nucleotide adsorption peak height desorption kinetics onto TiO_2 at pH 5

(a) ~1000 cm^{-1} ν(Ti-O-P) peak height and (b) ~1490 cm^{-1} ν(C-N), δ(C-H) vibrational bands.

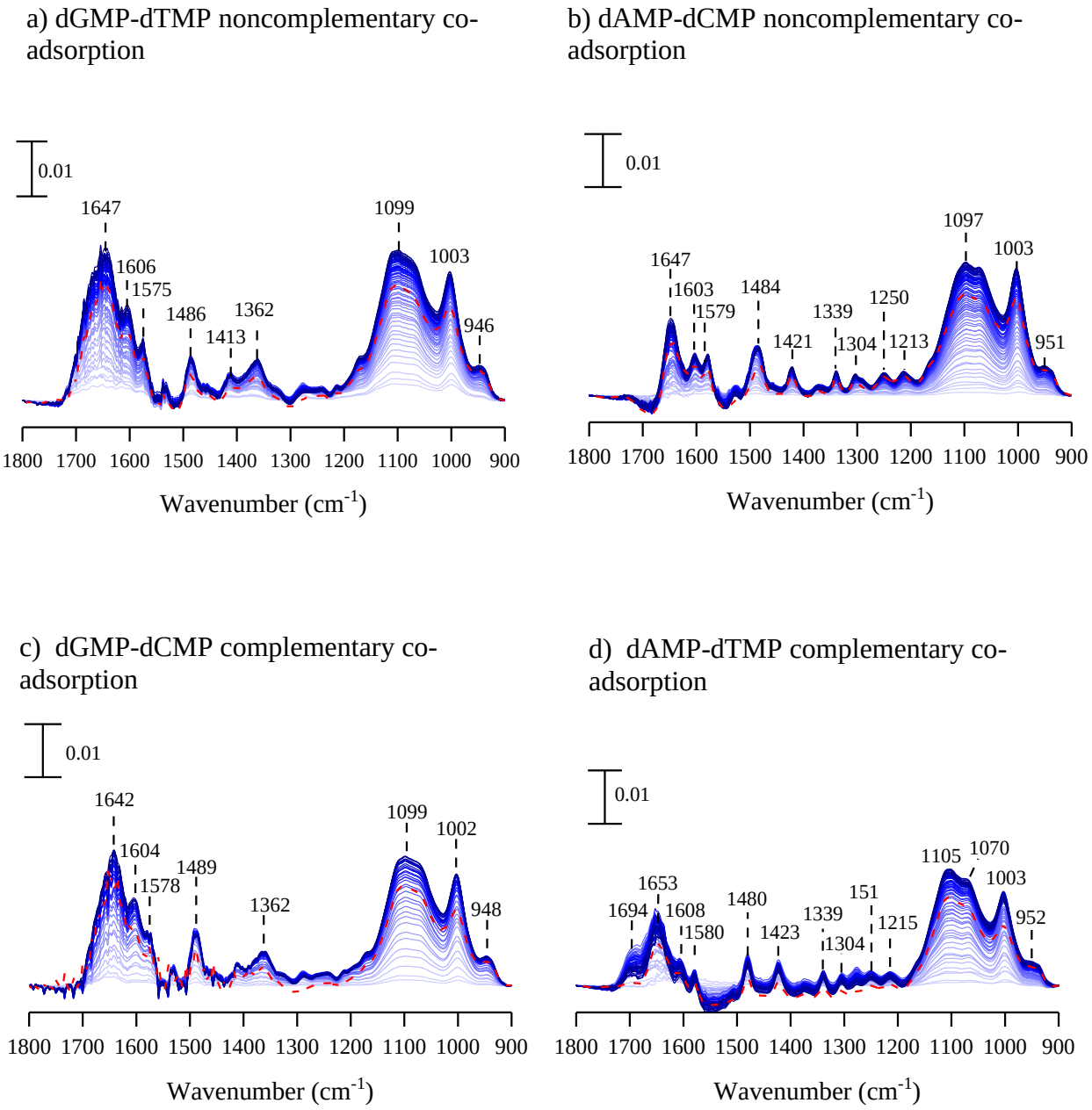

Figure 4.13 ATR-FTIR spectra at pH 5 of equimolar base pair solution adsorbed on TiO_2

a) dGMP-dTMP noncomplementary, b) dAMP-dCMP noncomplementary, c) dGMP-dCMP complementary and d) dAMP-dTMP complementary. ATR-FTIR spectra are collected as a function of adsorption time. These spectra are shown every 5 minutes from light to dark coloration. The red dotted line represents the desorption spectrum after 120 minutes.

a) Noncomplementary co-adsorption b) Complementary co-adsorption

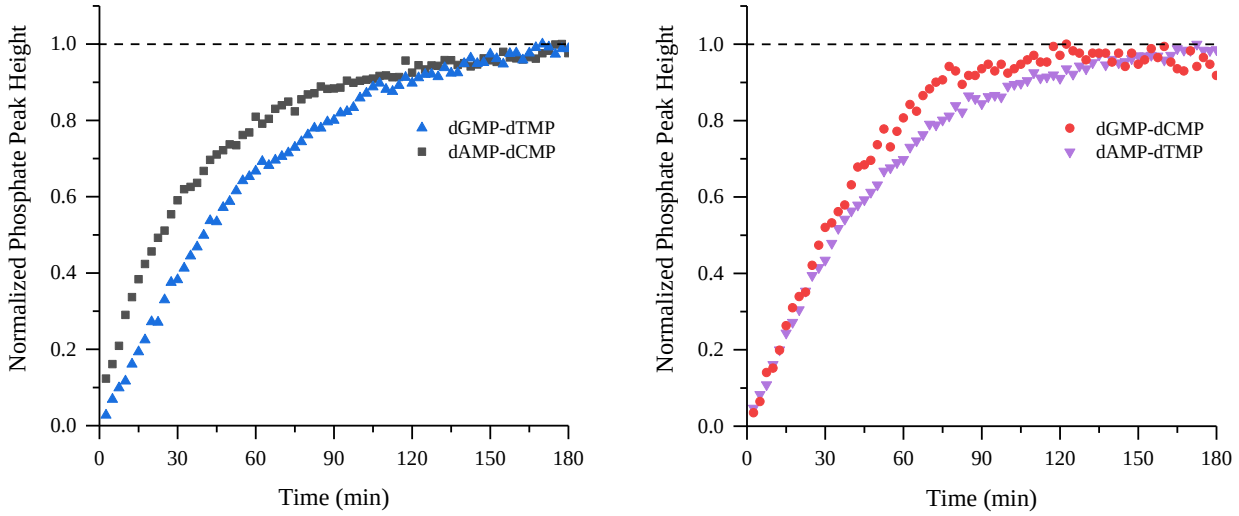

Figure 4.14 Changes to normalized phosphate peak height for two component nucleotide base pair adsorption onto TiO_2 at pH 5 using the ca. 1000 cm^{-1} ν(Ti-O-P)

a) noncomplementary nucleotide base pairs dGMP-dTMP (blue triangle) and dAMP-dCMP (gray square). b) complementary nucleotide base pairs dGMP-dCMP (red circle) and dAMP-dTMP (purple upside-down triangle).

a) dGMP-dTMP noncomplementary co-adsorption

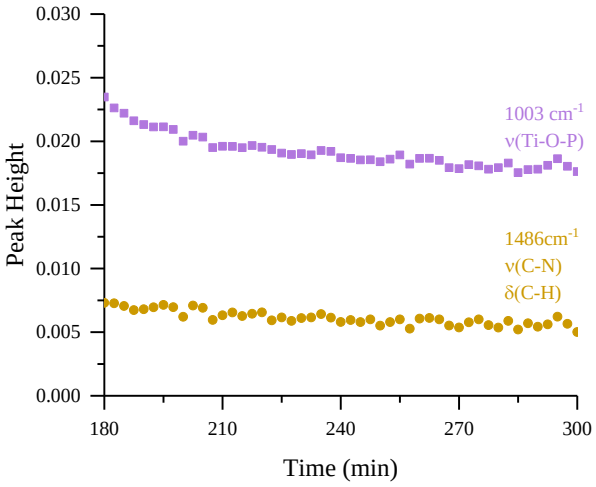

b) dAMP-dCMP noncomplementary co-adsorption

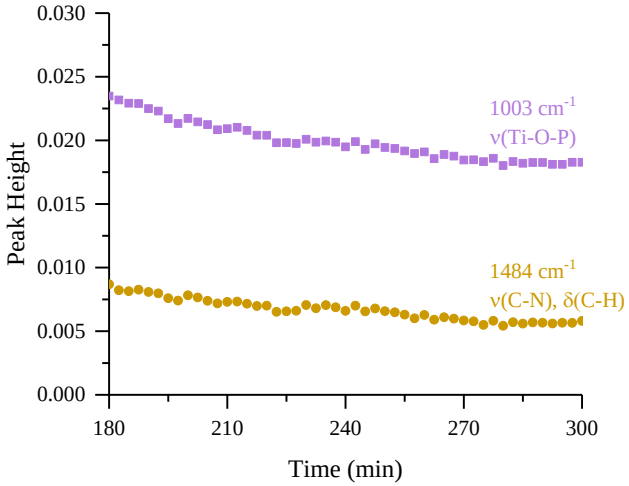

c) dGMP-dCMP complementary co-adsorption

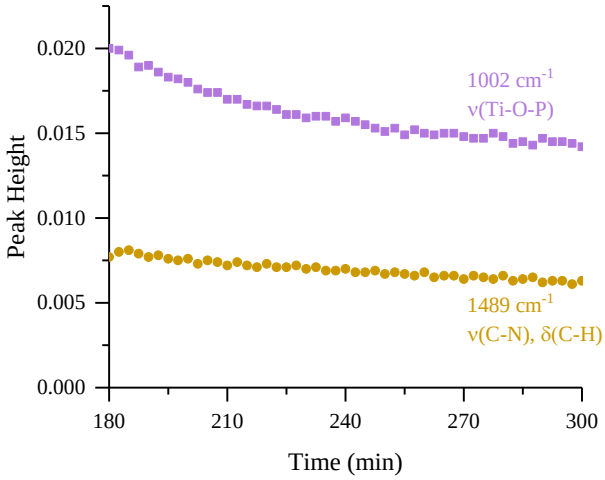

d) dAMP-dTMP complementary co-adsorption

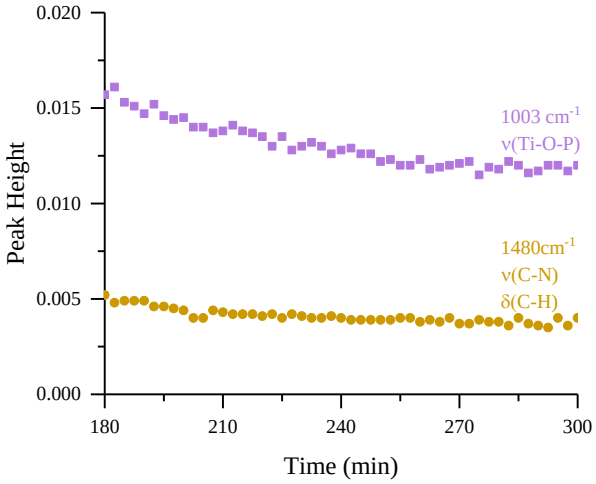

Figure 4.15 Changes to nucleotide peak height desorption of the ca. 1003 cm^{-1} ν(Ti-O-P) (purple) and ca. 1486 cm^{-1} ν(C-N), δ(C-H) (gold) onto TiO_2 at pH 5 for two component system

a) dGMP-dTMP noncomplementary, b) dAMP-dCMP noncomplementary, c) dGMP-dCMP complementary, and d) dAMP-dTMP complementary base pairs.

Chapter 5. Distinguishing Different Surface Interactions for Nucleotides Adsorbed onto Hematite and Goethite Particle Surfaces Through ATR-FTIR Spectroscopy and DFT Calculations

5.1 Abstract

Geochemical mineral interfaces can impact the fate and transport of environmental aqueous species. In this study, we investigate the surface chemistry of adsorbed nucleotides on two mineral surfaces, hematite and goethite using infrared spectroscopy and density functional theory (DFT) calculations. Attenuated total reflectance-Fourier transform infrared spectroscopy is used to probe the adsorption of individual deoxyadenosine monophosphate, deoxyguanosine monophosphate, deoxycytidine monophosphate and deoxythymidine monophosphate onto either hematite or goethite particle surfaces. Results show preferential adsorption of the phosphate group to either surface. Remarkably, the surface chemistry of the four adsorbed nucleotides onto hematite have similar experimental phosphate spectral shapes while having distinctly different spectral features on goethite. The experimentally measured frequencies for the phosphate region frequencies were compared to DFT calculations for nucleotides adsorbed in either a monodentate or bidentate bridging coordination through the phosphate group to a binuclear Fe cluster. Overall, our results show that monodentate is favored on goethite whereas a bidentate bridging complex is favored on hematite, regardless of nucleotide derivative.

5.2 Introduction

Geochemical mineral surfaces, such as goethite, can represent 50-70% of the total surface area in soils when they form coatings on other minerals. In fact, goethite is the most abundant iron oxyhydroxide and can represent 1-5 wt% in soils.[62,187] Hematite, is a common soil component and can be found in river waters and mineral dust.[188,189] Both goethite and hematite particles can have

large surface to volume ratios and act as excellent sorbents, simultaneously changing the physicochemical properties of the particle surfaces and affecting bioavailability of important elements, including phosphorous.

Previous studies have probed the interactions of oxyanions on both iron oxide and iron oxyhydroxide surfaces.[62,63,76,151,159] In general, it is found that surface coverage is a strong function of pH. Lower pH favors higher adsorbed compounds due to electrostatic attraction between the negatively charged oxyanion and positively charged surface.[65,76] Additionally, complexation at surfaces is a function of pH. Elzinga et al. probed phosphate adsorption onto hematite as a function of pH to measure different surface interactions. There is a mixture of binding modes present on the surface for the pH range investigated between 3.5 to 8.9.[65] These authors concluded that the dominant coordination to the surface between pH 3.5 to 7.0 was a protonated monodentate structure at high surface coverages whereas between pH 8.5-9.0, a deprotonated monodentate structure was present. For goethite, phosphate shows a deprotonated bidentate complex between pH 4-6, both deprotonated bidentate and a monoprotonated monodentate adsorbates between pH 7.5-7.9 and a deprotonated monodentate species at pH 12.8. These earlier studies show that iron mineral surface chemistry depends on solution phase pH, as well as and surface composition and structure.

Insights into potentially different complexation modes can facilitated by combining DFT calculations with experimental data. For example, Kubicki et al. investigated surface complexes of oxyanions with various iron and aluminum minerals by comparing experimental frequencies with DFT-calculated frequencies of binuclear metal clusters.[61] Notably, phosphate complexation with goethite demonstrated a pH dependence whereby a protonated bidentate species was dominant under acidic conditions and deprotonated monodentate was present for basic conditions.

The authors compared their results to similar studies by Arai and Sparks[66] and Persson et al.[190] with differing results due to non-identical experimental methods and particle synthesis procedures, suggesting that surface adsorption depends on different surface planes and particle size.[191–193] In particular, differences in particle synthesis, composition and morphology can result in lattice and edge defects that then lead to preferential adsorption on specific planes.[194] In a different study by Kubicki et al., the adsorption energies on different lattice planes were determined using Gaussian 16 calculations and different surface complexation modes for phosphate adsorbed onto goethite. The results suggested that an inner-sphere bidentate coordination was favored and preferential on the (101) and (100) plane but unfavorable on (001). Monodentate coordination was preferential on the (210) and (001) planes.

These studies for relatively simple inorganic oxyanions show that the chemistry on surfaces is highly complex and is not fully understood because complexation modes are dependent on multiple factors. The adsorption of even more complex molecules has just begun to be explored.[18,52,115,195] The availability of biomolecules and essential nutrients in solution is heavily impacted by adsorption. Additionally, large biomacromolecular structures, like DNA, have been shown to be stabilized on surfaces with increased persistence in aqueous environments through different biomes, providing a source of genetic information for gene transfer.[127] The conformation of DNA is related to the preferential adsorption of the phosphate backbone to various mineral surfaces. Martinez et al. adsorbed DNA onto goethite and were able to show that there was no change to DNA form which retained the B-form conformation that is measured in solution.[95] When Sit et al. adsorbed DNA onto hematite, the solution phase B-form conformation changed to show the Z-form upon adsorption.[106] However, a study aimed towards understanding the surface chemistry between the phosphate backbone and different iron-containing minerals has yet to be

done. To build complexity into the oxyanion phosphate but for a simpler adsorbate than DNA, a study of the monomeric units of DNA, the nucleotide, is a good place to start. From such studies, knowledge of how these important building blocks interact with particle surfaces can lay the foundation for larger macromolecules. Previous studies have shown that deoxyadenosine monophosphate preferentially binds to metal oxide surfaces, such as anatase, rutile and alumina, via the phosphate group rather than the ribose and nitrogenous rings.[76,156,171,177] However, these surfaces are not as common in the environment as iron oxides and oxyhydroxides. In terms of environmental relevance, nucleotides, and environmental DNA (or eDNA) can be readily found in aqueous systems through active cellular secretion or apoptosis.

In this study, we probe the adsorption of four different nucleotides: deoxyadenosine monophosphate (dAMP), deoxyguanosine monophosphate (dGMP), deoxycytidine monophosphate (dCMP), and deoxythymidine monophosphate (dTMP) on either hematite or goethite particle surfaces using attenuated total reflectance-Fourier transform infrared (ATR-FTIR) spectroscopy as an experimental probe. We compare the phosphate experimental frequencies to ab-initio frequencies for monodentate or bidentate biding modes on a binuclear iron cluster. We find definitive evidence that all four nucleotides have similar coordination modes on each of the particle surface types interrogated but that the coordination mode differs for goethite compared to hematite.

5.3 Experimental Methods

5.3.1 Materials

2’-deoxyadenosine-5’-monophopshate (dAMP), 2’-deoxyguanosine-5’-monophosphate (dGMP), 2’-deoxycytidine-5’-monophosphate (dCMP), 2’-deoxythmidine-5’-monophosphate

(dTMP), sodium chloride, 1N hydrochloric acid, and 1N sodium hydroxide were purchase from Sigma-Aldrich. Hematite and goethite particles were purchased from Alfa Aesar, MA.

5.3.2 Particle Characterization

The crystalline phase of iron oxide particles was determined with X-ray diffraction using an APEX II ultra-diffractometer with Mo Kα radiation at $\lambda = 0.70930$ Å. To determine the primary iron oxide particle sizes, an aqueous suspension of a 0.01 g/L was sonicated with a probe sonicator for 60 seconds in a room temperature water bath. Afterwards, a 15 uL aliquot was drop casted onto a formvar/carbon-coated 100 mesh copper grid and dried. The copper grid was imaged using an 80 kV JEOL-1400 Plus transmission electron microscope. Particle sizes were analyzed using ImageJ software for more than 70 particles. Specific surface area was determined using a Quantachrome Nova 4200e N2 adsorption isotherm under liquid nitrogen. Samples were first degassed at 80 ℃ for 18 hrs and a 15-multipoint isotherm was collected between P/P_0 of 0.05-0.95.

5.3.3 Attenuated Total Reflectance Fourier Transform Infrared (ATR-FTIR) Spectroscopy

The ATR-FTIR spectroscopy apparatus has been previously described.[18,43,76,106] Briefly, ATR-FTIR spectroscopy is based on the total internal reflection of an infrared beam at the interface between a high index medium (ATR crystal) and low index medium (aqueous sample). The reflection of the infrared beam at the interface creates an exponentially decaying evanescent wave that propagates into the sample where absorption of light occurs. The ATR accessory was a horizontal flow cell equipped with an amorphous material transmitting IR radiation (AMTIR) crystal. The infrared spectrophotometer is a Nicolet iS10 FTIR (Thermo-Fisher) equipped with a mercury cadmium telluride detector (MCT/A). Spectra were collected at a resolution of 4 cm^{-1}

averaged over 100 scans in the spectra range of 750 to 4000 cm^{-1}. All ATR-FTIR spectra were collected with OMNIC 9 software and linearly baseline corrected between 900 to 1800 cm^{-1}.

For single component solution phase spectra, separate solutions of 2 mM dAMP, 2 mM dGMP, 2 mM dCMP, and 2mM dTMP were prepared in 10mM NaCl and titrated to pH 5 using NaOH or HCl. A solution of 2mM dAMP was pipetted onto the ATMIR crystal and a spectrum was collected using a background of 10mM NaCl. Similar solution phase spectra were collected for the other three nucleotides.

For single component adsorption on hematite particles, a particle film was prepared by sonicating 2.5 mg α-Fe_2O_3 in 700 uL of Milli-Q water and drop casting the colloidal suspension onto the AMTIR crystal. The suspension was left to dry overnight resulting in a uniform particle film. A solution of 10mM NaCl at pH 5 was flowed over the film using a peristaltic pump at ~1 mL/min to remove loose particles and collect a background spectrum. A 20 uM nucleotide solution in 10 mM NaCl titrated to pH 5 was flowed over the film for 180 minutes. To facilitate desorption, a solution of 10 mM NaCl was flowed over the film at pH 5. Spectra were collected at increments of 2.5 minutes. This was done for all four nucleotides. The same method was performed for single component adsorption on goethite particle surfaces using 2.5 mg α-FeOOH.

5.3.4 DFT Calculations

Model complexes of dAMP bonded to an iron surface as: a bidentate complex [$Fe_2(OH_4)(OH_2)_4$dAMP·$(H_2O)_6$] and a monodentate complex [$Fe_2(OH_4)(OH_2)_5$dAMP·$(H_2O)_6$] were constructed. The iron clusters have six explicit H_2O molecules to represent hydrogen bonding interactions. Modeled clusters were energy minimized without symmetry or geometrical constraints with B3LYP functionals[196,197] and the 6-31G(d) basis set using Gaussian 16.[198] Frequencies were scaled by a factor of 0.960.[199]

5.4 Results and Discussion

5.4.1 Particle Characterization

Hematite particles have been previously characterized.[195] Briefly, α-Fe_2O_3 was confirmed hematite with XRD with particle size of 5-20 nm and specific surface area of 75.7 ± 8.2 m^2g^{-1}. Goethite particle phase was confirmed with XRD, with an average particle size of 388.5 ± 167.4 nm by 87.1 ± 28.8 nm (**Figure 5.7**). Specific surface area was measured to be 37.5 ± 12.1 m^2g^{-1}.

5.4.2 Analysis of Solution and Adsorbed Spectra

Figure 5.1 shows the molecular structures of the fully protonated forms of dAMP, dGMP, dCMP and dTMP along with the pK_a values of the phosphate group and nitrogenous rings. dAMP

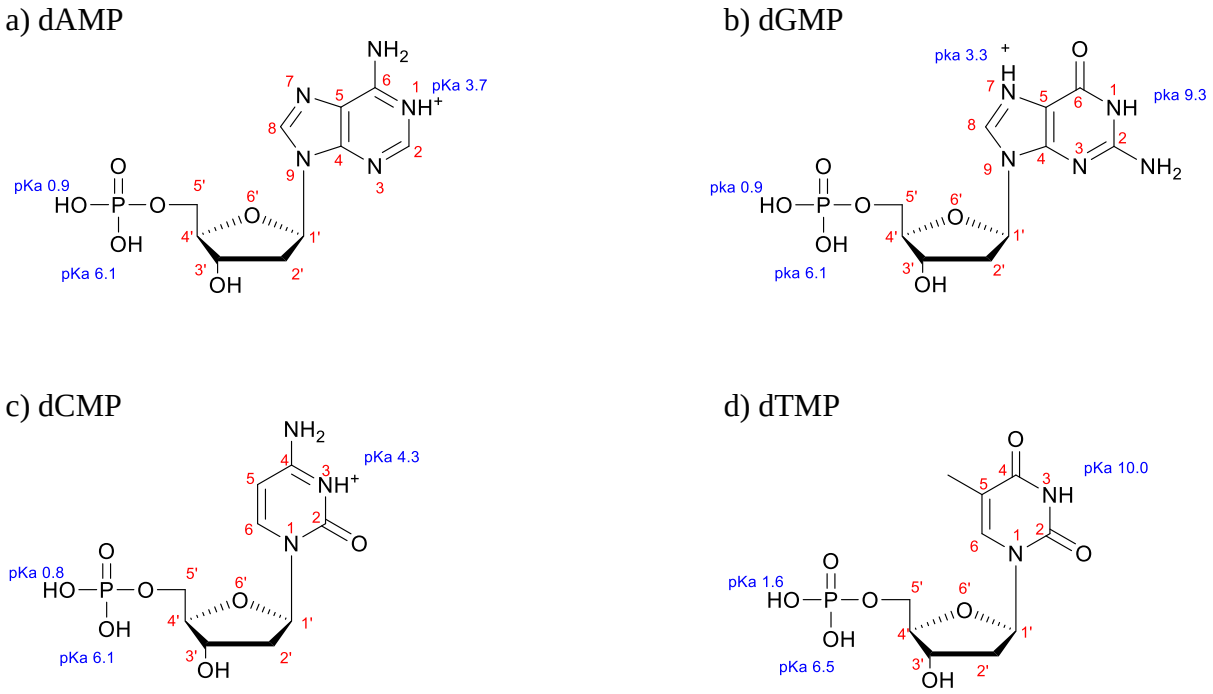

Figure 5.1 Nucleotide molecular structures

Molecular structures for a) deoxyadenosine monophosphate (dAMP), b) deoxyguanosine monophosphate (dGMP), c) deoxycytidine monophosphate (dCMP), and d) deoxythymidine monophosphate (dTMP) with pK_a values.

and dGMP are comprised of a purine ring while dCMP and dTMP contain a pyrimidine ring. The speciation of all four nucleotides at pH 5 is listed in **Table 5.1** At pH 5, the major form of all four

nucleotides is a monovalent anionic form with minor contributions from a zwitterionic and divalent anionic species. These negatively charged nucleotides are reflected in the zeta potential

Table 5.1 Nucleotide speciation table at pH 5

Speciation table for deoxyadenosine monophosphate (dAMP), deoxyguanosine monophosphate (dGMP), deoxycytidine monophosphate (dCMP), and deoxythymidine monophosphate (dTMP) at pH 5 using Henderson-Hasselbalch.

	$dX^{+}MP^{-}$	$dXMP^{-}$	$dXMP^{-2}$
dAMP	4.4	88.6	7.0
dGMP	1.8	91.0	7.2
dCMP	15.6	78.2	6.2
dTMP	0.0	96.9	3.1

measurements that range from -6 to -9 mV for all four nucleotides (**Table 5.2**). Solution phase spectral features are discussed in deeper detail elsewhere. Briefly, absorption in the region between 1200 to 1800 cm^{-1} can be assigned to the nucleoside group whereas features in the 900 to 1200 cm^{-1} range can be attributed to the phosphate group. Between all four nucleotides, the 1200 to 1800 cm^{-1} region is spectrally unique, whereas the 900 to 1200 cm^{-1} region can be similar because the phosphate group pK_a's are identical.

The solution phase spectra can be compared to adsorbed spectra and any spectral differences can be attributed to nucleotide interactions with the particle surface. **Figure 5.2** shows the temporal adsorption spectra for purine nucleotides on both hematite and goethite particles. Vibrational mode assignments can be found in (**Tables 5.3** and **Table 5.4**).[200] We observe a significant increase in intensity when the nucleotides are adsorbed onto either surface when compared to solution. The adsorbed spectra intensities are 30x larger than in the solution, despite the 100 times higher solution phase concentration. Consequently, the spectra are dominated by the adsorbed nucleotides with minimal contributions from solution phase species. When comparing the dAMP nucleoside 1200 to 1800 cm^{-1} region in solution to adsorbed spectra on either hematite or goethite, there is minimal peak shifting or broadening. However, there is a surface induced deprotonation of the nucleoside, as noted by the disappearance of the 1710 cm^{-1} $N1H^{+}$ feature upon

adsorption to both hematite and goethite particles. This has been previously observed on anatase and hematite particles.[76] For dGMP, minimal spectral differences are observed in the nucleoside region, upon adsorption onto either hematite or goethite. When the nucleotides are adsorbed onto hematite or goethite, the 900-1200 cm^{-1} phosphate region broadens and undergoes peak shifting. Previous studies have observed the preferential adsorption of the phosphate group over the nitrogenous nucleobases to various surfaces for nucleotides, oligonucleotides, and DNA.[76,95,106,115] This suggests that the nucleotides are directly bound to the iron surfaces via the phosphate group.

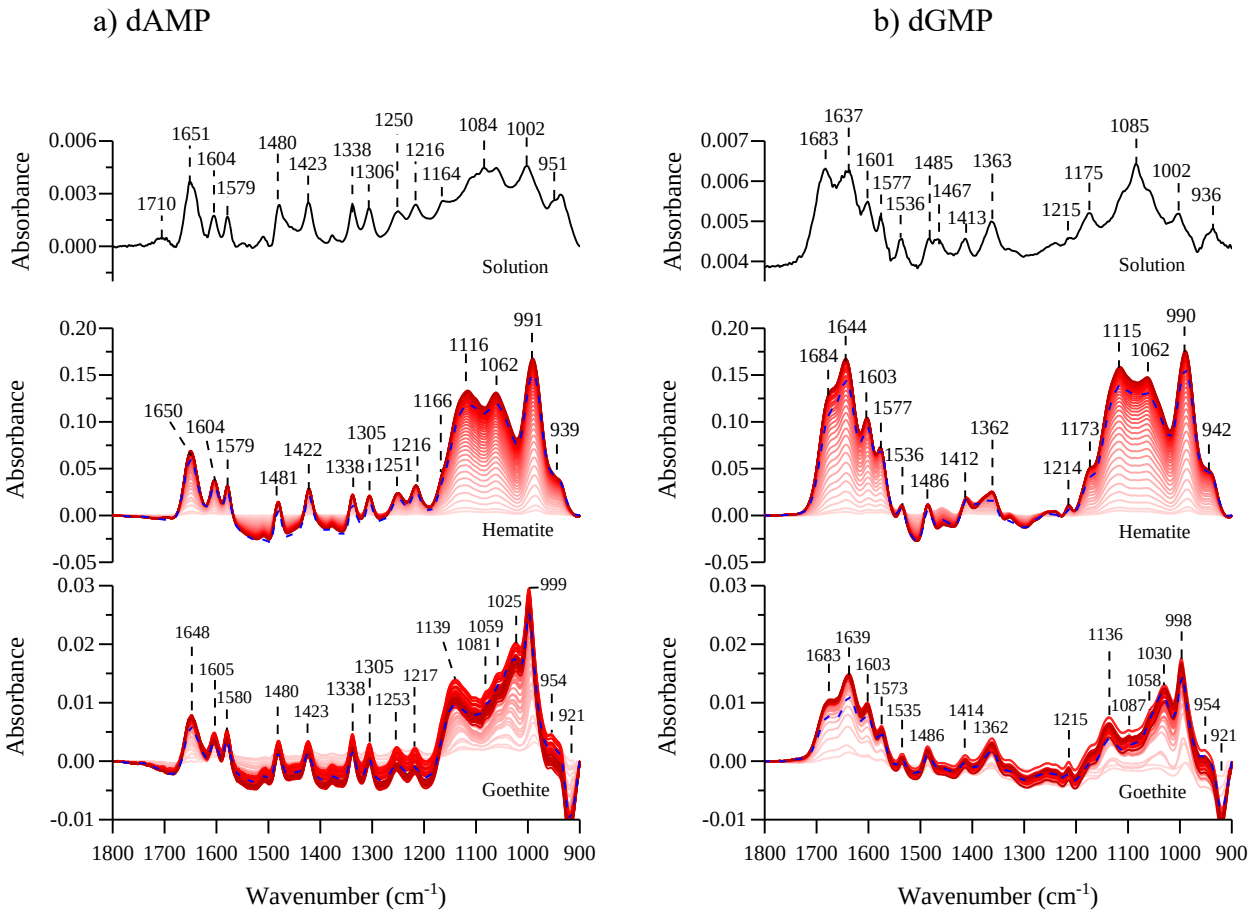

Figure 5.2 ATR-FTIR purine nucleotide spectra

a) dAMP and b) dGMP in solution (top), adsorbed on hematite (middle), and adsorbed on goethite (bottom). For adsorbed spectra, lighter red color spectra represent earlier time points where darker lines represent later time points and blue dotted line represents the desorption spectrum.

Figure 5.3 shows the pyrimidine ATR-FTIR nucleotide spectra in solution and adsorbed onto hematite or goethite. When the nucleoside regions are compared between solution and adsorbed on either particle surface for both nucleotides, there are minimal differences. Interestingly, dCMP does not undergo a nucleoside deprotonation, as was observed for dAMP. Surface induced deprotonation for dAMP but not for dCMP has been previously observed on anatase particles. Similar to what was observed for the purine nucleotides, the adsorbed phosphate absorption bands between 900 to 1200 cm^{-1} are broadened and shifted compared to the solution

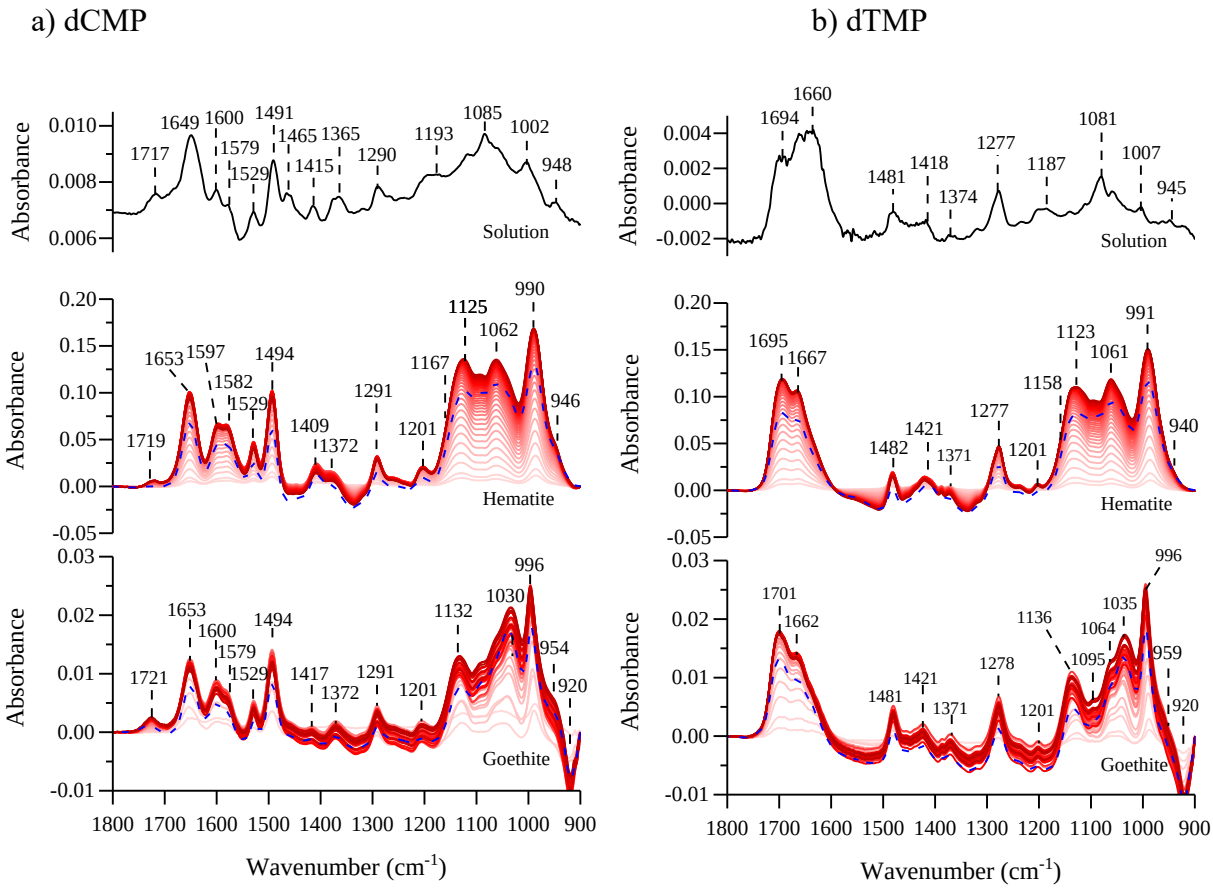

Figure 5.3 ATR-FTIR pyrimidine nucleotide spectra

a) dCMP and b) dTMP in solution (top), adsorbed on hematite (middle), and adsorbed on goethite (bottom). For adsorbed spectra, lighter red color spectra represent earlier time points where darker lines represent later time points and blue dotted line represents the desorption spectrum.

spectra. Similar conclusions can be made about the pyrimidine nucleotides being directly bound to the iron surfaces via the phosphate group.

a) Adsorbed on Hematite

b) Adsorbed on Goethite

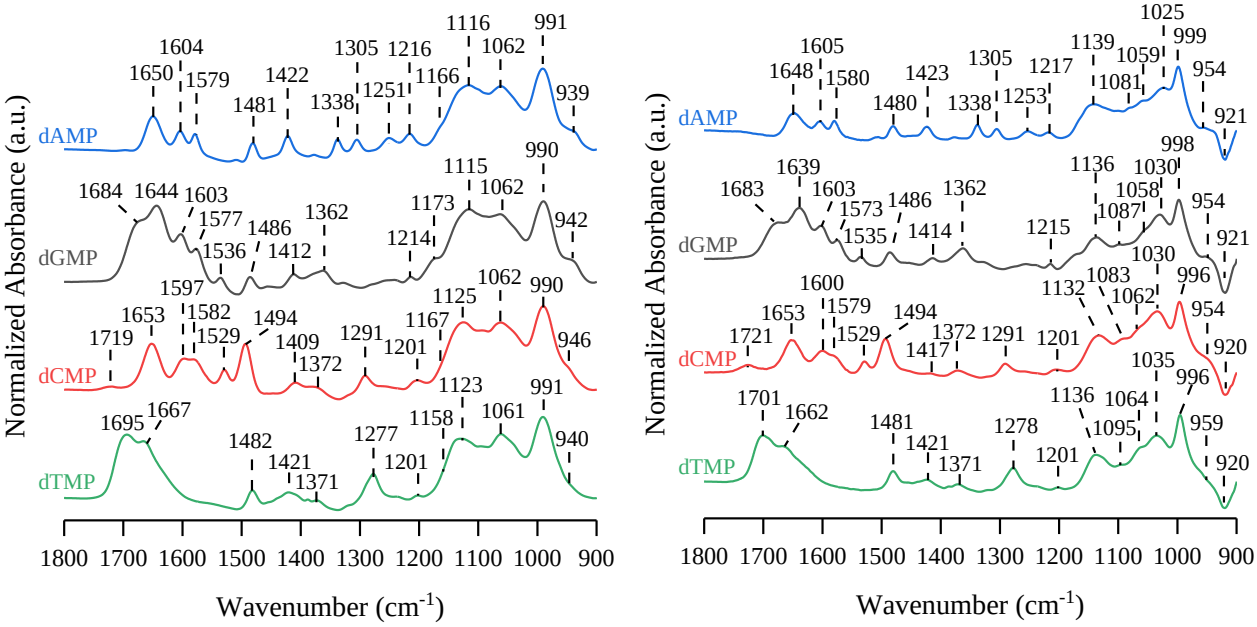

Figure 5.4 ATR-FTIR normalized spectra of dAMP, dGMP, dCMP and dTMP adsorbed onto a) hematite and b) goethite after 180 minutes of adsorption

An expanded view of the phosphate spectral region is shown in **Figure 5.4**, providing more insight into the surface chemistry of the directly bound phosphate group to the hematite or goethite surface. On hematite, the phosphate region spectral shape is similar for all four nucleotides with five major peak contributions: 1158-1173, 1115-1125, 1061-1062, 990-991, and 939-946 cm^{-1}. On goethite, the phosphate region has similar spectral shapes for all four nucleotides with six major peak contributions: 1132-1139, 1081-1095, 1058-1064, 1025-1035, 996-999, and 954-959 cm^{-1}. Interestingly, hematite has five major peaks whereas goethite has six major peaks. The fewer number of major peaks on hematite suggest an increase in phosphate symmetry and increased degeneracy. Also of significance is that when the phosphate region is compared between hematite

and goethite particles, the regions are found to be spectrally distinct. Sit et al. singly adsorbed nucleotides on TiO_2 and the phosphate regions manifested similar spectral shapes regardless of the nucleobase derivative. Adsorbed phosphate has been reported to contain a mixture of monodentate and bidentate binding modes on metal oxides where the relative distribution of binding modes are particle composition and facet dependent.[62,65,76] Because the phosphate spectral band shapes are different between the two particles, this would suggest there is a corresponding difference in complexation modes to the surface and additional analysis is needed to identify the relevant binding modes.

5.4.3 Comparison of Calculated to Experimental Phosphate Frequencies

Ab-initio calculations were carried out to better understand the adsorption of nucleotides and the reason for the differences between hematite and goethite spectra. Since all nucleotide spectra look similar on each of the surfaces, we have investigated only one of the nucleotides, dAMP, bound to a binuclear iron cluster in two different coordination states: an inner-sphere monodentate complex and a bidentate bridging complex as shown in **Figure 5.5**. dAMP was used as the model nucleotide as it can be compared to previous literature reports. The use of small metal clusters to model binding modes has been previously done with success and a similar approach is employed here.[61] During the optimization process, the unbound iron in the monodentate complex changed from 6-fold to 5-fold symmetry. Six explicit water molecules were added to the model to hydrate the phosphate and iron cluster. A previous study found that increasing coordinating waters from 6 to 18 did not significant change the resulting spectrum, so six water molecules were used in the calculation here.[156] Additionally, since the goal is to model the phosphate binding mode, the

coordinating water hydrated the phosphate and iron oxide cluster. The calculated spectra can be found in **Figure 5.8**.

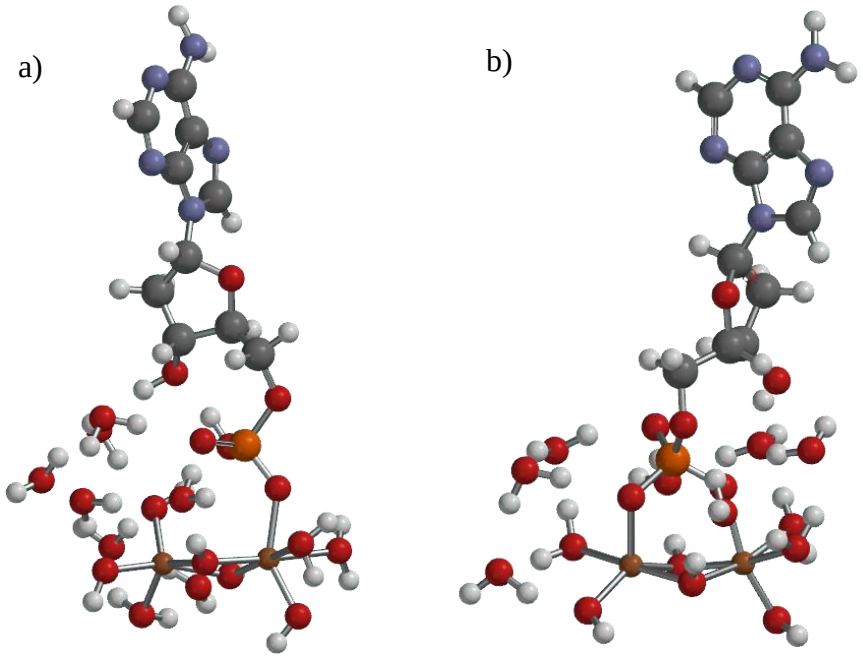

Figure 5.5 DFT calculated structures for dAMP adsorbed onto iron cluster in a) monodentate and b) bidentate binding modes

Atom colors are the following: carbon (gray), hydrogen (white), nitrogen (blue), oxygen (white), phosphorous (orange), and iron (dark orange).

The calculated monodentate dAMP phosphate region frequencies can be compared to both experimental hematite and goethite frequencies. The same can be done with bidentate dAMP phosphate frequencies. A comparison between calculated (scaled) and experimental peak positions can be found in **Figure 5.6**. Three criteria were used to determine the best fit for each dominant surface complexation mode: (i) slope closest to 1; (ii) best linear fit as determined by R^2 and; (iii) y-intercept closest to 0. For hematite (**Figure 5.6a**), both monodentate and bidentate bridging have nearly identical R^2 of 0.989 and 0.987, respectively. Since the slope and y-intercept are a better fit for the bidentate bridging, using the criteria given above, the dominant binding mode for hematite is determined to be bidentate bridging. For goethite (**Figure 5.6b**), the fitting parameters suggest

that monodentate is the dominant binding mode. The computational results indicate that the different particle surfaces give rise to different coordination modes for the relevant nucleotides.

a) Hematite b) Goethite

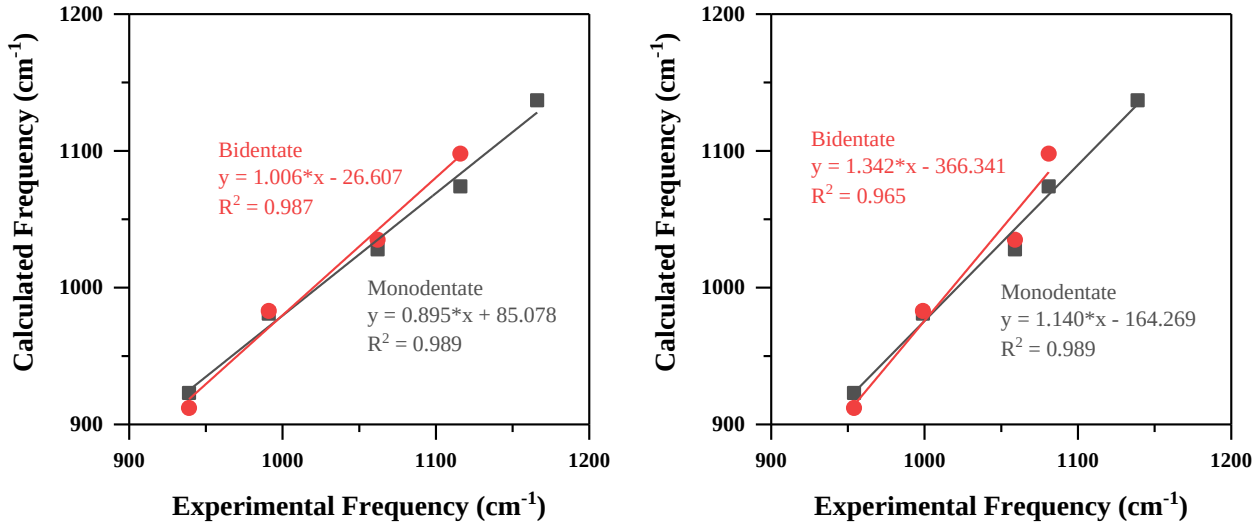

Figure 5.6 Correlation between ATR-FTIR experimental and Gaussian calculated frequencies for adsorbed dAMP

a) hematite and b) goethite in monodentate or bidentate bridging complex in the phosphate region of 900-1200 cm^{-1}

However, many previous studies have mentioned that there is often a mixture of binding modes on particle surfaces for a given set of conditions.[65,66] The imperfect fitting parameters observed in our study could be due to the presence of multiple binding modes that are manifested in the experimental frequencies. Moreover, many of these studies investigated inorganic phosphate adsorption on hematite or goethite while few studies have addressed nucleotide adsorption with an emphasis on probing the surface chemistry. Having a nucleoside attached to the phosphate group while complexed with a surface can break molecular symmetry, resulting in differences with previous literature observations. Past studies centered on inorganic phosphates with pK_a values that correspond to a tri-valent group with a higher pK_{a2} (7.2) than dAMP (pK_a = 6.1).[61] The third pK_a for the tri-valent inorganic phosphate is so large (pKa_3 = 12.4) that it is not relevant under

these conditions. This could lead to apparent differences between the assigned surface complexation disagreements from literature due to phosphate deprotonation for model surface complexes. As a consequence of phosphate deprotonation in the nucleotides studied here, differences in the assigned surface complexation modes from pervious literature reports may arise. However, what is clear from our results is that the surface chemistries are similar for all four nucleotides adsorbed on either hematite or goethite but are particle compositionally unique. These results taken all together show that surface interactions and complexation with nucleotides are different for these two phases of iron-mineral particle surfaces.

5.5 Conclusions

Herein, we have combined experimental spectroscopic data and ab-initio calculations to show that the interaction of selected nucleotides on two iron-mineral surfaces, goethite and hematite, is different. A monodentate binding mode is preferential on goethite while a bidentate mode is favored on hematite. This study provides a framework towards a more complete understanding regarding the behavior of more complex macromolecules, like DNA, by investigating the surface chemistry of the monomeric, nucleotide subunits.

5.6 Acknowledgements

Chapter 5, in full, has been submitted for publication of the material as it may appear in Journal of Physical Chemistry A. Sit, I.; Young, M. A.; Kubicki, J. D.; Grassian, V. H. Distinguishing Different Surface Interactions for Nucleotides Adsorbed onto Hematite and Goethite Particle Surfaces Through ATR-FTIR Spectroscopy and Ab-Initio Calculations. The dissertation author is the first author of this paper.

5.7 Supplemental Information

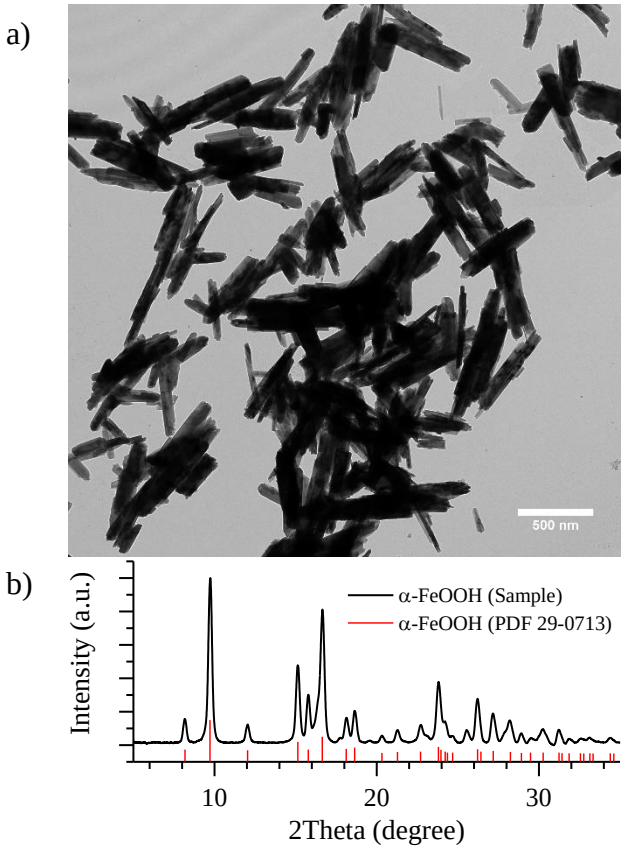

Figure 5.7 Goethite particle characterization

a) TEM micrograph of goethite particles and b) XRD data of experimental goethite with reference goethite reference lines.

Table 5.2 Zeta potential measurements for monophosphate nucleotides at pH 5

	Zeta Potential (mV)
dAMP	-9.1 ± 1.8
dGMP	-6.0 ± 1.2
dCMP	-8.5 ± 1.8
dTMP	-6.1 ± 3.6

Table 5.3 ATR-FTIR peak assignment table purine nucleotides, dAMP and dGMP, in solution and adsorbed on hematite particles and goethite particles

Vibrational modes[a]	Vibrational Frequency (cm^{-1})					
	Solution[200]		Adsorbed on Hematite		Adsorbed on Goethite	
	dAMP	dGMP	dAMP (Δ)[b]	dGMP (Δ)[b]	dAMP (Δ)[b]	dGMP (Δ)[b]
$\delta(NH^+)$	1710					
ν(C=O)		1683		1684 (+1)		1683 (+0)
δ(HOH)	1651	1637	1650 (-1)	1644 (+2)	1648 (-3)	1639 (+2)
purine ring	1604	1601	1604 (+0)	1603 (+3)	1605 (+1)	1603 (+3)
purine ring	1579	1577	1579 (+0)	1577 (+1)	1580 (+1)	1575 (+1)
purine ring		1536		1536 (-1)		1535 (-1)
ν(C-N), δ(C-H)	1480	1485	1481 (+1)	1486 (-1)	1480 (+0)	1486 (-1)
purine ring		1467				
$\delta(CH_2)$	1423	1413	1422 (-1)	1412 (+1)	1423 (+0)	1414 (+1)
purine ring	1338	1363	1338 (+0)	1362 (+4)	1338 (+0)	1362 (+4)
purine ring	1306		1305 (-1)		1305 (-1)	
$\delta(C6\text{-}NH_2)$	1250		1251 (+1)		1253 (+3)	
ν(N9-C1')	1216	1215	1216 (-1)	1214 (-1)	1217 (+1)	1215 (+0)
bidentate/monodentate			1166	1173		
bidentate/monodentate			1116	1115	1139	1136
bidentate/monodentate					1081	1087
bidentate/monodentate			1062	1062	1059	1058
bidentate/monodentate					1025	1030
ν(P-O)	1002	1002				
ν(Fe-O-P)			991	990	999	998
δ(POH)	951	949				
$\nu_s(P\text{-}(OFe)_2)$ of bidentate complexes			939	942	954	954

[a] $\nu_{s/as}$: symmetric/asymmetric stretch vibration; δ: bending vibration

[b] Δ: difference between adsorbed and solution phase wavenumber at last time point collected

Table 5.4 ATR-FTIR peak assignment table pyrimidine nucleotides, dCMP and dTMP, in solution and adsorbed on hematite particles and goethite particles

Vibrational modes[a]	Vibrational Frequency (cm^{-1})					
	Solution[200]		Adsorbed on Hematite		Adsorbed on Goethite	
	dCMP	dTMP	dCMP (Δ)[b]	dTMP (Δ)[b]	dCMP (Δ)[b]	dTMP (Δ)[b]
$\delta(N3H^+)$	1717		1719 (+2)		1721 (+1)	
ν(C2=O2)		1694		1695 (+1)		1701 (+7)
δ(HOH)	1649	1660	1653 (+4)	1667 (+3)	1653 (+4)	1662 (+2)
pyrmidine ring	1600		1597 (-3)		1600 (+0)	
pyrmidine ring	1577		1582 (+5)		1579 (+2)	
pyrmidine ring	1529		1529 (+0)		1529 (+0)	
ν(C-N), δ(C-H)	1491	1481	1494 (+3)	1482 (+1)	1494 (+3)	1481 (+0)
$\delta(CH_2)$	1415	1418	1409 (-6)	1421 (+3)	1417 (+2)	1421 (+3)
pyrimidine ring	1365	1374	1372 (+7)	1371 (+3)	1372 (+7)	1371 (+3)
pyrmidine ring	1290		1291 (+1)		1291 (+1)	
pyrmidine ring		1277		1277 (+0)		1278 (+1)
ν(N9-C1')	1201	1203	1201 (+0)	1201 (-2)	1201 (+0)	1201 (-2)
bidentate/monodentate			1167	1158		
bidentate/monodentate			1125	1128	1132	1136
bidentate/monodentate					1083	1094
bidentate/monodentate			1062	1061	1062	1064
bidentate/monodentate					1030	1035
ν(P-O)	1002	1007				
ν(Fe-O-P)			990	991	996	996
δ(POH)	948	945				
$\nu_s(P\text{-}(OFe)_2)$ of bidentate complexes			946	940	954	959

[a] $\nu_{s/as}$: symmetric/asymmetric stretch vibration; δ: bending vibration

[b] Δ: difference between adsorbed and solution phase wavenumber at last time point

a) Monodentate

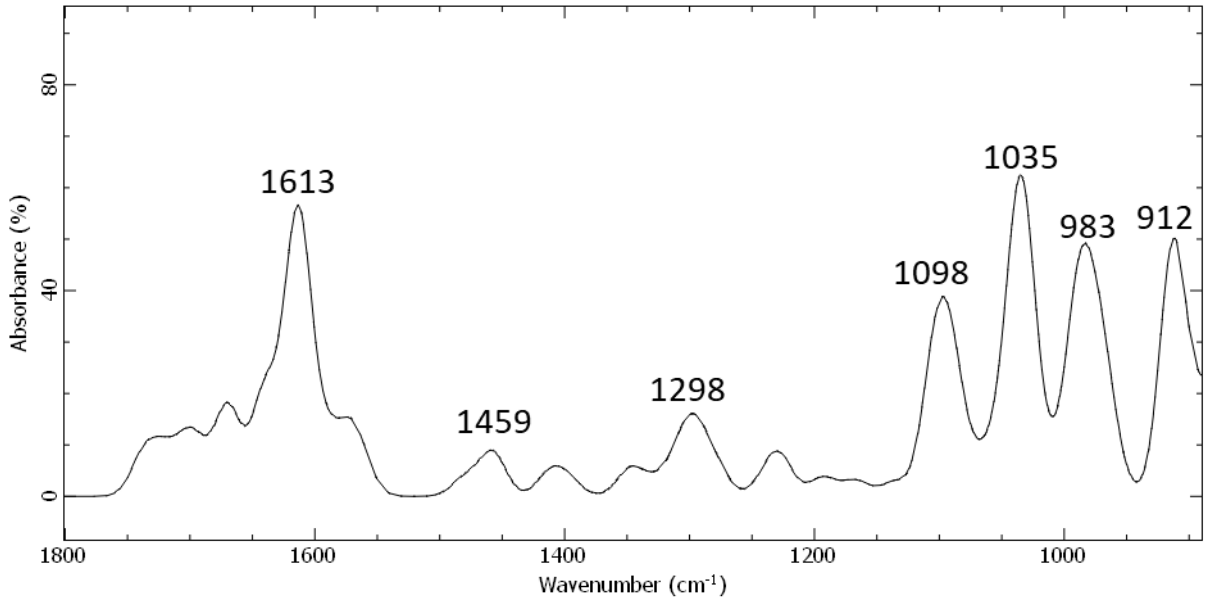

b) Bidentate

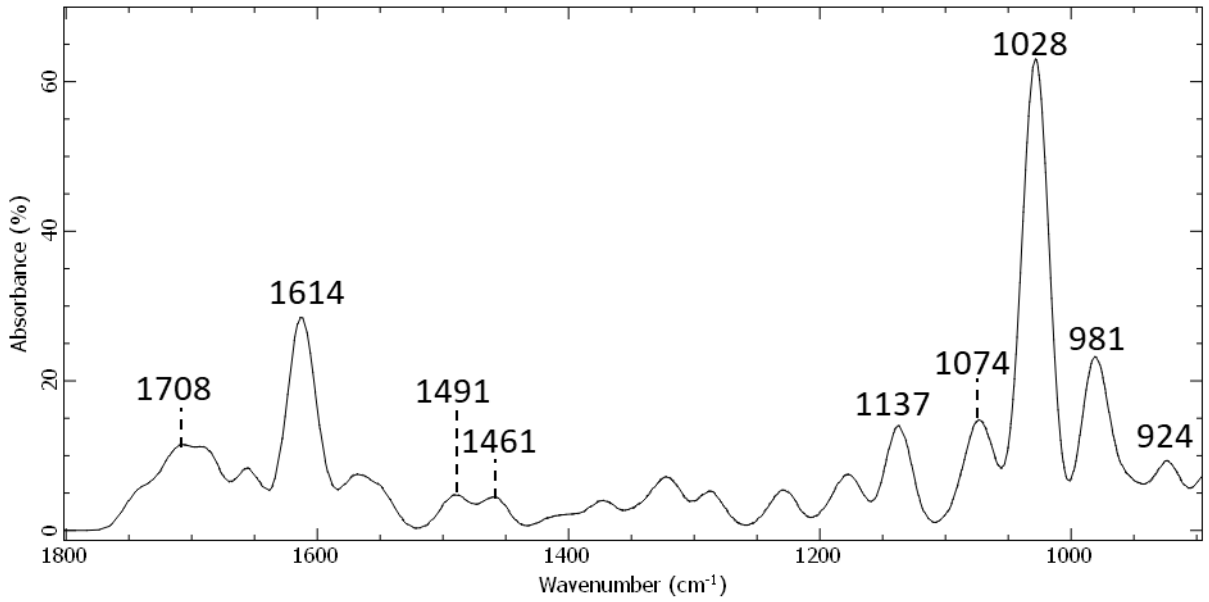

Figure 5.8 Ab-initio Gaussian calculations for dAMP adsorbed onto an iron cluster in a) monodentate and b) bidentate complex

Vibrational frequencies were scaled by 0.960.

Chapter 6. Formic and Acetic Acid pK_a Values Increase Under Nanoconfinement in Porous Silica

6.1 Abstract

Organic acids are prevalent in the environment and their acidity and the corresponding dissociation constants can change under varying environmental conditions. The impact of nanoconfinement on physicochemical properties of chemical species is poorly understood and is an emerging field of study. In this experimental investigation, we quantify the effect of nanoconfinement on one of the fundamental chemical reactions - the dissociation of acids. We used infrared and Raman spectroscopies to assess the pK_a constants of formic and acetic acids confined within silica nanopores with 4 nm diameters. We observe a decrease in acid dissociation constants (increase in the pK_a values) when acids are nanoconfined. Therefore, nanoconfinement stabilizes the protonated species. We attribute this observation to the decrease in the average dielectric response of nanoconfined aqueous solutions where the spatial rearrangement of the conjugate base and proton may be hindered. Additionally, the increased hydrogen bonding in nanoconfined conditions leads to a stabilization of the protonated form, resulting in an increase in pK_a value. Overall, the results of this study provide the first quantification of the pK_a values for nanoconfined formic and acetic acids and pave the way for a unifying theory predicting the impact of nanoconfinement on acid-base chemistry.

6.2 Introduction

Porous engineered and geochemical particles are commonly found in the environment and often have large surface to volume ratios that can sequester significant amounts of chemical species present in aqueous systems and facilitate their transformations at the solid-water interfaces inside nanopores. Many of these particles are silicates (e.g., pure minerals or sedimentary rocks and soils)

with pores that reach nano-scale dimensions. Theoretical, computational, and experimental studies have shown that nanoconfinement of a solid-water interface can often lead to unexpected chemical reactivities: increase in gas solubilities[201], enhanced chemisorption reactions[202–204], and lower chemical reaction barriers[205]. These deviations in reactivity when compared to unconfined counterparts have been tentatively explained by the disruption of the H-bonding network within nanopores and the decreases in water's properties: dielectric response[206], melting point[207], density[207,208], surface tension[207,208], and H_2O dissociation constant[209], when compared to bulk solution.[203,207,210–212] Here we hypothesize that the changes to the local H-bonding environments and dielectric response inside silica nanopores affect the dissociation constants of water-soluble organic acids.

Nanoconfinement effects on chemistry are poorly understood and constitute an emerging research field. So far very few studies of nanoconfinement effects on acidity indicate that in highly charged clay mineral interlayers, acidity of water increases by ~ 4 orders of magnitud.[209] Similarly, recent study by Zhu et al. show that the local pH inside silica nanopores is lowered, compared to adjacent bulk solution, due to selective uptake of protons inside the negatively charged pores.[213] Again, lower pH is reported for silica nanopores functionalized with 2-(dimethylamino)ethyl methacrylate (DMAEMA) and 2-(metacryloyloxy)ethyl phosphate (MEP) polymers, which was attributed to an increase in the deprotonation of these surface-bound species under nanoconfinement.[5] Additionally, Rubinovich et al. observed the equilibrium constants for the hybridization of single stranded DNA are shifted towards undissociated complexes in nanoconfined conditions due to entropic stabilization of these large molecules inside nanochannels.[214] These limited studies on acidity in nanopores indicate that de-protonation reactions may be enhanced under nanoconfinement, especially for those nanopores that have a

negative surface change. However, our results contradict this extrapolation and are in line with the observation for air-water interfaces, where protonated forms of organic acids are stabilized.[215] Currently, there is no fundamental understanding of how acid dissociation is affected by nanoconfinement. Environmentally relevant molecules, such as organic acids, humic substances, nucleotides, and DNA, have one or more acid dissociation constants and therefore understanding the impact of nanoconfinement on various types of acidic groups is urgently needed.

For these reasons, here we quantify the effect of nanoconfinement on the pK_a values for simple organic acids, formic and acetic acids (**Equation 6.1** and **6.2)**. Formic and acetic acids can be found in the environment from cellular processes cycle, fermentation and are the main

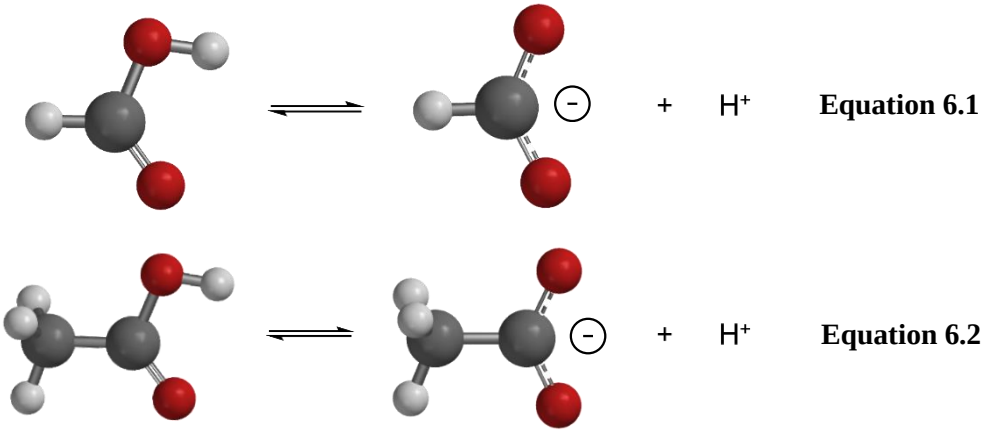

constituents of volatile organic acids.[216,217] These organic acids are also involved in many industrial processes like paper manufacturing, metal ore mining, and food production that can be in chemical runoff and introduced into aqueous environmental systems.[218,219] Additionally, many environmentally prevalent organic molecules, biomolecules and humic substances contain one or more carboxylic acid functional groups, and their deprotonation can be sensitive to nanoconfinement. These small organic acids can be used as convenient model systems to begin the investigation in an important field of study that could have large implications, acid-base chemistry in nanopores.

In this study, formic and acetic acids were nanoconfined in porous silica with 4 nm pore diameters. Acid dissociation constants for solutions and in nanoconfined in silica pores were determined using two vibrational spectroscopic methods, infrared and Raman spectroscopy. The dissociation constants quantified for acid solutions spectroscopically were also compared to potentiometric measurements. As a proof of concept, we show that vibrational spectroscopy can be used to experimentally determine acid dissociation constants in solution and in nanoconfined matrices. In addition to acid dissociation constants, vibrational spectroscopy can be used to gain insight into the intermolecular interactions within the nanoporous silica. This paper provides the framework for future studies to probe more complex molecules and milieu to model realistic systems.

6.3 Materials and Methods

6.3.1 Materials

Formic acid and glacial acetic acid were purchased from Fisher Scientific. Templated SBA-15 silica (SiO_2) with 4 nm pores was purchased from Sigma Aldrich. Silica particles were washed in de-ionized H_2O and dried at 40 ºC prior to use, as in our earlier work.[202,203,207] This treatment produced nanoporous SiO_2 surfaces with an average Si-OH site density of 1.8-2.0 -OH nm^{-2}.[202,203,207] 6N (certified 5.95 to 6.05N), 1 N HCl (certified 0.995 to 1.005N) and 1N NaOH titrants (certified 0.995 to 1.005N) were purchased from Fisher. 18N and 6N NaOH titrant was prepared using sodium hydroxide pellets (Fisher) and milliQ water. pH 1.68, 4 and 7 reference standards for calibrating the pH electrode were purchased from Fisher. All solutions were prepared using milliQ water with a resistivity of ≥ 18.2 MΩ-cm.

6.3.2 Solution preparation

25mM formic acid and 25mM acetic acid solutions were prepared. pH was measured and titrated using an OAKTON pH 700 meter equipped with a temperature probe. Three-point pH electrode calibration using pH 1.68, 4, and 7 reference standards were performed daily. 6N HCl, 6N NaOH, 1N HCl, and 1N NaOH were used to titrate solutions. Higher concentration of titrants was used to minimize solution dilution, which never fell below 24.6mM.

6.3.3 Attenuated Total Reflectance-Fourier Transform Infrared Spectroscopy

The ATR-FTIR spectroscopy set-up has been previously described.[18,43,76,106] ATR-FTIR spectroscopy is based off the total internal reflection of an infrared beam between the optically dense medium (ATR crystal) and an optically rare medium (sample). This reflection at the interface creates an evanescent wave that propagates into the sample where absorption of infrared light occurs. The ATR accessory is a horizontal flow cell equipped with an amorphous material transmitting IR radiation (AMTIR) crystal. The IR spectra were collected using a Nicolet iS10 FTIR spectrometer (Thermo-Fisher) equipped with a mercury cadmium telluride detector (MCT/A). Spectral resolution was 4 cm^{-1} and averaged over 100 scans over the range of 750-4000 cm^{-1}. All spectra were processed using OMNIC 9 software. Spectra were collected after a 30-minute purge with filtered CO_2-free air.

For solution phase spectra of formic acid, a solution of 25 mM formic acid was prepared and titrated to pH ranging from 2-6. ~800 uL of the titrated solution was pipetted onto the AMTIR crystal and a spectrum was taken. A spectrum of milliQ water without pH adjustment was used as the background. A similar method was used for 25 mM acetic acid solution titrated to pH ranging from 2-7.

For collecting spectra of nanoconfined formic acid, a suspension containing 10 mg of SiO_2 in 800 uL milliQ water was prepared and sonicated for 30 seconds to create a colloidal suspension. The solution was drop casted onto the AMTIR crystal and dried overnight with filtered CO_2-free air. To begin the 700 uL milliQ water was pipetted onto the SiO_2 film and a background spectrum was collected. The film was washed with 700 uL of 25 mM pH adjusted formic acid solution. The washing solution was removed and another 700 uL of 25 mM formic acid solution was pipetted onto the film and a sample spectrum was collected. A similar method was used to collect spectra of nanoconfined 25 mM acetic acid.

To determine the pK_a value of both the bulk solution as well as of nanoconfined formic acid, the intensity of ν(C=O) and $\nu_{as}(COO^-)$ vibrational bands were used since they represent the protonated and deprotonated formic acid forms, respectively. A linear baseline was used to determine peak heights (intensities). At pH 2, ν(C=O) was considered to represent the 98.3 mol % of the expected protonated form, while at pH 6, $\nu_{as}(COO^-)$ was considered to represent 99.4 mol % of deprotonated form determined by Henderson-Hasselbalch equation using a reported pK_a value of 3.75.[220–222] The protonated intensities were normalized to the intensity measured at pH 2 while the deprotonated intensities were normalized to that measured at pH 6, yielding a percentage of either protonated or deprotonated formic acid. Boltzmann functions were fit to the two measured species percentages, and the pK_a value was determined at the intersection of the lines fitted to the data points for protonated and deprotonated forms. The same method was used to determine the pK_a of 25 mM acetic acid solution (bulk phase and nanoconfined in SiO_2 pores). The intensity measured at pH 2 ν(C=O) was considered to represent the 99.8 mol % of protonated form, and at pH 7 $\nu_{as}(COO^-)$ to represent the 99.4 mol % of deprotonated form, calculated using the reported pK_a value of 4.75.[222–224]

6.3.4 Raman Spectroscopy

Raman spectra were collected using a Horiba XploRA plus Raman spectrometer with a cooled CCD detector (Jobin Yvon's Synapse camera). A HeNe laser was used with a 532 nm excitation and ~10 mW radiation power. A 10x microscope objective lens was used with a laser spot diameter of ~3 μm.

For solution formic acid measurements, 500 mM formic acid was prepared and titrated between pH 2 and pH 6 using 18 N NaOH or 6 N HCl solutions. Raman spectra were collected with a grating size of 1800nm, 5 accumulation and 20 s acquisition time. A similar calculation was done as ATR-FTIR to determine a pK_a value. The same procedure and pK_a calculation were done for 500 mM acetic acid between pH 2 and pH 7.

For nanoconfined formic acid measurements, solution of 7.5 mg/L SiO_2 and 500mM formic acid was titrated between pH 2 and pH 6 and equilibrated for 24 hrs at room temperature. The supernatant was discarded, and the resulting SiO_2-formic acid slurry was dabbed dry with a Kimwipe to remove excess solution and a Raman spectrum was collected while sample remained wet. Spectra were collected with a grating size of 1800nm, 15 accumulation and 60 s acquisition time. The same procedure was done for nanoconfined 500 mM acetic acid between pH 2 and pH 6.

6.3.5 Potentiometric Measurements

A solution of 25 mM formic acid was prepared using milliQ water. Certified 1 N NaOH was diluted to 0.1 N NaOH using milliQ water. 0.1 N NaOH was slowly added to the solution of 25 mM formic acid under stirring. After each addition of the titrant, the pH was measured. This was repeated until the pH did not change with further additions of the NaOH titrant. The pKa was determined to be the pH at half the volume used to reach the equivalence point using the 2nd

derivative x-intercept. The same procedure was used to determine pKa value for 25 mM acetic acid.

6.4 Results and Discussion

The pK_a values of formic and acetic acid solutions in bulk and nanoconfined conditions in SiO_2 nanopores were determined by monitoring ATR-FTIR and Raman characteristic band intensities of protonated and deprotonated forms. **Figure 6.1a-b** and **Figure 6.5** shows the ATR-FTIR spectra of formic acid solution between pH 2 and pH 6 and acetic acid solution between pH 2 and pH 7. The molecule is protonated at pH lower than the reported pK_a of the organic acid and deprotonated above the pK_a value. At the pK_a value, there are equimolar concentrations of protonated and deprotonated forms for a monoprotic molecule. For formic acid at pH 2, ATR-FTIR vibrational bands belonging to the protonated form are observed at 1718 and 1213 cm^{-1} which represent the ν(C=O) and δ(COH) modes, respectively.[225,226] As pH increases and formic acid deprotonates, the 1582, 1383 and 1351 cm^{-1} start to appear and grow in intensity. These absorption bands are assigned to the $\nu_{as}(COO^-)$, δ(CH), and $\nu_s(COO^-)$, respectively.[225,227,228] As the characteristic deprotonated bands appear, the characteristic protonated band disappear and become negligible at pH ≥ 5. The most pronounced changes in the intensities for the deprotonated and protonated forms occurs between pH 3-4, which agrees with the reported formic acid pK_a value of 3.75.[222,229,230] As formic acid deprotonates into formate, the ν(C=O) 1718 cm^{-1} peak intensity decreases while the 1582 cm^{-1} $\nu_{as}(COO^-)$ intensity increases.[228,231] These two characteristic peaks can be used to monitor the speciation form of the simple organic acid. Similar observations can be made about acetic acid spectra, the protonated peaks can be seen at 1712 and 1279 cm^{-1} assigned to the ν(C=O) and δ(COH) vibrational modes, respectively. As pH increases, the deprotonated peaks appear at 1552 and 1416 cm^{-1} assigned to $\nu_{as}(COO^-)$ and $\nu_s(COO^-)$, respectively. The most

pronounced changes in the spectra occur between pH 4-5, which agrees with the reported acetic pK_a value of 4.76.[222,223,232] The Raman spectra for solution phase formic and acetic acid have similar spectral responses to pH changes (**Figure 6.1c-d**). As pH increases for solution phase formic acid, the protonated bands represented by the 1721 cm^{-1} ν(C=O) and 712 cm^{-1} δ(COH) peak intensities decrease while the deprotonated 1353 cm^{-1} ν(COO^-) band intensity increases.[231] The

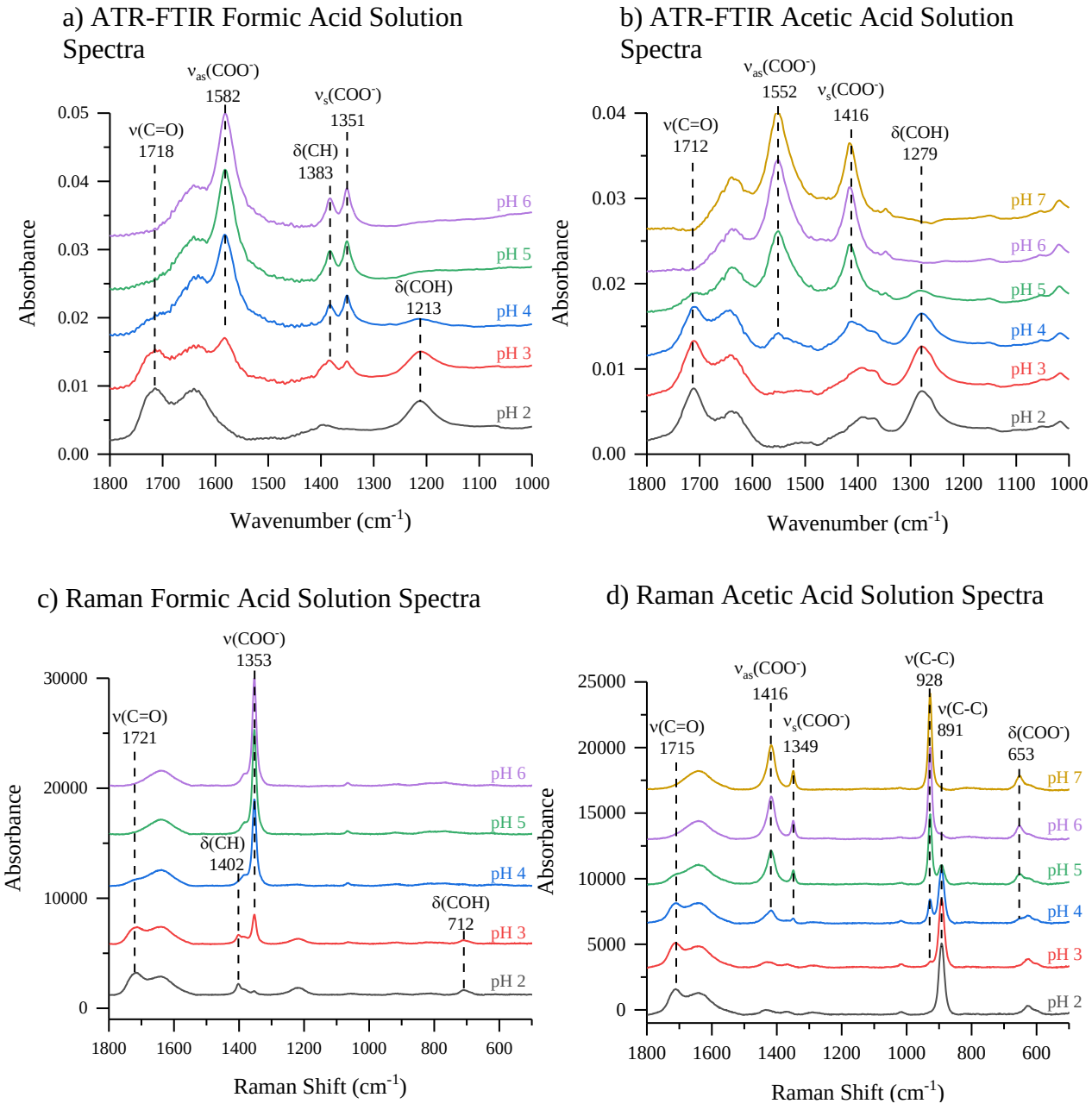

Figure 6.1. Solution spectra of a) ATR-FTIR formic acid, b) ATR-FTIR acetic acid, c) Raman formic acid, and d) Raman acetic acid

carboxylate band is very intense and when plotted on the same scale, swamps the δ(COH) band intensity. Significant spectral changes occur between pH 3 and pH 4, similar to what was observed

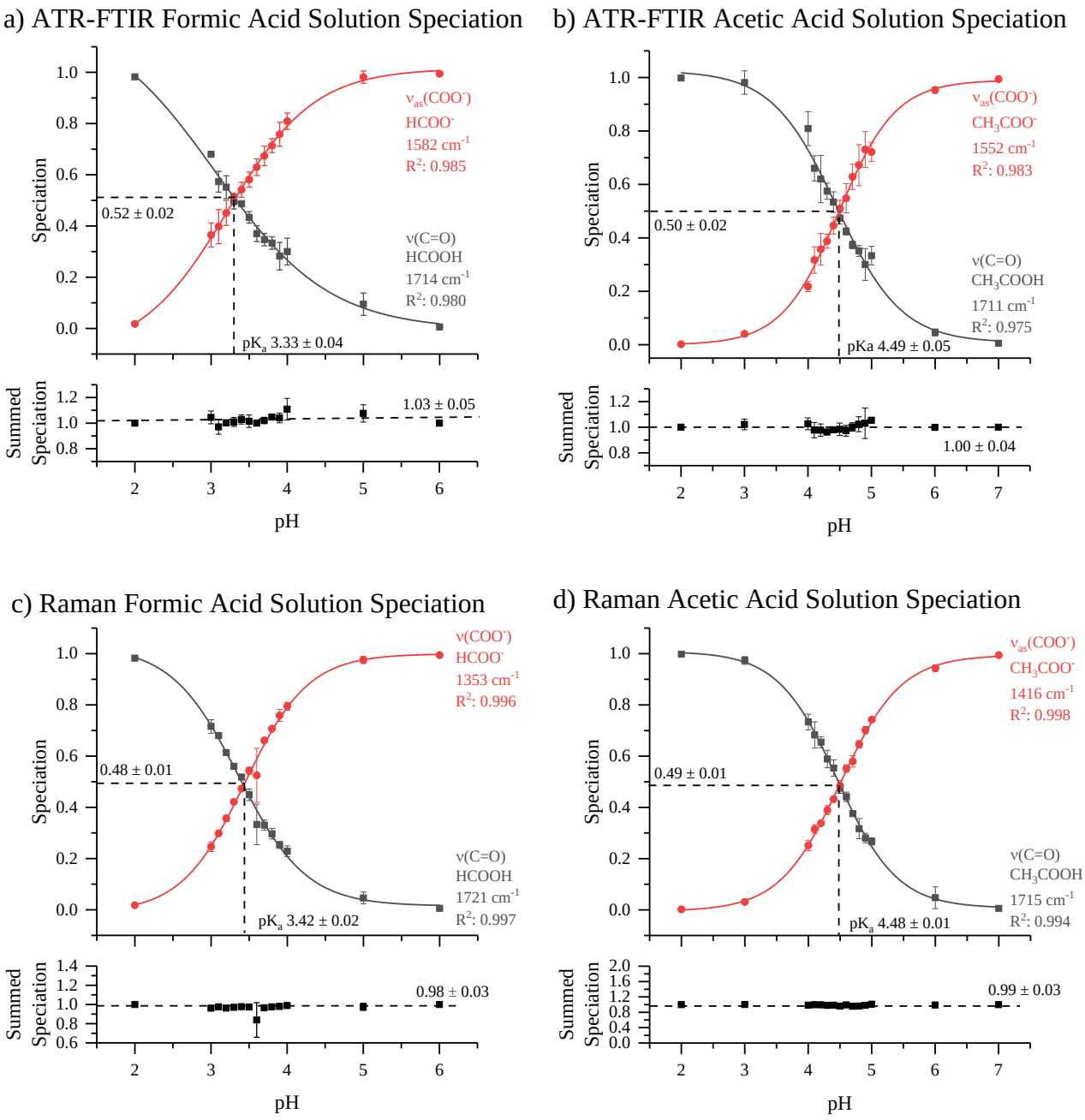

Figure 6.2 Solution phase speciation diagrams for formic and acetic acids using ATR-FTIR and Raman spectroscopy

Solution phase a) ATR-FTIR formic acid, b) ATR-FTIR acetic acid, c) Raman formic acid, and d) Raman acetic acid speciation curves using spectral peak intensities fitted with a Boltzmann function (top). Summed speciation for the protonated and deprotonated forms of organic acid (bottom). Error bars are 1σ.

in ATR-FTIR data. For solution phase acetic acid, as pH increases, the 1715 cm^{-1} ν(C=O) band and 891 cm^{-1} ν(C-C) decrease while the deprotonated carboxylate bands, 1416 cm^{-1} $\nu_{as}(COO^-)$, 1349 cm^{-1} $\nu_s(COO^-)$ and 928 cm^{-1} ν(C-C) bands increase. Again, significant spectra changes occur between pH 4 and pH 5.

Figure 6.6 shows ATR-FTIR and Raman spectral intensities for characteristic protonated and deprotonated peaks of formic and acetic acid solutions. For both organic acids, the highest intensity for the protonated form is observed at pH 2, whereas the highest intensity for the deprotonated form is observed at pH 6 or pH 7. Since these bands are considered characteristic, as the (de)protonated forms become the dominant species in the solution, peak intensities would also be dominant for their representative forms. However, since infrared absorption coefficients and Raman scattering cross-sections depend on specific vibrational modes, the data are normalized to reflect these differences. **Figure 6.2** shows a normalized speciation curve for formic and acetic acid at different pH values using characteristic vibrational bands for ATR-FTIR and Raman spectra. The intersection of the two fitted Boltzmann functions for the protonated and deprotonated forms correspond to the pK_a value of formic and acetic acid in solution. For formic acid, the intersection is 3.33 ± 0.04 and 3.42 ± 0.02 using ATR-FTIR and Raman spectra, respectively. For acetic acid, the intersection is 4.49 ± 0.05 and 4.48 ± 0.01 using ATR-FTIR and Raman spectra, respectively. As a measure of error, the intersection of the two Boltzmann functions should occur at 50 mol % protonated and 50 mol % deprotonated forms of the organic acids. Additionally, the summed speciation at each pH should be equal to one. There is negligible deviation from the ideal Boltzmann function intersection of 0.50 and a sum species average of 1.00 for both formic and acetic acid using ATR-FTIR and Raman spectroscopies. The Boltzmann fitting to the protonated and deprotonated speciation curves have R^2 values of ≥ 0.975 for both spectroscopic techniques

and both acids. Despite our measured solution pK_a values for formic and acetic acid deviating by 0.3-0.4 units from those reported in the literature, the values align well with potentiometric measurements performed in our laboratory (**Figure 6.7**), supporting that spectroscopic method can be used as an effective technique to determine molecular acid dissociation constants. As alkyl chain length increases, the acidity of the carboxylic acid decreases as the alkyl group destabilizes the carboxylate ion.[233] However, as the alkyl group lengthens, the inductive effect lessens as the added carbons are farther away from the carboxylate. This inductive effect is apparent at the difference in measured pK_a values for formic and acetic acid solutions of ca. one pH unit.

6.4.1 Effects of Nanoconfinement on Organic Acid Dissociation Constants

To explore the effects of nanoconfinement on acid pKa values, formic and acetic acid were introduced to a thin film of nanoporous SiO_2 particles. Using the same processing technique as bulk solution ATR-FTIR measurements, nanoconfined pK_a values can be determined. **Figure 6.3** shows ATR-FTIR and Raman spectra for nanoconfined formic and acetic acids. In general, (de)protonated peaks show the same response to increasing pH as was observed for bulk solutions, where protonated peaks disappear and deprotonated peaks appear. Peak shifting, changes to spectral intensities, and broadening and/or narrowing can be indicative of surface complexation when compared to solution spectra; as molecules ad sorb on SiO_2 surfaces inside nanopores, molecular symmetry can change leading to peak shifting or full width half max (FWHM) changes.[65,66] Additionally, if adsorption onto solid surface takes place, local concentrations are increased which can be observed in the significant increase in spectral intensities, sometimes as large as 100x.[76,106] However, this is not observed as measured ATR-FTIR intensities are similar for bulk solution samples and those in SiO_2 nanopores (**Figure 6.6** and **Figure 6.9**). For Raman intensities, the intensities measured for acids nanoconfined in silica pores are smaller than in

solution. Because of the absence of signal enhancement, we conclude that the organic acids are not complexing with the SiO_2 surfaces to any significant degree, and the majority of acids exist in the body of the nanopore. To show what the spectra would look like if the organic acids were

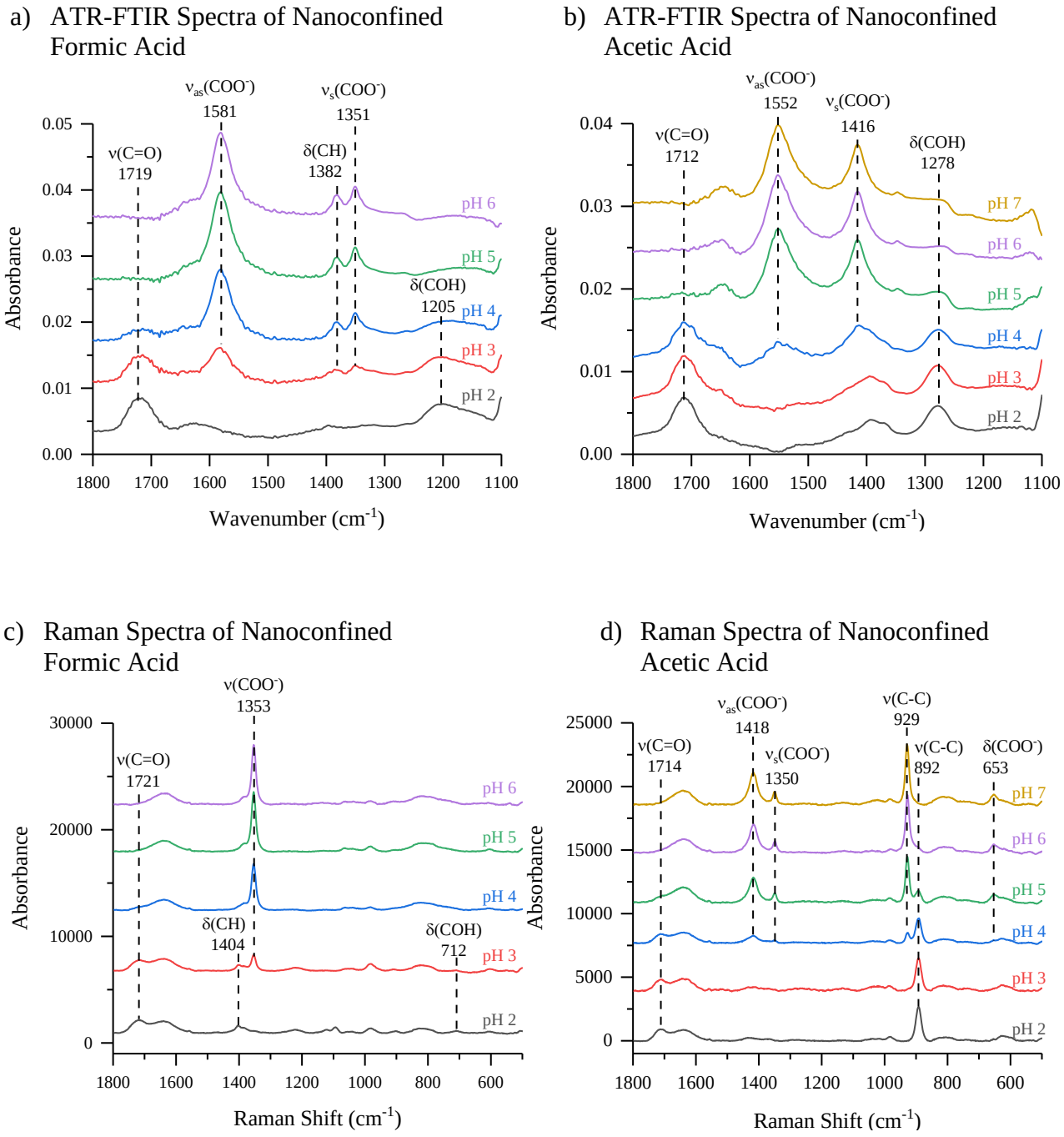

Figure 6.3 Nanoconfined spectra of a) ATR-FTIR formic acid, b) ATR-FTIR acetic acid, c) Raman formic acid, and d) Raman acetic acid

strongly adsorbed to the surface, acetic acid was adsorbed onto alumina at various pH values using ATR-FTIR spectroscopy (**Figure 6.10**). The spectra did not change despite varying the solution

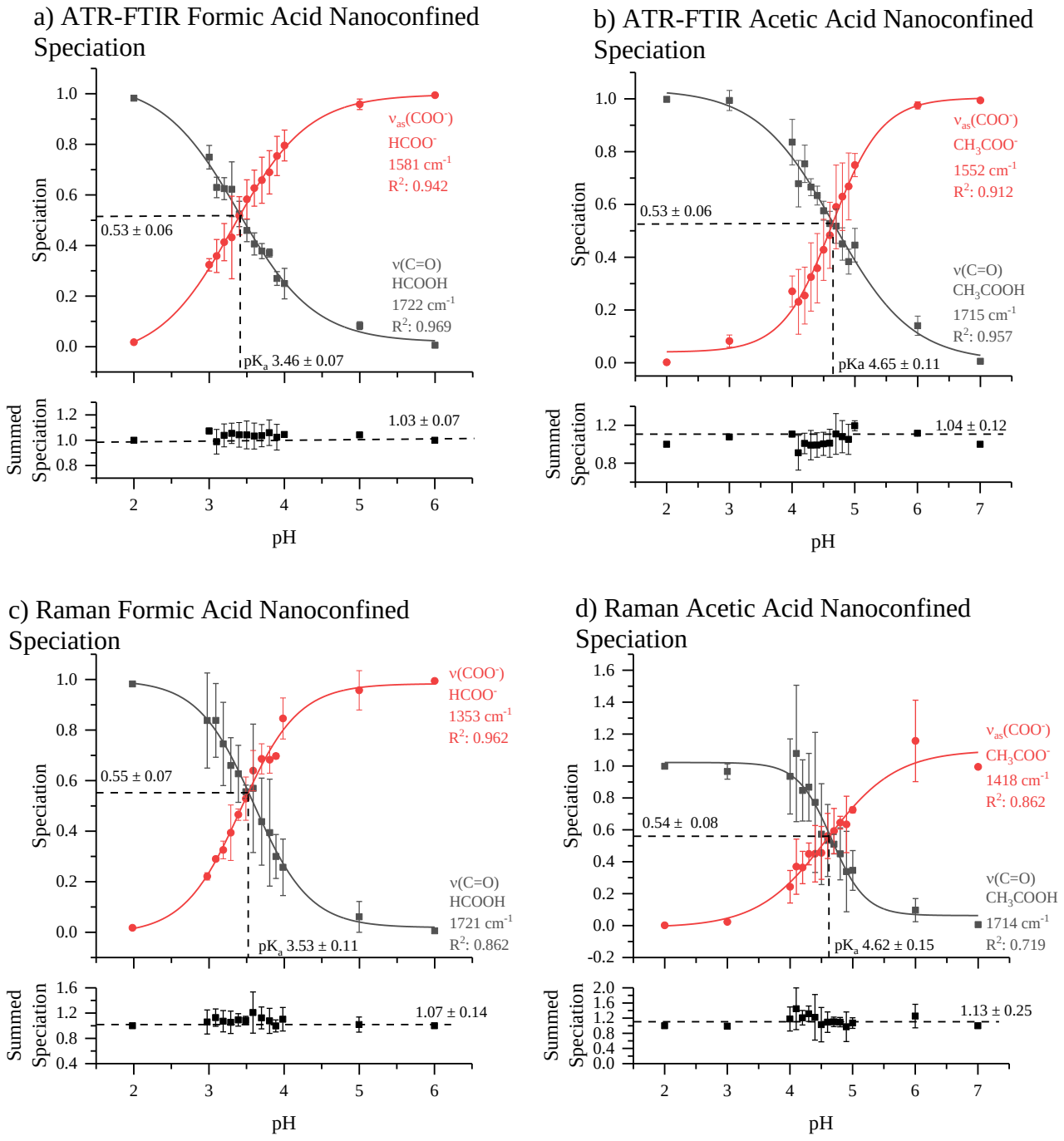

Figure 6.4 Nanoconfined speciation diagrams for formic and acetic acids using ATR-FTIR and Raman spectroscopy

Nanoconfined phase a) ATR-FTIR formic acid, b) ATR-FTIR acetic acid, c) Raman formic acid, and d) Raman acetic acid speciation curves using spectral peak intensities fitted with a Boltzmann function (top). Summed speciation for the protonated and deprotonated forms of organic acid (bottom). Error bars are 1σ

pH and showed peak shifting of the carboxylate peaks. In the case of formic and acetic acid nanoconfined in silica, spectral changes in response to changing pH was observed so the acids are not strongly adsorbed to the silica surface.

The nanoconfined spectra behave similarly to solution spectra in terms of decreasing intensities of the protonated bands and increasing intensities of de-protonated bands as pH

Table 6.1 Tabulated pK_a of solution and nanoconfined formic and acetic acid using ATR-FTIR and Raman spectroscopy

pK_a measurement summary of formic and acetic acid using spectroscopic solution intensities, and spectroscopic SiO_2 nanoconfined intensities. Error is 1σ.

	ATR-FTIR		Raman	
	Solution	**Nanoconfined**	**Solution**	**Nanoconfined**
Formic Acid pK_a	3.33 ± 0.04	3.46 ± 0.07	3.42 ± 0.02	3.53 ± 0.11
Acetic Acid pK_a	4.49 ± 0.05	4.65 ± 0.11	4.48 ± 0.01	4.62 ± 0.15

increases for both organic acids. However, the nanoconfined ATR-FTIR spectral intensities is ca. 30% of solution whereas Raman is ca. 50% of that measured in solution. Instead of the beam probing a volume of only organic acid and water, part of the sampled volume is being filled by silica, resulting in a lower concentration of acid molecules and lower intensity values. There is minimal peak shifting when solution and nanoconfined spectra are compared for either acid from both spectroscopic techniques. Additionally, the FWHM of protonated and deprotonated bands do not change significantly (data not shown).

Figure 6.4 shows the speciation curve for nanoconfined organic acids in SiO_2 nanopores using characteristic peak intensities of the protonated ν(C=O) band and deprotonated $\nu_{as}(COO^-)$ band (**Figure 6.9**). Tabulated pK_a values for vibrational measurements on solution and nanoconfined acids are shown in **Table 6.1**. Under nanoconfinement and using ATR-FTIR spectroscopy, formic acid has a pK_a value of 3.46 ± 0.07 and acetic acid has a pK_a value of 4.65 ± 0.11. Both pK_a values are higher than those in bulk solution by 0.13 (3.7%) and 0.16 (3.4%) pH units for formic and acetic acid, respectively. For pK_a values calculated using Raman spectroscopy

data, formic acid has a pK_a value of 3.53 ± 0.11 and acetic acid has a pK_a value of 4.62 ± 0.15. However, the R^2 fitting of the protonated and deprotonated Boltzmann functions vary drastically between ATR-FTIR and Raman results. The lowest ATR-FTIR R^2 fitting value is 0.912 which is for deprotonated acetic acid. The R^2 value for Raman speciation fittings for both acids are much lower and vary between 0.962 and 0.719, reducing confidence levels. The poor fitting could stem from inconsistent sampling or high solution concentration along with the drying process. The Raman spectra depends on the confocal focal plane and if there is an inconsistent amount of silica in spectra, the intensities will be inherently skewed. The concentration used for Raman spectra is 20x higher than used for ATR-FTIR. This get decent signal-to-noise in the spectra but it is possible that solution phase contributions swamped nanoconfined intensities. For these reasons along with a lower R^2 value for the Raman results, the ATR-FTIR results were considered to be more reliable and representative of a nanoconfined system. This suggests that the protonated forms of the organic acids are more stable compared to their deprotonated forms, resulting in a decrease in dissociation constants and increase in pKa values.

The increase in pK_a value under nanoconfinement suggests that the stabilization of the organic acid conjugate base is not as favorable. Gao et al. demonstrated an increase in carboxylic acid pK_a values in a confined nanochannel.[234] It was suggested that the decrease in dissociation stemmed from neighboring carboxylic groups having to overcome an electrostatic repulsion interaction from neighboring negatively charged carboxylate groups. Not only do the carboxylic groups have to overcome neighboring carboxylate charges, but also deprotonated silica surface charge; the point of zero charge for silica is around 4.2.[235,236] However, for electrostatic effects to be dominant, intermolecular interactions of organic acid-organic acid has to occur but this has not been observed in our study due to the low acid concentrations. It is recognized that formic and

acetic acids can polymerize to form linear or cyclic complexes.[237–239] However, this often occurs in gaseous phase or at very high concentrations (>5.25 M) of organic acid.[240,241] Yang et al. used Raman spectroscopy to monitor peak shifting in the OH stretch in a binary system of acetic acid-water as the volume fraction of the acid (V_{AA}) was varied.[241] Notable peak shifts begin at $V_{AA} > 0.30$ (~5.25 M). It was also noted that this was due to formation of linear dimers while $V_{AA} < 0.30$, hydrated monomers were the dominant species. Furthermore, another study concluded that the introduction of water into acetic acid cyclic dimer complexes, leads to water separated molecules, removing the hydrogen bonds formed in the dimer.[242]

For our study, $V_{AA} = 0.0014$ for ATR-FTIR and 0.035 for Raman spectroscopy, which is well below the onset of dimerization in solution. One could argue that under nanoconfinement, the organic acid could be sequestered or excluded from the pore, altering the volume fraction. However, the intensities of the characteristic solution and nanoconfined peaks are very similar (Figure S2 and S5). This suggests that the pores are not sequestering or excluding organic acids and that the solution concentration is similar to that of what is inside the pores. The caveat is that the V_{AA} onset of dimerization can be different under nanoconfinement than in solution, however, it would require the difference to be ~ 2 orders of magnitude. Thus, the interaction that is observed is of organic acid-water and <u>not</u> organic acid-organic acid nature. This means that electrostatic repulsion is not the dominant force for the observed increase in the pK_a values. Additionally, molecular size of non-solvated formic acid is approximately 3.4 Å and 4.9 Å for acetic acid.[243] The molecular size of solvated formic acid is approximately 11.4 Å and 12.5 Å for acetic acid.[243–245] The solvated sizes are rough estimations based on molecular sizes and distances. Both non-solvated and solvated sizes are significantly smaller than the 4 nm pores in this study, therefore we assume that steric effects are not dominant.

Under nanoconfinement, previous studies have shown that the dielectric response is significantly lowered ($\varepsilon = 2$)[206] compared to bulk water ($\varepsilon = 78$)[203,210,211]. Confined water molecules are more ordered (have less rotational freedom) and since nanopores are spatially limited, the density of dipoles is reduced.[207] These effects result in a reduced dielectric response for confined water. As the organic acid undergoes deprotonation in nanoconfined environments, the rearrangement and restructuring of water molecules to hydrate the conjugate base and proton is more difficult compared to hydrating the neutral acid. The reduced dielectric constant in a confined system could reduce the ability of water molecules to accept a proton from an organic acid, thus increasing the pK_a of the acid. Nie et al. used ab-initio calculations to show the increase in H-bond dissociation energy for carboxylic acids in protein interiors as the dielectric response of the media decreases.[246] The low dielectric environments enhance H-bonding interactions and are more stable than in higher dielectric media. This suggests that the deprotonation of carboxylic acids becomes more difficult in low dielectric media, thus explaining the observed increase in the pK_a value of two acids examined here. Moreover, Ilgen et al. found that the solvation energy of dissolved cations is decreased in a nanoconfined system compared to bulk solutions, which causes an increase in the inner-sphere complexation reactions within SiO_2 nanopores.[203] A reduction in the solvation energy of nanoconfined species could lead to increased complexation, including protonation of organic acids reported here. Adams et al. probed the transport of protons in confined reverse micelles as a function of size and acid concentration.[247] The authors reported an inability to execute a Grotthuss shuttling of protons due to the Eigen hydronium complex strong adsorption onto the polar surface. This causes a buildup of protons within confined environments and limits proton mobility suggesting that ability to deprotonate and transport a proton away through a

network of water molecules from an organic acid is hindered, stabilizing the acid. Zhu et al. investigated the pH difference between bulk solutions and within nanopores.[213] The authors concluded that the pH of nanopores can be lower than in bulk, due to selective uptake of proton into the pore volume. Additionally, the carbonyl and acidic proton have been shown to be the main active sites for hydrogen bonding.[248,249] Once the organic acids deprotonate, the electrons are delocalized in the carboxylate and the strong hydrogen bonding site is lost, reducing the stability of deprotonated acids. For these reasons, protonated organic acids are stabilized in nanopores, and is reflected in the increase of pK_a value under nanoconfined environments.

6.5 Conclusion

Nanoconfinement can significantly change molecular properties due to changes in the H-bonding structures and other characteristics of nanoconfined water. Using ATR-FTIR and Raman spectroscopies, acid dissociation constants for two small organic acids, formic and acetic acid, were experimentally determined. Under nanoconfinement, the pK_a of formic and acetic acids is increased, stabilizing the protonated form. This is most likely due to the reduced dielectric response of water and enhanced H-bonding interactions in nanoconfined environments, which makes deprotonation of organic acids more difficult. Additionally, the H-bonding interactions between the strong H-bonding sites of the C=O and OH group are lost when deprotonated. For these reasons, the stabilization of the protonated organic acid is reflected in the decrease in acid dissociation constant (increase in pK_a) under nanoconfined conditions.

6.6 Acknowledgements

Chapter 6, in full, has been submitted for publication of the material as it may appear in Environmental Science: Nano. Sit, I.; Grassian, V. H.; Ilgen, A. G. Formic and Acetic Acid pK_a Values Increase Under Nanoconfinement. The dissertation author is the first author of this paper.

6.7 Supplemental Information

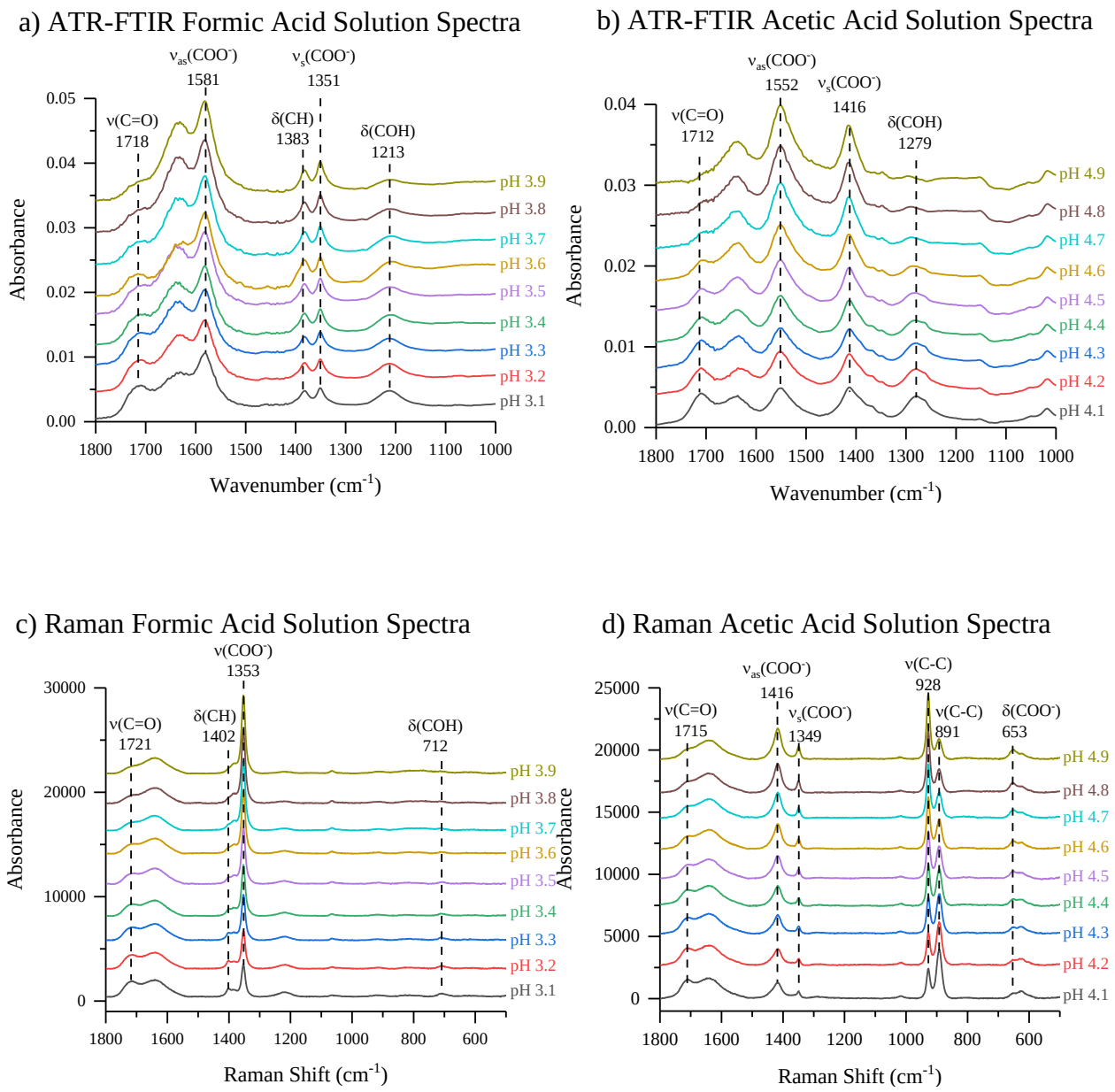

Figure 6.5 Solution spectra of a) ATR-FTIR formic acid, b) ATR-FTIR acetic acid, c) Raman formic acid, and d) Raman acetic acid

a) ATR-FTIR Formic Acid Solution Spectral Intensities

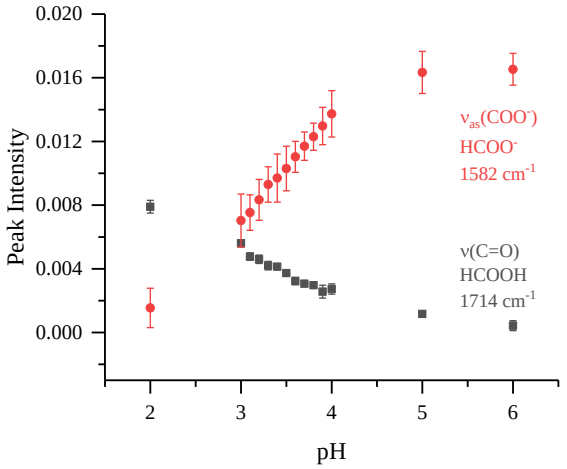

b) ATR-FTIR Acetic Acid Solution Spectral Intensities

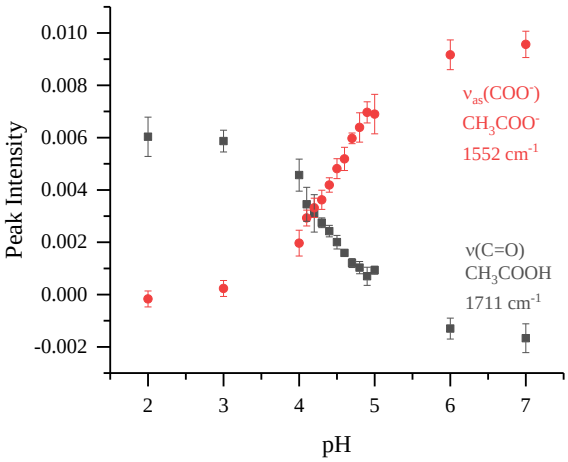

c) Raman Formic Acid Solution Spectral Intensities

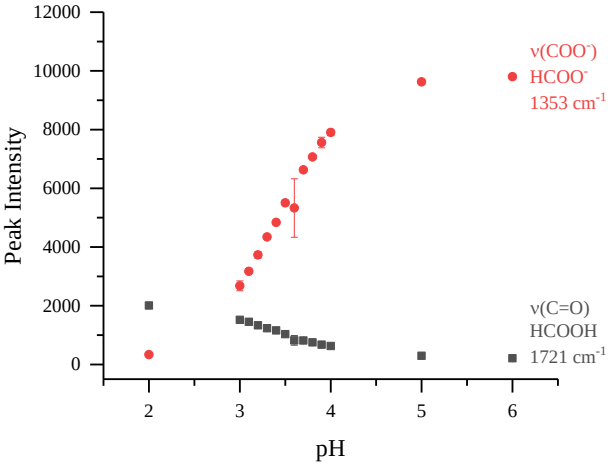

d) Raman Acetic Acid Solution Spectral Intensities

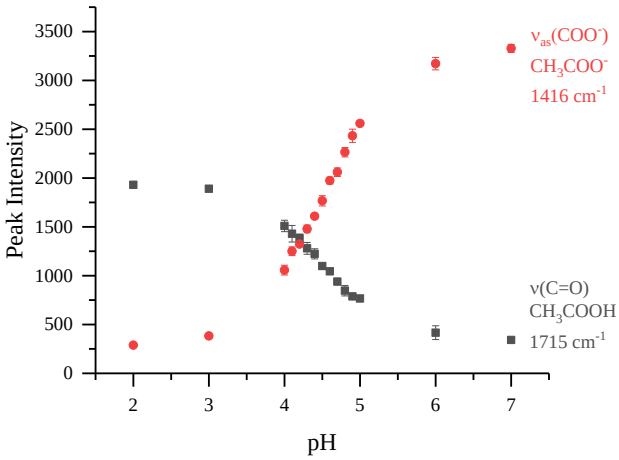

Figure 6.6 Solution spectral intensities for formic and acetic acids using ATR-FTIR and Raman spectroscopy

Solution spectral peak intensities for a) formic acid using ATR-FTIR spectroscopy, b) acetic acid using ATR-FTIR spectroscopy, c) formic acid using Raman spectroscopy, and d) acetic acid using Raman spectroscopy. The $\nu(C=O)$ peak is a characteristic peak for the protonated form of the organic acids whereas the $\nu_{as}(COO^-)$ band is characteristic for the deprotonated organic acid.

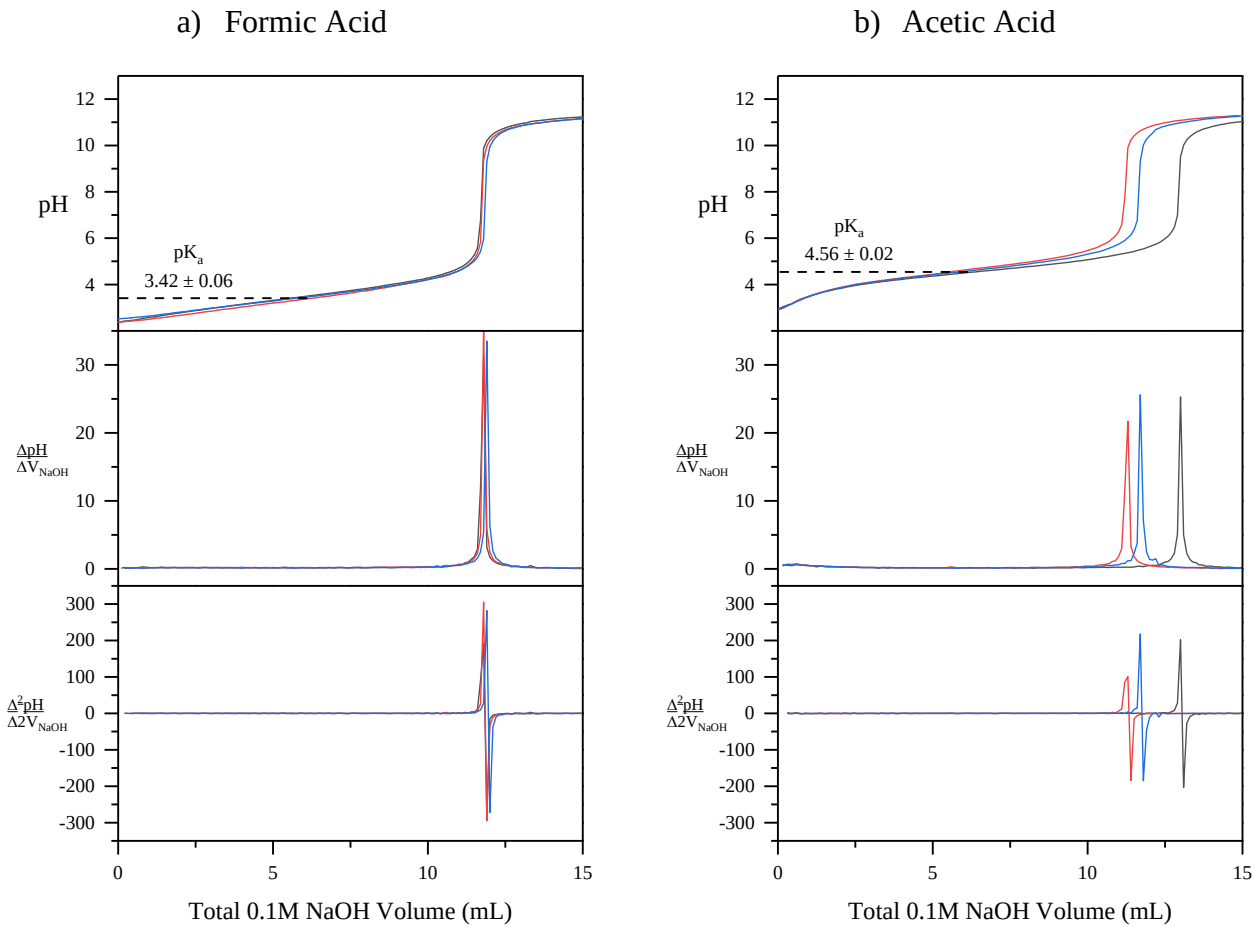

Figure 6.7 Potentiometric measurements of formic and acetic acids

Potentiometric triplicate measurements to determine solution pKa value for a) 25mM formic acid and b) 25mM acetic acid. pH measurements as a function of total NaOH volume added (top), first derivative of pH response (middle), and second derivative of pH response (bottom). pKa was determined at half the volume of the equivalence volume.

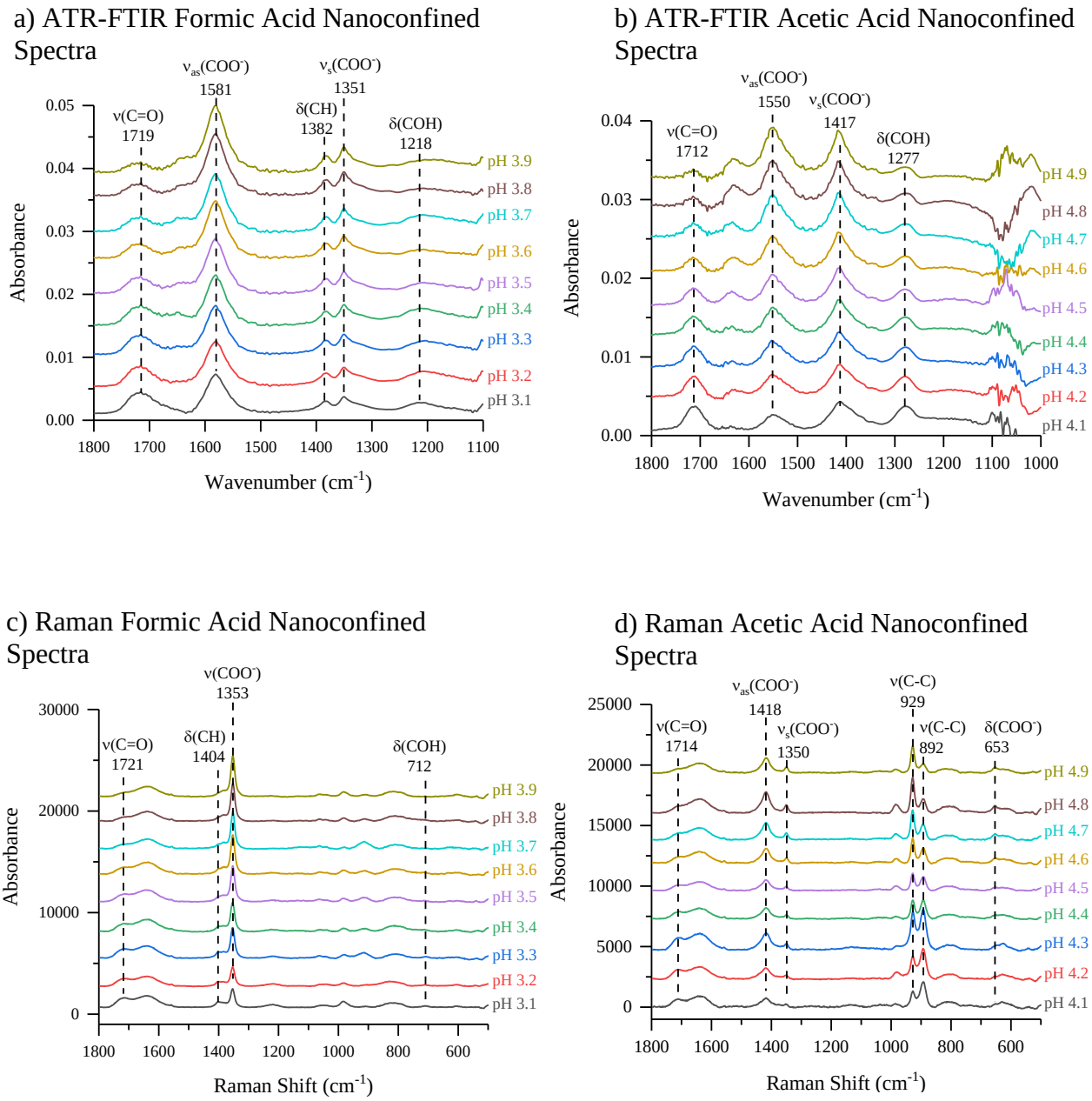

Figure 6.8 Nanoconfined spectra of formic and acetic acids using ATR-FTIR and Raman spectroscopy

Nanoconfined spectra of a) formic acid using ATR-FTIR spectroscopy, b) acetic acid using ATR-FTIR spectroscopy, c) formic acid using Raman spectroscopy, and d) acetic acid using Raman spectroscopy.

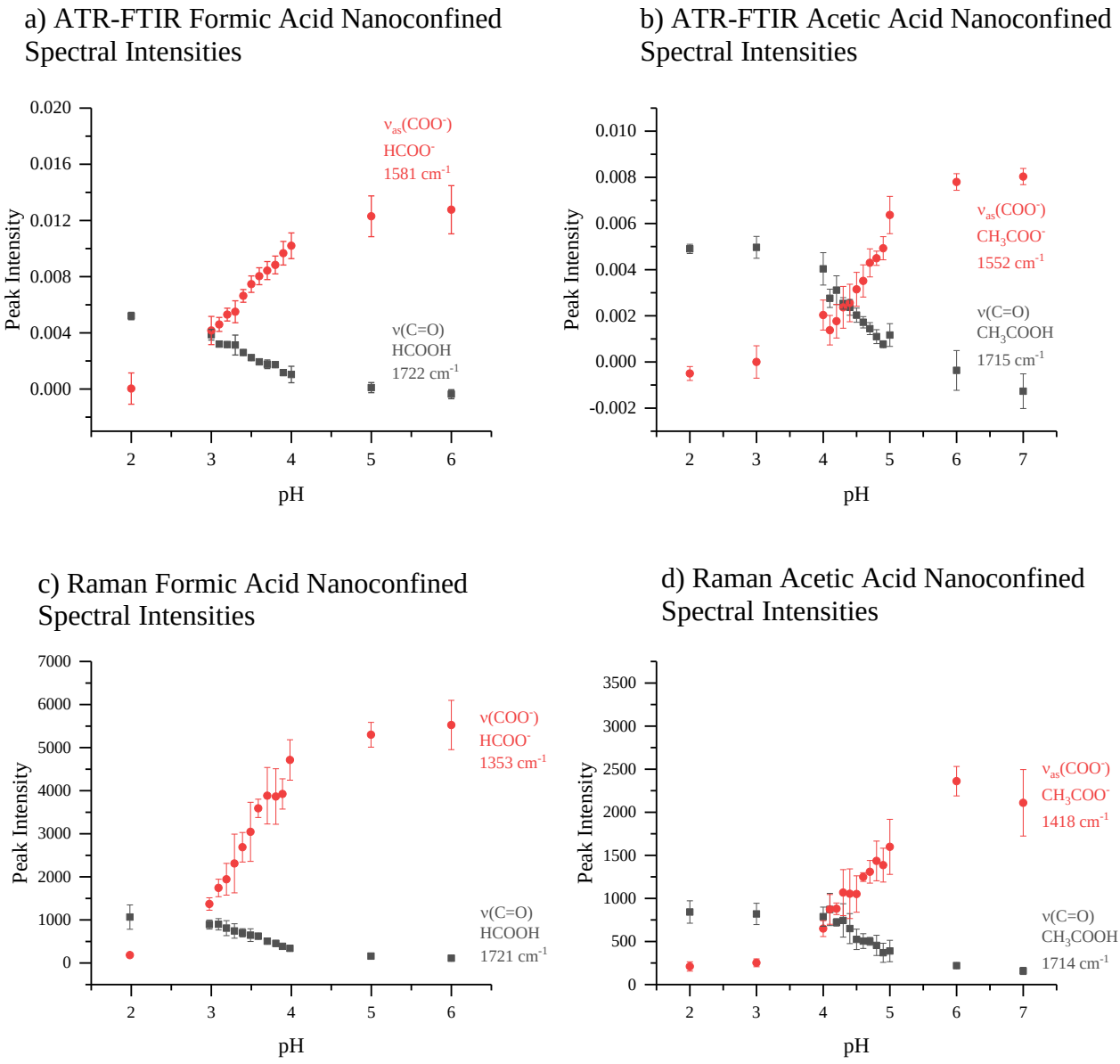

Figure 6.9 Nanoconfined spectral intensities for formic and acetic acid using ATR-FTIR and Raman spectroscopy

Nanoconfined spectral peak intensities for a) formic acid using ATR-FTIR spectroscopy, b) acetic acid using ATR-FTIR spectroscopy, c) formic acid using Raman spectroscopy, and d) acetic acid using Raman spectroscopy. The ν(C=O) peak is a characteristic peak for the protonated form of the organic acids whereas the $\nu_{as}(COO^-)$ band is characteristic for the deprotonated organic acid.

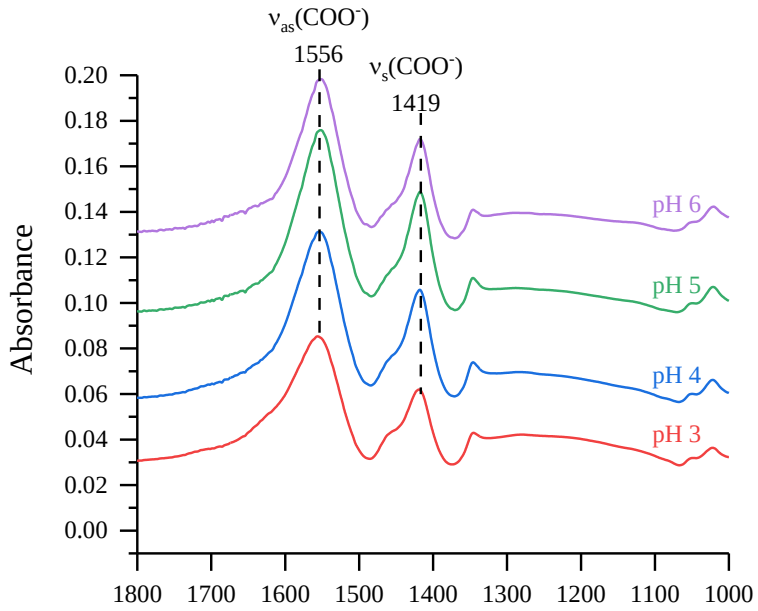

Figure 6.10 10mM acetic acid adsorbed on nanoporous alumina as a function of pH.

Spectra does not change as pH increases, suggesting that acetate is strongly complexed with the surface.

Chapter 7. Plasma Protein Adsorption on TiO_2 Nanoparticles: Impact of Surface Adsorption on Temperature-Dependent Structural Changes

7.1 Abstract

Protein adsorption on metal oxide nanoparticle surfaces is crucial to the behavior of oxide nanoparticles in biological systems. In this study, attenuated total reflection Fourier transform infrared (ATR-FTIR) spectroscopy was used for the first time to probe differences in the temperature-dependent conformational changes of two plasma proteins, bovine serum albumin (BSA) and fibrinogen (Fib), in solution and adsorbed on titanium dioxide nanoparticle (ca. 20 nm in diameter) surfaces. ATR-FTIR second derivative spectra and autocorrelation moving window two-dimensional correlation (MW2D) spectroscopy were used to identify the denaturation temperature range of these two proteins in aqueous solution and adsorbed. Generalized two-dimensional correlation spectroscopy (2DCOS) was done to investigate the protein unfolding pathway. The results show that the thermostability of BSA changed when adsorbed on the surface whereas there was no difference for solution phase Fib and adsorbed on TiO_2. The most notable fact was that solution BSA underwent significant structural changes upon adsorption whereas adsorbed Fib did not. Upon heating adsorbed BSA, no further changes occurred while BSA in solution undergone denaturation. In contract, solution and adsorbed Fib had identical denaturation temperatures and similar sequential secondary structural changes with increasing temperature. These studies show for the first time quantitatively that there are differences in the temperature-dependent structural changes of proteins adsorbed on nanoparticles surfaces and these changes depend on the initial interaction with the nanoparticle surface. Overall, the results of this study

provide new insights into understanding the effects of temperature on the structure of adsorbed protein on nanoparticle surfaces and the range of different behaviors that can occur.

7.2 Introduction

Protein adsorption on nanoparticle surfaces is crucial to understanding the behavior of nanoparticles in biological systems. Among all the different types of nanomaterials, titanium dioxide nanoparticles are one of the most prevalent metal oxide nanoparticles that have been used in various industries and consumer products, such as pigments, food additives, and cosmetics.[1,2,250,251] Additionally, TiO_2 based nanomaterials play an important role in biomedical applications including medical device coating, biosensors, and drug delivery.[252–254] The broad applications of TiO_2 nanoparticles bring significant benefits however, it raises concern for the potential negative impacts on human health.[1,255] Previous studies have shown that once nanoparticles are introduced into biological fluids, proteins can adsorb and functionality changes can occur.[46,256] Furthermore, implant-associated protein adsorption and conformational changes have been shown to promote undesired immune reactions.[257] Thus, the biocompatibility of TiO_2 nanoparticles has become critically important and the evaluation of the impact that adsorption has on protein structure is of great interest.

Despite the mode of human exposure to nanoparticles, studies have shown that they can enter the blood stream and accumulate in vital organs such as the liver and heart.[8,255] Once in this biological *milieu*, a dynamic, *in-situ* coating comprised mostly of proteins called a protein corona are formed around the nanoparticle.[5,46,47] As the nanoparticle translocate in the blood stream, the protein corona evolves as higher affinity proteins replace weaker bound proteins. The nanoparticle physiochemical properties change, altering the biodistribution and organ-specific toxicity.[5] Studies have investigated the kinetics and composition of nanoparticles in simple and complex biological

milieu.[42,43,258] However, determining how these proteins interact with nanoparticle surfaces is difficult to achieve.

Previous studies have reported that proteins undergo conformational change upon adsorption onto nanoparticle surfaces, suggesting that protein function could be altered.[43,47,256,259,260] It has been shown that the adsorbed protein conformation depends on a range of factors including pH, and the details of the surface functionality and surface chemistry of the nanoparticles.[28,47,261] In addition, when proteins are exposed to elevated temperatures, irreversible conformational change can occur, and specific protein functions can be lost.[26,27,262] This transition temperature has shown to be an important reference of protein thermal stability and can vary by protein.[260,263,264]

Serum albumin is the most abundant protein in blood which transports fatty acids and other vital small molecules throughout the circulatory system.[265,266] Bovine serum albumin (BSA) is commonly used as a model protein because it has similar properties, molecular weight, and an amino acid sequence to its human variant, human serum albumin.[47] Another important and prevalent protein in blood is fibrinogen (Fib) which plays a critical role in blood coagulation as well as adhesion of platelets.[267–269] Both of these proteins have been reported to readily adsorb onto nanoparticle surfaces when introduced into the blood serum.[270] Furthermore, both proteins have also been reported to undergo conformational changes to their secondary structures upon adsorption.[46,47,256,260,271] Despite these previous studies, few studies determine the denaturation mechanisms of both proteins in the dissolved and adsorbed state in real-time. Clearly, a non-destructive, *in-situ*, method is needed to elucidate the unfolding mechanisms of plasma proteins caused by adsorption onto nanoparticle surfaces.

Attenuated total reflectance-Fourier transform infrared spectroscopy (ATR-FTIR) can probe *in-situ* changes to protein structure by monitoring representative bands that are convoluted with secondary structure. Day et. al. suggests that the protein unfolding pathway is only accelerated and not changed by increasing temperature.[272] To accelerate the unfolding mechanism, a temperature-controlled ATR-FTIR crystal can be used while monitoring protein structural change. The band typically used to monitor conformational changes is the amide I band from 1600 to 1700 cm^{-1} which is convoluted with major protein secondary structures that are stabilized by hydrogen bonding.[259,273,274] As temperature is increased, disruption of hydrogen bonding and intensity changes to the amide I band can occur. Since the amide I band is comprised of multiple secondary motifs such as α-helix and β-sheets, a sensitive processing method is necessary to resolve spectral features.

Generalized two-dimension correlation spectroscopy (2DCOS) can be used to interpret FTIR data collected and analyze any changes that occur throughout a perturbation gradient.[110] The perturbation can be any external environmental change i.e. pH, concentration, or adsorption time. For this study, temperature is employed as the perturbation and induced changes to the amide I band can be monitored. Additionally, 2DCOS can determine the unfolding pathway by determining the sequential conformational changes to individual secondary structures. This kind of analysis has been used for determining concentration dependent adsorption mechanisms [260,275], aqueous protein temperature induced unfolding[26,276], and pH dependent unfolding mechanisms[277]. Despite the utility of 2DCOS, this analysis cannot elucidate the temperature at which large structural changes that is expected to occur when the denaturation temperature is reached.[110,272] To complement 2DCOS, autocorrelation moving window two-dimensional correlation spectroscopy

(MW2D) can be used to identify a specific region of large spectral intensity variations along a perturbation axis.[110,278]

In the present study, ATR-FTIR spectroscopy was used to provide a comprehensive, *in-situ* characterization of temperature-induced conformational changes of two plasma proteins, bovine serum albumin and fibrinogen, in solution and adsorbed on TiO_2 surfaces. Changes to the amide I band, which is comprised of multiple protein secondary structures, was monitored by 2DCOS and temperature specific transitions were analyzed by MW2D. 2DCOS elucidated the different unfolding mechanisms of proteins caused by interactions of proteins with nanoparticle surfaces or protein-protein interactions. This analysis provides new insights into the effects of adsorption on conformational changes and thermostability of two ubiquitous proteins.

7.3 Experimental Methods

7.3.1 Materials

Disodium phosphate, monopotassium phosphate, deuterium oxide, deuterium chloride, and sodium deuteroxide were acquired from Sigma-Aldrich. TiO_2 nanoparticles (P25, 22 nm, 86% anatase, 14% rutile) was purchased from Sigma Aldrich (718467) and characterized in a previous study.[47] Bovine serum albumin and bovine fibrinogen were acquired from Sigma-Aldrich. BSA is a 'soft', globular protein (~66 kDa, normal form 50 x 50 x 90Å) and an isoelectric point of 4.7.[279,280] BSA and Fib show differences in their physical properties. Fib is a large rod-like protein (~340 kDa, 60 × 65 × 450Å) that has an isoelectric point of 5.5.[260] Additionally, Fib is a trinodular structure with two terminal D-domains and a central E-domain.[260,281]

7.3.2 Attenuated Total Reflectance – Fourier Transform Infrared (ATR-FTIR) Spectroscopy

ATR-FTIR spectroscopy is based on the total internal reflection of an infrared beam at the interface between an optically dense medium (ATR crystal) and an optically rare medium (sample

medium) and uses an evanescent that penetrates the media of interest to detect protein adsorption on nanoparticles surfaces.[43] This is particularly useful for monitoring protein denaturation because of the sensitive intensity and frequency responses to conformational changes. ATR-FTIR spectra were obtained using a Nicolet iS10 FTIR spectrometer (Thermo-Fisher) equipped with a MCT/A detector at 4 cm^{-1} resolution using an average of 32 scans over a range of 400 to 4000 cm^{-1} wavenumber. Fresh protein solutions were prepared by dissolving BSA or Fib in 20 mM phosphate buffered saline (PBS, 10 mM disodium phosphate, 10 mM monopotassium phosphate, and 15 mM sodium chloride) with deuterium oxide (D_2O). D_2O was used instead of H_2O because the bending mode of D_2O is shifted to lower wavenumber around (1200 cm^{-1}) and does not overlap with the amide I region (1600-1700 cm^{-1}) while H_2O bending is centered around 1640 cm^{-1}.[28,282] Protein solutions were then adjusted to pD 7.4 with 1 M deuterium chloride (DCl) and 1 M sodium deuteroxide (NaOD). The pD value of the protein solutions were first measured with a standard pH electrode and corrected using the equation pD = pH + 0.4.[27]

To obtain spectra of proteins in solution at discrete temperatures, the protein solution (10 mg/mL) was heated with a PIKE TempPro ATR heater accessory over the range of 25 to 90 ℃ at a rate of 0.5 ℃/min. Background spectrum of the 20 mM PBS/D_2O solvent solution were also measured from 25 to 90 ℃ (with 5 ℃ interval) and subtracted from the sample spectrum at the corresponding temperatures.

To obtain spectra of adsorbed protein on the TiO_2 thin film at discrete temperatures, a thin film was first created by depositing 1 mL of a 2.5 mg/mL TiO_2 suspension onto an AMTIR trough crystal and dried overnight under a stream of dry air. 20 mM PBS/D_2O solution was flowed over the thin film for 15 minutes using a peristaltic pump at ~1 mL/min to remove any loosely bound nanoparticles and to collect the background spectra. For protein adsorption, 1 mg/mL of protein

solution in 20 mM PBS/D_2O was flowed over the nanoparticle thin film for 90 min. Subsequently, the film was washed with 20 mM PBS/D_2O for 15 minutes to remove loosely bound protein and to reach adsorption equilibrium. The equilibrated adsorbed protein film was then heated from 25 to 90 ℃ at a rate of 0.5 ℃/min for the temperature dependent study. Background spectra of TiO_2 thin film in PBS/D_2O were also measured at identical temperatures and subtracted from the sample spectra at the corresponding temperatures.

All subtracted spectra were further processed by Fourier self-deconvolution (FSD) to resolve the overlapping IR bands using a half-bandwidth of 19.8 cm^{-1} and a band-narrowing factor k = 1.8.[27,262] Both the spectra subtraction and FSD process are performed using OMNIC software. All spectra are modified to a linear baseline and the amide I band was normalized to 1.0 for comparison.

7.3.3 Two-Dimensional Correlation Spectroscopy (2DCOS)

2DCOS has been well studied as an analytical method to study changes induced by external perturbations such as temperature, time, and pH. Details of the mathematical algorithm can be found elsewhere.[110,119,120] Sequential protein structural changes can be determined by assigning secondary structures to correlation peaks in the synchronous (Φ) and asynchronous (Ψ) correlation maps. The synchronous and asynchronous maps can be interpreted by following Noda's rules.[110] Briefly, the off-diagonal Φ peaks indicate a coupled spectral intensity change. A positive Φ cross peak corresponds to spectral intensities changing in phase, either both increasing or decreasing. Whereas a negative Φ cross peak indicates that the signals are out of phase, one signal is increasing and the other is decreasing. The Ψ cross peaks are used to determine the sequential order of intensity changes. If the sign of $\Phi(\nu_1, \nu_2)$ is the same as $\Psi(\nu_1, \nu_2)$, then ν_1 occurs before ν_2. Conversely, if the sign of $\Phi(\nu_1, \nu_2)$ and $\Psi(\nu_1, \nu_2)$ are opposite, then ν_1 occurs after ν_2. For MW2D

correlation maps, it was demonstrated that the MW2D correlation is approximately proportional to the squared derivative of the spectral intensity with respect to the perturbation variable elsewhere.[112] This approximation was used to map the spectral intensity variations along a temperature perturbation to identify a specific temperature at which protein structure undergoes significant conformational changes. Baseline corrected, normalized, FSD processed spectra between 1600 to 1700 cm^{-1}, was used for analysis by 2DCOS and MW2D. 2DCOS and MW2D was coded and processed in MATLAB 2017b. The resultant correlation maps were plotted in Origin 2017. Both computational algorithms were checked by generating simulated spectra and compared to literature and 2dShige version 1.3 (Shigeaki Mortita, Kwansei-Gaukuin University, 2004–2005) developed by Noda.[120,283]

7.4 Results and Discussion

7.4.1 ATR-FTIR Spectroscopy of Solution Phase and Adsorbed Plasma Proteins

ATR-FTIR spectra and second derivative spectra are in **Figure 7.1** and **Figure 7.5**, respectively. **Figure 7.1** shows the temperature dependent ATR-FTIR spectra of BSA and Fib in solution and adsorbed on TiO_2 (22 nm) nanoparticle surfaces. The amide I band (1600-1700 cm-1), which attributed to the C=O symmetric stretching (major component) and C-N bending (minor component) of the amide backbone in proteins[43], was chosen for analysis as this region is widely used to investigate protein conformational changes.[28,46,47,256]

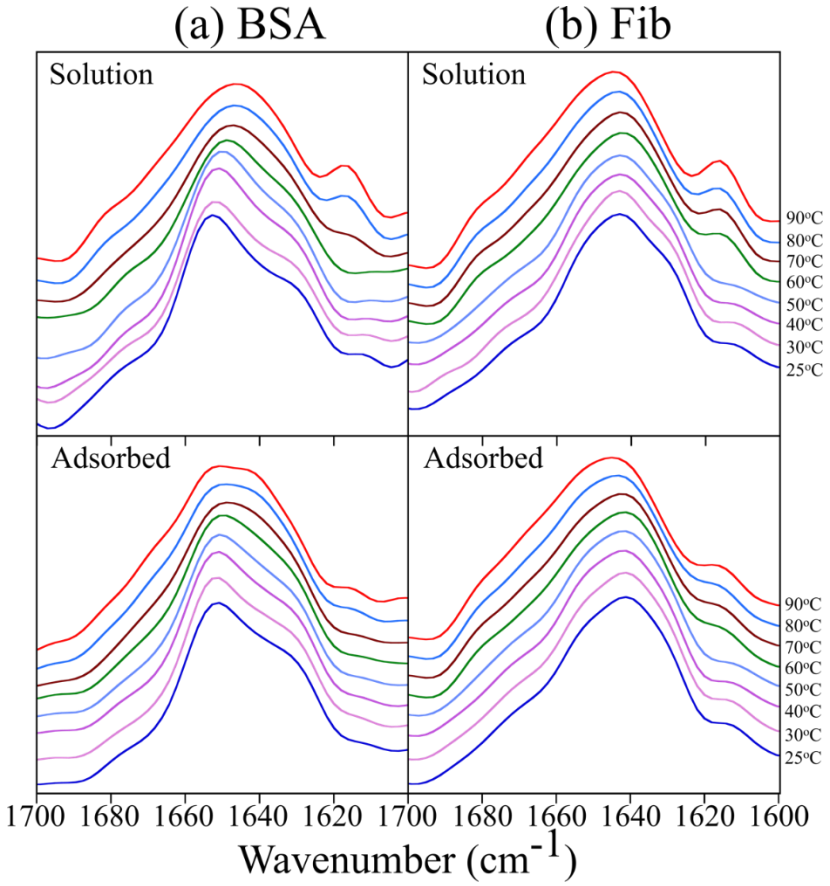

Figure 7.1 Normalized ATR-FTIR spectra over a temperature range of 25 to 90 ℃

(a) solution phase BSA (top) and adsorbed BSA on TiO_2 (22 nm) (bottom), (b) solution phase Fib (top) and adsorbed Fib on TiO_2 (22 nm) (bottom).

Generally, for all four sets of experiments shown in **Figure 7.1**, the spectral features below 50 ℃ are almost identical to those at 25 ℃ in the same experiment set. At temperatures higher than 50 ℃, the amide I band became broader and two shoulder bands began to appear around 1685 and 1615 cm^{-1}. The appearance of these two new bands are consistent with reported literature and can be attributed to the formation of intermolecular β-sheets from strong hydrogen bonding interactions during the temperature-induced β-sheet aggregation.[26,27,262] In addition, it was observed that these two bands remain even after cooling down to 25 ℃ (data not shown), indicating that this process irreversibly changes the secondary structure of the protein and these observations are in agreement with other studies.[27] Thus, the two bands at 1685 and 1615 cm^{-1} are considered

the diagnostic bands for the temperature-induced denaturation of proteins and are widely used in the identification of protein denaturation temperature.[26,27,262]

For solution phase BSA spectra (**Figure 7.1a**), the appearance of the intermolecular β-sheet bands are observed between 60 to 70 ℃. For solution phase Fib (**Figure 7.1b**), such marked spectral changes are seen between 50 to 60 ℃. BSA has been reported to denature around 70 ℃ while Fib has been observed to have two uncooperative transition temperatures, 55 and 95 ℃.[27,260,284] As suggested by Privalov and Medved, this is due to the different thermostabilities of D- and E-domain, where the D-domain is less stable than the E-domain.[281] Additionally, It is difficult to identify a specific temperature at which the diagnostic bands appear for adsorbed BSA and will be discussed via MW2D. For adsorbed Fib, the appearance of the diagnostic bands occurs between 50 to 60 ℃. Compared to the solution phase protein spectra, the appearances of the diagnostic peaks are not as prominent in both adsorbed protein spectra. Therefore, autocorrelation moving window two-dimensional correlation spectroscopy (MW2D) is applied to investigate changes in the adsorbed protein spectra.

7.4.2 Autocorrelation Moving Window Two-Dimensional Correlation Spectroscopy

In one-dimensional spectra, the amide I band is convoluted with multiple secondary structural elements; MW2D was done to elucidate changes to secondary structure at specific temperatures. **Figure 7.2a** shows the MW2D spectra of BSA in both solution and adsorbed on TiO_2 nanoparticles. Solution BSA shows several highly correlated peak intensity changes around 70 ℃. Several peaks that undergo detectable intensity changes can be assigned to absorptions due to secondary structural motifs that are hard to discern in the broad amide I band. **Table 7.1** is a summary of secondary structure peak assignments within the amide I band for both BSA and Fib.[26,27,47,110,262,282] The MW2D map of solution BSA indicate four relevant absorption bands that

undergo change at 70 °C. These absorptions occur at 1682 cm^{-1} (intermolecular β-sheet), 1668 cm^{-1} (turns), 1641 cm^{-1} (random chains), and 1616 cm^{-1} (intermolecular β-sheet). Below this temperature there are no other significant changes to secondary structure, suggesting that solution phase BSA has one transition temperature. Although changes in the β-sheet structure are detected, the α-helical band at ~1654 cm^{-1} is not detected in the MW2D map which is reported to be affected by unfolding.[27,256,282] Many studies have noted that the α-helix undergoes changes at the denaturation temperature, thus one would expect to see an autocorrelation peak for the α-

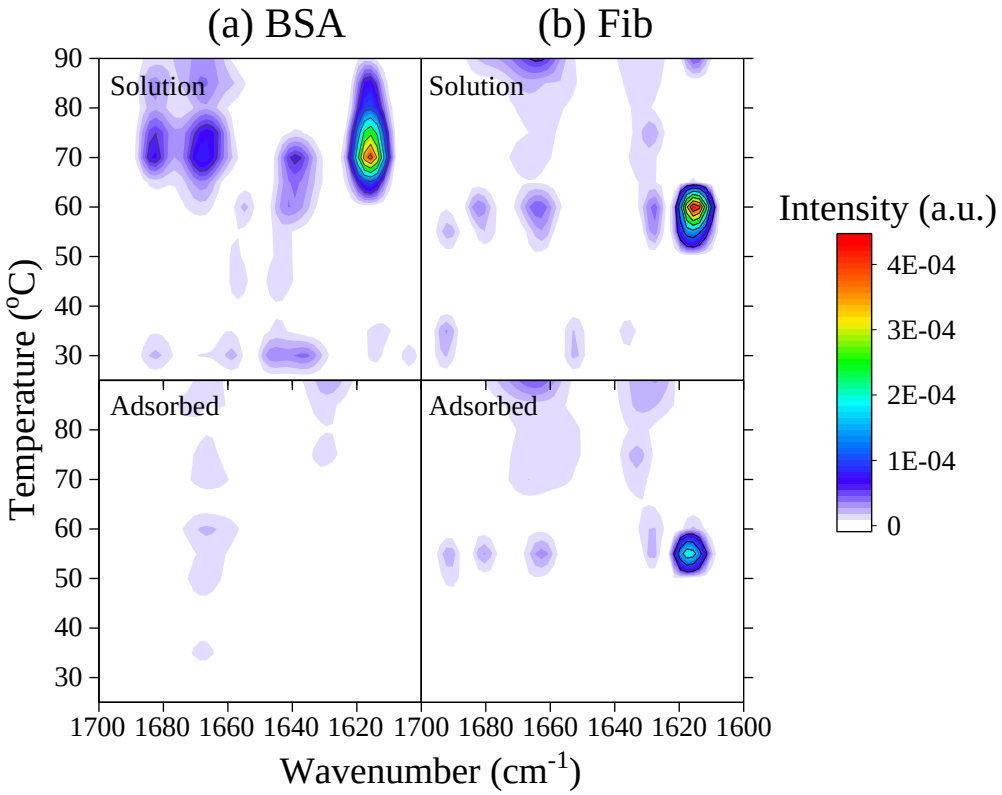

Figure 7.2 Autocorrelation moving window 2-dimensional correlation map of the amide I band shown in Figure 1 relating temperature to spectral intensity changes.

(a) BSA in solution (top) and adsorbed on 22 nm TiO_2 nanoparticles (bottom). (b) Fib in solution (top) and adsorbed on 22 nm TiO_2 nanoparticles (bottom). The intensity value represents the extent of spectral variation due to the external perturbation i.e. temperature.[110]

helix.[26,260,277] One possible explanation is that in the spectral processing for 2DCOS, there was a normalization step to the highest intensity band around ~1650 cm^{-1}. The α-helix structural motif is assigned somewhere between 1655-1648 cm^{-1}. Since the α-helix band is assigned to where the

normalization step occurs and 2DCOS monitors intensity change, the α-helix band intensity will remain constant and 2DCOS will not be able to detect any change. To gain information on the α-helix, the second derivative at the α-helix band can be analyzed, as shown in **Figure 7.5**. It can be seen that α-helix content indeed changes as temperature increases. This limitation in the use of MW2D has been noted previously in a study by Schmidt et. al. where the analysis of conformational change to other secondary structures coincided with quantification of secondary structure and surface saturation.[52]

Table 7.1 Vibrational frequencies (cm^{-1}) of the absorption bands associated with secondary structural elements of BSA and Fib in the amide I region

Vibrational Frequency (cm^{-1})		Assignment
25℃	90℃	
	1680-1685	Intermolecular β-sheets
1675-1663	1675-1663	Turns
1655-1648	1655-1648	α-helices
1645-1640	1645-1640	Random chains
1635-1627	1635-1627	Extended chains
1612-1610	1612-1610	Side chain moieties
	1614-1616	Intermolecular β-sheets

In contrast to BSA in solution phase, the MW2D map of adsorbed BSA does not show significant changes in the amide I band (**Figure 7.2a**). Compared to the second derivative of solution BSA at low temperatures, the conformation of BSA is altered upon adsorption (**Figure 7.5**). This conformational change has been reported by multiple studies and might offer an additional explanation to the minimized adsorbed BSA behavior.[28,46,47,256,260,285] BSA is a relatively 'soft' protein and was simulated to undergo very large spreading on the surface of the TiO_2 polymorphs, anatase and rutile.[286,287] Studies show that BSA irreversibly adsorbs as a monolayer on TiO_2, suggesting strong protein-surface interactions.[28,287,288] Additionally, previous studies suggest that protein unfolding is linked to interactions with surface hydroxyl groups.[28,289] It is possible that BSA initial loss of secondary structure is due to maximizing interactions between the

protein and the surface, which results in greater interactions with surface hydroxyl groups. After the initial adsorption-induced conformational change upon adsorption, BSA is not seen to display significant additional structural changes as temperature increases. This behavior suggests that the thermostability of a protein depends strongly on the *initial* interaction with the surface.

In the case of Fib, the MW2D for Fib in solution shows multiple peak intensities changing at 60 ℃, specifically to 1682, 1662, 1628 and 1616 cm^{-1} (**Figure 7.2b**). By using **Table 7.1**, these peaks can be assigned to intermolecular β-sheet, turns, extended chains, and intermolecular β-sheet, respectively. As noted above, and more evident in **Figure 7.2b**, the Fib protein structure does not show significant change below the denaturation temperature. However, above the denaturation temperature at 90 ℃, it appears that there is another conformational change is occurring. This could be the E-domain starting to unfold whereas the 60 ℃ transition temperature is the D-domain unfolding.

The MW2D correlation map for adsorbed Fib on TiO_2 is shown in **Figure 7.2b**. The correlation map is very similar compared to solution phase Fib, but the transition temperature occurs slightly earlier at 55 ℃. The conformational changes to the secondary structure are the same for solution Fib, suggesting identical unfolding mechanisms. Fib did not undergo significant conformational change upon adsorption which can be seen by comparing second derivative spectra of solution and adsorbed at 25 ℃ in **Figure 7.5**. This result agrees a previous study that reported minor Fib conformational changes upon adsorption on TiO_2.[290] At high concentrations, such as used in this study, it is possible that Fib adsorbs 'end-on' where the long axis is perpendicular to the TiO_2 surface thus, limiting interactions between the protein and the surface.[256] Additionally, it has been shown that Fib can be easily displaced with BSA, highlighting its weaker affinity to TiO_2.

[291] It is possible that Fib has minimal interactions with surface hydroxyl groups due to 'end-on' adsorption. Therefore, the thermostability is not impacted very much by surface interactions.

One limitation of MW2D is it only detects absolute peak intensity changes and cannot reveal whether the peak directionality, i.e. increasing or decreasing. Day et. al. investigated protein unfolding mechanisms at various temperatures and suggested the unfolding process of secondary structures is temporal and a sequential order occurs.[272] To further understand the impact of adsorption on the thermostability of BSA and Fib, it is necessary to employ generalized two-dimensional correlation spectroscopy that reveals the positive or negative intensity shifts as well as the sequential transformation between secondary structures.

7.4.3 Generalized Two-Dimensional Correlation Spectroscopy

2DCOS synchronous and asynchronous correlation maps for BSA and Fib in solution and adsorbed on TiO_2 is shown in **Figure 7.3** and **Figure 7.4**. Additionally, a diagonal intensity line trace spectrum of the synchronous 2DCOS map is displayed above each plot, indicating secondary structure peaks that change, either positively or negatively, due to temperature. A table summarizing the prominent peaks and the sequential order of secondary structure change is shown in **Table 7.2**. A thorough interpretation of both synchronous and asynchronous maps will not only elucidate the conformational changes in response to an increased temperature but also reveal their sequential order.

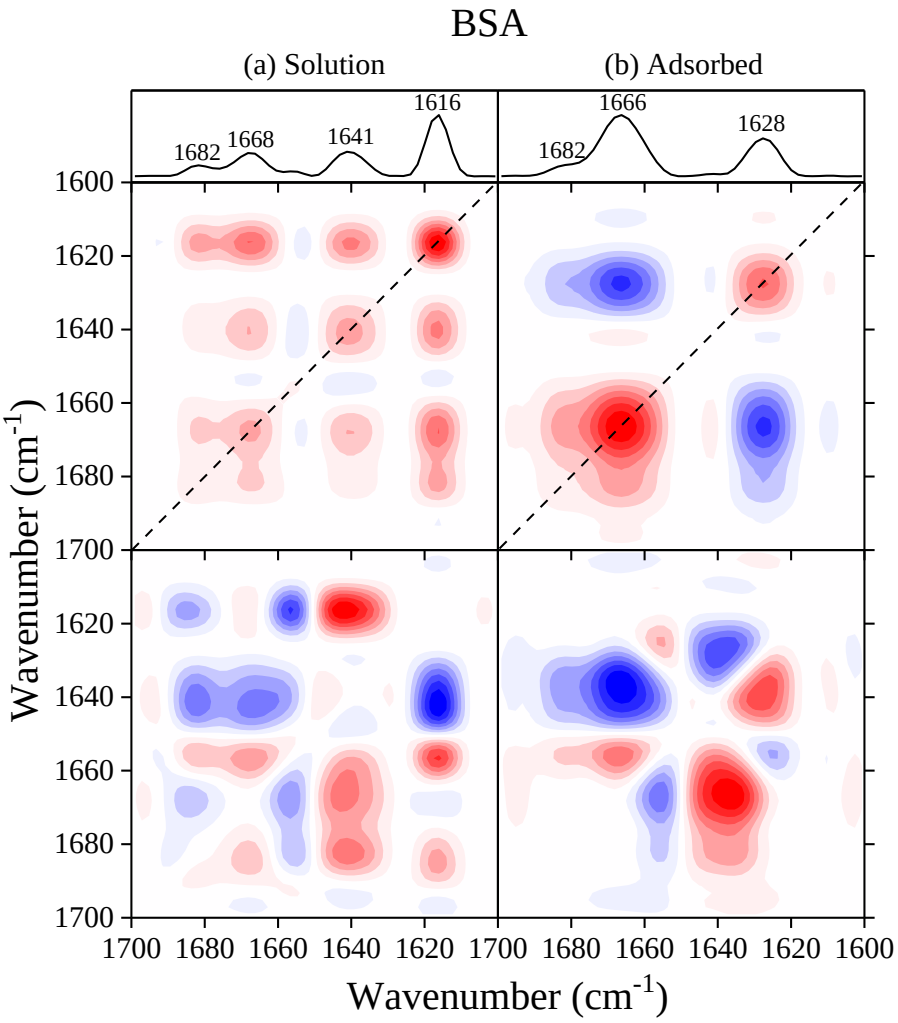

Figure 7.3 2DCOS maps for BSA in (a) solution and (b) adsorbed onto 22nm TiO_2 nanoparticles

Normalized intensity line trace for the dotted line in the synchronous 2DCOS and labeled amide I secondary structure peaks (top), synchronous 2DCOS (middle), asynchronous 2DCOS (bottom). Red and blue corresponds to positive and negative correlations, respectively.

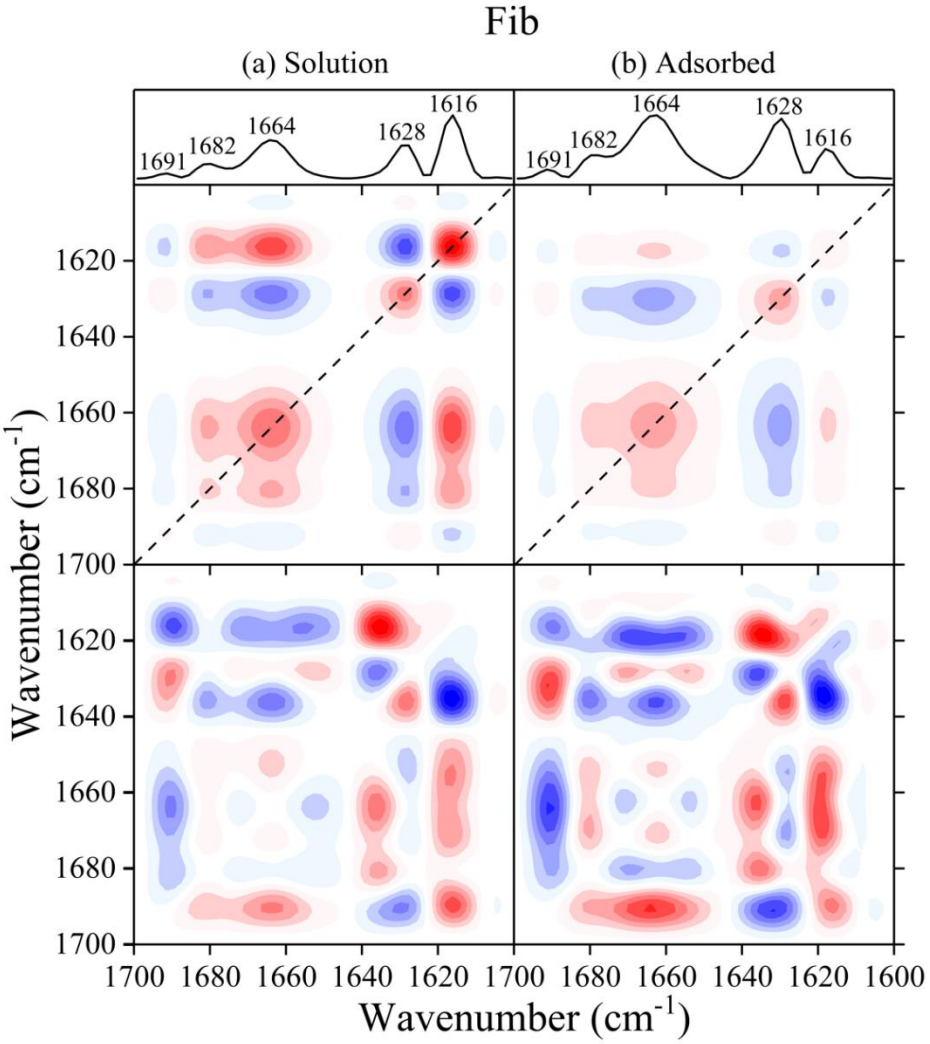

Figure 7.4 2DCOS maps for Fib in (a) solution and (b) adsorbed onto 22nm TiO_2 nanoparticles

Normalized intensity line trace for the dotted line in the synchronous 2DCOS and labeled amide I secondary structure peaks (top), synchronous 2DCOS (middle), asynchronous 2DCOS (bottom). Red and blue corresponds to positive and negative correlations, respectively.

Table 7.2 2DCOS analysis for BSA and Fib in solution and adsorbed onto TiO_2 nanoparticles, showing prominent cross peaks, synchronous and asynchronous cross peak signs and sequential order

Protein and Phase	Cross Peak	Synchronous	Asynchronous	Sequence
BSA Solution	(1682, 1668)	+	-	1682 < 1668
	(1682, 1641)	+	-	1682 < 1641
	(1682, 1616)	+	-	1682 < 1616
	(1668, 1641)	+	-	1668 < 1641
	(1668, 1616)	+	+	1668 > 1616
	(1641, 1616)	+	+	1641 > 1616
BSA Adsorbed	(1682, 1666)	+		
	(1682, 1628)	-	-	1682 > 1628
	(1666, 1628)	-	-	1666 > 1628
Fib Solution	(1682, 1664)	+	+	1682 > 1664
	(1682, 1628)	-	-	1682 > 1628
	(1682, 1616)	+	-	1682 < 1616
	(1664, 1628)	-		
	(1664, 1616)	+	-	1664 < 1616
	(1628, 1616)	-	+	1628 < 1616
Fib Adsorbed	(1682, 1664)	+	+	1682 > 1664
	(1682, 1628)	-	-	1682 > 1628
	(1682, 1616)	+		
	(1664, 1628)	-	+	1664 < 1628
	(1664, 1616)	+	-	1664 < 1616
	(1628, 1616)	-	+	1628 < 1616

The line trace intensity spectrum for BSA solution phase in **Figure 7.3a** indicates four peaks at 1682, 1668, 1641 and 1616 cm^{-1} assigned to intermolecular β-sheets, turns, random chains, and intermolecular β-sheets, respectively. Positive synchronous cross peaks (1682, 1668), (1682, 1641), (1682, 1616), (1668, 1641), (1661, 1616), and (1641, 1616) suggest that both intermolecular β-sheets, turns, and disordered structures all change in phase, either increasing or decreasing. To determine the intensity directionality, the 1682 and 1616 cm^{-1} intermolecular β-sheet bands were

chosen as reference peaks. As seen in **Figure 7.1a**, the 1616 cm^{-1} peak grows in with increasing temperature, thus turns and random chains bands also increase. The observed increase in all four detected peaks without a decreasing secondary structure is unusual. A decrease is expected as unfolding of ordered structures, such as α-helix, occurs at the denaturation temperature to enable an increase of other less ordered secondary structures.[27,260] Furthermore, there is no line trace intensity peak detected for the α-helix. **Figure 7.5** can be inspected for the α-helix band and it is seen that the band decreases as temperature increases. The negative asynchronous cross peaks are (1682, 1668), (1682, 1616), (1682, 1641), and (1668, 1641) while the positive asynchronous peaks are (1668, 1616) and (1641, 1616). The sequential order can be determined using Noda's rules as the following: 1641 cm^{-1} (random chains) → 1668 cm^{-1} (turns) → 1616 cm^{-1} (intermolecular β-sheet) → 1682 cm^{-1} (intermolecular β-sheet). As BSA denatured in solution, random chains are the first to form and the diagnostic intermolecular β-sheet bands were the last to form. Indicating that random chains are the most sensitive secondary structure in solution BSA. Furthermore, the α-helix structure is the only secondary structure to decrease in intensity indicating that the α-helix transitions into the other structures.

When BSA adsorbs onto TiO_2, the number of intensity line trace peaks (**Figure 7.3b**) decrease to only three, 1682, 1666, and 1628 cm^{-1} corresponding to intermolecular β-sheets, turns, and random chains, respectively (**Table 7.1**). The intermolecular β-sheet intensity increases, and the directionality of turns and random chains can be determined. From the negative (1682, 1628) synchronous cross peak, adsorbed BSA random chains decrease in intensity as temperature increases (**Table 7.2**). The in phase synchronous correlation for the (1682, 1666) cross peak indicate that both intermolecular β-sheet and turns increase. The last cross peak, (1666, 1628) has a negative synchronous value suggesting that the turn and extended chains have opposite responses

to temperature. The synchronous map shows a positive value for (1682, 1666) and a zero value in the asynchronous map (**Table 7.2**). This was previously reported in literature and can be attributed to frequency or bandwidth changes due to temperature that blur peak position and intensity in 2DCOS.[52] Accordingly, cross peaks that do not have asynchronous values will be ignored in determining sequential order. The sequence of secondary structural change is: 1682 cm^{-1} (intermolecular β-sheet), 1666 cm^{-1} (turns) → 1628 cm^{-1} (extended chains). Compared to BSA in solution, adsorbed BSA only shows the 1682 cm^{-1} diagnostic peak, which is weakly correlated suggesting that there is minimal change. As noted above, BSA may have unfolded upon adsorption and is no longer further denature as temperature is increased.

The 2DCOS maps of Fib in solution is shown in **Figure 7.4a**. The intensity line trace shows four peaks, 1682, 1664, 1628, 1616 cm^{-1} corresponding to intermolecular β-sheet, turns, extended chains, and intermolecular β-sheet, respectively. The synchronous cross peaks are in phase for both intermolecular β-sheet, 1682 and 1616 cm^{-1}, peaks and the 1664 cm^{-1} turn peak, suggesting that all three intensities increase in response to temperature (**Table 7.2**). The remaining (1682, 1628) and (1628, 1616) cross peaks are out of phase, indicating the 1628 cm^{-1} extended chains decrease in intensity. The turns and extended chains are uncorrelated. The sequential conformational order change for the structures are as follows: 1616 cm^{-1} (intermolecular β-sheet) → 1682 cm^{-1} (intermolecular β-sheet) → 1664 cm^{-1} (turns), 1628 cm^{-1} (extended chains). The unfolding of solution phase Fib starts with the formation of intermolecular β-sheets then turns while the extended chains decrease.

The corresponding 2DCOS maps for adsorbed Fib on TiO_2 are shown in **Figure 7.4b**. The intensity line trace depicts four peaks, 1682, 1664, 1628, 1616 cm^{-1} assigned to intermolecular β-sheet, turns, extended chains, and intermolecular β-sheet, respectively. The (1682, 1664) and

(1664, 1616) cross peak are in phase suggesting that the intermolecular beta sheets and turns are increasing in intensity (**Table 7.3**). On the other hand, the (1682, 1682), (1664, 1628) and (1628, 1616) cross peak are out of phase resulting in the extended is the only detectable structure that is decreasing. The (1682, 1616) cross peak is uncorrelated. Following the asynchronous cross peak signs and Noda's rules, the sequential order follows: 1682 cm^{-1} (intermolecular β-sheet), 1616 cm^{-1} (intermolecular β-sheet) → 1628 cm^{-1} (extended chains) → 1664 cm^{-1} (turns). Like Fib in solution, the diagnostic intermolecular β-sheet peaks are the first to form possibly followed by concurrent with or after, increase in extended chains and decrease in turns.

2DCOS provides a large amount of insight into adsorption mechanism of BSA and Fib on TiO_2 nanoparticle surfaces. BSA shows a strong thermostability dependence when adsorbed onto TiO_2. Upon adsorption, BSA's secondary structure is already altered, yielding a temperature sensitive conformation. This adsorption dependence could be attributed to BSA 'soft' nature and ability to undergo molecular transformations upon adsorption. Fib did not have a strong adsorption dependence on its thermostability which is associated with its weaker interaction with the surface. This suggests that the thermostability is reflected to a great extent by protein-surface interactions.

7.5 Conclusions

Understanding plasma protein adsorption is crucial to decipher the behavior and effects of nanoparticles in biological fluids. This study showed how protein conformational changes depend on nanoparticle adsorption and can change with temperature. The denaturation temperature of two plasma proteins, BSA and Fib, in dissolved and adsorbed on TiO_2 (22 nm) nanoparticles were compared. Protein thermostabilities were assessed by monitoring the appearance of diagnostic intermolecular β-sheet peaks. Adsorbed BSA did not have a denaturation temperature where its solution phase did, owing to the conformational changes due to adsorption onto TiO_2. Fib had a

similar thermostability dependence in solution and upon adsorption. Adsorbed protein thermostability is complex and in our studies shown here we propose it depends to a great extent on the *initial* interaction of the protein with the surface. Future studies should use techniques such as hydrogen-deuterium exchange mass spectrometry[292,293] and/or NMR spectroscopy[294,295] to better understand these interactions and the specific residues that are involved.

7.6 Acknowledgements

Chapter 7, in full, is a reprint of the material as it appears in Polyhedron. Sit, I.; Xu, Z.; Grassian, V. H. Plasma Protein Adsorption on TiO_2 Nanoparticles: Impact of Surface Adsorption on Temperature-Dependent Structural Changes. 2019, 171, 147–154. The dissertation author is the co-first author of this paper.

7.7 Supplemental Information

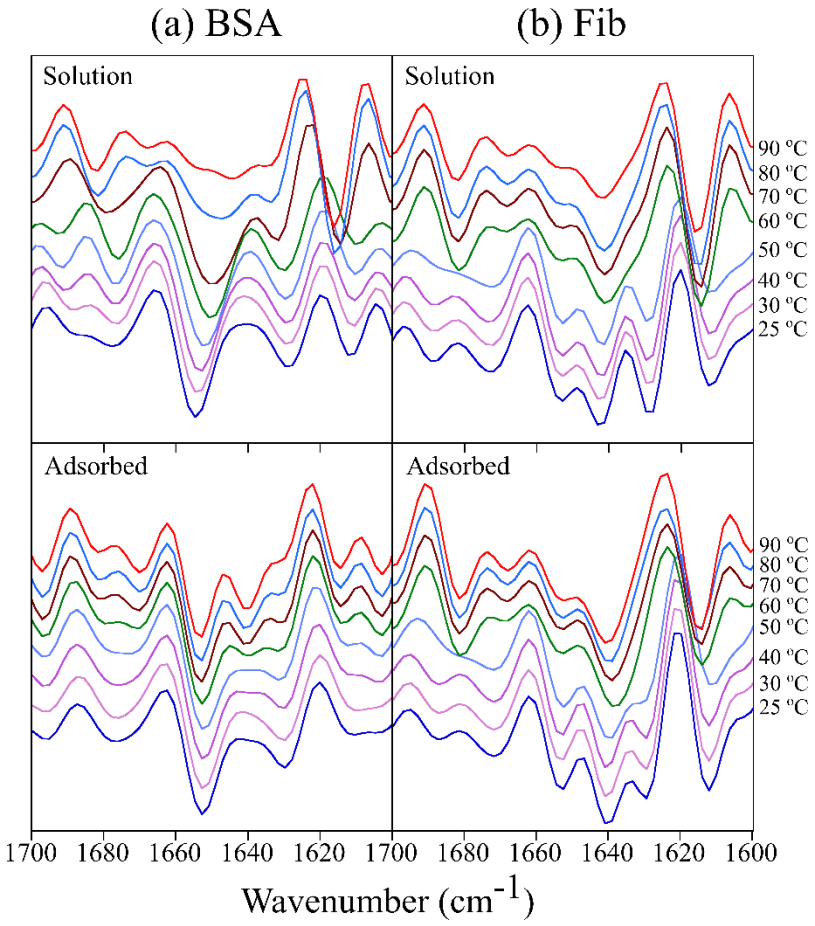

Figure 7.5 Normalized ATR-FTIR second derivative spectra BSA and Fib in solution and adsorbed on TiO_2

(a) BSA solution phase (top) and adsorbed on TiO_2 (bottom), (b) Fib solution phase (top) and adsorbed TiO_2 (bottom) over a temperature range of 25-90℃.

Chapter 8. Applications of Attenuated Total Reflection Fourier-Transform Infrared Spectroscopy to Investigate Nanomaterial Applications and Implications to Human Health

In this chapter, surface chemistry of various coatings on nanoparticles are probed with ATR-FTIR spectroscopy to emphasize the diverse applications that is possible with this *in-situ* spectroscopic method. There are two aspects discussed here that utilize the capabilities of ATR-FTIR spectroscopic analyses to probe the surfaces of nanoparticles to assess nanoparticle applications *for* human health and implications *to* human health.

For applications to human health, here we investigate gold nanorods which have been designed as a photoacoustic contrast agent for the detection of cancer imaging, oxidative stress, and theranostics by the Jokerst group at UC San Diego. It has been shown that there is an approximately 40x-fold photoacoustic enhancement of Ag_2S/Se-coated gold nanorods making these nanorods particularly useful for as biological imaging contrasting agents. For this study, ATR-FTIR spectroscopy was used to provide evidence of irreversible adsorption and displacement of ligands on the particle surface that leads to this large enhancement.

For implications of human health, there is great interest in the toxicity of nanoparticles with respect to pulmonary and cardiovascular systems. In this study we collaborated with the Chen group at UC San Diego to investigate and assess the cardiotoxicity of copper oxide nanoparticles. For this study, we used ATR-FTIR spectroscopy to gain a better understanding of the adsorption of bovine serum albumin, a physiological model protein, adsorbed on copper oxide nanoparticles. These nanoparticles were then dosed into a 3-D cardiac tissue scaffold to assess the toxicity of a nanoparticle with a biological coating. ATR-FTIR spectroscopy was used to characterize uncoated and coated particles to determine the irreversible adsorption of the protein onto the particle surface.

8.1 Photoacoustic Enhancement of Ferricyanide Treated Silver Chalcogenide Coated Gold Nanorods

8.1.1 Abstract

Plasmonic gold nanorods (AuNRs) are often employed as photoacoustic (PA) contrast agents due to their ease of synthesis, functionalization, and biocompatibility. These materials can produce activatable signal in response to a change in optical absorbance intensity or absorbance wavelength. Most interesting is the finding thatAg_2S/Se-coated AuNRs have a ~40-fold PA enhancement upon addition of an oxidant but with no change in absorption spectra. There was then great interest to further understand the mechanism underlying this enhancement. As detailed in Mantri et al., there was no evidence for aggregation and morphology changes. Attenuated total reflectance Fourier transform infrared (ATR-FTIR) spectroscopy suggests that PA enhancement is driven by the irreversible displacement of CTAB with HCF.

8.1.2 Introduction

Plasmonic gold nanostructures, like rods and spheres are widely used as photoacoustic contrast agents. Gold nanorods are easily tunable, have high photothermal conversion, easy to synthesize and functionalize, and have tunable localized surface plasmon resonance (LSPR).[296–298] These gold nanorods have bene previously used for PA-based cell tracking,[299] cancer imaging,[300–302] oxidative stress sensing,[303] and theranostics.[304,305]

PA imaging uses pulsed illumination to produce pressure waves that are detectable by conventional ultrasound transducers, where the absorption of light heats the nanoparticle in the millikelvin range.[306] The increase in nanoparticle temperature causes a thermal expansion that creates a pressure wave that propagates through the medium. There are several methods to enhance the PA signal created from AuNRs. First, is to increase the laser fluence and decreasing the pulse

width.[307,308] Second, is to increase the concentration of contrasting agent.[309] Third, is to functionalize and coat the surface with ligands reduce the thermal resistance at the particle-medium interface.[310–312] Engineering AuNRs with LSPRs and which are responsive to chemical cues has been the most common technique for PA signal modulation.[308,313]

My contribution for this collaborative project were to determine the interactions of two ligands on the nanoparticle surfaces, cetrimonium bromide (CTAB) and potassium hexacyanoferrate(III) (HCF). CTAB was used to stabilize and create monodisperse nanoparticles while HCF was used to selectively remove a silver shell in a previous control experiment. In the previous experiment, HCF was added to Ag_2S/Ag_2Se-AuNR to act as a "negative control", where PA enhancement was not supposed to happen. However, there was a surprising ~40-fold PA enhancement for two coatings over bare AuNR. This enhancement negated the negative control and additional studies had to be done. The objective of the current project is to investigate why there was a ~40-fold PA enhancement with the addition of HCF to Ag_2S/Ag_2Se-AuNR. Herein, ATR-FTIR spectroscopy was used to investigate the interactions of HCF with CTAB and the particle surfaces.

8.1.3 Materials

All ligands and nanoparticles were provided by the Yash Mantri from the Jokerst Group at UCSD. The comprehensive material list, nanoparticle synthesis, and characterization can be found in the published paper.[314]

8.1.4 Attenuated Total Reflectance-Fourier Transform Infrared Spectroscopy Method

Infrared spectra were collected using a Nicolet iS10 FTIR spectrophotometer with a mercury cadmium telluride detector. Spectra were averaged over 100 scans with a 4 cm^{-1} resolution over the spectral range from 750 to 4000 cm^{-1}; OMNIC 9 software was used to collect data. The

software was also used for background subtractions and baseline corrections. For solution-phase spectra, samples were pipetted onto the AMTIR crystal and covered. The chamber was purged with dry air to remove atmospheric gases for approximately 30 min before each spectrum was collected. All *in-situ* spectroscopic measurements involved collecting spectra every 2.5 min during an aqueous over the sample as described below.

For dynamic, *in-situ* measurements, a dry nanoparticle thin film was first created by drop casting 1 mL of a ~27 nM nanoparticle concentration onto the crystal and dried overnight with a continuous dry air purge. For displacement reactions on silver chalcogenide coated-AuNRs, water was flowed at ~1 mL/min for 60 min to remove loose particles followed by a background scan.

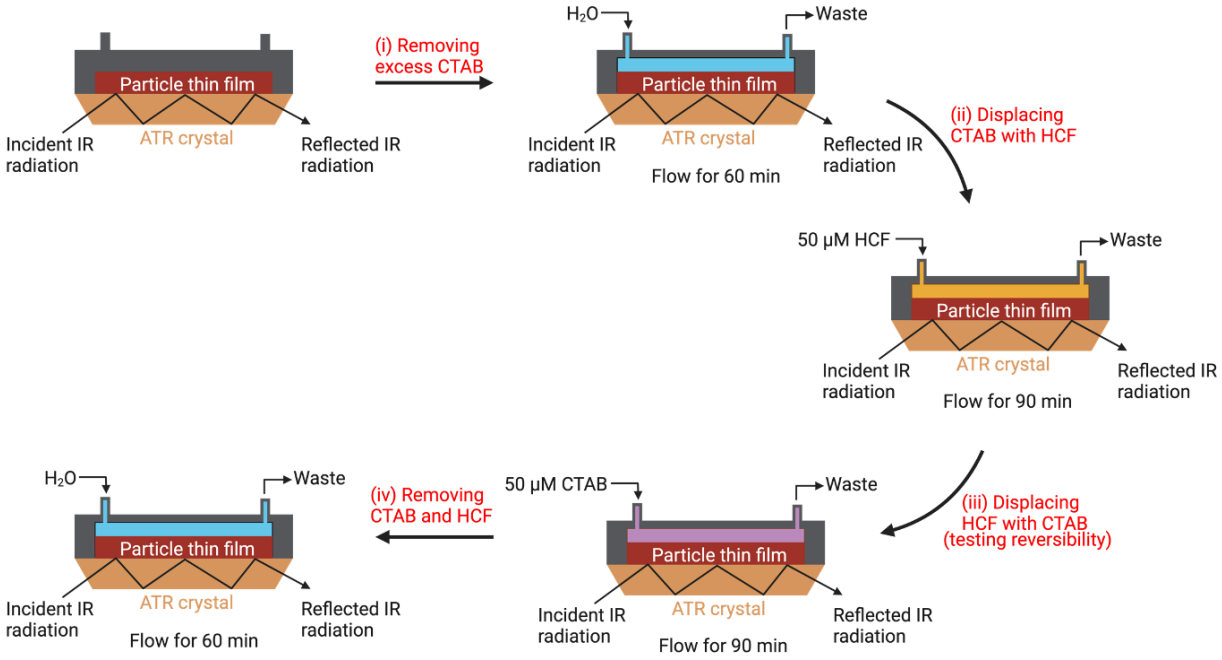

Figure 8.1 Experimental setup for *in-situ* dynamic ATR-FTIR measurements

A dry nanoparticle thin film was first created by drop casting 1 mL of a ~27 nM nanoparticle concentration onto the crystal and dried overnight with a continuous dry air purge. (i) For displacement reactions on silver chalcogenide coated-AuNRs, water was flowed at ~1 mL/min for 60 min to remove loose particles followed by a background scan. (ii) Next, 50 µM HCF was flowed over for the film for 90 min and another scan was taken. (iii) Then, 50 µM CTAB was flowed over the thin film for 90 min and another scan was taken. (iv) Finally for desorption, water was flowed over the film for 60 min.

Next, 50 µM HCF was flowed over for the film for 90 min and another scan was taken. Then, 50

μM CTAB was flowed over the thin film for 90 min and another scan was taken. Finally for desorption, water was flowed over the film for 60 min.

For displacement reactions on AuNR, a dried particle film was created by drop casting 1 mL of ~27 nM particles onto the AMTIR crystal and dried overnight. Water background, HCF adsorption, CTAB displacement and water desorption were similarly done as previously mentioned but at ~0.2 mL/min. The flow rate was reduced to minimize film dewetting on the AMTIR crystal because the AuNR thin film was less stable on the AMTIR crystal compared to the silver chalcogenide coated AuNRs. **Figure 8.1** shows a cartoon for the experimental setup for the ATR-FTIR spectral measurements.

8.1.5 Results and Discussion

Figure 8.2a and **Figure 8.3a** show the dried thin film spectrum of CTAB-stabilized Ag_2S/AuNR and Ag_2Se/AuNR, respectively. Significant v(C-H) vibrations at 2917 and 2849 cm^{-1} from methyl and methylene groups from CTAB coatings are observed with both particles. The particles also had a strong positive zeta potential before HCF addition due to CTAB stabilization.[315] This suggests that a large amount CTAB was present in the colloidal suspension and that CTAB remained on the film when the suspension was dried. For the *in-situ* temporal adsorption spectra, water was initially flowed over the film to remove excess CTAB and loose particles (**Figure 8.4a**). CTAB related peaks decreased with minimal peak shifts, thus indicating the removal of excess CTAB only. Flowing water for 60 minutes results a plateau for CTAB peak intensity changes; the maximum amount of CTAB is removed from the particle surface at this point (**Figure 8.4b**).

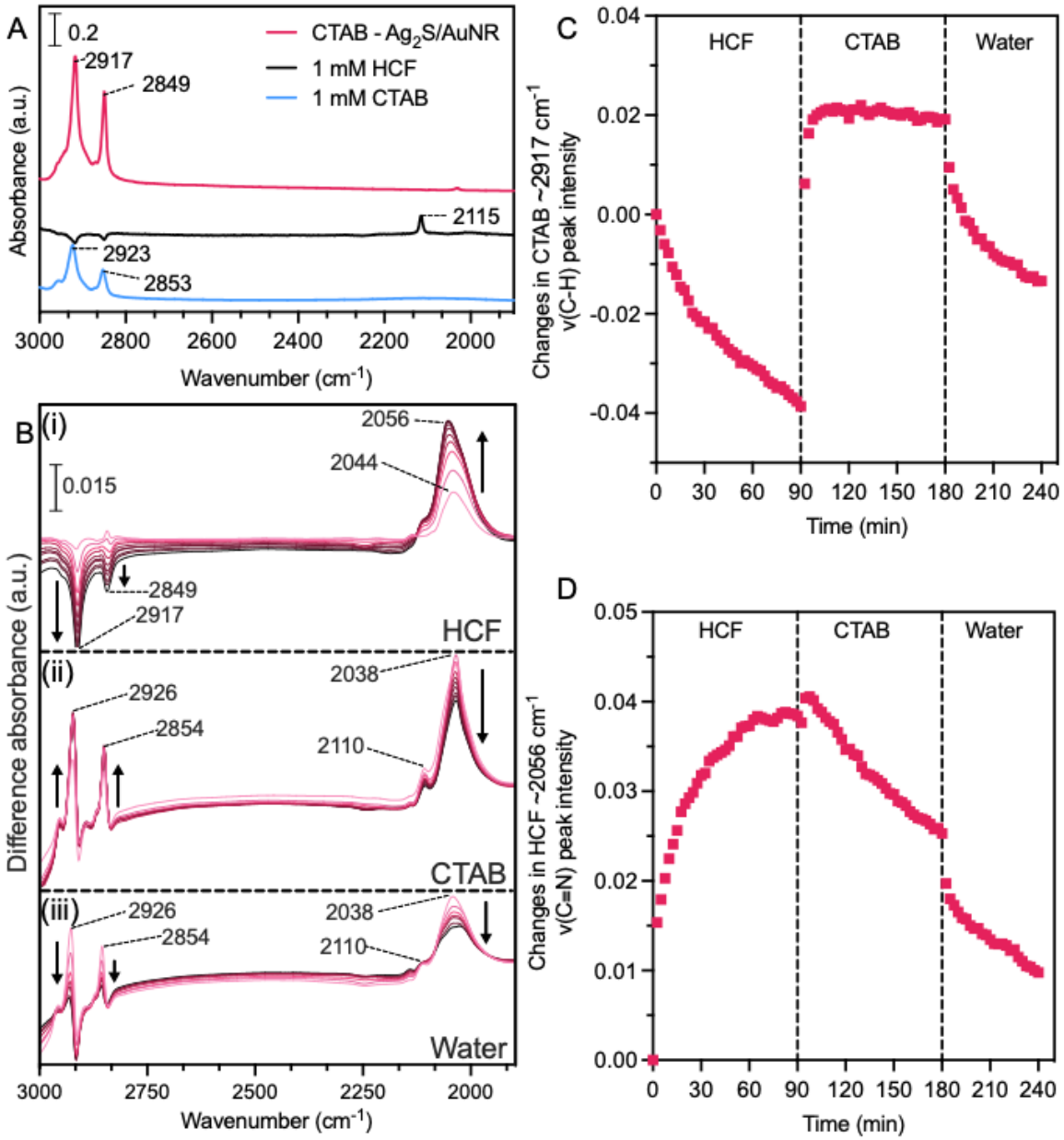

Figure 8.2 Dynamic *in-situ* ATR-FTIR spectra of Ag_2S/AuNR upon HCF treatment

A) Reference spectra for a dried thin film of CTAB-stabilized Ag_2S/AuNR on an AMTIR crystal; 1 mM solution phase HCF and 1 mM solution phase CTAB are shown. B). Here, in-situ time dependent ATR-FTIR difference spectra for a CTAB stabilized Ag_2S/AuNR following: (i) 50 µM HCF flow adsorption. Increase in the 2056 cm^{-1} ν(C≡N) band with the simultaneous decrease in the 2917 and 2849 cm^{-1} ν(C-H) bands as a function of time suggesting a displacement of CTAB with HCF; (ii) 50 µM CTAB flow adsorption following HCF adsorption. CTAB can partially desorb loosely bound HCF while forming multilayers on direct surface bound HCF as seen by a change in peak intensity as a function of time; and (iii) water desorption flow. These spectra show the desorption of multilayer CTAB and changes to the surface coordination of adsorbed HCF. Temporal spectra in B are collected every 10 minutes from light to dark coloration. C) Changes in the CTAB ~2917 cm^{-1} ν(C-H) peak intensity. D) Changes in the HCF 2056 cm^{-1} ν(C≡N) peak intensity.

Figure 8.2b shows the *in-situ* ATR-FTIR spectra as HCF, CTAB, and water are flowed across the nanorod film (three consecutive flow streams after the initial water wash). The 2044 cm^{-1} peak appears as the HCF flowed over the Ag_2S/AuNR thin film while the CTAB ν(C-H) 2917 and 2849 cm^{-1} decreases (**Figure 8.2b(i)**). This suggests that HCF has higher affinity for the nanoparticle surface and displaces CTAB. Solution phase 50 μM HCF has negligible spectral absorbance values and minimally contributes to the adsorbed intensity (data not shown).

Surface interactions were determined using the 1 mM HCF solution phase spectra (**Figure 8.2a**) as a reference. The 2115 cm^{-1} peak for the 1mM HCF solution phase is assigned to the ν(C≡N) vibrational mode. The 2044 cm^{-1} peak appears when HCF is adsorbed onto Ag_2S/AuNR. Versus the 2115 cm^{-1} solution phase peak, the adsorbed 2044 cm^{-1} peak is broader and shifts to a lower peak position, thus indicating that HCF is complexing with the surface.

Solution phase HCF is a centrosymmetric molecule and when adsorbed onto the nanorod surface, the symmetry changes and new peaks appear.[316] The interaction with the surface also leads to broadening of the infrared peaks. Previous studies also report strong interactions of ferro- and ferricyanide ions adsorbing onto Ag electrodes via an Ag-C≡N.[317] At earlier time points and subsequently low surface coverage, the initially adsorbed HCF peak appears at 2044 cm^{-1}. The peak shifts to 2057 cm^{-1} at higher surface coverage. The peak shift as adsorption time increases could suggest a surface concentration-dependent interaction with the Ag_2S/AuNR surface.

Following the adsorption of HCF, CTAB was flowed over the film to observe any reversible displacement reactions (**Figure 8.2b(ii)**). Positive peaks at 2926 and 2854 cm^{-1} are now observed to increase in intensities and are assigned to CTAB ν(C-H). Interestingly, the 2926 and 2824 cm^{-1} peak more closely resemble solution phase CTAB but are different than the displaced peak positions at 2917 and 2854 cm^{-1} when flowed with HCF. This suggests that the CTAB is

forming a multilayer on top of HCF rather than interacting directly with the Ag_2S/AuNR surface, supporting that HCF has a higher affinity to the surface than CTAB. A slight decrease in the 2038 cm^{-1} HCF peak is observed and could be due to the desorption of loosely bound HCF. Additionally, the ν(C≡N) peak shape narrowed, and the position shifted from 2057 cm^{-1} to 2038 cm^{-1} when CTAB was flowed over the HCF-adsorbed film. Introducing CTAB into the aqueous flow caused multilayer interactions between HCF and CTAB.

When the thin film is desorbed with pure water (**Figure 8.2b(iii)**), there is a drastic decrease in the ν(C-H) 2926 and 2854 cm^{-1} peak intensity indicating that the multilayer CTAB is reversibly adsorbed. HCF also desorbs as noted by the decrease in peak intensities. Peak broadening is also seen suggesting low surface coverage conditions.

Similar analyses can be made with Ag_2Se/AuNR (**Figure 8.3**). When the film is flowed with HCF, the surface-complexed HCF 2049 cm^{-1} peak appears while a loosely bound CTAB is displaced. With the CTAB and water desorption flow streams, HCF related peaks can be seen to decrease, indicating partial desorption. Multilayer reversible CTAB adsorption is observed with the ν(C-H) peak positions resembling solution phase positions and with intensities falling to baseline values. When comparing the adsorbed HCF spectra between Ag_2S/AuNR and Ag_2Se/AuNR, varying surface complexation modes are seen as noted by the HCF peak position and broadening. This suggests that the surface complexation mode is dependent on nanoparticle composition and surface coverage. The slight desorption of HCF from Ag_2Se/AuNRs (27-fold) could explain the lower PA enhancement compared to Ag_2S/AuNRs (42-fold).

Bare AuNRs show minimal adsorption of HCF and CTAB (**Figure 8.5**). When water is finally flowed over the AuNRs, all molecules are completely desorbed, thus suggesting a fully reversible physisorption process. Thus, HCF is directly complexed with the chalcogenide coating

and not the core gold nanorod. This explains why AuNRs treated with HCF show no PA enhancement.

8.1.6 Conclusion

In this work, we report the surprising PA enhancement of silver chalcogenide-coated gold nanorods upon treatment with HCF. HCF treated nanoparticles showed no changes in absorbance but a significant (up to 42-fold) PA enhancement. Ag_2S/AuNRs showed higher PA efficiency compared to Ag_2Se/AuNRs. Dynamic *in-situ* interactions between HCF and the silver chalcogenide surfaced revealed the irreversible displacement of CTAB with HCF from the nanoparticle shell surface. HCF was shown to specifically interact with the Ag_2S/Ag_2Se shell and not the AuNR core, explaining why the PA enhancement was only observed for the coated AuNRs. Herein, is an example of how the composition of surface species can influence the properties of nanoparticles. This shows how ATR-FTIR spectroscopy can be used to probe the nanoparticle surface to gain insight into the interactions of molecular species.

8.1.7 Supplemental Information

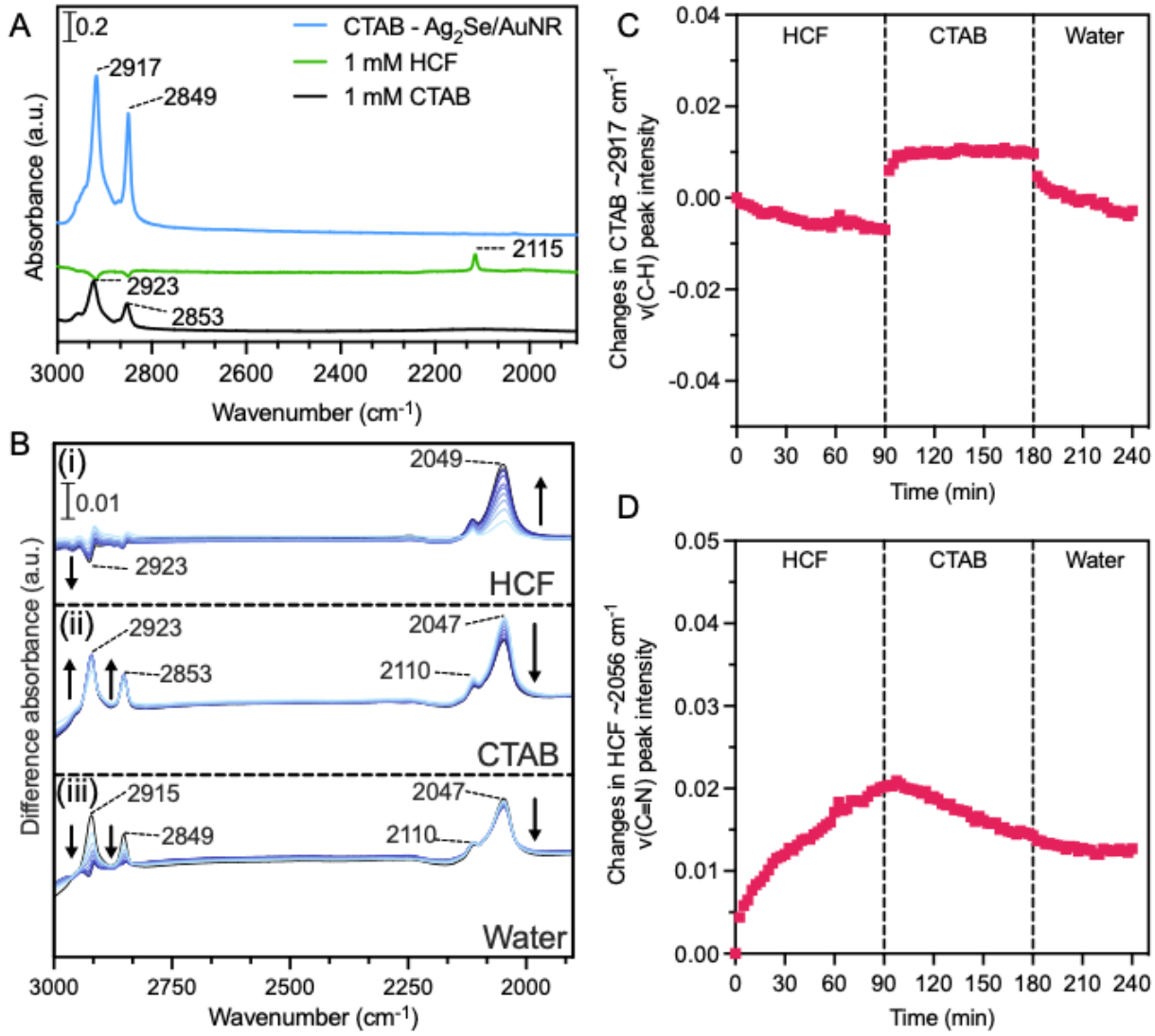

Figure 8.3 Dynamic *in-situ* ATR-FTIR spectra of Ag_2Se/AuNR on HCF treatment

A) Reference spectra for dried thin film of CTAB stabilized Ag_2Se/AuNR on an AMTIR crystal, 1 mM solution phase HCF and 1 mM solution phase CTAB. B) in-situ time dependent ATR-FTIR difference spectra for a CTAB stabilized Ag_2Se/AuNR following: (i) 50 µM HCF flow adsorption. Increase in the 2049 cm^{-1} ν(C≡N) band with the simultaneous decrease in the 2923 cm^{-1} ν(C-H) bands as a function of time suggesting a displacement of CTAB with HCF. (ii) 50 µM CTAB flow adsorption following HCF adsorption. CTAB can partially desorb loosely bound HCF while forming multilayers on directly surface bound HCF as seen by a change in peak intensity as a function of time. (iii) water desorption flow. These spectra show the desorption of multilayer CTAB and changes to the surface coordination of adsorbed HCF. Temporal spectra in B are collected every 10 minutes from light to dark coloration. C) Changes in the CTAB ~2923 cm^{-1} ν(C-H) peak intensity. D) Changes in the HCF 2049 cm^{-1} ν(C≡N) peak intensity.

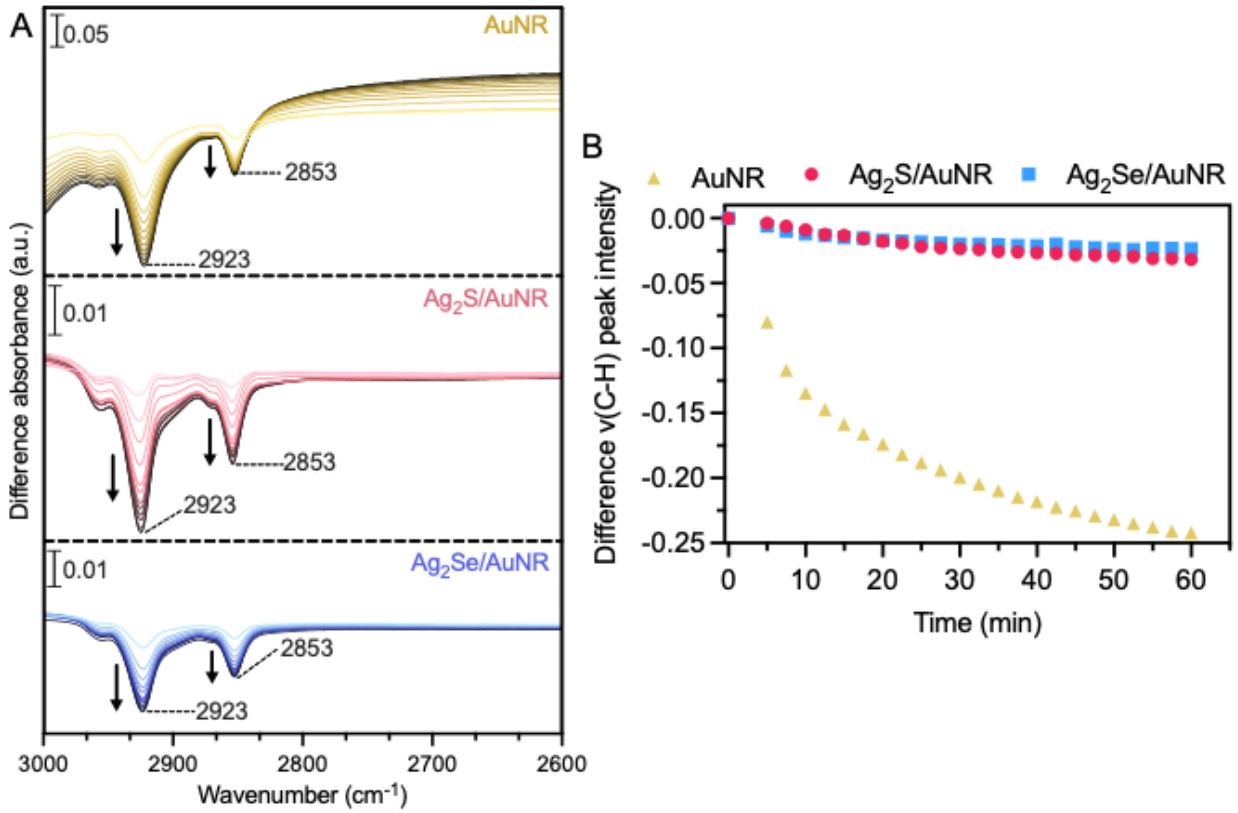

Figure 8.4 Time dependent ATR-FTIR difference spectra for initial water wash show CTAB desorption.

A) ATR-FTIR spectra of 60 min water wash for AuNR (gold), Ag_2S/AuNR (pink), and Ag_2Se/AuNR (blue) show decrease in ν(C-H) peaks indicating CTAB desorption. Note the larger scale bar for AuNR, suggesting significant removal of CTAB compared to Ag_2S/AuNR and Ag_2Se/AuNR. B) Changes in the CTAB ~2923 cm^{-1} ν(C-H) peak intensity.

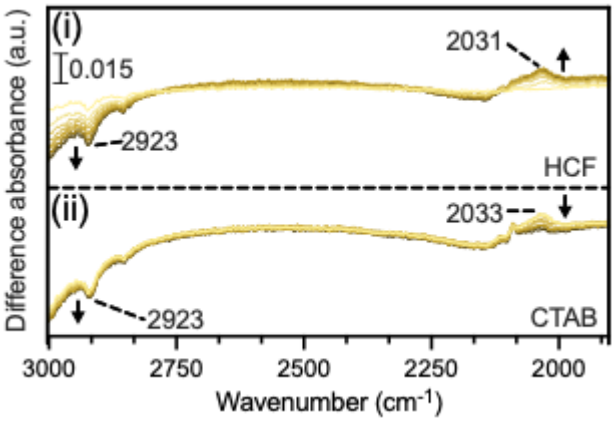

Figure 8.5 Dynamic *in-situ* ATR-FTIR spectra of AuNR on HCF treatment

(i) HCF is seen to displace CTAB noted by the positive 2031 cm^{-1} ν(C≡N) peak and negative 2923 cm^{-1} ν(C-H) peak. (ii) CTAB is seen to fully desorb HCF noted by the drastic decrease in the 2033 cm^{-1} peak intensity. This suggests that HCF is loosely bound to the AuNR surface and not directly coordinated. Spectra are shown every 10 minutes from light to dark coloration.

8.2 Evaluation of CuO Nanoparticle Toxicity on 3D Bioprinted Human iPSC-derived Cardiac Tissues

8.2.1 Introduction

According to the World Health Organization (WHO), air pollution is the single largest environmental threat to human health.[318,319] In 2015, ambient air pollution was responsible for 4.2 million deaths worldwide, and is projected by 2060 to cause 6 to 9 million deaths per year.[320] Mounting epidemiological evidence on the negative health effects of air pollution suggests that the morbidity and mortality is increased in non-communicable diseases, such as cardiovascular and respiratory diseases.[318–320] When air pollution is evaluated, small particulate matter (PM), a mixture of solid and liquid particles of organic and inorganic substances suspended in air, is considered to be a key player in contributing to disease.[318,319,321] Of these particles, nanoparticles (NP, PM less than 100 nm in diameter), are being increasingly recognized as a significant health hazard. In the years between reports published in 2005 and 2021, the WHO determined that enough

epidemiological evidence had been reached to connect NP exposure with a variety of short term and long term health effects, and recommended general guidelines for the particulates.[318] However, the mechanisms leading from NP exposure to long term health effects, particularly cardiovascular diseases, are not well studied or understood. Current hypotheses suggest that through a variety of pathways, nanoparticles can increase the amount of reactive oxygen species (ROS) to a level above what the body can handle, leading to oxidative stress.[321] In one proposed mechanism, inhaled NPs are translocated across the alveolar membrane into the bloodstream, after which they can interact with the vascular endothelium before settling in secondary organs, affecting function.[321–323]

Many nanoparticles that are prevalent in industrial or polluted environments are reported to elicit inflammation and genotoxicity, which can promote abnormal cardiac function.[324–326] The impact and toxicity of these particles on physiological systems are of great importance to determine the safety and efficacy of nanoparticles. This is done to develop regulatory affairs to guide the usage of nanoparticles. As an example of how these risk assessment studies guides the usage of nanoparticles, in August 2022 the European Union has banned the use of a specific titanium dioxide as a food whitener, citing the potential genotoxicity of consuming the additive.[327] Previously, titanium dioxide was regarded as a non-hazardous material but as more research and studies are done, risk assessments can change. Despite this one example case, there are thousands of types of nanoparticles incorporated into consumer products and incidentally produced as process by products that have not been assessed for human exposure.[328] Therefore, there is a need to investigate the impact of nanoparticles on human health.

Most current studies evaluating NP toxicity in heart tissue are either in animal models or 2D culture models, where both have limitations. Although animal models can showcase complex organ response, intrinsic species-species differences often make results and dosing studies non-

translatable. For example, mouse models have resting heart rate 10 times higher than the average human and differences in pharmacokinetic properties.[329,330] Although 2D culture models are an appealing *in vitro* model, they lack important extracellular-cell, cell-cell, and cell-tissue interactions, and do a poor job replicating an *in vivo* heart response.[329,331,332] In a previous study by the Chen group at UCSD, they were able to print a 3D cardiac tissue with both alignment and stress cues, leading to a microtissue exhibiting beating phenotype.[333]

For this study, we tested the impact of CuO (copper oxide) NPs on cardiac micro-tissues. CuO NPs are one of the most toxic metal oxide nanoparticles, yet are widely used in many commercial fields including batteries, surfactants, paints and textiles, antimicrobial agents.[334–337] Thus, the need for greater understanding of the toxicological effect of CuO NPs is paramount, so that we can develop better protective therapies. However, there are limited *in vitro* studies investigating the impacts of the NPs in human cardiac cells [338], and even fewer in 3D cardiac tissue.[339] Before the NPs reach cardiac tissue in an in vivo setting, interactions with proteinaceous bodily fluid will occur, such as blood or lung epithelial, and proteins can adsorb onto the NP. Protein adsorption has been shown to alter NP physicochemical properties and decrease toxicity.[340,341] For this reason, CuO were coated with bovine serum albumin (BSA) to mimic the adsorption of a model protein. BSA is often used as a substitute for human serum albumin due to its properties and structural similarities.[342] We decided to add to this growing research by dosing our previously developed cardiac microtissues with 0 μg/mL, 0.1 μg/mL, 1 μg/mL, 10 μg/mL, and 100 μg/mL. We evaluated the impact of increasing dose on the viability of the micro-tissues utilizing a CCK-8 assay, discovering a LD_{50} of 7.176 μg/mL. We then utilized our pillar model to evaluate the impact of toxicity on beating frequency and force output, observing a downward trend in tissue force as toxicity increased. Lastly, we investigated the pathways of cardiac toxicity,

observing an increase in apoptosis markers as well as mitochondrial biogenesis. For this project, I was responsible for providing the protein coated nanoparticles that were used for the *in vitro* cardiac tissue toxicity studies.

8.2.2 Copper Oxide Nanoparticle Coating and Characterization

CuO nanoparticles were purchased from US Research Nanomaterials and then subsequently characterized. CuO nanoparticles were calcined at 200 °C for 3 hours to sterilize and remove any adsorbed organics. The crystalline phase of CuO was confirmed to be tenorite using X-ray diffraction with an APEX II ultra-diffractometer with Cu Kα radiation at $\lambda = 1.54056$ Å. For primary nanoparticle size, an aqueous suspension of 0.005 g/L was sonicated using a 750 W probe sonicator at 20% amplitude for 60 seconds with 15 seconds rest over 30 minutes in a room temperature water bath. From the sonicated solution, a 15 μL aliquot was drop casted onto a formvar/carbon-coated 100 mesh copper grid and dried. The CuO nanoparticles on the copper grid was imaged using an 80 kV JEOL-1400 plus transmission electron microscope (TEM). Particle size was analyzed using ImageJ software for more than 100 particles. Specific surface area was determined using a Quantachrome Nova 4200e BET apparatus. Triplicate samples were degassed at 200 °C for 3 hours and a 15-multipoint isotherm was collected between P/P_0 of 0.05-0.95.

8.2.3 Copper Oxide Nanoparticle Surface Adsorption Characterization by ATR-FTIR Spectroscopy

Attenuated total reflectance-Fourier transform infrared (ATR-FTIR) spectroscopy was used to characterize coated copper oxide nanoparticles. Infrared spectra were collected using a Nicolet iS10 Fourier Transform Infrared Spectroscope from Thermo-Fisher equipped with a mercury cadmium telluride detector. Spectra was collected at a resolution of 4 cm^{-1} between 750 to 4000 cm^{-1} and averaged over 100 scans using OMNIC 9 software. Spectra were linearly baseline

corrected between 900 to 1800 cm^{-1}. All spectra taken were after purging the sample chamber with zero air for approximately 30 minutes. 5 mg of CuO in 500 µL MilliQ water solution was sonicated for 30 seconds and then drop casted onto an amorphous material transmitting IR radiation (AMTIR) crystal and dried overnight. MilliQ water was introduced into the flow cell over the CuO nanoparticle thin film for 30 minutes at ~1 mL/min to remove loose particles and to collect a

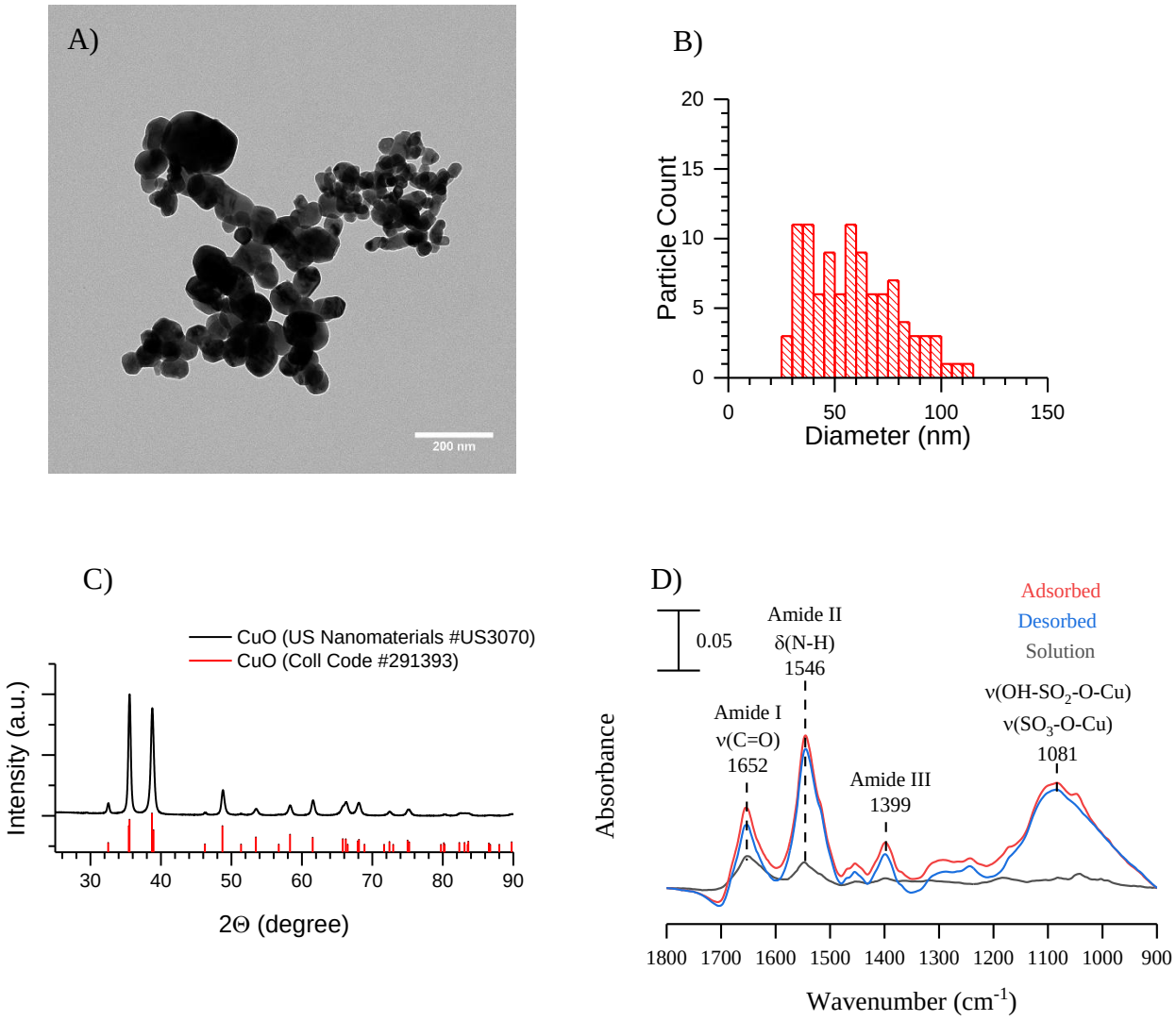

Figure 8.6 CuO nanoparticle characterization

(A) TEM micrograph of CuO NPs. (B) Size histogram of CuO nanoparticle taken from TEM and averaged over 100 particles. Average particle size is 60 ± 23 nm. (C) XRD diffractograms of CuO nanoparticles with reference patterns. (D) ATR-FTIR spectra of solution phase 0.05 wt% BSA in RPMI media (black), adsorbed spectra after 180 minutes on CuO nanoparticle film (red), desorbed spectra after 120 minutes (blue).

background spectrum. A solution of 0.05 wt% (BSA) in RPMI media was titrated to pH 7.4,

sonicated for 30 minutes, and diluted 5-fold with MilliQ water. The solution was flowed over the nanoparticle film at a rate of ~1 mL/min for 180 minutes and a spectrum was taken. To facilitate desorption, MilliQ water was flowed over the film for 120 minutes and a spectrum was taken.

8.2.4 Preparation of Copper Oxide Nanoparticles for Cardiac Micro-Tissue Dosing

The coating and dispersion method was adapted from a dispersion standard operating procedure but done at room temperature. To prepare CuO nanoparticles for *in vitro* studies, nanoparticles were simultaneously dispersed and coated with BSA. 15.36 mg of CuO were first weighed out and pre-wetted with 30 µL of EtOH. 6 mL of 0.05 wt% BSA in RPMI media was added to the nanoparticles and titrated to pH 7.4. The colloidal suspension was sonicated for 30 minutes using the same method for sonication as previously mentioned. Prior to *in vitro* studies, sonicated samples were diluted to 100 µg CuO/mL with RPMI and analyzed using a Malvern Zetasizer Nano dynamic light scattering instrument in triplicate measurements.

8.2.5 Results and Discussion

Figure 8.6a is a TEM micrograph of CuO NPs and the size distribution analysis is shown in **Figure 8.6b**. Size analysis shows a primary particle size of 60 ± 23 nm. XRD confirms the CuO tenorite phase (**Figure 8.6c**). The specific surface area was measured as 7 ± 1 m^2/g. DLS for BSA coated CuO measured a hydrodynamic size of 140 ± 72 nm and a zeta potential of -9 ± 2 mV.

NPs were coated with BSA to mimic the adsorption of nonspecific proteins if exposed to the blood stream, a highly proteinaceous medium, before reaching the cardiac tissue. ATR-FTIR spectra can be seen of solution phase BSA in RMPI, adsorbed BSA on CuO, and post desorption in **Figure 8.6d**. Solution phase BSA has several absorption bands at 1652, 1546 and 1399 cm^{-1} representing the Amide I, II and III band, respectively. Comparison between solution and adsorbed spectra can be done where any spectral differences can be attributed to surface adsorption and

interactions. The Amide I band (1,700 to 1600 cm^{-1}) and the Amide II bands (1600 to 1500 cm^{-1}) are highly sensitive to the surrounding environment and represent protein secondary structure. As a qualitative measurement, the intensity ratio of Amide I/II can be indicative of conformational changes between two systems. In the case of solution phase the Amide I/II, the ratio is > 1. However, when adsorbed onto CuO, the Amide I/II ratio is < 1. This suggests that the adsorption process is altering protein conformation. This aligns well with previous literature that also report changes to adsorbed BSA conformation on TiO_2 and SiO_2.[18,28,47] Interestingly, a when the RMPI-BSA solution is adsorbed to CuO, a broad band appears between 1,200 and 900 cm^{-1} that is not seen in solution phase. A component of RMPI, is HEPES buffer which contain sulfate groups. Sulfate has been observed to strongly adsorbed and complex with surfaces resulting in broad band seen between 900 and 1200 cm^{-1} region. [10,101] Therefore, the broad bands observed in the spectra are due to S-O stretch of adsorbed sulfate. Upon desorption, the spectrum changes very little and indicates negligible changes to peak position and intensity when compared to adsorbed, suggesting BSA and adsorbed sulfate groups are irreversibly adsorbed.

8.2.6 Conclusion

This study successfully showcased the utility of the cardiac micro-tissue platform for evaluating the toxic impact of the environmental pollutant, CuO NPs. Because 3D tissues recapitulate the cell-cell, cell-tissue, and cell-extracellular matrix interactions that influence cell behavior, it is vital to evaluate the phenotypic and genotypic responses of cells to NPs in these formats. However, to date, only one study has been previously published investigating the behavior of CuO NPs in cardiac micro-tissues [339].

In this study, we found that the response to CuO NPs is highly dose dependent, and half of all the cardiac tissue was dead at a concentration of 7.176 μg/mL. Interestingly however, the

beating frequency of the tissue was not significantly impacted at doses up to 10 μg/mL, suggesting that the electrical signaling pathways related to contraction are not significantly impacted by CuO NPs. Conversely, relative displacement of the small pillar by the cardiac tissue was significantly impacted at 10 μg/mL at 48 hours. This suggests two things; 1) that even though current *in vitro* research for NP dosing is often up to a max of 48 hours, longer time points may showcase more toxicity, perhaps at even lower doses than 10 μg/mL and 2) that the increase in apoptotic cells indicated by both the CCK-8 data and qPCR analysis leads to a decrease in force output.

The study showcased how both functional output data and gene expression data can be extracted from a single model to further understand the toxicity of nanoparticles. Future studies should interrogate additional doses between 10 μg/mL and 100 μg/mL to further understand the impact on mitochondrial biogenesis. Moreover, these studies should be investigated for a longer period to gain further knowledge on the dose dependent nature of toxicity, especially as most of the population will be interacting with small doses of environmental pollution over a long period of time. With these studies, we are hopeful that new therapies can be derived to combat the increasing threat of environmental pollution.

8.3 Acknowledgements

A portion of Chapter 8 is reproduced with permission from Journal of Physical Chemistry C. Mantri, Y.; Sit, I.; Zhou, J.; Grassian, V. H.; Jokerst, J. V. Photoacoustic Enhancement of Ferricyanide-Treated Silver Chalcogenide-Coated Gold Nanorods. 2022, 126 (17), 7605–7614. The dissertation author is a co-author of this paper. A portion of Chapter 8 has been submitted for publication of the material as it may appear in Environmental Science and Technology. Miller, K. L.; Sit, I.; Xiang, Y.; Wu, J.; Pustelnik, J.; Tang, M.; Kiratitanaporn, W.; Grassian, V. H.; Chen,

S. Evaluation of CuO Nanoparticle Toxicity on 3D Bioprinted Human iPSC-derived Cardiac Tissues. The dissertation author is a co-author of this paper.

Appendix A: Generalized 2DCOS MATLAB Code

```
%%for data input, create a matrix named data2 with, row 1 as perturbation variable increments
        %%column 1 as the x-axis spectral variable i.e. 900-1800 cm-1

%%numspec is an array used to count how many spectra there are
%%wavenum is the wave number array
%%dens is the contour line density, can change this variable to change the density of contour lines for the 2D maps.
%% n is number of spectra in the data set using numspec
%%data is the data matrix where the first column is the wavenumbers

%name of the plots, will be appended with “Asynchronous” or “Synchronous” then name string
name = 'Solution Acetic Acid';

%sets data equal to the input data set, datasafe is a variable that is
%unmodified that contains the data set
data = data2(2:end,:);

%takes the average of the data set across one row, returning a column
%vector. so this takes the average at one wavenumber for every temperature
avg = mean(data(:,2:end),2);
%subtracting the avg to give a 'dynamic' wavenumber matrix
data = [data(:,1), data(:,2:end)-avg];

numspec = data(1,2:end);
wavenum = data(:,1);
dens = 20;
n = length(numspec);

synch = data(:,2:end) * (data(:,2:end)')/(n-1);

N = zeros(n);

%populates the first row with 1/(pi*integer)
for i=2:(n)
   N(1,i) = 1/(pi * (i-1));
end
%sets top-right half diagonals equal to previous (i-1,j-1)
for i=2:(n-1)
   for j=i:(n)
      N(i,j) = N(i-1,j-1);
   end
end
%sets the bottom left side equal to the negative of top right half
for i=2:(n)
   for j=1:i
      N(i,j) = -N(j,i);
   end
end

asynch = data(:,2:end) * N * data(:,2:end)'/(n-1);
asynch = asynch';
```

```
%%you can change the axis dimensions with uncommenting the axis, xticks and ytick lines.

figure;
meshgrid(wavenum,wavenum);
contour(wavenum,wavenum,asynch,dens);
colorbar;
title(['Asynchronous ', name])
set(gca,'Ydir','reverse');
set(gca,'Xdir','reverse');
% axis([1700, 1600,1700, 1600])
% xticks(1700:-10:1600)
% yticks(1700:-10:1600)

figure;
meshgrid(wavenum,wavenum);
contour(wavenum,wavenum,synch,dens);
colorbar;
title(['Synchronous ', name])
set(gca,'Ydir','reverse');
set(gca,'Xdir','reverse');
% axis([1700, 1600,1700, 1600])
% xticks(1600:10:1700)
% yticks(1600:10:1700)

[rowsize, colsize] = size (asynch);
autocorr = [];
for row = 1:rowsize
      autocorr = [autocorr, synch(row,row)];
end

autocorr = autocorr';
figure;
plot(wavenum,autocorr)
title(['Autocorrelation ', name])
xlim([900 1800])
set(gca,'Xdir','reverse');
% axis([1700, 1600,1700, 1600])
```

Appendix B: Moving Window 2DCOS MATLAB Code

```
%%for data input, create a matrix named data2 with, row 1 as perturbation variable increments
        %%column 1 as the x-axis spectral variable i.e. 900-1800 cm-1

%%numspec is an array used to count how many spectra there are
%%wavenum is the wave number array
%%dens is the contour line density
%% n is number of spectra in the data set using numspec
%%data is the data matrix where the first column is the wavenumbers

%%name of the plots, will be appended with "MW2DCOS" then name string
name = 'Solution 25mM Acetic Acid 1200-1330';

%sets data equal to the input data set, datasafe is a variable that is
%unmodified that contains the data set


intens = data2(2:end,2:end);
temp = data2(1,2:end);
tempplot = temp;
%takes the average of the data set across one row, returning a column
%vector. so this takes the average at one wavenumber for every temperature
avgdata = mean(intens,2);
%subtracting the avg to give a 'dynamic' wav enumber matrix
intens = intens-avgdata;

wavenum = data2(2:end,1);
dens = 50;

avgtemp = mean(temp);
temp = temp-avgtemp;

%concat is to get rid of n-1 problems with differences of the first
%temperature
concat = ones(length(wavenum),1);
concat = concat * eps;

dvdt = diff(intens,1,2)./diff(temp);
dvdt = horzcat(concat,dvdt);

dvdt2 = diff(dvdt,1,2)./diff(temp);
dvdt2 = horzcat(concat,dvdt2);

auto = dvdt.^2;
auto = auto';
synch = dvdt';
asynch = -dvdt2';

figure;
```

```
meshgrid(wavenum,tempplot);
contour(wavenum,tempplot,auto,dens);

title(['MW2DCOS ', name])
set(gca,'Xdir','reverse');
% axis([900, 1800, 0, 150])
% xticks(1600:10:1700)
% yticks(1600:10:1700)
```

References

(1) Lee, J.; Mahendra, S.; Alvarez, P. J. J. Nanomaterials in the Construction Industry: A Review of Their Applications and Environmental Health and Safety Considerations. *ACS Nano* **2010**, *4* (7), 3580–3590. https://doi.org/10.1021/nn100866w.

(2) Weir, A.; Westerhoff, P.; Fabricius, L.; Hristovski, K.; Von Goetz, N. Titanium Dioxide Nanoparticles in Food and Personal Care Products. *Environ. Sci. Technol.* **2012**, *46* (4), 2242–2250. https://doi.org/10.1021/es204168d.

(3) Azimi, A.; Azari, A.; Rezakazemi, M.; Ansarpour, M. Removal of Heavy Metals from Industrial Wastewaters: A Review. *ChemBioEng Rev.* **2017**, *4* (1), 37–59. https://doi.org/10.1002/cben.201600010.

(4) Meng, A.; Zhang, L.; Cheng, B.; Yu, J. Dual Cocatalysts in TiO_2 Photocatalysis. *Adv. Mater.* **2019**, *31* (30), 1807660. https://doi.org/10.1002/adma.201807660.

(5) Arami, H.; Khandhar, A.; Liggitt, D.; Krishnan, K. M. In Vivo Delivery, Pharmacokinetics, Biodistribution and Toxicity of Iron Oxide Nanoparticles. *Chem. Soc. Rev.* **2015**, *44* (23), 8576–8607. https://doi.org/10.1039/c5cs00541h.

(6) Ustunol, I. B.; Gonzalez-Pech, N. I.; Grassian, V. H. pH-Dependent Adsorption of α-Amino Acids, Lysine, Glutamic Acid, Serine and Glycine, on TiO_2 Nanoparticle Surfaces. *J. Colloid Interface Sci.* **2019**, *554*, 362–375. https://doi.org/10.1016/j.jcis.2019.06.086.

(7) Jeng, H. A.; Swanson, J. Toxicity of Metal Oxide Nanoparticles in Mammalian Cells. *J. Environ. Sci. Heal. Part A* **2006**, *41* (12), 2699–2711. https://doi.org/10.1080/10934520600966177.

(8) Abdelhalim, M. A. K. Exposure to Gold Nanoparticles Produces Cardiac Tissue Damage That Depends on the Size and Duration of Exposure. *Lipids Health Dis.* **2011**, *10*, 9. https://doi.org/10.1186/1476-511x-10-205.

(9) Schulz, H.; Harder, V.; Ibald-Mulli, A.; Khandoga, A.; Koenig, W.; Krombach, F.; Radykewicz, R.; Stampfl, A.; Thorand, B.; Peters, A. Cardiovascular Effects of Fine and Ultrafine Particles. *J. Aerosol Med.* **2005**, *18* (1), 1–22. https://doi.org/10.1089/jam.2005.18.1.

(10) Wongrakpanich, A.; Mudunkotuwa, I. A.; Geary, S. M.; Morris, A. S.; Mapuskar, K. A.; Spitz, D. R.; Grassian, V. H.; Salem, A. K. Size-Dependent Cytotoxicity of Copper Oxide Nanoparticles in Lung Epithelial Cells. *Environ. Sci. Nano* **2016**, *3* (2), 365–374. https://doi.org/10.1039/C5EN00271K.

(11) Singh, S. P.; Kumari, M.; Kumari, S. I.; Rahman, M. F.; Mahboob, M.; Grover, P. Toxicity Assessment of Manganese Oxide Micro and Nanoparticles in Wistar Rats after 28 Days of

Repeated Oral Exposure. *J. Appl. Toxicol.* **2013**, *33* (10), 1165–1179. https://doi.org/10.1002/jat.2887.

(12) Situm, A.; Rahman, M. A.; Allen, N.; Kabengi, N.; Al-Abadleh, H. A. ATR-FTIR and Flow Microcalorimetry Studies on the Initial Binding Kinetics of Arsenicals at the Organic–Hematite Interface. *J. Phys. Chem. A* **2017**, *121* (30), 5569–5579. https://doi.org/10.1021/acs.jpca.7b03426.

(13) Dutta, T.; Bagchi, D.; Bera, A.; Das, S.; Adhikari, T.; Pal, S. K. Surface Engineered ZnO-Humic/Citrate Interfaces: Photoinduced Charge Carrier Dynamics and Potential Application for Smart and Sustained Delivery of Zn Micronutrient. *ACS Sustain. Chem. Eng.* **2019**, *7* (12), 10920–10930. https://doi.org/10.1021/acssuschemeng.9b01917.

(14) Wang, X.; Wang, X.; Wang, M.; Zhang, D.; Yang, Q.; Liu, T.; Lei, R.; Zhu, S.; Zhao, Y.; Chen, C. Probing Adsorption Behaviors of BSA onto Chiral Surfaces of Nanoparticles. *Small* **2018**, *14* (16), 1703982. https://doi.org/10.1002/smll.201703982.

(15) Pelaz, B.; del Pino, P.; Maffre, P.; Hartmann, R.; Gallego, M.; Rivera-Fernández, S.; de la Fuente, J. M.; Nienhaus, G. U.; Parak, W. J. Surface Functionalization of Nanoparticles with Polyethylene Glycol: Effects on Protein Adsorption and Cellular Uptake. *ACS Nano* **2015**, *9* (7), 6996–7008. https://doi.org/10.1021/acsnano.5b01326.

(16) Huang, R.; Carney, R. P.; Ikuma, K.; Stellacci, F.; Lau, B. L. T. Effects of Surface Compositional and Structural Heterogeneity on Nanoparticle–Protein Interactions: Different Protein Configurations. *ACS Nano* **2014**, *8* (6), 5402–5412. https://doi.org/10.1021/nn501203k.

(17) Rashid, M.; Price, N. T.; Gracia Pinilla, M. Á.; O'Shea, K. E. Effective Removal of Phosphate from Aqueous Solution Using Humic Acid Coated Magnetite Nanoparticles. *Water Res.* **2017**, *123*, 353–360. https://doi.org/10.1016/j.watres.2017.06.085.

(18) Sit, I.; Xu, Z.; Grassian, V. H. Plasma Protein Adsorption on TiO_2 Nanoparticles: Impact of Surface Adsorption on Temperature-Dependent Structural Changes. *Polyhedron* **2019**, *171*, 147–154. https://doi.org/10.1016/J.POLY.2019.06.036.

(19) Phan, H. T.; Haes, A. J. Impacts of pH and Intermolecular Interactions on Surface-Enhanced Raman Scattering Chemical Enhancements. *J. Phys. Chem. C* **2018**, *122* (26), 14846–14856. https://doi.org/10.1021/acs.jpcc.8b04019.

(20) Wang, F.; Widejko, R. G.; Yang, Z.; Nguyen, K. T.; Chen, H.; Fernando, L. P.; Christensen, K. A.; Anker, J. N. Surface-Enhanced Raman Scattering Detection of pH with Silica-Encapsulated 4-Mercaptobenzoic Acid-Functionalized Silver Nanoparticles. *Anal. Chem.* **2012**, *84* (18), 8013–8019. https://doi.org/10.1021/ac3018179.

(21) Wei, H.; Vikesland, P. J. PH-Triggered Molecular Alignment for Reproducible SERS Detection via an AuNP/Nanocellulose Platform. *Sci. Rep.* **2015**, *5*, 18131. https://doi.org/10.1038/srep18131.

(22) Xie, L.-Q.; Ding, D.; Zhang, M.; Chen, S.; Qiu, Z.; Yan, J.-W.; Yang, Z.-L.; Chen, M.-S.; Mao, B.-W.; Tian, Z.-Q. Adsorption of Dye Molecules on Single Crystalline Semiconductor Surfaces: An Electrochemical Shell-Isolated Nanoparticle Enhanced Raman Spectroscopy Study. *J. Phys. Chem. C* **2016**, *120* (39), 22500–22507. https://doi.org/10.1021/acs.jpcc.6b07763.

(23) Schwaminger, S. P.; Fraga-García, P.; Selbach, F.; Hein, F. G.; Fuß, E. C.; Surya, R.; Roth, H.-C.; Blank-Shim, S. A.; Wagner, F. E.; Heissler, S.; Berensmeier, S. Bio-Nano Interactions: Cellulase on Iron Oxide Nanoparticle Surfaces. *Adsorption* **2017**, *23* (2), 281–292. https://doi.org/10.1007/s10450-016-9849-y.

(24) Zhou, W.; Liu, Y.-L.; Stallworth, A. M.; Ye, C.; Lenhart, J. J. Effects of PH, Electrolyte, Humic Acid, and Light Exposure on the Long-Term Fate of Silver Nanoparticles. *Environ. Sci. Technol.* **2016**, *50* (22), 12214–12224. https://doi.org/10.1021/acs.est.6b03237.

(25) Shakiba, S.; Hakimian, A.; Barco, L. R.; Louie, S. M. Dynamic Intermolecular Interactions Control Adsorption from Mixtures of Natural Organic Matter and Protein onto Titanium Dioxide Nanoparticles. *Environ. Sci. Technol.* **2018**, *52* (24), 14158–14168. https://doi.org/10.1021/acs.est.8b04014.

(26) Lu, R.; Li, W.-W. W.; Katzir, A.; Raichlin, Y.; Yu, H.-Q. Q.; Mizaikoff, B. Probing the Secondary Structure of Bovine Serum Albumin during Heat-Induced Denaturation Using Mid-Infrared Fiberoptic Sensors. *Analyst* **2015**, *140* (3), 765–770. https://doi.org/10.1039/c4an01495b.

(27) Murayama, K.; Tomida, M. Heat-Induced Secondary Structure and Conformation Change of Bovine Serum Albumin Investigated by Fourier Transform Infrared Spectroscopy. *Biochemistry* **2004**, *43* (36), 11526–11532. https://doi.org/10.1021/bi0489154.

(28) Xu, Z. Z.; Grassian, V. H. Bovine Serum Albumin Adsorption on TiO_2 Nanoparticle Surfaces: Effects of pH and Coadsorption of Phosphate on Protein-Surface Interactions and Protein Structure. *J. Phys. Chem. C* **2017**, *121* (39), 21763–21771. https://doi.org/10.1021/acs.jpcc.7b07525.

(29) Kim, J.; Doudrick, K. Emerging Investigator Series: Protein Adsorption and Transformation on Catalytic and Food-Grade TiO_2 Nanoparticles in the Presence of Dissolved Organic Carbon. *Environ. Sci. Nano* **2019**, *6* (6), 1688–1703. https://doi.org/10.1039/C9EN00130A.

(30) Sun, T. Y.; Gottschalk, F.; Hungerbühler, K.; Nowack, B. Comprehensive Probabilistic Modelling of Environmental Emissions of Engineered Nanomaterials. *Environ. Pollut.* **2014**, *185*, 69–76. https://doi.org/10.1016/j.envpol.2013.10.004.

(31) Piccinno, F.; Gottschalk, F.; Seeger, S.; Nowack, B. Industrial Production Quantities and Uses of Ten Engineered Nanomaterials in Europe and the World. *J. Nanoparticle Res.* **2012**, *14* (9 LB-Piccinno2012), 1109. https://doi.org/10.1007/s11051-012-1109-9.

(32) Giese, B.; Klaessig, F.; Park, B.; Kaegi, R.; Steinfeldt, M.; Wigger, H.; von Gleich, A.; Gottschalk, F. Risks, Release and Concentrations of Engineered Nanomaterial in the

Environment. *Sci. Rep.* **2018**, *8* (1), 1565. https://doi.org/10.1038/s41598-018-19275-4.

(33) Gondikas, A. P.; Kammer, F. von der; Reed, R. B.; Wagner, S.; Ranville, J. F.; Hofmann, T. Release of TiO_2 Nanoparticles from Sunscreens into Surface Waters: A One-Year Survey at the Old Danube Recreational Lake. *Environ. Sci. Technol.* **2014**, *48* (10), 5415–5422. https://doi.org/10.1021/es405596y.

(34) Gottschalk, F.; Nowack, B. The Release of Engineered Nanomaterials to the Environment. *J. Environ. Monit.* **2011**, *13* (5), 1145–1155. https://doi.org/10.1039/C0EM00547A.

(35) Chen, F.; Zhao, E. R.; Hableel, G.; Hu, T.; Kim, T.; Li, J.; Gonzalez-Pech, N. I.; Cheng, D. J.; Lemaster, J. E.; Xie, Y.; Grassian, V. H.; Sen, G. L.; Jokerst, J. V. Increasing the Efficacy of Stem Cell Therapy via Triple-Function Inorganic Nanoparticles. *ACS Nano* **2019**, *13* (6), 6605–6617. https://doi.org/10.1021/acsnano.9b00653.

(36) Gonzalez-Pech, N. I.; Stebounova, L. V; Ustunol, I. B.; Park, J. H.; Renee Anthony, T.; Peters, T. M.; Grassian, V. H. Size, Composition, Morphology, and Health Implications of Airborne Incidental Metal-Containing Nanoparticles. *J. Occup. Environ. Hyg.* **2019**, *16* (6), 387–399. https://doi.org/10.1080/15459624.2018.1559925.

(37) Stebounova, L. V; Gonzalez-Pech, N. I.; Park, J. H.; Anthony, T. R.; Grassian, V. H.; Peters, T. M. Particle Concentrations in Occupational Settings Measured with a Nanoparticle Respiratory Deposition (NRD) Sampler. *Ann. Work Expo. Heal.* **2018**, *62* (6), 699–710. https://doi.org/10.1093/annweh/wxy033.

(38) Stebounova, L. V; Gonzalez-Pech, N. I.; Peters, T. M.; Grassian, V. H. Physicochemical Properties of Air Discharge-Generated Manganese Oxide Nanoparticles: Comparison to Welding Fumes. *Environ. Sci. Nano* **2018**, *5* (3), 696–707. https://doi.org/10.1039/C7EN01046J.

(39) Karlsson, H. L.; Gustafsson, J.; Cronholm, P.; Möller, L. Size-Dependent Toxicity of Metal Oxide Particles—A Comparison between Nano- and Micrometer Size. *Toxicol. Lett.* **2009**, *188* (2), 112–118. https://doi.org/10.1016/j.toxlet.2009.03.014.

(40) Karlsson, H. L.; Cronholm, P.; Gustafsson, J.; Möller, L. Copper Oxide Nanoparticles Are Highly Toxic: A Comparison between Metal Oxide Nanoparticles and Carbon Nanotubes. *Chem. Res. Toxicol.* **2008**, *21* (9), 1726–1732. https://doi.org/10.1021/tx800064j.

(41) Mudunkotuwa, I. A.; Grassian, V. H. Histidine Adsorption on TiO_2 Nanoparticles: An Integrated Spectroscopic, Thermodynamic, and Molecular-Based Approach toward Understanding Nano–Bio Interactions. *Langmuir* **2014**, *30* (29), 8751–8760. https://doi.org/10.1021/la500722n.

(42) Mudunkotuwa, I. A.; Grassian, V. H. Biological and Environmental Media Control Oxide Nanoparticle Surface Composition: The Roles of Biological Components (Proteins and Amino Acids), Inorganic Oxyanions and Humic Acid. *Environ. Sci.* **2015**, *2* (5), 429–439. https://doi.org/10.1039/c4en00215f.

(43) Mudunkotuwa, I. A.; Al Minshid, A.; Grassian, V. H. ATR-FTIR Spectroscopy as a Tool to Probe Surface Adsorption on Nanoparticles at the Liquid-Solid Interface in Environmentally and Biologically Relevant Media. *Analyst* **2014**, *139* (5), 870–881. https://doi.org/10.1039/c3an01684f.

(44) Precupas, A.; Gheorghe, D.; Botea-Petcu, A.; Leonties, A. R.; Sandu, R.; Popa, V. T.; Mariussen, E.; Naouale, E. Y.; Rundén-Pran, E.; Dumit, V.; Xue, Y.; Cimpan, M. R.; Dusinska, M.; Haase, A.; Tanasescu, S. Thermodynamic Parameters at Bio–Nano Interface and Nanomaterial Toxicity: A Case Study on BSA Interaction with ZnO, SiO2, and TiO2. *Chem. Res. Toxicol.* **2020**, *33* (8), 2054–2071. https://doi.org/10.1021/acs.chemrestox.9b00468.

(45) Xue, M.; Sampath, J.; Gebhart, R. N.; Haugen, H. J.; Lyngstadaas, S. P.; Pfaendtner, J.; Drobny, G. Studies of Dynamic Binding of Amino Acids to TiO_2 Nanoparticle Surfaces by Solution NMR and Molecular Dynamics Simulations. *Langmuir* **2020**, *36* (35), 10341–10350. https://doi.org/10.1021/acs.langmuir.0c01256.

(46) Givens, B. E.; Diklich, N. D.; Fiegel, J.; Grassian, V. H. Adsorption of Bovine Serum Albumin on Silicon Dioxide Nanoparticles: Impact of pH on Nanoparticle-Protein Interactions. *Biointerphases* **2017**, *12* (2), 9. https://doi.org/10.1116/1.4982598.

(47) Givens, B. E.; Xu, Z. Z.; Fiegel, J.; Grassian, V. H. Bovine Serum Albumin Adsorption on SiO_2 and TiO_2 Nanoparticle Surfaces at Circumneutral and Acidic pH: A Tale of Two Nano-Bio Surface Interactions. *J. Colloid Interface Sci.* **2017**, *493*, 334–341. https://doi.org/10.1016/j.jcis.2017.01.011.

(48) Wu, H.; Gonzalez-Pech, N. I.; Grassian, V. H. Displacement Reactions between Environmentally and Biologically Relevant Ligands on TiO_2 Nanoparticles: Insights into the Aging of Nanoparticles in the Environment. *Environ. Sci. Nano* **2019**, *6* (2), 489–504. https://doi.org/10.1039/C8EN00780B.

(49) He, J.; Yang, X.; Men, B.; Bi, Z.; Pu, Y.; Wang, D. Heterogeneous Fenton Oxidation of Catechol and 4-Chlorocatechol Catalyzed by Nano-Fe3O4: Role of the Interface. *Chem. Eng. J.* **2014**, *258*, 433–441. https://doi.org/10.1016/j.cej.2014.07.063.

(50) Morsch, S.; van Driel, B. A.; van den Berg, K. J.; Dik, J. Investigating the Photocatalytic Degradation of Oil Paint Using ATR-IR and AFM-IR. *ACS Appl. Mater. Interfaces* **2017**, *9* (11), 10169–10179. https://doi.org/10.1021/acsami.7b00638.

(51) Long, J.-J.; Liu, B.; Wang, G.-F.; Shi, W. Photocatalitic Stripping of Fixed Reactive Red X-3B Dye from Cotton with Nano-TiO_2/UV System. *J. Clean. Prod.* **2017**, *165*, 788–800. https://doi.org/10.1016/j.jclepro.2017.07.149.

(52) Schmidt, M. P.; Martinez, C. E. Kinetic and Conformational Insights of Protein Adsorption onto Montmorillonite Revealed Using in Situ ATR-FTIR/2D-COS. *Langmuir* **2016**, *32* (31), 7719–7729. https://doi.org/10.1021/acs.langmuir.6b00786.

(53) Gankanda, A.; Cwiertny, D. M.; Grassian, V. H. Role of Atmospheric CO_2 and H_2O

Adsorption on ZnO and CuO Nanoparticle Aging: Formation of New Surface Phases and the Impact on Nanoparticle Dissolution. *J. Phys. Chem. C* **2016**, *120* (34), 19195–19203. https://doi.org/10.1021/acs.jpcc.6b05931.

(54) Jayalath, S.; Wu, H.; Larsen, S. C.; Grassian, V. H. Surface Adsorption of Suwannee River Humic Acid on TiO_2 Nanoparticles: A Study of pH and Particle Size. *Langmuir* **2018**, *34* (9), 3136–3145. https://doi.org/10.1021/acs.langmuir.8b00300.

(55) Lehman, S. E.; Mudunkotuwa, I. A.; Grassian, V. H.; Larsen, S. C. Nano–Bio Interactions of Porous and Nonporous Silica Nanoparticles of Varied Surface Chemistry: A Structural, Kinetic, and Thermodynamic Study of Protein Adsorption from RPMI Culture Medium. *Langmuir* **2016**, *32* (3), 731–742. https://doi.org/10.1021/acs.langmuir.5b03997.

(56) Lehman, S. E.; Morris, A. S.; Mueller, P. S.; Salem, A. K.; Grassian, V. H.; Larsen, S. C. Silica Nanoparticle-Generated ROS as a Predictor of Cellular Toxicity: Mechanistic Insights and Safety by Design. *Environ. Sci. Nano* **2016**, *3* (1), 56–66. https://doi.org/10.1039/C5EN00179J.

(57) Jayalath, S.; Larsen, S. C.; Grassian, V. H. Surface Adsorption of Nordic Aquatic Fulvic Acid on Amine-Functionalized and Non-Functionalized Mesoporous Silica Nanoparticles. *Environ. Sci. Nano* **2018**, *5* (9), 2162–2171. https://doi.org/10.1039/C8EN00618K.

(58) Kolasinski, K. W. *Surface Science: Foundations of Catalysis and Nanoscience, Third Edition*; Wiley, 2012.

(59) Guerrini, L.; Alvarez-Puebla, R. A.; Pazos-Perez, N. Surface Modifications of Nanoparticles for Stability in Biological Fluids. *Materials (Basel).* **2018**, *11* (7), 1154.

(60) Tamura, H.; Mita, K.; Tanaka, A.; Ito, M. Mechanism of Hydroxylation of Metal Oxide Surfaces. *J. Colloid Interface Sci.* **2001**, *243* (1), 202–207. https://doi.org/10.1006/jcis.2001.7864.

(61) Kubicki, J. D.; Kwon, K. D.; Paul, K. W.; Sparks, D. L. Surface Complex Structures Modelled with Quantum Chemical Calculations: Carbonate, Phosphate, Sulphate, Arsenate and Arsenite. *Eur. J. Soil Sci.* **2007**, *58* (4), 932–944. https://doi.org/10.1111/j.1365-2389.2007.00931.x.

(62) Kubicki, J. D.; Paul, K. W.; Kabalan, L.; Zhu, Q.; Mrozik, M. K.; Aryanpour, M.; Pierre-Louis, A.-M.; Strongin, D. R. ATR–FTIR and Density Functional Theory Study of the Structures, Energetics, and Vibrational Spectra of Phosphate Adsorbed onto Goethite. *Langmuir* **2012**, *28* (41), 14573–14587. https://doi.org/10.1021/la303111a.

(63) Kwon, K. D.; Kubicki, J. D. Molecular Orbital Theory Study on Surface Complex Structures of Phosphates to Iron Hydroxides: Calculation of Vibrational Frequencies and Adsorption Energies. *Langmuir* **2004**, *20* (21), 9249–9254. https://doi.org/10.1021/la0487444.

(64) Rubasinghege, G.; Kyei, P. K.; Scherer, M. M.; Grassian, V. H. Proton-Promoted

Dissolution of α-FeOOH Nanorods and Microrods: Size Dependence, Anion Effects (Carbonate and Phosphate), Aggregation and Surface Adsorption. *J. Colloid Interface Sci.* **2012**, *385* (1), 15–23. https://doi.org/10.1016/J.JCIS.2012.06.049.

(65) Elzinga, E. J.; Sparks, D. L. Phosphate Adsorption onto Hematite: An in Situ ATR-FTIR Investigation of the Effects of pH and Loading Level on the Mode of Phosphate Surface Complexation. *J. Colloid Interface Sci.* **2007**, *308* (1), 53–70. https://doi.org/10.1016/J.JCIS.2006.12.061.

(66) Arai, Y.; Sparks, D. L. ATR–FTIR Spectroscopic Investigation on Phosphate Adsorption Mechanisms at the Ferrihydrite–Water Interface. *J. Colloid Interface Sci.* **2001**, *241* (2), 317–326. https://doi.org/10.1006/JCIS.2001.7773.

(67) de Alwis, C.; Perrine, K. A. In Situ PM-IRRAS at the Air/Electrolyte/Solid Interface Reveals Oxidation of Iron to Distinct Minerals. *J. Phys. Chem. A* **2020**, *124* (33), 6735–6744. https://doi.org/10.1021/acs.jpca.0c03592.

(68) de Alwis, C.; Leftwich, T. R.; Perrine, K. A. New Approach to Simultaneous In Situ Measurements of the Air/Liquid/Solid Interface Using PM-IRRAS. *Langmuir* **2020**, *36* (13), 3404–3414. https://doi.org/10.1021/acs.langmuir.9b03958.

(69) Han, J.; Ro, H.-M. Interpreting Competitive Adsorption of Arsenate and Phosphate on Nanosized Iron (Hydr)Oxides: Effects of pH and Surface Loading. *Environ. Sci. Pollut. Res.* **2018**, *25* (28), 28572–28582. https://do.org/10.1007/s11356-018-2897-y.

(70) Du, P.; Moulijn, J. A.; Mul, G. Selective Photo(Catalytic)-Oxidation of Cyclohexane: Effect of Wavelength and TiO_2 Structure on Product Yields. *J. Catal.* **2006**, *238* (2), 342–352. https://doi.org/10.1016/j.jcat.2005.12.011.

(71) Nakamura, R.; Imanishi, A.; Murakoshi, K.; Nakato, Y. In Situ FTIR Studies of Primary Intermediates of Photocatalytic Reactions on Nanocrystalline TiO_2 Films in Contact with Aqueous Solutions. *J. Am. Chem. Soc.* **2003**, *125* (24), 7443–7450. https://doi.org/10.1021/ja029503q.

(72) Mueller, R.; Kammler, H. K.; Wegner, K.; Pratsinis, S. E. OH Surface Density of SiO_2 and TiO_2 by Thermogravimetric Analysis. *Langmuir* **2003**, *19* (1), 160–165. https://doi.org/10.1021/la025785w.

(73) Lagström, T.; Gmür, T. A.; Quaroni, L.; Goel, A.; Brown, M. A. Surface Vibrational Structure of Colloidal Silica and Its Direct Correlation with Surface Charge Density. *Langmuir* **2015**, *31* (12), 3621–3626. https://doi.org/10.1021/acs.langmuir.5b00418.

(74) Barisik, M.; Atalay, S.; Beskok, A.; Qian, S. Size Dependent Surface Charge Properties of Silica Nanoparticles. *J. Phys. Chem. C* **2014**, *118* (4), 1836–1842. https://doi.org/10.1021/jp410536n.

(75) Kosmulski, M. The PH-Dependent Surface Charging and Points of Zero Charge: V. Update. *J. Colloid Interface Sci.* **2011**, *353* (1), 1–15. https://doi.org/10.1016/j.jcis.2010.08.023.

(76) Sit, I.; Sagisaka, S.; Grassian, V. H. Nucleotide Adsorption on Iron(III) Oxide Nanoparticle Surfaces: Insights into Nano–Geo–Bio Interactions Through Vibrational Spectroscopy. *Langmuir* **2020**, *36* (51), 15501–15513. https://doi.org/10.1021/acs.langmuir.0c02633.

(77) Smedley, P. L.; Kinniburgh, D. G. A Review of the Source, Behaviour and Distribution of Arsenic in Natural Waters. *Appl. Geochemistry* **2002**, *17* (5), 517–568. https://doi.org/10.1016/S0883-2927(02)00018-5.

(78) Lounsbury, A. W.; Yamani, J. S.; Johnston, C. P.; Larese-Casanova, P.; Zimmerman, J. B. The Role of Counter Ions in Nano-Hematite Synthesis: Implications for Surface Area and Selenium Adsorption Capacity. *J Hazard Mater* **2016**, *310*, 117–124. https://doi.org/10.1016/j.jhazmat.2016.01.078.

(79) Jordan, N.; Franzen, C.; Lützenkirchen, J.; Foerstendorf, H.; Hering, D.; Weiss, S.; Heim, K.; Brendler, V. Adsorption of Selenium(vi) onto Nano Transition Alumina. *Environ. Sci. Nano* **2018**, *5* (7), 1661–1669. https://doi.org/10.1039/C8EN00293B.

(80) Barrón, V.; Torrent, J. Surface Hydroxyl Configuration of Various Crystal Faces of Hematite and Goethite. *J. Colloid Interface Sci.* **1996**, *177* (2), 407–410. https://doi.org/10.1006/jcis.1996.0051.

(81) Rubasinghege, G.; Lentz, R. W.; Park, H.; Scherer, M. M.; Grassian, V. H. Nanorod Dissolution Quenched in the Aggregated State. *Langmuir* **2010**, *26* (3), 1524–1527. https://doi.org/10.1021/la903950e.

(82) Rubasinghege, G.; Lentz, R. W.; Scherer, M. M.; Grassian, V. H. Simulated Atmospheric Processing of Iron Oxyhydroxide Minerals at Low PH: Roles of Particle Size and Acid Anion in Iron Dissolution. *Proc. Natl. Acad. Sci.* **2010**, *107* (15), 6628–6633. https://doi.org/10.1073/pnas.0910809107.

(83) Satzer, P.; Svec, F.; Sekot, G.; Jungbauer, A. Protein Adsorption onto Nanoparticles Induces Conformational Changes: Particle Size Dependency, Kinetics, and Mechanisms. *Eng. Life Sci.* **2016**, *16* (3), 238–246. https://doi.org/10.1002/elsc.201500059.

(84) Deacon, G. B.; Phillips, R. J. Relationships between the Carbon-Oxygen Stretching Frequencies of Carboxylato Complexes and the Type of Carboxylate Coordination. *Coord. Chem. Rev.* **1980**, *33* (3), 227–250. https://doi.org/10.1016/S0010-8545(00)80455-5.

(85) Carter, D. C.; Ho, J. X. Structure of Serum Albumin. In *Advances in Protein Chemistry*; Anfinsen, C. B., Edsall, J. T., Richards, F. M., Eisenberg, D. S., Eds.; Academic Press, 1994; Vol. 45, pp 153–203. https://doi.org/10.1016/S0065-3233(08)60640-3.

(86) Alexov, E. G.; Gunner, M. R. Incorporating Protein Conformational Flexibility into the Calculation of PH-Dependent Protein Properties. *Biophys. J.* **1997**, *72* (5), 2075–2093. https://doi.org/10.1016/S0006-3495(97)78851-9.

(87) Nguyen, P. A.; Soto, C. S.; Polishchuk, A.; Caputo, G. A.; Tatko, C. D.; Ma, C.; Ohigashi, Y.; Pinto, L. H.; DeGrado, W. F.; Howard, K. P. PH-Induced Conformational Change of

the Influenza M2 Protein C-Terminal Domain. *Biochemistry* **2008**, *47* (38), 9934–9936. https://doi.org/10.1021/bi801315m.

(88) Turci, F.; Ghibaudi, E.; Colonna, M.; Boscolo, B.; Fenoglio, I.; Fubini, B. An Integrated Approach to the Study of the Interaction between Proteins and Nanoparticles. *Langmuir* **2010**, *26* (11), 8336–8346. https://doi.org/10.1021/la904758j.

(89) Erhayem, M.; Sohn, M. Stability Studies for Titanium Dioxide Nanoparticles upon Adsorption of Suwannee River Humic and Fulvic Acids and Natural Organic Matter. *Sci. Total Environ.* **2014**, *468–469*, 249–257. https://doi.org/10.1016/j.scitotenv.2013.08.038.

(90) Márquez, A.; Berger, T.; Feinle, A.; Hüsing, N.; Himly, M.; Duschl, A.; Diwald, O. Bovine Serum Albumin Adsorption on TiO_2 Colloids: The Effect of Particle Agglomeration and Surface Composition. *Langmuir* **2017**, *33* (10), 2551–2558. https://doi.org/10.1021/acs.langmuir.6b03785.

(91) Philippe, A.; Schaumann, G. E. Interactions of Dissolved Organic Matter with Natural and Engineered Inorganic Colloids: A Review. *Environ. Sci. Technol.* **2014**, *48* (16), 8946–8962. https://doi.org/10.1021/es502342r.

(92) Erhayem, M.; Sohn, M. Effect of Humic Acid Source on Humic Acid Adsorption onto Titanium Dioxide Nanoparticles. *Sci. Total Environ.* **2014**, *470–471*, 92–98. https://doi.org/10.1016/j.scitotenv.2013.09.063.

(93) Dobson, K. D.; McQuillan, A. J. In Situ Infrared Spectroscopic Analysis of the Adsorption of Aromatic Carboxylic Acids to TiO_2, ZrO_2, Al_2O_3, and Ta_2O_5 from Aqueous Solutions. *Spectrochim. Acta Part A Mol. Biomol. Spectrosc.* **2000**, *56* (3), 557–565. https://doi.org/10.1016/S1386-1425(99)00154-7.

(94) Barreto, M. S. C.; Elzinga, E. J.; Alleoni, L. R. F. The Molecular Insights into Protein Adsorption on Hematite Surface Disclosed by In-Situ ATR-FTIR/2D-COS Study. *Sci. Rep.* **2020**, *10* (1), 13441. https://doi.org/10.1038/s41598-020-70201-z.

(95) Schmidt, M. P.; Martínez, C. E. Ironing Out Genes in the Environment: An Experimental Study of the DNA–Goethite Interface. *Langmuir* **2017**, *33* (34), 8525–8532. https://doi.org/10.1021/acs.langmuir.7b01911.

(96) Liu, F.; Zhang, Y.; Wang, H.; Li, L.; Zhao, W.; Shen, J.-W.; Liang, L. Study on the Adsorption Orientation of DNA on Two-Dimensional MoS2 Surface via Molecular Dynamics Simulation: A Vertical Orientation Phenomenon. *Chem. Phys.* **2020**, *529*, 110546. https://doi.org/10.1016/j.chemphys.2019.110546.

(97) Chen, W.; Qian, C.; Liu, X.-Y.; Yu, H.-Q. Two-Dimensional Correlation Spectroscopic Analysis on the Interaction between Humic Acids and TiO_2 Nanoparticles. *Environ. Sci. Technol.* **2014**, *48* (19), 11119–11126. https://doi.org/10.1021/es502502n.

(98) Larkin, P. Chapter 5 - Origin of Group Frequencies. In *Infrared and Raman Spectroscopy*; Larkin, P., Ed.; Elsevier: Oxford, 2011; pp 63–72. https://doi.org/10.1016/B978-0-12-

386984-5.10005-9.

(99) Woods, D. A.; Bain, C. D. Total Internal Reflection Spectroscopy for Studying Soft Matter. *Soft Matter* **2014**, *10* (8), 1071–1096. https://doi.org/10.1039/C3SM52817K.

(100) Hug, S. J.; Sulzberger, B. In Situ Fourier Transform Infrared Spectroscopic Evidence for the Formation of Several Different Surface Complexes of Oxalate on TiO_2 in the Aqueous Phase. *Langmuir* **1994**, *10* (10), 3587–3597. https://doi.org/10.1021/la00022a036.

(101) Mudunkotuwa, I. A.; Al Minshid, A.; Grassian, V. H. ATR-FTIR Spectroscopy as a Tool to Probe Surface Adsorption on Nanoparticles at the Liquid-Solid Interface in Environmentally and Biologically Relevant Media. *Analyst* **2014**, *139* (5), 870–881. https://doi.org/10.1039/c3an01684f.

(102) *Internal Reflection Spectroscopy: Theory and Applications*; Mirabella, F. M., Ed.; MARCEL DEKKER, INC: New York, 1992.

(103) Wu, H.; Or, V. W.; Gonzalez-Calzada, S.; Grassian, V. H. CuS Nanoparticles in Humid Environments: Adsorbed Water Enhances the Transformation of CuS to CuSO4. *Nanoscale* **2020**, *12* (37), 19350–19358. https://doi.org/10.1039/D0NR05934J.

(104) Wu, H.; Huang, L.; Rose, A.; Grassian, V. H. Impact of Surface Adsorbed Biologically and Environmentally Relevant Coatings on TiO_2 Nanoparticle Reactivity. *Environ. Sci. Nano* **2020**, *7* (12), 3783–3793. https://doi.org/10.1039/D0EN00706D.

(105) Boateng, L. K.; Mirshahghassemi, S.; Wu, H.; Flora, J. R. V; Grassian, V. H.; Lead, J. R. Mechanistic Study of Oil Adsorption onto PVP-Coated Magnetic Nanoparticles: An Integrated Experimental and Molecular Dynamics Study to Inform Remediation. *Environ. Sci. Nano* **2021**. https://doi.org/10.1039/D0EN00907E.

(106) Sit, I.; Wu, H.; Grassian, V. H. Environmental Aspects of Oxide Nanoparticles: Probing Oxide Nanoparticle Surface Processes Under Different Environmental Conditions. *Annu. Rev. Anal. Chem.* **2021**, *14* (1), 489–514. https://doi.org/10.1146/annurev-anchem-091420-092928.

(107) Jin, P.; Song, J.; Wang, X. C.; Jin, X. Two-Dimensional Correlation Spectroscopic Analysis on the Interaction between Humic Acids and Aluminum Coagulant. *J. Environ. Sci.* **2018**, *64*, 181–189. https://doi.org/10.1016/j.jes.2017.06.018.

(108) Szwed, J.; Cieślik-Boczula, K.; Czarnik-Matusewicz, B.; Jaszczyszyn, A.; Gąsiorowski, K.; Świątek, P.; Malinka, W. Moving-Window 2D Correlation Spectroscopy in Studies of Fluphenazine–DPPC Dehydrated Film as a Function of Temperature. *J. Mol. Struct.* **2010**, *974* (1), 192–202. https://doi.org/10.1016/j.molstruc.2010.03.053.

(109) Ashton, L.; Blanch, E. W. PH-Induced Conformational Transitions in α-Lactalbumin Investigated with Two-Dimensional Raman Correlation Variance Plots and Moving Windows. *J. Mol. Struct.* **2010**, *974* (1), 132–138. https://doi.org/10.1016/j.molstruc.2010.03.005.

(110) Noda, I. Vibrational Two-Dimensional Correlation Spectroscopy (2DCOS) Study of Proteins. *Spectrochim. Acta Part a-Molecular Biomol. Spectrosc.* **2017**, *187*, 119–129. https://doi.org/10.1016/j.saa.2017.06.034.

(111) Noda, I. Chapter 2 - Advances in Two-Dimensional Correlation Spectroscopy (2DCOS); Laane, J. B. T.-F. and A. in M. S., Ed.; Elsevier, 2018; pp 47–75. https://doi.org/10.1016/B978-0-12-811220-5.00002-2.

(112) Morita, S.; Shinzawa, H.; Tsenkova, R.; Noda, I.; Ozaki, Y. Computational Simulations and a Practical Application of Moving-Window Two-Dimensional Correlation Spectroscopy. *J. Mol. Struct.* **2006**, *799* (1–3), 111–120. https://doi.org/10.1016/j.molstruc.2006.03.023.

(113) Liu, J.; Zhu, R.; Liang, X.; Ma, L.; Lin, X.; Zhu, J.; He, H.; Parker, S. C.; Molinari, M. Synergistic Adsorption of Cd(II) with Sulfate/Phosphate on Ferrihydrite: An in Situ ATR-FTIR/2D-COS Study. *Chem. Geol.* **2018**, *477*, 12–21. https://doi.org/10.1016/j.chemgeo.2017.12.004.

(114) Han, J.; Ro, H.-M. Characterizing Preferential Adsorption of Phosphate on Binary Sorbents of Goethite and Maghaemite Using in Situ ATR-FTIR and 2D Correlation Spectroscopy. *Sci. Rep.* **2019**, *9* (1), 6130. https://doi.org/10.1038/s41598-019-42575-2.

(115) Schmidt, M. P.; Martínez, C. E. Supramolecular Association Impacts Biomolecule Adsorption onto Goethite. *Environ. Sci. Technol.* **2018**, *52* (7), 4079–4089. https://doi.org/10.1021/acs.est.7b06173.

(116) Gomaa, A. I.; Sedman, J.; Ismail, A. A. An Investigation of the Effect of Microwave Treatment on the Structure and Unfolding Pathways of β-Lactoglobulin Using FTIR Spectroscopy with the Application of Two-Dimensional Correlation Spectroscopy (2D-COS). *Vib. Spectrosc.* **2013**, *65*, 101–109. https://doi.org/10.1016/j.vibspec.2012.11.019.

(117) Liu, F.; Li, X.; Sheng, A.; Shang, J.; Wang, Z.; Liu, J. Kinetics and Mechanisms of Protein Adsorption and Conformational Change on Hematite Particles. *Environ. Sci. Technol.* **2019**, *53* (17), 10157–10165. https://doi.org/10.1021/acs.est.9b02651.

(118) Pazderka, T.; Kopecky Jr, V. 2D Correlation Spectroscopy and Its Application in Vibrational Spectroscopy Using Matlab. *Tech. Comput. Prague* **2008**, 978–80. https://doi.org/10.1016/B978-0-12-849883-5.00010-3.

(119) Noda, I. Two-Dimensional Infrared (2D IR) Spectroscopy: Theory and Applications. *Appl. Spectrosc.* **1990**, *44* (4), 550–561. https://doi.org/10.1366/0003702904087398.

(120) Morita, S.; Shinzawa, H.; Noda, I.; Ozaki, Y. Effect of Band Position Shift on Moving-Window Two-Dimensional Correlation Spectroscopy. *J. Mol. Struct.* **2006**, *799* (1–3), 16–22. https://doi.org/10.1016/j.molstruc.2006.03.017.

(121) Banfield, J. F.; Zhang, H. Nanoparticles in the Environment. *Rev. Mineral. Geochemistry* **2001**, *44* (1), 1–58. https://doi.org/10.2138/rmg.2001.44.01.

(122) Hochella, M. F.; Lower, S. K.; Maurice, P. A.; Penn, R. L.; Sahai, N.; Sparks, D. L.; Twining, B. S. Nanominerals, Mineral Nanoparticles, and Earth Systems. *Science (80-.).* **2008**, *319* (5870), 1631 LP – 1635. https://doi.org/10.1126/science.1141134.

(123) Waychunas, G. A.; Kim, C. S.; Banfield, J. F. Nanoparticulate Iron Oxide Minerals in Soils and Sediments: Unique Properties and Contaminant Scavenging Mechanisms. *J. Nanoparticle Res.* **2005**, *7* (4), 409–433. https://doi.org/10.1007/s11051-005-6931-x.

(124) Hua, M.; Zhang, S.; Pan, B.; Zhang, W.; Lv, L.; Zhang, Q. Heavy Metal Removal from Water/Wastewater by Nanosized Metal Oxides: A Review. *J. Hazard. Mater.* **2012**, *211–212*, 317–331. https://doi.org/10.1016/j.jhazmat.2011.10.016.

(125) Liu, J.; Zhao, Z.; Jiang, G. Coating Fe3O4 Magnetic Nanoparticles with Humic Acid for High Efficient Removal of Heavy Metals in Water. *Environ. Sci. Technol.* **2008**, *42* (18), 6949–6954. https://doi.org/10.1021/es800924c.

(126) Parikh, S. J.; Chorover, J. ATR-FTIR Spectroscopy Reveals Bond Formation During Bacterial Adhesion to Iron Oxide. *Langmuir* **2006**, *22* (20), 8492–8500. https://doi.org/10.1021/la061359p.

(127) Pietramellara, G.; Ascher, J.; Borgogni, F.; Ceccherini, M. T.; Guerri, G.; Nannipieri, P. Extracellular DNA in Soil and Sediment: Fate and Ecological Relevance. *Biol. Fertil. Soils* **2009**, *45* (3), 219–235. https://doi.org/10.1007/s00374-008-0345-8.

(128) Zaia, D. A. M. Adsorption of Amino Acids and Nucleic Acid Bases onto Minerals: A Few Suggestions for Prebiotic Chemistry Experiments. *Int. J. Astrobiol.* **2012**, *11* (4), 229–234. https://doi.org/10.1017/S1473550412000195.

(129) Pedreira-Segade, U.; Michot, L. J.; Daniel, I. Effects of Salinity on the Adsorption of Nucleotides onto Phyllosilicates. *Phys. Chem. Chem. Phys.* **2018**, *20* (3), 1938–1952. https://doi.org/10.1039/C7CP07004G.

(130) He, L.; Wei, X.; Ma, X.; Yin, X.; Song, M.; Donninger, H.; Yaddanapudi, K.; McClain, C. J.; Zhang, X. Simultaneous Quantification of Nucleosides and Nucleotides from Biological Samples. *J. Am. Soc. Mass Spectrom.* **2019**, *30* (6), 987–1000. https://doi.org/10.1007/s13361-019-02140-7.

(131) Vlasova, N. N.; Markitan, O. V. Adsorption of Pyrimidine Nucleotides on a Titanium Dioxide Surface. *Colloid J.* **2018**, *80* (4), 364–370. https://doi.org/10.1134/S1061933X18040142.

(132) Vlasova, N. N.; Markitan, O. V. Adsorption Complexes of Purine Nucleotides on a Titanium Dioxide Surface. *Colloid J.* **2019**, *81* (1), 14–20. https://doi.org/10.1134/S1061933X19010149.

(133) Pedreira-Segade, U.; Feuillie, C.; Pelletier, M.; Michot, L. J.; Daniel, I. Adsorption of Nucleotides onto Ferromagnesian Phyllosilicates: Significance for the Origin of Life. *Geochim. Cosmochim. Acta* **2016**, *176*, 81–95. https://doi.org/10.1016/j.gca.2015.12.025.

(134) Feuillie, C.; Daniel, I.; Michot, L. J.; Pedreira-Segade, U. Adsorption of Nucleotides onto Fe–Mg–Al Rich Swelling Clays. *Geochim. Cosmochim. Acta* **2013**, *120*, 97–108. https://doi.org/10.1016/J.GCA.2013.06.021.

(135) Villafañe-Barajas, S. A.; Baú, J. P. T.; Colín-García, M.; Negrón-Mendoza, A.; Heredia-Barbero, A.; Pi-Puig, T.; Zaia, D. A. M. Salinity Effects on the Adsorption of Nucleic Acid Compounds on Na-Montmorillonite: A Prebiotic Chemistry Experiment. *Orig. Life Evol. Biosph.* **2018**, *48* (2), 181–200. https://doi.org/10.1007/s11084-018-9554-9.

(136) Hashizume, H. Adsorption of Nucleic Acid Bases, Ribose, and Phosphate by Some Clay Minerals. *Life* **2015**, *5* (1), 637–650. https://doi.org/10.3390/life5010637.

(137) Arai, Y.; Sparks, D. L. Phosphate Reaction Dynamics in Soils and Soil Components: A Multiscale Approach. *Adv. Agron.* **2007**, *94*, 135–179. https://doi.org/10.1016/S0065-2113(06)94003-6.

(138) Holman, I.; Whelan, M.; Howden, N.; Bellamy, P.; Willby, N.; Rivas-Casado, M.; McConvey, P. Phosphorus in Groundwater—An Overlooked Contributor to Eutrophication? *Hydrol. Process.* **2008**, *22*, 5121–5127. https://doi.org/10.1002/hyp.7198.

(139) Kent, R.; Johnson, T. D.; Rosen, M. R. Status and Trends of Orthophosphate Concentrations in Groundwater Used for Public Supply in California. *Environ. Monit. Assess.* **2020**, *192* (8), 550. https://doi.org/10.1007/s10661-020-08504-x.

(140) Elzinga, E. J.; Kretzschmar, R. In Situ ATR-FTIR Spectroscopic Analysis of the Co-Adsorption of Orthophosphate and Cd(II) onto Hematite. *Geochim. Cosmochim. Acta* **2013**, *117*, 53–64. https://doi.org/10.1016/J.GCA.2013.04.003.

(141) Tejedor-Tejedor, M. I.; Anderson, M. A. The Protonation of Phosphate on the Surface of Goethite as Studied by CIR-FTIR and Electrophoretic Mobility. *Langmuir* **1990**, *6* (3), 602–611. https://doi.org/10.1021/la00093a015.

(142) Tejedor-Tejedor, M. I.; Anderson, M. A. "In Situ" ATR-Fourier Transform Infrared Studies of the Goethite (-FeOOH)-Aqueous Solution Interface. *Langmuir* **1986**, *2* (2), 203–210. https://doi.org/10.1021/la00068a016.

(143) Roberts, L. C.; Hug, S. J.; Ruettimann, T.; Billah, M. M.; Khan, A. W.; Rahman, M. T. Arsenic Removal with Iron(II) and Iron(III) in Waters with High Silicate and Phosphate Concentrations. *Environ. Sci. Technol.* **2004**, *38* (1), 307–315. https://doi.org/10.1021/es0343205.

(144) Su, C.; Puls, R. W. Arsenate and Arsenite Removal by Zerovalent Iron: Effects of Phosphate, Silicate, Carbonate, Borate, Sulfate, Chromate, Molybdate, and Nitrate, Relative to Chloride. *Environ. Sci. Technol.* **2001**, *35* (22), 4562–4568. https://doi.org/10.1021/es010768z.

(145) Violante, A.; Pigna, M. Competitive Sorption of Arsenate and Phosphate on Different Clay Minerals and Soils. *SOIL Sci. Soc. Am. J.* **2002**, *66* (6), 1788–1796.

https://doi.org/10.2136/sssaj2002.1788.

(146) Hiemstra, T.; Van Riemsdijk, W. H. Surface Structural Ion Adsorption Modeling of Competitive Binding of Oxyanions by Metal (Hydr)Oxides. *J. Colloid Interface Sci.* **1999**, *210* (1), 182–193. https://doi.org/10.1006/jcis.1998.5904.

(147) Arco-Lázaro, E.; Agudo, I.; Clemente, R.; Bernal, M. P. Arsenic(V) Adsorption-Desorption in Agricultural and Mine Soils: Effects of Organic Matter Addition and Phosphate Competition. *Environ. Pollut.* **2016**, *216*, 71–79. https://doi.org/10.1016/J.ENVPOL.2016.05.054.

(148) Shabarova, Zoe A.; Bogdanov, A. A. Properties of Nucleotides. In *Advanced Organic Chemistry of Nucleic Acids*; John Wiley & Sons, Ltd, 2007; pp 93–180. https://doi.org/10.1002/9783527615933.ch04.

(149) Mathlouthi, M.; Seuvre, A.-M.; Koenig, J. L. F.t.-i.r. and Laser-Raman Spectra of Adenine and Adenosine. *Carbohydr. Res.* **1984**, *131* (1), 1–15. https://doi.org/10.1016/0008-6215(84)85398-7.

(150) Wu, R. R.; He, C. C.; Hamlow, L. A.; Nei, Y. -w.; Berden, G.; Oomens, J.; Rodgers, M. T. N3 Protonation Induces Base Rotation of 2′-Deoxyadenosine-5′-Monophosphate and Adenosine-5′-Monophosphate. *J. Phys. Chem. B* **2016**, *120* (20), 4616–4624. https://doi.org/10.1021/acs.jpcb.6b04052.

(151) El-Mahdaoui, L.; Neault, J. F.; Tajmir-Riahi, H. A. Carbohydrate-Nucleotide Interaction. The Effects of Mono- and Disaccharides on the Solution Structure of AMP, DAMP, ATP, GMP, DGMP, and GTP Studied by FTIR Difference Spectroscopy. *J. Inorg. Biochem.* **1997**, *65* (2), 123–131. https://doi.org/10.1016/S0162-0134(96)00097-9.

(152) Tajmir-Riahi, H.-A.; Messaoudi, S. The Effects of Monovalent Cations Li+, Na+, K+, NH4 +, Rb+ and Cs+ on the Solid and Solution Structures of the Nucleic Acid Components. Metal Ion Binding and Sugar Conformation. *J. Biomol. Struct. Dyn.* **1992**, *10* (2), 345–365. https://doi.org/10.1080/07391102.1992.10508652.

(153) Yan, W.; Jing, C. Molecular Insights into Glyphosate Adsorption to Goethite Gained from ATR-FTIR, Two-Dimensional Correlation Spectroscopy, and DFT Study. *Environ. Sci. Technol.* **2018**, *52* (4), 1946–1953. https://doi.org/10.1021/acs.est.7b05643.

(154) Antelo, J.; Avena, M.; Fiol, S.; López, R.; Arce, F. Effects of pH and Ionic Strength on the Adsorption of Phosphate and Arsenate at the Goethite–Water Interface. *J. Colloid Interface Sci.* **2005**, *285* (2), 476–486. https://doi.org/10.1016/j.jcis.2004.12.032.

(155) Luengo, C.; Brigante, M.; Antelo, J.; Avena, M. Kinetics of Phosphate Adsorption on Goethite: Comparing Batch Adsorption and ATR-IR Measurements. *J. Colloid Interface Sci.* **2006**, *300* (2), 511–518. https://doi.org/10.1016/j.jcis.2006.04.015.

(156) Fry, R. A.; Kwon, K. D.; Komarneni, S.; Kubicki, J. D.; Mueller, K. T. Solid-State NMR and Computational Chemistry Study of Mononucleotides Adsorbed to Alumina. *Langmuir*

2006, *22* (22), 9281–9286. https://doi.org/10.1021/la061561s.

(157) Tribe, L.; Kwon, K. D.; Trout, C. C.; Kubicki, J. D. Molecular Orbital Theory Study on Surface Complex Structures of Glyphosate on Goethite: Calculation of Vibrational Frequencies. *Environ. Sci. Technol.* **2006**, *40* (12), 3836–3841. https://doi.org/10.1021/es052363a.

(158) Lanzl, C. A.; Baltrusaitis, J.; Cwiertny, D. M. Dissolution of Hematite Nanoparticle Aggregates: Influence of Primary Particle Size, Dissolution Mechanism, and Solution PH. *Langmuir* **2012**, *28* (45), 15797–15808. https://doi.org/10.1021/la3022497.

(159) Kumar, E.; Bhatnagar, A.; Hogland, W.; Marques, M.; Sillanpää, M. Interaction of Inorganic Anions with Iron-Mineral Adsorbents in Aqueous Media — A Review. *Adv. Colloid Interface Sci.* **2014**, *203*, 11–21. https://doi.org/10.1016/j.cis.2013.10.026.

(160) Xu, C.-Y.; Xu, R.-K.; Li, J.-Y.; Deng, K.-Y. Phosphate-Induced Aggregation Kinetics of Hematite and Goethite Nanoparticles. *J. Soils Sediments* **2017**, *17* (2), 352–363. https://doi.org/10.1007/s11368-016-1550-y.

(161) Weng, L.; Van Riemsdijk, W. H.; Hiemstra, T. Humic Nanoparticles at the Oxide−Water Interface: Interactions with Phosphate Ion Adsorption. *Environ. Sci. Technol.* **2008**, *42* (23), 8747–8752. https://doi.org/10.1021/es801631d.

(162) Hiemstra, T.; Antelo, J.; van Rotterdam, A. M. D. (Debby.; van Riemsdijk, W. H. Nanoparticles in Natural Systems II: The Natural Oxide Fraction at Interaction with Natural Organic Matter and Phosphate. *Geochim. Cosmochim. Acta* **2010**, *74* (1), 59–69. https://doi.org/10.1016/J.GCA.2009.10.019.

(163) Wei, T.; Kaewtathip, S.; Shing, K. Buffer Effect on Protein Adsorption at Liquid/Solid Interface. *J. Phys. Chem. C* **2009**, *113* (6), 2053–2062. https://doi.org/10.1021/jp806586n.

(164) Hua, M.; Zhang, S.; Pan, B.; Zhang, W.; Lv, L.; Zhang, Q. Heavy Metal Removal from Water/Wastewater by Nanosized Metal Oxides: A Review. *J. Hazard. Mater.* **2012**, *211–212*, 317–331. https://doi.org/10.1016/j.jhazmat.2011.10.016.

(165) Pedreira-Segade, U.; Hao, J.; Razafitianamaharavo, A.; Pelletier, M.; Marry, V.; Le Crom, S.; Michot, L. J.; Daniel, I. How Do Nucleotides Adsorb Onto Clays? *Life (Basel, Switzerland)* **2018**, *8* (4). https://doi.org/10.3390/life8040059.

(166) Mauvisseau, Q.; Harper, L. R.; Sander, M.; Hanner, R. H.; Kleyer, H.; Deiner, K. The Multiple States of Environmental DNA and What Is Known about Their Persistence in Aquatic Environments. *Environ. Sci. Technol.* **2022**, *56* (9), 5322–5333. https://doi.org/10.1021/acs.est.1c07638.

(167) Poté, J.; Rosselli, W.; Wigger, A.; Wildi, W. Release and Leaching of Plant DNA in Unsaturated Soil Column. *Ecotoxicol. Environ. Saf.* **2007**, *68* (2), 293–298. https://doi.org/10.1016/j.ecoenv.2006.11.004.

(168) Poté, J.; Ceccherini, M. T.; Van, V. T.; Rosselli, W.; Wildi, W.; Simonet, P.; Vogel, T. M. Fate and Transport of Antibiotic Resistance Genes in Saturated Soil Columns. *Eur. J. Soil Biol.* **2003**, *39* (2), 65–71. https://doi.org/10.1016/S1164-5563(03)00003-7.

(169) Harrison, J. B.; Sunday, J. M.; Rogers, S. M. Predicting the Fate of EDNA in the Environment and Implications for Studying Biodiversity. *Proc. R. Soc. B Biol. Sci.* **2019**, *286* (1915), 20191409. https://doi.org/10.1098/rspb.2019.1409.

(170) Pedreira-Segade, U.; Michot, L. J.; Daniel, I. Effects of Salinity on the Adsorption of Nucleotides onto Phyllosilicates. *Phys. Chem. Chem. Phys.* **2018**, *20* (3), 1938–1952. https://doi.org/10.1039/C7CP07004G.

(171) Cleaves, H. J.; Jonsson, C. M.; Jonsson, C. L.; Sverjensky, D. A.; Hazen, R. M. Adsorption of Nucleic Acid Components on Rutile (TiO_2) Surfaces. *Astrobiology* **2010**, *10* (3), 311–323. https://doi.org/10.1089/ast.2009.0397.

(172) Zhang, X.; Wang, F.; Liu, B.; Kelly, E. Y.; Servos, M. R.; Liu, J. Adsorption of DNA Oligonucleotides by Titanium Dioxide Nanoparticles. *Langmuir* **2014**, *30* (3), 839–845. https://doi.org/10.1021/la404633p.

(173) Budnyak, T. M.; Vlasova, N. N.; Golovkova, L. P.; Markitan, O.; Baryshnikov, G.; Ågren, H.; Slabon, A. Nucleotide Interaction with a Chitosan Layer on a Silica Surface: Establishing the Mechanism at the Molecular Level. *Langmuir* **2021**, *37* (4), 1511–1520. https://doi.org/10.1021/acs.langmuir.0c03050.

(174) Banyay, M.; Sarkar, M.; Gräslund, A. A Library of IR Bands of Nucleic Acids in Solution. *Biophys. Chem.* **2003**, *104* (2), 477–488. https://doi.org/10.1016/S0301-4622(03)00035-8.

(175) Connor, P. A.; McQuillan, A. J. Phosphate Adsorption onto TiO_2 from Aqueous Solutions: An in Situ Internal Reflection Infrared Spectroscopic Study. *Langmuir* **1999**, *15* (8), 2916–2921. https://doi.org/10.1021/la980894p.

(176) Kosmulski, M. The Significance of the Difference in the Point of Zero Charge between Rutile and Anatase. *Adv. Colloid Interface Sci.* **2002**, *99* (3), 255–264. https://doi.org/10.1016/S0001-8686(02)00080-5.

(177) Feuillie, C.; Sverjensky, D. A.; Hazen, R. M. Attachment of Ribonucleotides on α-Alumina as a Function of PH, Ionic Strength, and Surface Loading. *Langmuir* **2015**, *31* (1), 240–248. https://doi.org/10.1021/la504034k.

(178) Soria, F. A.; Di Valentin, C. Binding Group of Oligonucleotides on TiO_2 Surfaces: Phosphate Anions or Nucleobases? *Appl. Surf. Sci.* **2022**, *575*, 151560. https://doi.org/10.1016/j.apsusc.2021.151560.

(179) James Cleaves, H.; Crapster-Pregont, E.; Jonsson, C. M.; Jonsson, C. L.; Sverjensky, D. A.; Hazen, R. A. The Adsorption of Short Single-Stranded DNA Oligomers to Mineral Surfaces. *Chemosphere* **2011**, *83* (11), 1560–1567. https://doi.org/10.1016/j.chemosphere.2011.01.023.

(180) Carneiro, C. E. A.; Berndt, G.; de Souza Junior, I. G.; de Souza, C. M. D.; Paesano, A.; da Costa, A. C. S.; di Mauro, E.; de Santana, H.; Zaia, C. T. B. V; Zaia, D. A. M. Adsorption of Adenine, Cytosine, Thymine, and Uracil on Sulfide-Modified Montmorillonite: FT-IR, Mössbauer and EPR Spectroscopy and X-Ray Diffractometry Studies. *Orig. Life Evol. Biosph.* **2011**, *41* (5), 453. https://doi.org/10.1007/s11084-011-9244-3.

(181) Sowerby, S. J.; Cohn, C. A.; Heckl, W. M.; Holm, N. G. Differential Adsorption of Nucleic Acid Bases: Relevance to the Origin of Life. *Proc. Natl. Acad. Sci.* **2001**, *98* (3), 820–822. https://doi.org/10.1073/pnas.98.3.820.

(182) Hashizume, H.; van der Gaast, S.; Theng, B. K. G. Adsorption of Adenine, Cytosine, Uracil, Ribose, and Phosphate by Mg-Exchanged Montmorillonite. *Clay Miner.* **2010**, *45* (4), 469–475. https://doi.org/10.1180/claymin.2010.045.4.469.

(183) Scipioni, R.; Schmidt, D. A.; Boero, M. A First Principles Investigation of Water Dipole Moment in a Defective Continuous Hydrogen Bond Network. *J. Chem. Phys.* **2009**, *130* (2), 24502. https://doi.org/10.1063/1.3054197.

(184) Stelling, A. L.; Liu, A. Y.; Zeng, W.; Salinas, R.; Schumacher, M. A.; Al-Hashimi, H. M. Infrared Spectroscopic Observation of a G–C+ Hoogsteen Base Pair in the DNA:TATA-Box Binding Protein Complex Under Solution Conditions. *Angew. Chemie Int. Ed.* **2019**, *58* (35), 12010–12013. https://doi.org/10.1002/anie.201902693.

(185) Stelling, A. L.; Xu, Y.; Zhou, H.; Choi, S. H.; Clay, M. C.; Merriman, D. K.; Al-Hashimi, H. M. Robust IR-Based Detection of Stable and Fractionally Populated G-C+ and A-T Hoogsteen Base Pairs in Duplex DNA. *FEBS Lett.* **2017**, *591* (12), 1770–1784. https://doi.org/10.1002/1873-3468.12681.

(186) Mo, Y. Probing the Nature of Hydrogen Bonds in DNA Base Pairs. *J. Mol. Model.* **2006**, *12* (5), 665–672. https://doi.org/10.1007/s00894-005-0021-y.

(187) Schwertmann, U.; Taylor, R. M.; Dixon, J. B.; Weed, S. B. Minerals in Soil Environments. *Soil Sci. Soc. Am. B. Ser. Eds. JB Dixon, SB Weed, Madison, Wisconsin, EUA* **1989**, *379*.

(188) Huang, X.; Hou, X.; Zhang, X.; Rosso, K. M.; Zhang, L. Facet-Dependent Contaminant Removal Properties of Hematite Nanocrystals and Their Environmental Implications. *Environ. Sci. Nano* **2018**, *5* (8), 1790–1806. https://doi.org/10.1039/C8EN00548F.

(189) Baltrusaitis, J.; Cwiertny, D. M.; Grassian, V. H. Adsorption of Sulfur Dioxide on Hematite and Goethite Particle Surfaces. *Phys. Chem. Chem. Phys.* **2007**, *9* (41), 5542–5554. https://doi.org/10.1039/B709167B.

(190) Persson, P.; Nilsson, N.; Sjöberg, S. Structure and Bonding of Orthophosphate Ions at the Iron Oxide–Aqueous Interface. *J. Colloid Interface Sci.* **1996**, *177* (1), 263–275. https://doi.org/10.1006/jcis.1996.0030.

(191) Villalobos, M.; Escobar-Quiroz, I. N.; Salazar-Camacho, C. The Influence of Particle Size and Structure on the Sorption and Oxidation Behavior of Birnessite: I. Adsorption of As(V)

and Oxidation of As(III). *Geochim. Cosmochim. Acta* **2014**, *125*, 564–581. https://doi.org/10.1016/j.gca.2013.10.029.

(192) Villalobos, M.; Carrillo-Cárdenas, M.; Gibson, R.; López-Santiago, N. R.; Morales, J. A. The Influence of Particle Size and Structure on the Sorption and Oxidation Behaviour of Birnessite: II. Adsorption and Oxidation of Four Polycyclic Aromatic Hydrocarbons. *Environ. Chem.* **2014**, *11* (3), 279–288. https://doi.org/10.1071/EN13161.

(193) Salazar-Camacho, C.; Villalobos, M. Goethite Surface Reactivity: III. Unifying Arsenate Adsorption Behavior through a Variable Crystal Face – Site Density Model. *Geochim. Cosmochim. Acta* **2010**, *74* (8), 2257–2280. https://doi.org/10.1016/j.gca.2010.01.025.

(194) Livi, K. J. T.; Villalobos, M.; Leary, R.; Varela, M.; Barnard, J.; Villacís-García, M.; Zanella, R.; Goodridge, A.; Midgley, P. Crystal Face Distributions and Surface Site Densities of Two Synthetic Goethites: Implications for Adsorption Capacities as a Function of Particle Size. *Langmuir* **2017**, *33* (36), 8924–8932. https://doi.org/10.1021/acs.langmuir.7b01814.

(195) Ustunol, I. B.; Coward, E. K.; Quirk, E.; Grassian, V. H. Interaction of Beta-Lactoglobulin and Bovine Serum Albumin with Iron Oxide (α-Fe2O3) Nanoparticles in the Presence and Absence of Pre-Adsorbed Phosphate. *Environ. Sci. Nano* **2021**, *8* (10), 2811–2823. https://doi.org/10.1039/D1EN00388G.

(196) Becke, A. D. Density-functional Thermochemistry. III. The Role of Exact Exchange. *J. Chem. Phys.* **1993**, *98* (7), 5648–5652. https://doi.org/10.1063/1.464913.

(197) Lee, C.; Yang, W.; Parr, R. G. Development of the Colle-Salvetti Correlation-Energy Formula into a Functional of the Electron Density. *Phys. Rev. B. Condens. Matter* **1988**, *37* (2), 785–789. https://doi.org/10.1103/physrevb.37.785.

(198) Frisch, M. J.; Trucks, G. W.; Schlegel, H. B.; Scuseria, G. E.; Robb, M. a.; Cheeseman, J. R.; Scalmani, G.; Barone, V.; Petersson, G. a.; Nakatsuji, H.; Li, X.; Caricato, M.; Marenich, a. V.; Bloino, J.; Janesko, B. G.; Gomperts, R.; Mennucci, B.; Hratchian, H. P.; Ortiz, J. V.; Izmaylov, a. F.; Sonnenberg, J. L.; Williams; Ding, F.; Lipparini, F.; Egidi, F.; Goings, J.; Peng, B.; Petrone, A.; Henderson, T.; Ranasinghe, D.; Zakrzewski, V. G.; Gao, J.; Rega, N.; Zheng, G.; Liang, W.; Hada, M.; Ehara, M.; Toyota, K.; Fukuda, R.; Hasegawa, J.; Ishida, M.; Nakajima, T.; Honda, Y.; Kitao, O.; Nakai, H.; Vreven, T.; Throssell, K.; Montgomery Jr., J. a.; Peralta, J. E.; Ogliaro, F.; Bearpark, M. J.; Heyd, J. J.; Brothers, E. N.; Kudin, K. N.; Staroverov, V. N.; Keith, T. a.; Kobayashi, R.; Normand, J.; Raghavachari, K.; Rendell, a. P.; Burant, J. C.; Iyengar, S. S.; Tomasi, J.; Cossi, M.; Millam, J. M.; Klene, M.; Adamo, C.; Cammi, R.; Ochterski, J. W.; Martin, R. L.; Morokuma, K.; Farkas, O.; Foresman, J. B.; Fox, D. J. G16_C01. 2016, p Gaussian 16, Revision C.01, Gaussian, Inc., Wallin.

(199) III, R. D. J. NIST Computational Chemistry Comparison and Benchmark Database http://cccbdb.nist.gov/.

(200) Sit, I.; Quirk, E.; Hettiarachchi, E.; Grassian, V. H. Differential Surface Interactions and

Surface Templating of Nucleotides (DGMP, DCMP, DAMP, and DTMP) on Oxide Particle Surfaces. *Langmuir* **2022**. https://doi.org/10.1021/acs.langmuir.2c01604.

(201) Qiao, C.; Yu, X.; Song, X.; Zhao, T.; Xu, X.; Zhao, S.; Gubbins, K. E. Enhancing Gas Solubility in Nanopores: A Combined Study Using Classical Density Functional Theory and Machine Learning. *Langmuir* **2020**, *36* (29), 8527–8536. https://doi.org/10.1021/acs.langmuir.0c01160.

(202) Knight, A. W.; Ilani-Kashkouli, P.; Harvey, J. A.; Greathouse, J. A.; Ho, T. A.; Kabengi, N.; Ilgen, A. G. Interfacial Reactions of Cu(Ii) Adsorption and Hydrolysis Driven by Nano-Scale Confinement. *Environ. Sci. Nano* **2020**, *7* (1), 68–80. https://doi.org/10.1039/C9EN00855A.

(203) Ilgen, A. G.; Kabengi, N.; Leung, K.; Ilani-Kashkouli, P.; Knight, A. W.; Loera, L. Defining Silica–Water Interfacial Chemistry under Nanoconfinement Using Lanthanides. *Environ. Sci. Nano* **2021**, *8* (2), 432–443. https://doi.org/10.1039/D0EN00971G.

(204) Ferreira, D. R.; Schulthess, C. P. The Nanopore Inner Sphere Enhancement Effect on Cation Adsorption: Sodium, Potassium, and Calcium. *Soil Sci. Soc. Am. J.* **2011**, *75* (2), 389–396. https://doi.org/10.2136/sssaj2010.0130nps.

(205) Epsztein, R.; DuChanois, R. M.; Ritt, C. L.; Noy, A.; Elimelech, M. Towards Single-Species Selectivity of Membranes with Subnanometre Pores. *Nat. Nanotechnol.* **2020**, *15* (6), 426–436. https://doi.org/10.1038/s41565-020-0713-6.

(206) Fumagalli, L.; Esfandiar, A.; Fabregas, R.; Hu, S.; Ares, P.; Janardanan, A.; Yang, Q.; Radha, B.; Taniguchi, T.; Watanabe, K.; Gomila, G.; Novoselov, K. S.; Geim, A. K. Anomalously Low Dielectric Constant of Confined Water. *Science (80-.).* **2018**, *360* (6395), 1339–1342. https://doi.org/10.1126/science.aat4191.

(207) Knight, A. W.; Kalugin, N. G.; Coker, E.; Ilgen, A. G. Water Properties under Nano-Scale Confinement. *Sci. Rep.* **2019**, *9* (1), 8246. https://doi.org/10.1038/s41598-019-44651-z.

(208) Takei, T.; Mukasa, K.; Kofuji, M.; Fuji, M.; Watanabe, T.; Chikazawa, M.; Kanazawa, T. Changes in Density and Surface Tension of Water in Silica Pores. *Colloid Polym. Sci.* **2000**, *278* (5), 475–480. https://doi.org/10.1007/s003960050542.

(209) Liu, X.; Lu, X.; Wang, R.; Meijer, E. J.; Zhou, H. Acidities of Confined Water in Interlayer Space of Clay Minerals. *Geochim. Cosmochim. Acta* **2011**, *75* (17), 4978–4986. https://doi.org/10.1016/j.gca.2011.06.011.

(210) Senapati, S.; Chandra, A. Dielectric Constant of Water Confined in a Nanocavity. *J. Phys. Chem. B* **2001**, *105* (22), 5106–5109. https://doi.org/10.1021/jp011058i.

(211) Varghese, S.; Kannam, S. K.; Hansen, J. S.; Sathian, S. P. Effect of Hydrogen Bonds on the Dielectric Properties of Interfacial Water. *Langmuir* **2019**, *35* (24), 8159–8166. https://doi.org/10.1021/acs.langmuir.9b00543.

(212) Breynaert, E.; Houlleberghs, M.; Radhakrishnan, S.; Grübel, G.; Taulelle, F.; Martens, J. A. Water as a Tuneable Solvent: A Perspective. *Chem. Soc. Rev.* **2020**, *49* (9), 2557–2569. https://doi.org/10.1039/C9CS00545E.

(213) Zhu, Y.; Derami, H. G.; Gupta, P.; Gupta, R.; Singamaneni, S.; Jun, Y.-S. Ionic Surface Propensity Controls pH in Nanopores. *Chem* **2022**. https://doi.org/10.1016/j.chempr.2022.07.021.

(214) Rubinovich, L.; Polak, M. The Intrinsic Role of Nanoconfinement in Chemical Equilibrium: Evidence from DNA Hybridization. *Nano Lett.* **2013**, *13* (5), 2247–2251. https://doi.org/10.1021/nl4008198.

(215) Lesnicki, D.; Wank, V.; Cyran, J. D.; Backus, E. H. G.; Sulpizi, M. Lower Degree of Dissociation of Pyruvic Acid at Water Surfaces than in Bulk. *Phys. Chem. Chem. Phys.* **2022**, *24* (22), 13510–13513. https://doi.org/10.1039/D2CP01293F.

(216) Mamlouk, D.; Gullo, M. Acetic Acid Bacteria: Physiology and Carbon Sources Oxidation. *Indian J. Microbiol.* **2013**, *53* (4), 377–384. https://doi.org/10.1007/s12088-013-0414-z.

(217) Farahani, H.; Shokouhi, M.; Rahimi-Nasrabadi, M.; Zare-Dorabei, R. Green Chemistry Approach to Analysis of Formic Acid and Acetic Acid in Aquatic Environment by Headspace Water-Based Liquid-Phase Microextraction and High-Performance Liquid Chromatography. *Toxicol. Environ. Chem.* **2016**, *98* (7), 714–726. https://doi.org/10.1080/02772248.2015.1126283.

(218) Budsberg, E.; Morales-Vera, R.; Crawford, J. T.; Bura, R.; Gustafson, R. Production Routes to Bio-Acetic Acid: Life Cycle Assessment. *Biotechnol. Biofuels* **2020**, *13* (1), 154. https://doi.org/10.1186/s13068-020-01784-y.

(219) Deshmukh, G.; Manyar, H. Production Pathways of Acetic Acid and Its Versatile Applications in the Food Industry. In *Biotechnological Applications of Biomass*; Basso, T. P., Basso, T. O., Basso, L. C., Eds.; IntechOpen: Rijeka, 2020. https://doi.org/10.5772/intechopen.92289.

(220) Kim, M. H.; Kim, C. S.; Lee, H. W.; Kim, K. Temperature Dependence of Dissociation Constants for Formic Acid and 2,6-Dinitrophenol in Aqueous Solutions up to 175 °C. *J. Chem. Soc., Faraday Trans.* **1996**, *92* (24), 4951–4956. https://doi.org/10.1039/FT9969204951.

(221) Wang, X.; Fu, H.; Du, D.; Zhou, Z.; Zhang, A.; Su, C.; Ma, K. The Comparison of PKa Determination between Carbonic Acid and Formic Acid and Its Application to Prediction of the Hydration Numbers. *Chem. Phys. Lett.* **2008**, *460* (1), 339–342. https://doi.org/10.1016/j.cplett.2008.05.074.

(222) Dutra, F. R.; Silva, C. de S.; Custodio, R. On the Accuracy of the Direct Method to Calculate PKa from Electronic Structure Calculations. *J. Phys. Chem. A* **2021**, *125* (1), 65–73. https://doi.org/10.1021/acs.jpca.0c08283.

(223) Goldberg, R. N.; Kishore, N.; Lennen, R. M. Thermodynamic Quantities for the Ionization Reactions of Buffers. *J. Phys. Chem. Ref. Data* **2002**, *31* (2), 231–370. https://doi.org/10.1063/1.1416902.

(224) Samuelsen, L.; Holm, R.; Lathuile, A.; Schönbeck, C. Buffer Solutions in Drug Formulation and Processing: How PKa Values Depend on Temperature, Pressure and Ionic Strength. *Int. J. Pharm.* **2019**, *560*, 357–364. https://doi.org/10.1016/j.ijpharm.2019.02.019.

(225) Moreno, M. A.; Gálvez, O.; Maté, B.; Herrero, V. J.; Escribano, R. Formate Ion: Structure and Spectroscopic Properties. *J. Phys. Chem. A* **2011**, *115* (1), 70–75. https://doi.org/10.1021/jp108326x.

(226) Park, J.-Y.; Woon, D. E. Theoretical Modeling of Formic Acid (HCOOH), Formate (HCOO–), and Ammonium (NH4+) Vibrational Spectra in Astrophysical Ices. *Astrophys. J.* **2006**, *648* (2), 1285–1290. https://doi.org/10.1086/506175.

(227) Park, J.; Woon, D. E. Theoretical Modeling of Formic Acid (HCOOH), Formate (HCOO–), and Ammonium (NH4+) Vibrational Spectra in Astrophysical Ices. *Astrophys. J.* **2006**, *648* (2), 1285–1290. https://doi.org/10.1086/506175.

(228) Ito, K.; Bernstein, H. The Vibrational Spectra of the Formate, Acetate, and Oxalate Ions. *Can. J. Chem.* **2011**, *34*, 170–178. https://doi.org/10.1139/v56-021.

(229) Kim, M. H.; Kim, C. S.; Lee, H. W.; Kim, K. Temperature Dependence of Dissociation Constants for Formic Acid and 2{,}6-Dinitrophenol in Aqueous Solutions up to 175 °C. *J. Chem. Soc.{,} Faraday Trans.* **1996**, *92* (24), 4951–4956. https://doi.org/10.1039/FT9969204951.

(230) Wang, X.; Fu, H.; Du, D.; Zhou, Z.; Zhang, A.; Su, C.; Ma, K. The Comparison of PKa Determination between Carbonic Acid and Formic Acid and Its Application to Prediction of the Hydration Numbers. *Chem. Phys. Lett.* **2008**, *460* (1), 339–342. https://doi.org/https://doi.org/10.1016/j.cplett.2008.05.074.

(231) Olbert-Majkut, A.; Ahokas, J.; Lundell, J.; Pettersson, M. Raman Spectroscopy of Formic Acid and Its Dimers Isolated in Low Temperature Argon Matrices. *Chem. Phys. Lett.* **2009**, *468* (4), 176–183. https://doi.org/10.1016/j.cplett.2008.12.011.

(232) Samuelsen, L.; Holm, R.; Lathuile, A.; Schönbeck, C. Buffer Solutions in Drug Formulation and Processing: How PKa Values Depend on Temperature, Pressure and Ionic Strength. *Int. J. Pharm.* **2019**, *560*, 357–364. https://doi.org/https://doi.org/10.1016/j.ijpharm.2019.02.019.

(233) Chandra, A.; Chattopadhyay, S. Chain Length and Acidity of Carboxylic Acids Influencing Adsorption/Desorption Mechanism and Kinetics over Anion Exchange Membrane. *Colloids Surfaces A Physicochem. Eng. Asp.* **2020**, *589*, 124395. https://doi.org/10.1016/j.colsurfa.2019.124395.

(234) Gao, H.-L.; Zhang, H.; Li, C.-Y.; Xia, X.-H. Confinement Effect of

Protonation/Deprotonation of Carboxylic Group Modified in Nanochannel. *Electrochim. Acta* **2013**, *110*, 159–163. https://doi.org/10.1016/j.electacta.2012.12.080.

(235) Knight, A. W.; Tigges, A. B.; Ilgen, A. G. Adsorption of Copper (II) on Mesoporous Silica: The Effect of Nano-Scale Confinement. *Geochem. Trans.* **2018**, *19* (1), 13. https://doi.org/10.1186/s12932-018-0057-4.

(236) Kosmulski, M. PH-Dependent Surface Charging and Points of Zero Charge. IV. Update and New Approach. *J. Colloid Interface Sci.* **2009**, *337* (2), 439–448. https://doi.org/10.1016/j.jcis.2009.04.072.

(237) Farfán, P.; Echeverri, A.; Diaz, E.; Tapia, J. D.; Gómez, S.; Restrepo, A. Dimers of Formic Acid: Structures, Stability, and Double Proton Transfer. *J. Chem. Phys.* **2017**, *147* (4), 44312. https://doi.org/10.1063/1.4985880.

(238) Rodziewicz, P.; Doltsinis, N. L. Formic Acid Dimerization: Evidence for Species Diversity from First Principles Simulations. *J. Phys. Chem. A* **2009**, *113* (22), 6266–6274. https://doi.org/10.1021/jp9007575.

(239) Nishi, N.; Nakabayashi, T.; Kosugi, K. Raman Spectroscopic Study on Acetic Acid Clusters in Aqueous Solutions: Dominance of Acid−Acid Association Producing Microphases. *J. Phys. Chem. A* **1999**, *103* (50), 10851–10858. https://doi.org/10.1021/jp9929061.

(240) Tang, M.; Larish, W. A.; Fang, Y.; Gankanda, A.; Grassian, V. H. Heterogeneous Reactions of Acetic Acid with Oxide Surfaces: Effects of Mineralogy and Relative Humidity. *J. Phys. Chem. A* **2016**, *120* (28), 5609–5616. https://doi.org/10.1021/acs.jpca.6b05395.

(241) Yang, B.; Li, Y.; Gong, N.; Cao, X.; Wang, S.; Sun, C. Study of Molecular Association in Acetic Acid-Water Binary Solution by Raman Spectroscopy. *Spectrochim. Acta Part A Mol. Biomol. Spectrosc.* **2019**, *213*, 463–466. https://doi.org/10.1016/j.saa.2018.08.029.

(242) Chocholoušová, J.; Vacek, J.; Hobza, P. Acetic Acid Dimer in the Gas Phase, Nonpolar Solvent, Microhydrated Environment, and Dilute and Concentrated Acetic Acid: Ab Initio Quantum Chemical and Molecular Dynamics Simulations. *J. Phys. Chem. A* **2003**, *107* (17), 3086–3092. https://doi.org/10.1021/jp027637k.

(243) Soffientini, S.; Bernasconi, L.; Imberti, S. The Hydration of Formic Acid and Acetic Acid. *J. Mol. Liq.* **2015**, *205*, 85–92. https://doi.org/10.1016/j.molliq.2014.11.030.

(244) Krishnakumar, P.; Maity, D. K. Microhydration of Neutral and Charged Acetic Acid. *J. Phys. Chem. A* **2017**, *121* (2), 493–504. https://doi.org/10.1021/acs.jpca.6b09257.

(245) Aloisio, S.; Hintze, P. E.; Vaida, V. The Hydration of Formic Acid. *J. Phys. Chem. A* **2002**, *106* (2), 363–370. https://doi.org/10.1021/jp012190l.

(246) Nie, B.; Stutzman, J.; Xie, A. A Vibrational Spectral Maker for Probing the Hydrogen-Bonding Status of Protonated Asp and Glu Residues. *Biophys. J.* **2005**, *88* (4), 2833–2847. https://doi.org/10.1529/biophysj.104.047639.

(247) Adams, E. M.; Hao, H.; Leven, I.; Rüttermann, M.; Wirtz, H.; Havenith, M.; Head-Gordon, T. Proton Traffic Jam: Effect of Nanoconfinement and Acid Concentration on Proton Hopping Mechanism. *Angew. Chemie Int. Ed.* **2021**, *60* (48), 25419–25427. https://doi.org/10.1002/anie.202108766.

(248) Nie, B.; Stutzman, J.; Xie, A. A Vibrational Spectral Maker for Probing the Hydrogen-Bonding Status of Protonated Asp and Glu Residues. *Biophys. J.* **2005**, *88* (4), 2833–2847. https://doi.org/https://doi.org/10.1529/biophysj.104.047639.

(249) Soffientini, S.; Bernasconi, L.; Imberti, S. The Hydration of Formic Acid and Acetic Acid. *J. Mol. Liq.* **2015**, *205*, 85–92. https://doi.org/https://doi.org/10.1016/j.molliq.2014.11.030.

(250) Shi, H.; Magaye, R.; Castranova, V.; Zhao, J. Titanium Dioxide Nanoparticles: A Review of Current Toxicological Data. *Part. Fibre Toxicol.* **2013**, *10* (1), 1. https://doi.org/10.1186/1743-8977-10-15.

(251) Suttiponparnit, K.; Jiang, J.; Sahu, M.; Suvachittanont, S.; Charinpanitkul, T.; Biswas, P. Role of Surface Area, Primary Particle Size, and Crystal Phase on Titanium Dioxide Nanoparticle Dispersion Properties. *Nanoscale Res Lett* **2010**, *6* (1), 1. https://doi.org/10.1007/s11671-010-9772-1.

(252) Mun, K.-S.; Alvarez, S. D.; Choi, W.-Y.; Sailor, M. J. A Stable, Label-Free Optical Interferometric Biosensor Based on TiO_2 Nanotube Arrays. *ACS Nano* **2010**, *4* (4), 2070–2076. https://doi.org/10.1021/nn901312f.

(253) Wu, S.; Weng, Z.; Liu, X.; Yeung, K. W. K.; Chu, P. Functionalized TiO_2 Based Nanomaterials for Biomedical Applications. *Adv. Funct. Mater.* **2014**, *24* (35), 5464–5481. https://doi.org/10.1002/adfm.201400706.

(254) Chen, X.; Selloni, A. Introduction: Titanium Dioxide (TiO_2) Nanomaterials. *Chem. Rev.* **2014**, *114* (19), 9281–9282. https://doi.org/10.1021/cr500422r.

(255) Oberdörster, G.; Oberdörster, E.; Oberdörster, J. Nanotoxicology: An Emerging Discipline Evolving from Studies of Ultrafine Particles. *Environ. Health Perspect.* **2005**, 823–839. https://doi.org/10.1289/ehp.7339.

(256) Roach, P.; Farrar, D.; Perry, C. C. Interpretation of Protein Adsorption: Surface-Induced Conformational Changes. *J. Am. Chem. Soc.* **2005**, *127* (22), 8168–8173. https://doi.org/10.1021/ja042898o.

(257) Tang, L.; Hu, P. T. and W. Surface Chemistry Influences Implant Biocompatibility. *Current Topics in Medicinal Chemistry*. 2008, pp 270–280. https://doi.org/http://dx.doi.org/10.2174/156802608783790901.

(258) Gebauer, J. S.; Malissek, M.; Simon, S.; Knauer, S. K.; Maskos, M.; Stauber, R. H.; Peukert, W.; Treuel, L. Impact of the Nanoparticle–Protein Corona on Colloidal Stability and Protein Structure. *Langmuir* **2012**, *28* (25), 9673–9679. https://doi.org/10.1021/la301104a.

(259) Roach, P.; Farrar, D.; Perry, C. C. Surface Tailoring for Controlled Protein Adsorption: Effect of Topography at the Nanometer Scale and Chemistry. *J. Am. Chem. Soc.* **2006**, *128* (12), 3939–3945. https://doi.org/10.1021/ja056278e.

(260) Brandes, N.; Welzel, P. B.; Werner, C.; Kroh, L. W. Adsorption-Induced Conformational Changes of Proteins onto Ceramic Particles: Differential Scanning Calorimetry and FTIR Analysis. *J. Colloid Interface Sci.* **2006**, *299* (1), 56–69. https://doi.org/10.1016/j.jcis.2006.01.065.

(261) Szewczuk-Karpisz, K.; Wiśniewska, M.; Myśliwiec, D. Albumin Adsorption Influence on the Stability of the Mesoporous Zirconia Suspension. *J. Ind. Eng. Chem.* **2015**, *32*, 113–119. https://doi.org/10.1016/j.jiec.2015.08.005.

(262) Yuan, B.; Murayama, K.; Yan, H. Study of Thermal Dynamics of Defatted Bovine Serum Albumin in D2O Solution by Fourier Transform Infrared Spectra and Evolving Factor Analysis. *Appl. Spectrosc.* **2007**, *61* (9), 921–927. https://doi.org/10.1366/000370207781745919.

(263) Tigerst; xf. Thermostability of Proteins. *Bios* **2005**, *76* (1), 22–27.

(264) Bischof, J. C.; He, X. Thermal Stability of Proteins. *Ann. N. Y. Acad. Sci.* **2006**, *1066* (1), 12–33.

(265) Dominguez-Medina, S.; Blankenburg, J.; Olson, J.; Landes, C. F.; Link, S. Adsorption of a Protein Monolayer via Hydrophobic Interactions Prevents Nanoparticle Aggregation under Harsh Environmental Conditions. *ACS Sustain. Chem. Eng.* **2013**, *1* (7), 833–842. https://doi.org/10.1021/sc400042h.

(266) Roche, M.; Rondeau, P.; Singh, N. R.; Tarnus, E.; Bourdon, E. The Antioxidant Properties of Serum Albumin. *FEBS Lett.* **2008**, *582* (13), 1783–1787. https://doi.org/10.1016/j.febslet.2008.04.057.

(267) Kannel, W. B.; Wolf, P. A.; Castelli, W. P.; D'Agostino, R. B. Fibrinogen and Risk of Cardiovascular Disease. *Jama* **1987**, *258* (9), 1183–1186. https://doi.org/10.1001/jama.1987.03400090067035.

(268) Danesh, J.; Lewington, S.; Thompson, S. G.; Lowe, G.; Collins, R.; Kostis, Jb.; Wilson, A. C.; Folsom, A. R.; Wu, K.; Benderly, M. Plasma Fibrinogen Level and the Risk of Major Cardiovascular Diseases and Nonvascular Mortality: An Individual Participant Meta-Analysis. *JAMA J. Am. Med. Assoc.* **2005**, *294* (14), 1799–1809. https://doi.org/10.1001/jama.294.14.1799.

(269) Ernst, E.; Resch, K. L. Fibrinogen as a Cardiovascular Risk Factor: A Meta-Analysis and Review of the Literature. *Ann. Intern. Med.* **1993**, *118* (12), 956–963. https://doi.org/10.7326/0003-4819-118-12-199306150-00008.

(270) Rahman, M.; Laurent, S.; Tawil, N.; Yahia, L.; Mahmoudi, M. *Protein-Nanoparticle Interactions*; Springer Berlin Heidelberg, 2013; Vol. 15. https://doi.org/10.1007/978-3-642-

37555-2.

(271) Yang, Q.; Zhang, Y.; Liu, M.; Ye, M.; Zhang, Y.; Yao, S. Study of Fibrinogen Adsorption on Hydroxyapatite and TiO_2 Surfaces by Electrochemical Piezoelectric Quartz Crystal Impedance and FTIR–ATR Spectroscopy. *Anal. Chim. Acta* **2007**, *597* (1), 58–66. https://doi.org/10.1016/j.aca.2007.06.025.

(272) Day, R.; Bennion, B. J.; Ham, S.; Daggett, V. Increasing Temperature Accelerates Protein Unfolding without Changing the Pathway of Unfolding. *J. Mol. Biol.* **2002**, *322* (1), 189–203. https://doi.org/10.1016/s0022-2836(02)00672-1.

(273) Maruyama, T.; Katoh, S.; Nakajima, M.; Nabetani, H.; Abbott, T. P.; Shono, A.; Satoh, K. FT-IR Analysis of BSA Fouled on Ultrafiltration and Microfiltration Membranes. *J. Memb. Sci.* **2001**, *192* (1–2), 201–207. https://doi.org/10.1016/S0376-7388(01)00502-6.

(274) Steiner, G.; Tunc, S.; Maitz, M.; Salzer, R. Conformational Changes during Protein Adsorption. FT-IR Spectroscopic Imaging of Adsorbed Fibrinogen Layers. *Anal. Chem.* **2007**, *79* (4), 1311–1316. https://doi.org/10.1021/ac061341j.

(275) Tao, Y. C.; Wu, Y. Q.; Zhang, L. P. Advancements of Two Dimensional Correlation Spectroscopy in Protein Researches. *Spectrochim. Acta Part a-Molecular Biomol. Spectrosc.* **2018**, *197*, 185–193. https://doi.org/10.1016/j.saa.2018.01.039.

(276) Bernabeu, A.; Contreras, L. M.; Villalain, J. Two-Dimensional Infrared Correlation Spectroscopy Study of the Interaction of Oxidized and Reduced Cytochrome c with Phospholipid Model Membranes. *Biochim. Biophys. Acta-Biomembranes* **2007**, *1768* (10), 2409–2420. https://doi.org/10.1016/j.bbamem.2007.05.002.

(277) Saguer, E.; Alvarez, P.; Sedman, J.; Ramaswamy, H. S.; Ismail, A. A. Heat-Induced Gel Formation of Plasma Proteins: New Insights by FTIR 2D Correlation Spectroscopy. *Food Hydrocoll.* **2009**, *23* (3), 874–879. https://doi.org/10.1016/j.foodhyd.2008.03.013.

(278) Thomas, M.; Richardson, H. H. Two-Dimensional FT-IR Correlation Analysis of the Phase Transitions in a Liquid Crystal, 4 ’-n-Octyl-4-Cyanobiphenyl (8CB). *Vib. Spectrosc.* **2000**, *24* (1), 137–146. https://doi.org/10.1016/s0924-2031(00)00086-2.

(279) Salis, A.; Boström, M.; Medda, L.; Cugia, F.; Barse, B.; Parsons, D. F.; Ninham, B. W.; Monduzzi, M. Measurements and Theoretical Interpretation of Points of Zero Charge/Potential of BSA Protein. *Langmuir* **2011**, *27* (18), 11597–11604. https://doi.org/10.1021/la2024605.

(280) Rezwan, K.; Studart, A. R.; Vörös, J.; Gauckler, L. J. Change of ζ Potential of Biocompatible Colloidal Oxide Particles upon Adsorption of Bovine Serum Albumin and Lysozyme. *J. Phys. Chem. B* **2005**, *109* (30), 14469–14474. https://doi.org/10.1021/jp050528w.

(281) Privalov, P. L.; Medved, L. V. Domains in the Fibrinogen Molecule. *J. Mol. Biol.* **1982**, *159* (4), 665–683. https://doi.org/10.1016/0022-2836(82)90107-3.

(282) Schwinte, P.; Voegel, J.-C.; Picart, C.; Haikel, Y.; Schaaf, P.; Szalontai, B. Stabilizing Effects of Various Polyelectrolyte Multilayer Films on the Structure of Adsorbed/Embedded Fibrinogen Molecules: An ATR-FTIR Study. *J. Phys. Chem. B* **2001**, *105* (47), 11906–11916.

(283) Pazderka, T.; Kopecký, V. *2D Correlation Spectroscopy and Its Application in Vibrational Spectroscopy Using Matlab*; 2019. https://doi.org/10.1016/B978-0-12-849883-5.00010-3.

(284) Chen, Y.; Mao, H.; Zhang, X.; Gong, Y.; Zhao, N. Thermal Conformational Changes of Bovine Fibrinogen by Differential Scanning Calorimetry and Circular Dichroism. *Int. J. Biol. Macromol.* **1999**, *26* (2–3), 129–134.

(285) Bouhekka, A.; Burgi, T. In Situ ATR-IR Spectroscopy Study of Adsorbed Protein: Visible Light Denaturation of Bovine Serum Albumin on TiO_2. *Appl. Surf. Sci.* **2012**, *261*, 369–374. https://doi.org/10.1016/j.apsusc.2012.08.017.

(286) Giuseppina, R.; Fabio, G. Molecular Modelling of Protein Adsorption on the Surface of Titanium Dioxide Polymorphs. *Philos. Trans. R. Soc. A Math. Phys. Eng. Sci.* **2012**, *370* (1963), 1444–1462. https://doi.org/10.1098/rsta.2011.0266.

(287) Noh, H.; Vogler, E. A. Volumetric Interpretation of Protein Adsorption: Partition Coefficients, Interphase Volumes, and Free Energies of Adsorption to Hydrophobic Surfaces. *Biomaterials* **2006**, *27* (34), 5780–5793. https://doi.org/https://doi.org/10.1016/j.biomaterials.2006.07.038.

(288) Kim, J.; Somorjai, G. A. Molecular Packing of Lysozyme, Fibrinogen, and Bovine Serum Albumin on Hydrophilic and Hydrophobic Surfaces Studied by Infrared−Visible Sum Frequency Generation and Fluorescence Microscopy. *J. Am. Chem. Soc.* **2003**, *125* (10), 3150–3158. https://doi.org/10.1021/ja028987n.

(289) Givens, B. E.; Xu, Z. Z.; Fiegel, J.; Grassian, V. H. Bovine Serum Albumin Adsorption on SiO 2 and TiO 2 Nanoparticle Surfaces at Circumneutral and Acidic pH: A Tale of Two Nano-Bio Surface Interactions. *J. Colloid Interface Sci.* **2017**, *493*, 334–341. https://doi.org/10.1016/j.jcis.2017.01.011.

(290) Yang, Q.; Zhang, Y.; Liu, M.; Ye, M.; Zhang, Y.; Yao, S. Study of Fibrinogen Adsorption on Hydroxyapatite and TiO_2 Surfaces by Electrochemical Piezoelectric Quartz Crystal Impedance and FTIR–ATR Spectroscopy. *Anal. Chim. Acta* **2007**, *597* (1), 58–66. https://doi.org/10.1016/J.ACA.2007.06.025.

(291) Pegueroles, M.; Tonda-Turo, C.; Planell, J. A.; Gil, F.-J.; Aparicio, C. Adsorption of Fibronectin, Fibrinogen, and Albumin on TiO_2: Time-Resolved Kinetics, Structural Changes, and Competition Study. *Biointerphases* **2012**, *7* (1), 1–13. https://doi.org/10.1007/s13758-012-0048-4.

(292) Komives, E. A. Protein–Protein Interaction Dynamics by Amide H/2H Exchange Mass Spectrometry. *Int. J. Mass Spectrom.* **2005**, *240* (3), 285–290. https://doi.org/https://doi.org/10.1016/j.ijms.2004.09.016.

(293) Truhlar, S. M. E.; Croy, C. H.; Torpey, J. W.; Koeppe, J. R.; Komives, E. A. Solvent Accessibility of Protein Surfaces by Amide H/2H Exchange MALDI-TOF Mass Spectrometry. *J. Am. Soc. Mass Spectrom.* **2006**, *17* (11), 1490–1497. https://doi.org/https://doi.org/10.1016/j.jasms.2006.07.023.

(294) Lundqvist, M.; Sethson, I.; Jonsson, B.-H. Protein Adsorption onto Silica Nanoparticles: Conformational Changes Depend on the Particles' Curvature and the Protein Stability. *Langmuir* **2004**, *20* (24), 10639–10647. https://doi.org/10.1021/la0484725.

(295) Calzolai, L.; Franchini, F.; Gilliland, D.; Rossi, F. Protein−Nanoparticle Interaction: Identification of the Ubiquitin−Gold Nanoparticle Interaction Site. *Nano Lett.* **2010**, *10* (8), 3101–3105. https://doi.org/10.1021/nl101746v.

(296) Shahbazi, K.; Frey, W.; Chen, Y.-S.; Aglyamov, S.; Emelianov, S. Photoacoustics of Core–Shell Nanospheres Using Comprehensive Modeling and Analytical Solution Approach. *Commun. Phys.* **2019**, *2* (1), 119. https://doi.org/10.1038/s42005-019-0216-7.

(297) Knights, O. B.; Ye, S.; Ingram, N.; Freear, S.; McLaughlan, J. R. Optimising Gold Nanorods for Photoacoustic Imaging in Vitro. *Nanoscale Adv.* **2019**, *1* (4), 1472–1481. https://doi.org/10.1039/C8NA00389K.

(298) Lohse, S. E.; Murphy, C. J. The Quest for Shape Control: A History of Gold Nanorod Synthesis. *Chem. Mater.* **2013**, *25* (8), 1250–1261. https://doi.org/10.1021/cm303708p.

(299) Dhada, K. S.; Hernandez, D. S.; Suggs, L. J. In Vivo Photoacoustic Tracking of Mesenchymal Stem Cell Viability. *ACS Nano* **2019**, *13* (7), 7791–7799. https://doi.org/10.1021/acsnano.9b01802.

(300) Jokerst, J. V; Cole, A. J.; Van de Sompel, D.; Gambhir, S. S. Gold Nanorods for Ovarian Cancer Detection with Photoacoustic Imaging and Resection Guidance via Raman Imaging in Living Mice. *ACS Nano* **2012**, *6* (11), 10366–10377. https://doi.org/10.1021/nn304347g.

(301) Guo, D.; Huang, Y.; Jin, X.; Zhang, C.; Zhu, X. A Redox-Responsive, In-Situ Polymerized Polyplatinum(IV)-Coated Gold Nanorod as An Amplifier of Tumor Accumulation for Enhanced Thermo-Chemotherapy. *Biomaterials* **2021**, *266*, 120400. https://doi.org/10.1016/j.biomaterials.2020.120400.

(302) Li, P.-C.; Wei, C.-W.; Liao, C.-K.; Chen, C.-D.; Pao, K.-C.; Wang, C.-R. C.; Wu, Y.-N.; Shieh, D.-B. Photoacoustic Imaging of Multiple Targets Using Gold Nanorods. *IEEE Trans. Ultrason. Ferroelectr. Freq. Control* **2007**, *54* (8), 1642–1647. https://doi.org/10.1109/TUFFC.2007.435.

(303) Mantri, Y.; Davidi, B.; Lemaster, J. E.; Hariri, A.; Jokerst, J. V. Iodide-Doped Precious Metal Nanoparticles: Measuring Oxidative Stress in Vivo via Photoacoustic Imaging. *Nanoscale* **2020**, *12* (19), 10511–10520. https://doi.org/10.1039/D0NR03047C.

(304) Kim, T.; Zhang, Q.; Li, J.; Zhang, L.; Jokerst, J. V. A Gold/Silver Hybrid Nanoparticle for Treatment and Photoacoustic Imaging of Bacterial Infection. *ACS Nano* **2018**, *12* (6), 5615–

5625. https://doi.org/10.1021/acsnano.8b01362.

(305) Cavigli, L.; Centi, S.; Borri, C.; Tortoli, P.; Panettieri, I.; Streit, I.; Ciofini, D.; Magni, G.; Rossi, F.; Siano, S.; Ratto, F.; Pini, R. 1064-Nm-Resonant Gold Nanorods for Photoacoustic Theranostics within Permissible Exposure Limits. *J. Biophotonics* **2019**, *12* (10), e201900082. https://doi.org/10.1002/jbio.201900082.

(306) Xu, M.; Wang, L. V. Photoacoustic Imaging in Biomedicine. *Rev. Sci. Instrum.* **2006**, *77* (4), 41101. https://doi.org/10.1063/1.2195024.

(307) Shi, Y.; Qin, H.; Yang, S.; Xing, D. Thermally Confined Shell Coating Amplifies the Photoacoustic Conversion Efficiency of Nanoprobes. *Nano Res.* **2016**, *9* (12), 3644–3655. https://doi.org/10.1007/s12274-016-1234-3.

(308) Mantri, Y.; Jokerst, J. V. Engineering Plasmonic Nanoparticles for Enhanced Photoacoustic Imaging. *ACS Nano* **2020**, *14* (8), 9408–9422. https://doi.org/10.1021/acsnano.0c05215.

(309) Zhong, J.; Wen, L.; Yang, S.; Xiang, L.; Chen, Q.; Xing, D. Imaging-Guided High-Efficient Photoacoustic Tumor Therapy with Targeting Gold Nanorods. *Nanomedicine* **2015**, *11* (6), 1499–1509. https://doi.org/10.1016/j.nano.2015.04.002.

(310) Jokerst, J. V; Thangaraj, M.; Kempen, P. J.; Sinclair, R.; Gambhir, S. S. Photoacoustic Imaging of Mesenchymal Stem Cells in Living Mice via Silica-Coated Gold Nanorods. *ACS Nano* **2012**, *6* (7), 5920–5930. https://doi.org/10.1021/nn302042y.

(311) Chen, Y.-S.; Frey, W.; Kim, S.; Kruizinga, P.; Homan, K.; Emelianov, S. Silica-Coated Gold Nanorods as Photoacoustic Signal Nanoamplifiers. *Nano Lett.* **2011**, *11* (2), 348–354. https://doi.org/10.1021/nl1042006.

(312) Yim, W.; Borum, R. M.; Zhou, J.; Mantri, Y.; Wu, Z.; Zhou, J.; Jin, Z.; Creyer, M.; Jokerst, J. V. Ultrasmall Gold Nanorod-Polydopamine Hybrids for Enhanced Photoacoustic Imaging and Photothermal Therapy in Second near-Infrared Window. *Nanotheranostics* **2022**, *6* (1), 79–90. https://doi.org/10.7150/ntno.63634.

(313) Moore, C.; Jokerst, J. V. Strategies for Image-Guided Therapy, Surgery, and Drug Delivery Using Photoacoustic Imaging. *Theranostics* **2019**, *9* (6), 1550–1571. https://doi.org/10.7150/thno.32362.

(314) Mantri, Y.; Sit, I.; Zhou, J.; Grassian, V. H.; Jokerst, J. V. Photoacoustic Enhancement of Ferricyanide-Treated Silver Chalcogenide-Coated Gold Nanorods. *J. Phys. Chem. C* **2022**, *126* (17), 7605–7614. https://doi.org/10.1021/acs.jpcc.2c01727.

(315) He, J.; Unser, S.; Bruzas, I.; Cary, R.; Shi, Z.; Mehra, R.; Aron, K.; Sagle, L. The Facile Removal of CTAB from the Surface of Gold Nanorods. *Colloids Surf. B. Biointerfaces* **2018**, *163*, 140–145. https://doi.org/10.1016/j.colsurfb.2017.12.019.

(316) Cheah, M. H.; Chernev, P. Electrochemical Oxidation of Ferricyanide. *Sci. Rep.* **2021**, *11* (1), 23058. https://doi.org/10.1038/s41598-021-02355-3.

(317) Loo, B. H.; Lee, Y. G.; Liang, E. J.; Kiefer, W. Surface-Enhanced Raman Scattering from Ferrocyanide and Ferricyanide Ions Adsorbed on Silver and Copper Colloids. *Chem. Phys. Lett.* **1998**, *297*, 83–89. https://doi.org/10.1016/S0009-2614(98)01120-8.

(318) World Health Organization. *WHO Global Air Quality Guidelines: Particulate Matter (PM2.5 and PM10), Ozone, Nitrogen Dioxide, Sulfur Dioxide and Carbon Monoxide*; 2021.

(319) World Health Organization. *Ambient Air Pollution: A Global Assessment of Exposure and Burden of Disease*; 2016.

(320) Landrigan, P. J. Air Pollution and Health. *Lancet Public Heal.* **2017**, *2* (1), e4–e5. https://doi.org/10.1016/S2468-2667(16)30023-8.

(321) Miller, M. R.; Shaw, C. A.; Langrish, J. P. From Particles to Patients: Oxidative Stress and the Cardiovascular Effects of Air Pollution. *Future Cardiol.* **2012**, *8* (4), 577–602. https://doi.org/10.2217/fca.12.43.

(322) Ucciferri, N.; Collnot, E. M.; Gaiser, B. K.; Tirella, A.; Stone, V.; Domenici, C.; Lehr, C. M.; Ahluwalia, A. In Vitro Toxicological Screening of Nanoparticles on Primary Human Endothelial Cells and the Role of Flow in Modulating Cell Response. *Nanotoxicology* **2014**, *8* (6), 697–708. https://doi.org/10.3109/17435390.2013.831500.

(323) Raftis, J. B.; Miller, M. R. Nanoparticle Translocation and Multi-Organ Toxicity: A Particularly Small Problem. *Nano Today* **2019**, *26*, 8–12. https://doi.org/10.1016/j.nantod.2019.03.010.

(324) Park, E.-J.; Kim, S.-W.; Yoon, C.; Kim, Y.; Kim, J. S. Disturbance of Ion Environment and Immune Regulation Following Biodistribution of Magnetic Iron Oxide Nanoparticles Injected Intravenously. *Toxicol. Lett.* **2016**, *243*, 67–77. https://doi.org/10.1016/j.toxlet.2015.11.030.

(325) Jomova, K.; Valko, M. Advances in Metal-Induced Oxidative Stress and Human Disease. *Toxicology* **2011**, *283* (2), 65–87. https://doi.org/10.1016/j.tox.2011.03.001.

(326) Yang, H.; Liu, C.; Yang, D.; Zhang, H.; Xi, Z. Comparative Study of Cytotoxicity, Oxidative Stress and Genotoxicity Induced by Four Typical Nanomaterials: The Role of Particle Size, Shape and Composition. *J. Appl. Toxicol.* **2009**, *29* (1), 69–78. https://doi.org/10.1002/jat.1385.

(327) Belder, T. De. European Union: Titanium Dioxide Banned as a Food Additive in the EU https://www.fas.usda.gov/data/european-union-titanium-dioxide-banned-food-additive-eu (accessed Oct 28, 2022).

(328) Love, S. A.; Maurer-Jones, M. A.; Thompson, J. W.; Lin, Y.-S.; Haynes, C. L. Assessing Nanoparticle Toxicity. *Annu. Rev. Anal. Chem.* **2012**, *5* (1), 181–205. https://doi.org/10.1146/annurev-anchem-062011-143134.

(329) Veldhuizen, J.; Migrino, R. Q.; Nikkhah, M. Three-Dimensional Microengineered Models

of Human Cardiac Diseases. *J. Biol. Eng.* **2019**, *13* (1), 1–12. https://doi.org/10.1186/s13036-019-0155-6.

(330) Mathur, A.; Loskill, P.; Shao, K.; Huebsch, N.; Hong, S. G.; Marcus, S. G.; Marks, N.; Mandegar, M.; Conklin, B. R.; Lee, L. P.; Healy, K. E. Human IPSC-Based Cardiac Microphysiological System for Drug Screening Applications. *Sci. Rep.* **2015**, *5*, 1–7. https://doi.org/10.1038/srep08883.

(331) Huebsch, N.; Loskill, P.; Deveshwar, N.; Spencer, C. I.; Judge, L. M.; Mandegar, M. A.; Fox, C. B.; Mohamed, T. M. A.; Ma, Z.; Mathur, A.; Sheehan, A. M.; Truong, A.; Saxton, M.; Yoo, J.; Srivastava, D.; Desai, T. A.; So, P. L.; Healy, K. E.; Conklin, B. R. Miniaturized IPS-Cell-Derived Cardiac Muscles for Physiologically Relevant Drug Response Analyses. *Sci. Rep.* **2016**, *6*, 1–12. https://doi.org/10.1038/srep24726.

(332) Zuppinger, C. 3D Cardiac Cell Culture: A Critical Review of Current Technologies and Applications. *Front. Cardiovasc. Med.* **2019**, 1–9. https://doi.org/10.3389/fcvm.2019.00087.

(333) Miller, K. L.; Xiang, Y.; Yu, C.; Pustelnik, J.; Wu, J.; Ma, X.; Matsui, T.; Imahashi, K.; Chen, S. Rapid 3D BioPrinting of a Human IPSC-Derived Cardiac Micro-Tissue for High-Throughput Drug Testing. *Organs-on-a-Chip* **2021**, *3* (March), 100007. https://doi.org/10.1016/j.ooc.2021.100007.

(334) Zhou, H.; Yao, L.; Jiang, X.; Sumayyah, G.; Tu, B.; Cheng, S.; Qin, X.; Zhang, J.; Zou, Z.; Chen, C. Pulmonary Exposure to Copper Oxide Nanoparticles Leads to Neurotoxicity via Oxidative Damage and Mitochondrial Dysfunction. *Neurotox. Res.* **2021**, *39* (4), 1160–1170. https://doi.org/10.1007/s12640-021-00358-6.

(335) Naz, S.; Gul, A.; Zia, M. Toxicity of Copper Oxide Nanoparticles: A Review Study. *IET Nanobiotechnology* **2020**, *14* (1), 1–13. https://doi.org/10.1049/iet-nbt.2019.0176.

(336) Hamouda, R. A.; Heikal, H. S. Comparative Toxicological Effects of Biologically and Chemically Synthesized Copper Oxide Nanoparticles on Mice. *Int. J. Nanomedicine* **2020**, 3827–3842. https://doi.org/10.2147/IJN.S241922.

(337) Keller, A. A.; Adeleye, A. S.; Conway, J. R.; Garner, K. L.; Zhao, L.; Cherr, G. N.; Hong, J.; Gardea-Torresdey, J. L.; Godwin, H. A.; Hanna, S.; Ji, Z.; Kaweeteerawat, C.; Lin, S.; Lenihan, H. S.; Miller, R. J.; Nel, A. E.; Peralta-Videa, J. R.; Walker, S. L.; Taylor, A. A.; Torres-Duarte, C.; Zink, J. I.; Zuverza-Mena, N. Comparative Environmental Fate and Toxicity of Copper Nanomaterials. *NanoImpact* **2017**, *7*, 28–40. https://doi.org/10.1016/j.impact.2017.05.003.

(338) Lu, R. X. Z.; Radisic, M. Organ-on-a-Chip Platforms for Evaluation of Environmental Nanoparticle Toxicity. *Bioact. Mater.* **2021**, *6* (9), 2801–2819. https://doi.org/10.1016/j.bioactmat.2021.01.021.

(339) Lu, R. X. Z.; Lai, B. F. L.; Benge, T.; Wang, E. Y.; Davenport Huyer, L.; Rafatian, N.; Radisic, M. Heart-on-a-Chip Platform for Assessing Toxicity of Air Pollution Related

Nanoparticles. *Adv. Mater. Technol.* **2021**, *6* (2), 1–15. https://doi.org/10.1002/admt.202000726.

(340) Corbo, C.; Molinaro, R.; Parodi, A.; Toledano Furman, N. E.; Salvatore, F.; Tasciotti, E. The Impact of Nanoparticle Protein Corona on Cytotoxicity, Immunotoxicity and Target Drug Delivery. *Nanomedicine* **2015**, *11* (1), 81–100. https://doi.org/10.2217/nnm.15.188.

(341) Yamada, Y.; Fichman, G.; Schneider, J. P. Serum Protein Adsorption Modulates the Toxicity of Highly Positively Charged Hydrogel Surfaces. *ACS Appl. Mater. Interfaces* **2021**, *13* (7), 8006–8014. https://doi.org/10.1021/acsami.0c21596.

(342) Gelamo, E. L.; Tabak, M. Spectroscopic Studies on the Interaction of Bovine (BSA) and Human (HSA) Serum Albumins with Ionic Surfactants. *Spectrochim. Acta Part A Mol. Biomol. Spectrosc.* **2000**, *56* (11), 2255–2271. https://doi.org/10.1016/S1386-1425(00)00313-9.